On the origins of pediatric brain cancer

Bockaj, Irena

DOI:
10.33612/diss.156023051

On the origins of pediatric brain cancer
Exploring the role of genome instability in development and disease

Irena Bočkaj

The work described in this thesis was conducted at the Departments of Pediatric Oncology and Hematology/Pediatrics and the European Research Institute for the Biology of Ageing (ERIBA), University Medical Centre Groningen, University of Groningen, the Netherlands.

Cover design & Layout: Irena Bočkaj

Printing: Gildeprint B.V., www.gildeprint.nl

university of groningen

On the origins of pediatric brain cancer

Exploring the role of genome instability in development and disease

PhD thesis

to obtain the degree of PhD at the
University of Groningen
on the authority of the
Rector Magnificus Prof. C. Wijmenga
and in accordance with
the decision by the College of Deans.

This thesis will be defended in public on

Monday 15 February 2021 at 11.00 hours

by

Irena Bočkaj

born on 19 September 1988
in Mostar, Bosnia & Herzegovina

Supervisor
Prof. E.S.J.M. de Bont

Co-supervisor
Dr. S.W.M. Bruggeman

Assessment Committee
Prof. H.J.P. te Riele
Prof. B.J.L. Eggen
Prof. M.A.T.M. van Vugt

Table of Contents

General Introduction

Pediatric brain cancer & brain development

1

On the origins of pediatric brain cancer: when normal development goes astray

Irena Bočkaj [1] & Sophia W. M. Bruggeman [1]

[1] Department of Ageing Biology/ERIBA, University Medical Center Groningen, University of Groningen, Antonius Deusinglaan 1, 9713 AV Groningen, the Netherlands

Introduction

Children with cancer account for less than 1% of all cancers diagnosed worldwide every year, yet it is the leading cause of death by disease in this age-group in the developed world[1,2]. Current research suggests that around 10% of all children with cancer harbor a cancer predisposition syndrome with germline mutations[3–5]. In consequence, the remaining majority of childhood cancers cannot be prevented nor screened for. Approximately 80% of children will survive five years after diagnosis (versus only 20% in low- and middle-income countries)[1].

For a long time, childhood cancers were believed to be similar to their tissue-related adult counterparts, and were treated as such. Therefore, an important milestone has been achieved by fully separating childhood from adult cancers at the histological and molecular levels[6]. This will hopefully in the future lead to the development of less damaging and more specific treatments for childhood cancers.

Of all childhood cancers, brain tumors account for more than 20% of malignancies in children and remain the primary cause of cancer related death[3]. Over the past decade, colossal efforts to unfold the genomic landscape of the full spectrum of childhood brain cancers revealed a far more complex collection of diseases than previously appreciated[7–10]. Indeed, the field of neuro-oncology has experienced a tremendous shift in the understanding of this disease thanks to technological advancements in genome- and epigenome-wide profiling[8,9,11–14]. However, to date, 40 to 80 % of children still succumb to the disease within five years after diagnosis, and for those who are effectively cured, the long-term sequelae resulting from unspecific treatment strategies remain a major source of concern. These side-effects greatly impair survivors from efficiently participating in society as they reach adulthood[15]. Hopefully, the current effort to unravel the genetic make-up of these cancers will expand the toolbox of therapeutically targetable options and bring the first successful omics-based clinical trials to light. In the meantime, understanding the molecular and genetic pathogenesis of all brain cancers in children will offer better opportunities to develop tailored therapies.

The most common brain malignancies are gliomas followed by medulloblastomas (MB) (Fig 1 ; red ; 20% of total brain cancer cases). The majority of pediatric gliomas are non-malignant, slow-growing lesions graded I or II by the

WHO classification of central nervous system (CNS) tumors (also termed low-grade glioma (LGG) (Fig 1 ; black)[16]. Malignant transformation of LGG is rare. Their outcome is typically good as they are effectively managed under current treatment strategies[17]. Nevertheless, an important fraction of gliomas evolves rapidly and are therefore classified as WHO grade III or IV high-grade gliomas (HGGs) (Fig 1 ; light and dark green ; 16% of total brain cancer cases).

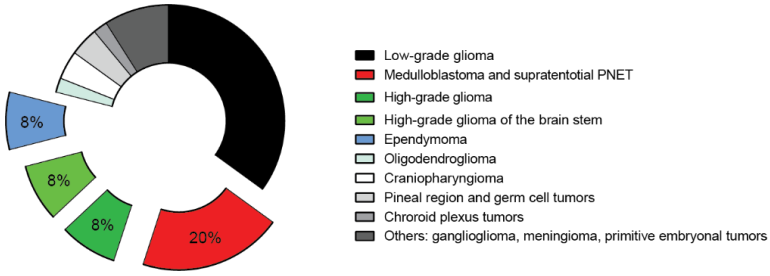

Figure 1. Distribution of pediatric brain tumors based on histological classification for children between 0 and 14 years of age. Figure and data were adapted from Yoko T. Udaka *et al.*[18]

Most of the underlying etiology of childhood brain cancers remains to be unveiled as there are few known risk factors. Contrary to adult cancers, it is not believed that environmental cues contribute to the pathogenesis of brain cancer in children, with the exception of tumors secondary to radiation therapy in the head and neck region[19–22]. However, the high predisposition to develop brain cancer in several inherited genetic syndromes (Ataxia Telangiectasia, Neurofibromatosis, Tuberous Sclerosis, Li-Fraumeni syndrome, von Hippel-Lindau, Turcot and Gorlin syndromes and constitutional Mismatch Repair (MMR) deficiency, to name a few) suggests that specific mutations are strong contributors to childhood CNS tumors[5,23]. It also appears that the study of these heritable disorders helps to uncover new molecular oncogenic drivers of none-germline brain cancers and thus helps shaping the venue of a genetic based classification.

Molecular classification of pediatric brain cancers

Until recently, the classification and nomenclature of brain cancers was solely based on morphological aspects evaluated by pathologists under the microscope. Pediatric brain cancers were subdivided into ten major types (Fig 1), depending on cellular morphology and the brain area of tumor location[24]. At the present day, the latest WHO brain cancer classification has incorporated genetically informed hallmarks to the morphology based classification[16]. As such, the 2016 WHO classification displays major rearrangements in the categories of high-grade gliomas and medulloblastomas. It incorporates new entities both defined by histologic and molecular features[16].

Here, we will summarize the current state-of-the field in molecular characterization of medulloblastoma (MB) and high-grade glioma (HGG). These tumors are also the focus of this thesis.

Medulloblastoma

MB is the most common pediatric brain malignancy[18]. It localizes to the posterior fossa region of the brain including the cerebellum[25]. Although it can also be found sporadically in adults, MB essentially remains a pediatric disease. MBs are historically defined as embryonal tumors and therefore incorporated in this general category by the WHO classification of CNS tumors[16,24]. Over the years, and with the rise of large-scale genomic sequencing, convincing data ensures that MBs are in fact heterogeneous at the molecular level and composed of discrete entities that should therefore be subcategorized. From 2008, first Kool *et al*. followed by Cho *et al.* and Northcott *et al.*, provided the first genetically-informed classifications that separate MB into four molecular subgroups, namely: Sonic-hedgehog (SHH), WNT, Group 3 and Group 4 (Fig 2A)[26–28]. This is now a consensus classification and has been incorporated in the new WHO grading of brain tumors, is used in routine diagnostics, and helps guide clinical trials design and future therapeutic decisions[16]. Since then, the avenue of multi-omics technologies and the enlargement of patient cohorts with increasing numbers of tumor tissue from international collaborations has

further enriched multi-omics (transcript-, gen-, epigen-, prote-omic) data generation[10,26,29–35]. The latest studies have highlighted further stratification within the four consensus subgroups and an even more complex classification emerged with up to 12 molecular subtypes [13,30,36].

Very recently, single-cell sequencing approaches have added to this complexity and revealed extensive intra-tumoral heterogeneity in MB (see also **Chapter 3** of this thesis). Importantly, single cell sequencing allows addressing questions on the developmental origins of MB and adds a spatial dimension that enables studying genetic intra-tumor evolution[37].

Here, specific attention is given to SHH-MB as it is one of the primary interests of the work described in this thesis (**Chapter 3** and **Chapter 4**) (Fig 2B).

SHH medulloblastoma

SHH-MB is the most frequent subtype of MB (30% of all MB cases). They arise mainly on the cerebellar hemispheres in contrast to the three other subgroups that are typically found in the midline region of the cerebellum[38]. Interestingly, their incidence follows a bimodal age distribution where SHH-MB is the major subtype in infants (up to 3 years of age) and adults (older than 17 years old). They appear to be less frequent during childhood[28] (Fig 2B). Furthermore, infant and adult medulloblastoma display distinct gene expression patterns, as well as differences in copy number alterations, mutations, and tumor localization. This patient age-related heterogeneity within the SHH-subgroup strongly suggests that developmental cues underly tumor biology[13,29,30,39–42]. Deregulation of the SHH signaling pathway characterizes SHH-MB. The presence of mutually exclusive mutations of SHH-players highlights the importance of this key neuro-developmental pathway in driving tumorigenesis[39,43]. The mutational landscape includes inactivation of Patched Homologue 1 (*PTCH1*) and Suppressor of Fused Homologue (*SUFU*) (germline or somatic), activating mutation of Smoothened Homologue (*SMO*), and *GLI2* amplifications[44]. Typical chromosomal rearrangements have also been attributed to SHH-MB, such as loss of chromosomes 9q, 10q, 14q and 17p and gain of chromosomes 2, 3q and 9p[13,29] (Fig 2A). Three independent studies further sub-stratified SHH-MB into four subtypes segregating by age and mutational status:

SHHα and SHHδ corresponding to childhood and adult, respectively, while SHHβ and SHHɣ correspond to infants[13,30,36]. The SHHα subtype associated with *TP53* mutations harbors the worst prognosis and is the most genomically unstable[30] (Fig 2B) (See also **Chapter 3** and **Chapter 4** of this thesis).

WNT medulloblastoma

WNT-MB shows the best prognosis of all MB, with a 5-year survival of 95%. The mean age of diagnosis is ~11 years old, however WNT-MB can be seen as early as 4 years old up until early adulthood. Mutations in the WNT pathway are a hallmark for these tumors and *CTNNB1* is most frequently affected (85% of patients). Germline mutations in the *APC* gene are also found. The WNT-MB genome is deprived of copy number alterations except for a frequent monosomy of chromosome 6 (80%)[29]. The latest molecular stratification identified two subtypes, WNTα and WNTβ diverging by age of diagnosis (10 years old versus 20, respectively) and the frequency of the monosomy 6[30].

Group 3 and Group 4 medulloblastoma

The stratification of Group 3 and Group 4 medulloblastomas is not as obvious as that of the SHH and WNT entities. Indeed, no recurrently affected pathway has yet been identified, making a thorough subcategorization ambiguous. Thus, it is still in debate whether these two groups should be seen as separate entities, as they share many common molecular traits. Nonetheless, the WHO and several other studies acknowledge the benefit of their distinction. Cavalli *et al.* identified three subgroups in both Group 3 and Group 4 MB: Group 3α, -β, -ɣ, and Group 4α, -β, -ɣ[30]. Schwalbe *et al*. identified high- and low-risk patients by splitting Group3/4 in four subtypes[36]. Finally, a large analysis of more than a thousand Group 3 and Group 4 MB identified eight types (I-VIII)[10] (Fig 2A). Group 3 occurs in infants and children whereas Group 4 occurs across all age groups. They both associate with poor prognosis and 30-40% of the patients will have metastatic disease at diagnosis[45]. At the molecular level, *MYC* amplifications are characteristic of Group 3-MB whereas *MYCN* and *CDK6* amplifications are that of Group 4-MB[29]. Both groups harbor a typical

isochromosome 17q (i17q) which is associated with impaired *TP53* function and is a hallmark for these two groups[46] (Fig 2A).

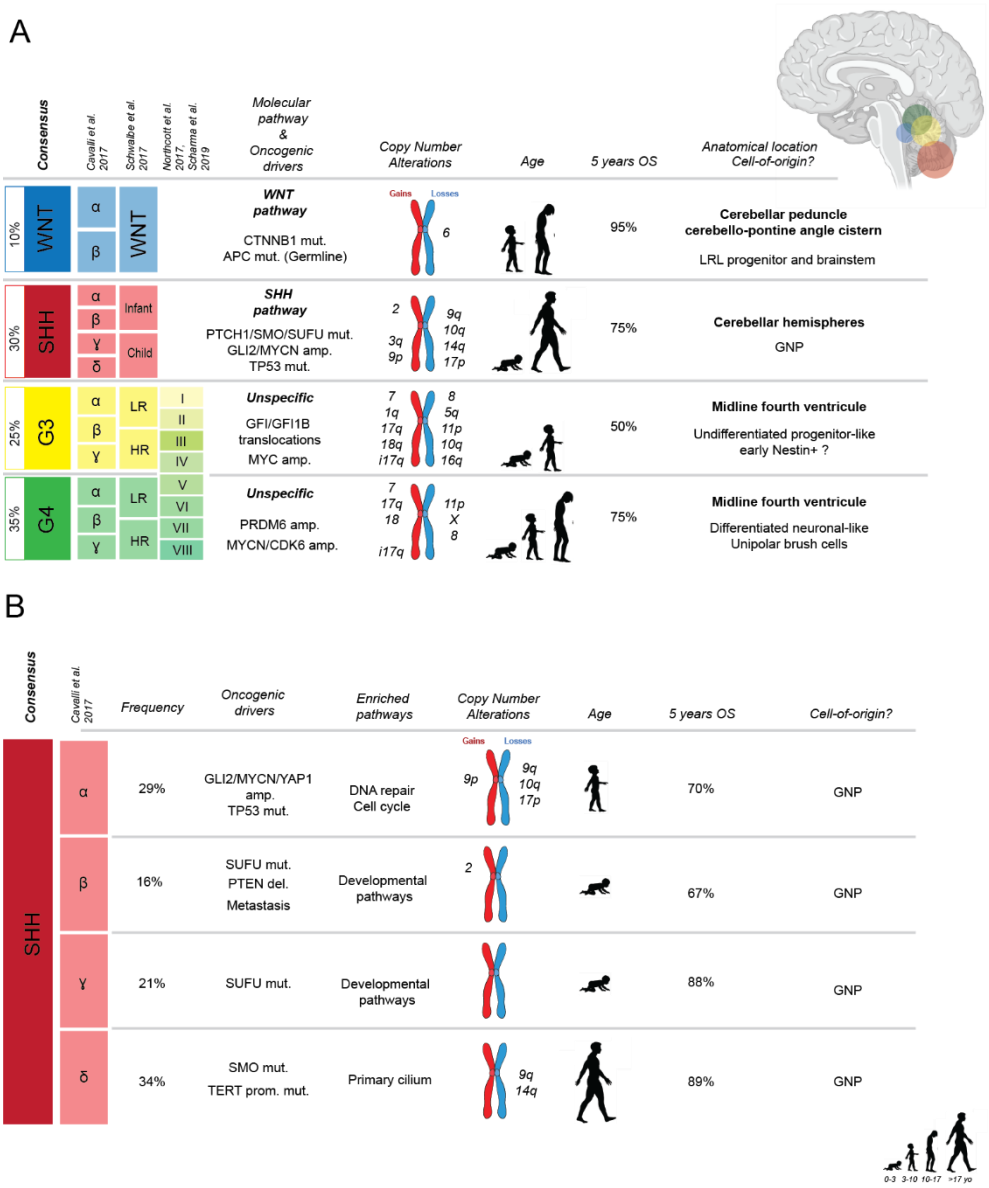

Figure 2. Clinico-pathological features of pediatric medulloblastoma and their genomic characteristics. (A) Table A) describes the current knowledge on molecular characteristics of pediatric medulloblastoma and their associated clinical features. **(B)** Table B) focuses on the SHH-subtypes and the current subtyping characteristics based on Cavalli *et al.*[30].

On the origin of Medulloblastoma

Given the highly inter-tumoral heterogeneous nature of MB, over the years great attention has been given to decipher their origin(s). All four subgroups have been thought to arise from different neuronal lineages within the cerebellum[47,48]. Recently, two elegant RNA-sequencing studies at the single-cell level confirmed the previous finding of Cerebellar Granule Neuron Progenitors (CGNPs) as the SHH-MB cell-of-origin[11,49–51] (Fig 2B). These same studies highlighted the neuronal-like Unipolar Brush Cells (UBC) as the putative cell-of-origin for Group 4-MB, whereas Group 3-MB resembled more undifferentiated-progenitor-like cells, perhaps originating from an early Nestin+ progenitor[11]. WNT-MB are thought to take root either outside the cerebellum from a brainstem derived progenitor or from a very early progenitor of the lower rhombic lip (LRL)[11] (Fig 2A). Further heterogeneity within the SHH-MB subgroup itself raises the question of differential origins among the subtypes -α, -β, -ɣ and -δ (Fig 2B).

A corrupted SHH pathway during cerebellar development drives SHH-MB

The cerebellar granule neuron represents the majority of the cells populating the cerebellum[52]. From late embryogenesis (E13.5 in mice, E57 in humans), successive expansion, migration and differentiation waves of the CGNP lineage shape the forming cerebellum. These CGNPs are a highly dynamic cell population that expands up to three weeks after birth in mice and up to two years over human postnatal development[52]. In mice, early CGNPs become committed to their lineage around embryonic day E13.5[53]. They arise in the upper rhombic lip (uRL) region of the hindbrain, from where they migrate tangentially over the surface of the cerebellar primordium[53–55] (Fig 3a.). Here, they form a secondary germinal zone, the External Granular Layer (EGL) (Fig 3b.). The proliferative peak of CGNPs occurs around birth (Postnatal day 0, P0). At this time, CGNP expansion is driven by the morphogen Sonic Hedgehog (SHH) secreted by the underlying layer of Purkinje cells. Between P4 and P7, the first CGNPs of the EGL become post-mitotic as they start differentiating. Terminally differentiating granule neurons cease proliferation and migrate inwards across the Purkinje Cell layer to their final destination until around postnatal day P14 (Fig 3c.). This second migratory wave of mature CGNPs forms

the Internal Granular Layer (IGL) of the cerebellum[54,56–59] (Fig 3d.). It is accepted that the mouse cerebellum is fully developed at postnatal day P21 (Fig 3e.). Besides the longer gestational period, the development of human CGNPs generally resembles that of the mouse[60].

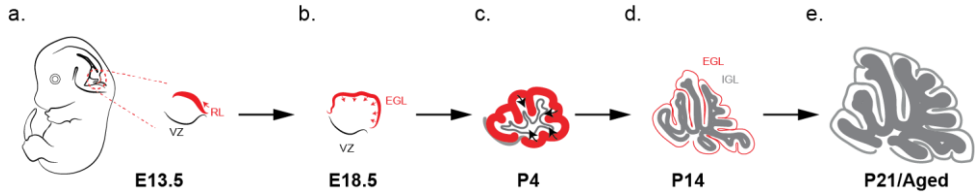

Figure 3. Timeline of murine cerebellar development from E13.5 to adult age. Graph depicting the key developmental stages of murine cerebellar development from granule neuron lineage commitment at E13.5 (a) through expansion and migration at E18.5 (b). Neonatal sustained proliferation in the EGL leads to foliation of the cerebellum. CGNP terminal differentiation and migration forms the IGL (c) up to P14 (d). In mice, cerebellum is fully developed at P21 when the EGL has disappeared (e). Graph adapted from[61]. E=embryonic, P=postnatal, EGL=external granule layer, IGL=internal granule layer

Developmental transitions within (neural) cell lineages might be related to the concept of tumor propagating cells, or cancer stem cells (CSCs), which was brought into the scientific community in the 2000s[62–65]. CSCs have the capacity of self-renewal, differentiation and proliferation and thus sustain tumor growth. They have been well identified in brain cancers, including medulloblastomas and gliomas[66,67]. CSCs are thought to arise from a stem/progenitor cell that by acquisition of a genetic event hijacks normal developmental pathways to sustain growth[67,68]. In theory, at every transitional stage it is possible for a stem/progenitor cell to acquire a mutation that locks the (pre-)cancer cell into a transcriptional program, later mirrored in the growing tumor[48]. Various studies have highlighted the correlation between cerebellar development and age group of the SHH-MB subtypes, including our own (see **Chapter 3** of this thesis). A mutation in the SHH pathway might have a different effect depending on the developmental stage of the targeted cell, thus explaining that age-specific characteristics of the cell-of-origin might be employed during oncogenesis and subsequently mirrored in SHH-MB subtypes (Fig 4). Therefore, deciphering the dynamics of SHH-MB pathways through the lens of cerebellar developmental biology is of utmost importance to better understand the

pathways underlying tumorigenesis, and ultimately develop more specific therapies (Fig 4).

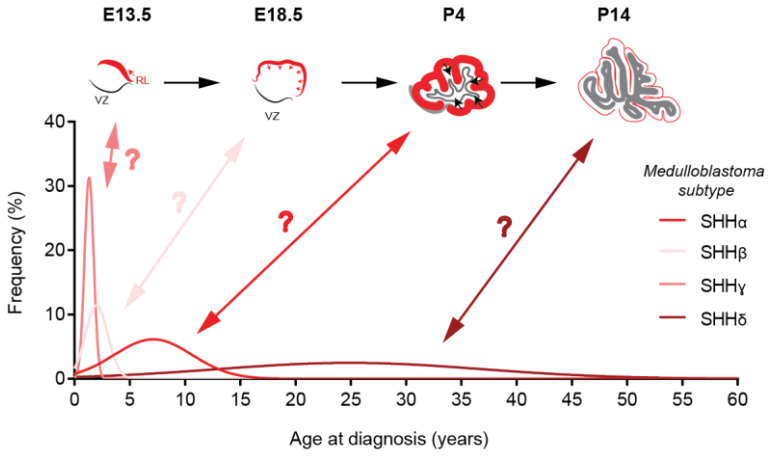

Figure 4. Proposed time line correlation between cerebellar development in mice and age incidence of the SHH-MB subgroups. Graph representing a putative correlation between cerebellar development and initiation of SHH-MB subtypes. A mutation in the SHH pathway might have a different effect depending on the developmental stage of the targeted cell thus explaining that age-specific characteristics of the cell-of-origin are employed during oncogenesis and mirrored in SHH-MB sub types. The age distribution of SHH-MB subtypes was adapted from Cavalli *et al.*[30]. E= embryonic, P=postnatal, SHH = Sonic Hedgehog

High grade Gliomas

Within the subgroup of pediatric high-grade gliomas (HGGs), distinct molecular and epigenetic entities have been identified[9,69,70]. Each subtype is defined by recurrent oncogenic drivers, presents unique clinical characteristics and specific neuroanatomical localizations, raising the hypothesis of a multiplicity of cells-of-origin for pediatric HGGs as well[9]. In 2012, the key discovery of a novel oncogenic mutation in histone genes in a striking 50% of pediatric HGGs imposed a re-evaluation of disease classification with addition of "Diffuse midline glioma, H3K27M–mutant" as an entity to the 2016 WHO classification[9,16,69,71–74]. Since then, these histone mutants with deliberate oncogenic features, termed "oncohistones", have drawn much interest from the field of epigenetics and oncology in general. To remain within the scope of this dissertation, below we will briefly introduce all HGG subgroups with a special emphasis on the subgroup of histone mutant gliomas, as this entity is the subject of the research in **Chapters 5** and **6** of this thesis.

Based on the most recently published molecular meta-analysis of a cohort of more than 1000 pediatric HGGs, four main subgroups have been identified: histone mutant HGG, IDH mutant HGG, $BRAF^{V600E}$ mutant HGG, and finally the remaining HGG classified as "wild-type" that deserve further molecular characterization in the future[9,75].

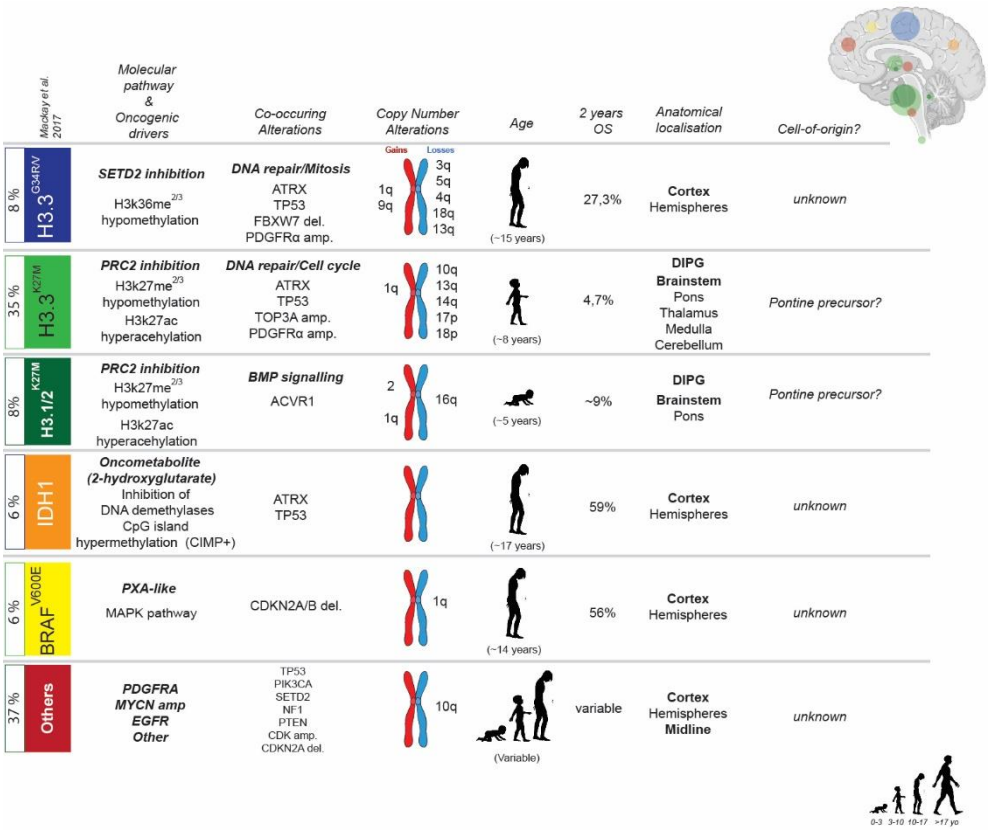

Figure 5. Clinico-pathological features of pediatric high-grade gliomas and their genomic characteristics. Table describing the current knowledge on molecular characteristics of pediatric high-grade gliomas and their associated clinical features. Data is based on Mackay *et al.*[9]. OS = Overall survival, DIPG= Diffuse Intrinsic Pontine Glioma, PXA = pleomorphic xanthoastrocytoma

Histone mutant gliomas

The K27M mutation (that substitutes the lysine (K) 27 by a methionine (M) on the histone H3 tail) is the first reported histone mutation ever to be associated with human cancers[69,71,72]. Since the original discovery in 2012, it is now known that many different tumors carry mutations in histones[76]. In pediatric gliomas, three histone H3 genes are found affected: *H3F3A* encoding histone variant H3.3 and *HIST1H3B* or *HIST1H3C* encoding H3.1. *HIST2H3C* mutations (gene for histone variant H3.2) have also been reported[9]. While canonical histones have been reported with only one type of mutations (H3.1K27M and H3.2K27M oncohistones), H3.3 is seen mutated at two different sites leading to the H3.3K27M and H3.3G34R/V

oncohistones (Fig 5). Much attention has been drawn to elucidating the oncogenic programs driven by the different oncohistones. The epigenetic and transcriptional mechanisms ensuing oncohistone expression begin to be unraveled. Nowadays, several hypotheses exist as to how H3K27M exerts its oncogenic effects, while the H3.3G34R/V oncohistone is less understood. Later, I discuss some of these mechanisms.

The K27M substitution is the most frequent histone mutation (~80% of histone mutant gliomas). While affecting all histone H3 variants, it is predominantly found on the histone H3.3 variant (~70% of histone mutant gliomas). The substitution of Glycine 34 by a Valine or Arginine (G34R/V) has only been described in histone variant H3.3 and accounts for 14% of histone gliomas[9] (Fig 5). Interestingly, mutations correlate strongly with anatomical localizations of the tumors (Fig 5). G34 mutant gliomas are selectively hemispheric and affect older children/adolescents (median age at diagnosis is 15 years). K27M gliomas arise mostly in the midline/brainstem region of the brain (thalamus, pons, medulla, cerebellum) and are found in younger patients (8-9 years)[9]. Within the K27M subgroup, H3.1-K27M is localized only in the pons, whereas H3.3-K27M mutations may be found all along the midline. H3.1-K27M usually affects younger children (~5 years at diagnosis) (Fig 5). Gliomas of the pons, also known as Diffuse Intrinsic Pontine Gliomas (DIPG) represent 80% of midline gliomas and are the pediatric brain malignancy with the worst outcome. Strikingly, the H3.3-K27M subtype associates with an extremely dismal prognosis with less than 5% of patients surviving 2 years after diagnosis, regardless of tumor localization[9]. H3.1-K27M and H3.3-G34R/V gliomas are thought to have a slightly better overall survival of ~10% and ~27% respectively (Fig 5). What exactly explains the aggressiveness of H3.3-K27M gliomas remains unclear to date.

Adding yet a further degree of complexity, the histone mutations also associate with specific co-occurring genetic alterations, which may act together to promote tumorigenesis[9]. Association of DNA repair mutations with H3.3-K27M and H3.3-G34R/V implies a complex interplay between H3.3, DNA damage and tumorigenesis, whereas mitogenic signaling during brainstem development seems to act in concert with H3.1 driver mutations[9] (Fig 5). Furthermore, H3.3 mutant

gliomas associate with specific copy number variations, both focal (amplifications and deletions) and structural (gross alterations), therefore they are defined as aneuploid[9,31]. On the contrary, H3.1 gliomas exhibit a more normal karyotype (Fig 5)[9].

IDH mutant gliomas

Next to histone mutant HGG, it is also recognized that a subset of HGG (~6%) harbor a driver mutation in *IDH1* (isocitrate dehydrogenase 1) gene (Fig 5). Interestingly, *IDH* mutations are frequently found in adult glioblastoma, whereas in pediatric settings they are present mostly in young adults (median of 17 years old at diagnosis)[77]. The most common alteration in the *IDH* gene is an amino-acid substitution at R132H[9]. It confers the IDH enzyme with the capacity to produce 2-hydroxyglutarate, an oncometabolite[78]. This oncometabolite inhibits DNA demethylases causing a widespread genome hypermethylation on CpG islands, also known as CIMP phenotype, conferring oncogenic potential[79] (Fig 5). Pediatric IDH mutant gliomas are associated with better prognosis as the 2 years overall survival reaches 59%[9,69,77]. IDH mutant gliomas often co-associate with *TRP53* and *ATRX* alterations and these tumors exclusively localize to the cerebral hemispheres[9] (Fig 5).

$BRAF^{V600E}$ mutant gliomas

About 6% of pediatric HGG harbor $BRAF^{V600E}$ mutations[9] (Fig 5). They are predominantly localized to the cortical hemispheres and share histologic features with pleomorphic xanthoastrocytomas (PXA)(a LGG subtype), hence the denomination as PXA-like[70,80] (Fig 5). They frequently harbor homozygous *CDKN2A/B* deletions and present a good prognosis (56% overall survival after 2 years)[9] (Fig 5).

Other gliomas

Within the remaining fraction of H3/IDH/BRAF-wild-type gliomas, various molecular subgroups are emerging[75]. For example, amplifications of *MYCN* may be a driving event for a subset of H3-wild-type brainstem gliomas[75,81,82]. Other subgroups may

be driven by amplifications or mutations in receptor tyrosine kinases such as *PDGFRA* and *EGFR* [69,82,83] (Fig 5). Current knowledge highlights prognostic differences between these subgroups[82]. Because of the high diversity within HGG and the impact that their molecular architecture may have on prognostication, further histo-molecular definition is of importance to establish accurate treatment modalities in clinical trials.

On the origins of high-grade glioma

Because HGG subgroups differ from each other in terms of gene expression, epigenetic landscape, mutational profile, tumor location, age of onset and prognosis, it is very likely that they arise from different cells-of-origin[9,70,80,82]. These can be distinct types of cells, or identical cells but transformed at distinct developmental time points. Multiple genetic and epigenetic alterations have been found to initiate gliomagenesis[9] (Fig 5). However, the identity of the cell-of-origin that acquires this primary oncogenic hit during brain development still remains elusive.

Brain development is the result of waves of proliferation of successive neural stem and progenitor (NSC) populations. NSCs have the ability to self-renew via symmetric proliferative cell divisions[84–86]. Therefore, before the onset of neurogenesis (*e.g.* production of neurons), a rapid expansion of the neuroepithelium occurs to expand the pool of NSCs (expansion phase from E10.5 to E11.5 in mouse brain development)[87] (Fig 6). From E12.5 in mice, transcriptional switches take place and progressively augment asymmetric cell divisions of the NSCs to produce committed progenitors, first towards the neuronal lineage[87]. At this point, NSCs start dividing asymmetrically towards an intermediate progenitor cell (IPC) which is meant to first expand then generate the majority of the neurons (neurogenesis from E12.5-E16.5 in mice)[87]. Close before birth, NSCs switch to gliogenesis and produce astrocyte and oligodendrocyte progenitor cells (APCs and OPCs respectively)[87] (Fig 6).

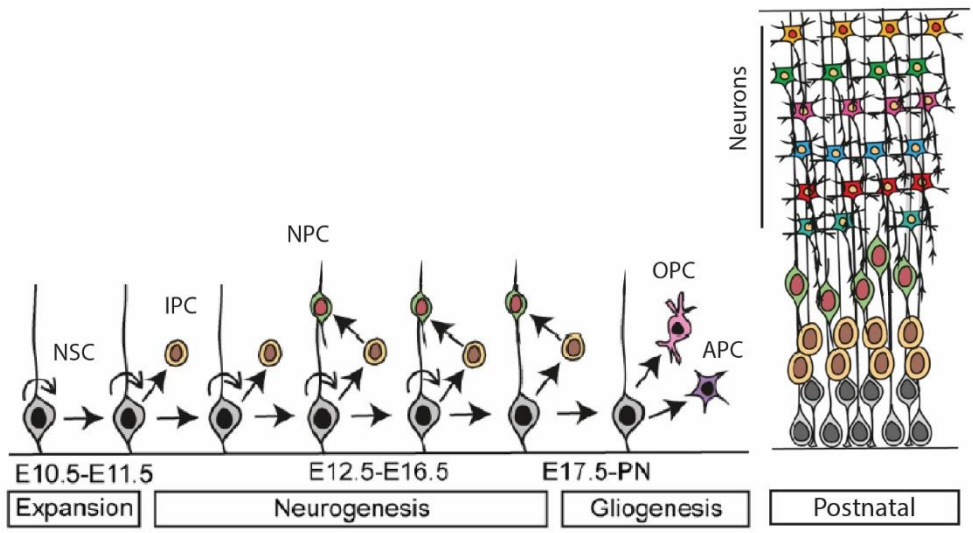

Figure 6. Timeline of murine cortical development from early embryogenesis up to birth
Murine cortical development can be separated in four main phases: from E10.5 to E11.5 where the NSC pool expands to prepare for later production of neurons from E12.5-E16.5, called neurogenesis. After neurogenesis, NSC switch to the production of glial precursor cells (APCs and OPCs) during a phase called gliogenesis, which takes place from E17.5 and extends up to after birth. Postnatally, the brain cortex is composed of a basal layer of rarely dividing NSCs and neural progenitors, differentiated neurons and glial cells (not shown). E=embryonic day ; PN=postnatal ; NSC=neural stem cell ; IPC=intermediate progenitor cell ; NPC=neural progenitor cell ; OPC=oligodendrocyte progenitor cell ; APC=astrocyte progenitor cell. Adapted from[87]

Several cell types have been proven competent to oncogenic transformation and therefore suggested putative glioma-cells-of-origin – these include NSCs and the more differentiated progenitors OPCs and APCs[88–91] (Fig 6). This suggests that at any stage of neural development, a given cell, already committed to a lineage or not yet, might be susceptible to acquire oncogenic transformation (for more detail, see **Chapter 2** of this thesis). This also explains the high histologic diversity within HGG, with some subtypes resembling the astrocytic lineage, some others the oligodendrocytic lineage and some harboring a more undifferentiated state[16].

Besides the cellular heterogeneity that governs the brain architecture, all brain regions do not develop at the same time. Waves of localized proliferation dictated by secreted morphogens (*e.g*. SHH, FGFs, WNTs) orchestrate brain regionalization[92]. In early embryogenesis, the neuroepithelium can be divided into 3 main regions (anterior to posterior respectively) : forebrain, midbrain and hindbrain

(Fig 7A). Looking at a surrogate marker to trace proliferative cell populations – that is the transcription factor *E2f1*, a key regulator of DNA synthesis genes[93] -- in the Allen Brain Atlas database, we could identify a proliferative wave that moved postero-anteriorly in the mouse embryonic brain: from the hindbrain to the midbrain and finally to the forebrain (Fig 7B; regions of interest shown in dashed red squares). Interestingly, this postero-anterior temporality of brain development seems to mirror the tumors age distribution where hindbrain/midline gliomas are mostly found in younger children, rarely in adults, and hemispheric gliomas in older children, young adolescents and adults (Fig 5).

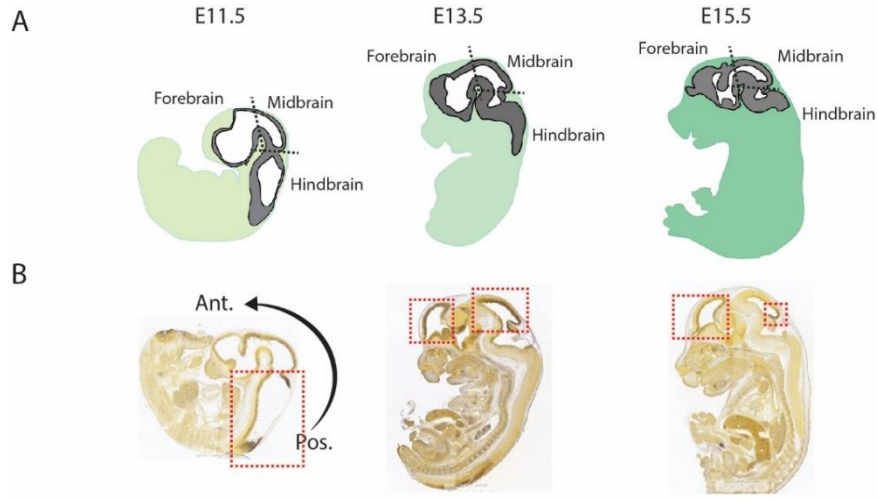

Figure 7. Antero-posterior regionalization of the developing mouse brain is mirrored by pediatric histone mutant HGG age incidence and anatomical localization.
(A) Schematic representation of E11.5, E13.5 and E15.5 (from left to right) mouse embryos and the localization of the three main brain regions (Forebrain, Midbrain, Hindbrain separated by dashed lines). **(B)** RNA in situ hybridization images from the Allen brain atlas showing the regional specificity of the E2f1 transcription factor in embryonic mouse brains over time (E11.5. E13.5 and E15.5 from left to right). Regions of interest are indicated in dashed red squares and show high E2f1 positivity. Tissue slides were counterstained with Feulgen HP yellow nuclear stain (Anatech Ltd.).

Furthermore, this spatial-temporal connection with brain development seems exceptionally prominent in histone mutant gliomas (Fig 8), a finding that we will discuss more in detail below.

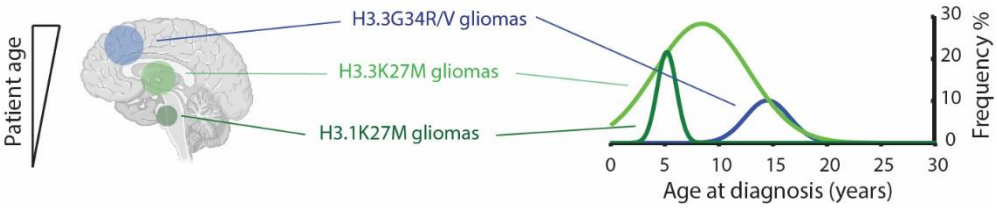

Figure 8. Age distribution of histone mutant high-grade gliomas depending on the driver oncohistone. Schematic representation of the anatomical distribution of histone mutant pediatric HGG correlated to patient age. Graph shows incidence peak of H3.3 mutant brainstem gliomas, H3.1 mutant brainstem gliomas and H3.3 mutant hemispheric gliomas. This correlation argues towards a separate cellular origin for these three groups. Data is adapted from Mackay *et al*.[9]

Origins of oncohistone-driven-gliomas

The striking spatial-temporal distribution of histone mutant gliomas suggests that oncohistone driven tumorigenesis is highly tied with developmental pathways. However, it remains elusive what role each histone variant plays in the developmental pathways of the midline or the brain cortex (Fig 8).

In contrast to SHH-MB, the cell(s)-of-origin for histone mutant gliomas have yet to be identified. Recent literature suggests that the transforming ability of each oncohistone is highly dependent on the cell-of-origin[94]. Thus, looking at developmental pathways through the lens of histone variant usage and chromatin landscape may shed light on potential new candidates for histone mutant gliomas' cell(s)-of-origin (see **Chapter 5** of this thesis).

A number of studies suggest a neonatal pontine progenitor at the root of H3.3K27M gliomas, which proliferation peak overlaps with the incidence peak of H3.3K27M brainstem gliomas[95–98] (Fig 8). H3.1K27M is thought to arise from a different cell-of-origin, because DNA methylation profiling and transcriptome data comparing H3.1K27M and H3.3K27M gliomas showed significant difference between these two groups[99]. We might speculate that the cell-of-origin for H3.1 mutant brainstem glioma would have a narrower temporal and spatial distribution given the younger age of incidence and the restricted localization to the pons (Fig 5 and 8). Interestingly, a mouse study from Pathania *et al.* showed that the embryonic

brainstem was only sensitive to H3.3K27M driven transformation in a specific window of time during development. Postnatal ectopic expression of this oncohistone, in combination with its recurrent genomic alterations, did not give rise to tumors, thus challenging previous findings[94,100].

The origins of hemispheric G34 gliomas are far less studied, therefore no candidate cell-of-origin has been proposed yet. So far, we only know from the Pathania *et al*. study that no tumors formed when H3.3G34R was injected into embryonic hindbrain (E12.5) or cortex (E13.5) via intra-uterine electroporation, whether being in combination with Trp53 loss and/or ATRX[94].

Histone H3 variants and their link to cancer

Histone H3 variants

To address the effects of histone H3 mutations on tumor growth, it is important to first understand the primary functions of the core histones H3 and their variants. Two core histones H3 (H3.1 and H3.2), four variants (H3.3, histone H3-like centromeric protein A – CENPA – , H3.Y, H3.X) and two testis specific variants (H3.1t and H3.5) have been described to date[101]. At the protein level, the primary sequence may vary from one histone variant to the other, with H3.3 remaining the closest related to canonical histone H3.1 and differs by only five amino-acids[102]. Next to their variable protein sequence, histone variants differ in their expression patterns. Canonical histones H3.1 and H3.2 are encoded by a cluster of ten and three genes, respectively, and are therefore the most abundant variant in mammalian cells[103,104]. They are incorporated into chromatin in a replication-dependent manner during S-phase. On the contrary, non-canonical histone H3.3 is encoded by two separate genes, *H3F3A* and *H3F3B*. H3.3 is expressed and deposited onto chromatin throughout the cell-cycle[101].

Histones are an essential constituent of chromatin. All histone variants exhibit core structural roles in the packaging of DNA and in regulation of gene expression. Histones represent the platform for many enzymes that modify them on specific amino-acid residues. Many of these chromatin modifiers have essential

roles in development, proliferation, differentiation and also described roles in cancer development[105,106].

In addition to their canonical role in the packaging of chromatin and modulation of gene expression, histones H3.1 but mostly H3.3 carry out functions linked to maintenance of genomic integrity. For instance, H3.3 is enriched in regions where genome stability is at risk, such as telomeres and pericentric heterochromatin. In addition, H3.3 has been implicated in both single- and double-strand DNA break repair. Thus, histones are the site of a large panel of possible post translational modifications (PTMs) leading to a plethora of possible PTMs combinations regulating chromatin processes from transcription to DNA repair. All of which may exacerbate the impact of a mutation[107].

Multiple histone H3 mutations have been identified, all somatic, heterozygous and mutually exclusive[9,69,108–110]. It is intriguing that always only one allele is affected. This raises the idea of a strong transforming power of the oncohistones. Oncohistones have first been reported in pediatric gliomas[71,100]. Since then, multiple other (pediatric) malignancies were linked to oncohistones[110–115] and notwithstanding that all four core histones have been found mutated in various pathologies, histone H3 mutations remain the most common[76].

H3.3G34R/V and its relation with SETD2

The G34R/V mutation affects the non-canonical histone variant H3.3 at an amino acid residue in close proximity to an important site of post-translational modification, the lysine (K) 36 on the H3 tail. The H3K36 residue is a target site for methylation by the trimethyl-transferase SETD2 and participates in gene activation[116–118]. It is thought that the mutated residue is trapped within the catalytic site of SETD2 and thereby inactivates its methylase activity[119]. This leads to a loss of H3K36 di- and tri-methyl marks on the nucleosomes harboring the oncohistones[87]. However, the effect of SETD2 inhibition remains local and does not affect the global H3K36 methylation landscape[121]. In consequence, the downstream effect at the gene expression level remains subtle and does not explain the oncogenic power of this oncohistone. Interestingly, several recent studies have linked the H3K36me^3 mark to various DNA

repair pathways[122–124]. Therefore, H3.3G34R/V may be associated with an additional effect on genome maintenance, which adds another layer to the understanding of its oncogenic potential[120,125].

H3K27M and its relation with EZH2

By a comparable mechanism, H3K27M is thought to inhibit the methylase activity of EZH2, a H3K27 methyltransferase enzyme, constituent of the Polycomb repressive complex 2 (PRC2). Although the mutant histone only accounts for 5-15% of the total histone H3 pool, its presence leads to a global hypomethylation with a genome-wide loss of H3K27me$^{2/3}$ marks[100]. Because the H3K27 residue is also a site of acetylation by histone acetyl-transferases (HATs), hypomethylation leaves room for installment of a hyperacetylated phenotype and in consequence de-repression of normally repressed genes[100,126,127]. Curiously, genome-wide analysis of H3K27me^3 distribution showed loci-specific enrichment of the mark besides the global hypomethylation, meaning that residual activity of the PRC2 complex exists that may be necessary to sustain tumor growth[126,128–130].

Furthermore, adding another layer of complexity, the differential distribution across the genome between H3.3 (located on active genes, heterochromatic regions and telomeres) and the canonical histones H3.1 and H3.2 (distributed across the whole chromatin) suggests that their oncohistone counterparts H3.3K27M and H3.1/.2K27M exert different genome-wide effects depending on their chromatin location[101,131,132].

Future of oncohistone-driven gliomas in the clinic

The fundamental knowledge on the origin of the histone subtypes gives important insight into future clinical applications in the treatment of these tumors. Much can be learned from the Medulloblastoma field where molecular subtyping considerably changed how clinicians look at the disease and influenced treatment strategies (See ***Medulloblastoma*** section). Indeed, various studies, including ours (see **Chapter 3** of this thesis) showed that treatment needs to vary from one cell-of-origin to the next. Thus, glioma subtypes should be treated as separate entities as the molecular

oncogenic drivers differ significantly, and their sensitivity to different treatments will vary too. For instance, H3.3 gliomas have a more “cell-cycle/DNA repair” signature (Fig 5) which means that genotoxic agents might be more suitable to treat these types of gliomas, whereas H3.1 would be more sensitive to growth factor (receptor) inhibitors.

Concluding remarks

Although the oncohistones harbor strong oncogenic power, they rarely occur alone in gliomas[9]. It is recommendable to take the recurrent co-occurring alterations identified in each histone group into account, since we believe that they give an indication of the developmental programs active at the time of oncogenic transformation. Such comprehensive insight into tumor biology is, to our opinion, crucial in developing therapies that are truly targeting the disease.

In this context, infantile malignancies (SHHɣ-, SHHβ-MB, and H3.1K27M HGG) alter developmental pathways to sustain oncogenesis, whereas DNA repair and cell cycle alterations are predominantly affected in older children (SHHα-MB and H3.3K27M and H3.3G34R/V gliomas) (Fig 2B and 5). It is intriguing that both childhood SHHα-MB and histone H3.3 mutant gliomas display altered DNA repair pathways and substantial genomic instability with recurrent copy number alterations (Fig 2B and 5). In fact, these two tumor types are categorized as highly aneuploid within the sphere of pediatric malignancies, which typically does not exhibit extensive genome instability[133].

It would be interesting to fully unravel why DNA repair pathways are selectively co-altered at this age in the midline region of the brain, and what role genomic instability plays in the oncogenic process of these two malignancies. This might help us identify targetable vulnerabilities, as we imagine that interfering with increased DNA damage could be used as an Achilles' heel, especially if these tumors exhibit genomic/chromosomal instability.

SCOPE OF THIS THESIS

As highlighted in the introductory **Chapter 1**, we uncover disruption of genome maintenance pathways as an under-investigated potential oncogenic facilitator in pediatric diseases, despite the acknowledged presence of genome instability in some SHH-MB and HGG subtypes. Therefore, **Chapter 2** further digs into the role of genome instability in tumor development through the lens of developmental biology. It describes how fluctuating genome maintenance pathways during central nervous system development create intrinsic windows of vulnerability for neurodevelopmental disorders and oncogenesis.

Looking into tumor origins, **Chapter 3** elaborates on the transcriptional landscape of the SHH-MB cell lineage-of-origin, the cerebellar granule neuron progenitor (CGNP). Here, we discover cell-of-origin age-specific transcriptional programs reflected in SHH-MB, which further enables to sub-stratify SHH-MB into subtypes according to shared transcriptional programs with developing CGNPs. This has led to the identification, among others, of an enrichment for processes linked to cell-cycle regulation and genome maintenance pathways in neonatal CGNPs, which high expression coincided with a subset of older patients' transcriptomes. This finding suggests that a spurt in CGNP proliferation might be a critical event during cerebellar development that brings along the risk of developing child- and adulthood medulloblastoma due to increased replication dependent genome instability.

Therefore, in **Chapter 4**, we set out to investigate the consequences of genomic instability during cerebellar development and if this could lead to medulloblastoma initiation. By the means of a transgenic mouse model using *Mad2l1* and *Trp53* conditional knockout alleles, we were able to specifically target chromosomal instability (CIN) to the MB cell lineage-of-origin. Our data provided the knowledge that the highly proliferative cerebellum is able to overcome CIN. Indeed, mutant mice developed normally seemingly without being vulnerable to CIN-induced oncogenesis in the cerebellum. This finding raises an important question concerning aneuploidy tolerance in the cerebellum and in the central nervous system in general.

In **Chapter 5** we investigate the identity of the histone H3.3 mutant pontine glioma cell-of-origin. We generated a map of histone variant usage over postnatal hindbrain development and uncovered the pons region of the brain to use more H3.3 variant at neonatal time points than other brain parts. Based on this map, we were able to isolate a pontine neural stem cell that conserved the histone usage landscape upon *in vitro* culturing, as well as core transcriptomic and behavioral characteristics. Altogether, this chapter lays the foundation for the identification of the presumptive H3.3 pontine glioma cell-of-origin and opens the avenue for better tools to model and therefore understand pontine glioma initiation.

Towards a better understanding of H3.3 glioma initiating pathways, **Chapter 6** uses an *in vitro* model to look at the consequences of histone H3.3 mutations on the maintenance of genome integrity. In this chapter, we uncover a vulnerability to replication stress induced genomic instability in an oncohistone chromatin context. This chapter clearly shows how disturbing histones (*e.g.,* by mutations) causes pleiotropic effects, from transcriptional imbalances to genome maintenance disruption.

Finally, in **Chapter 7** we summarize and discuss the results described in this thesis.

REFERENCES

1. Bhakta, N. *et al.* Childhood cancer burden: a review of global estimates. *Lancet Oncol.* **20**, e42–e53 (2019).

2. Steliarova-Foucher, E. *et al.* International incidence of childhood cancer, 2001–10: a population-based registry study. *Lancet Oncol.* **18**, 719–731 (2017).

3. Zhang, J. *et al.* Germline mutations in predisposition genes in pediatric cancer. *N. Engl. J. Med.* **373**, 2336–2346 (2015).

4. Scollon, S., Anglin, A. K., Thomas, M., Turner, J. T. & Wolfe Schneider, K. A Comprehensive Review of Pediatric Tumors and Associated Cancer Predisposition Syndromes. *J. Genet. Couns.* **26**, 387–434 (2017).

5. Kuhlen, M. *et al.* Family-based germline sequencing in children with cancer. *Oncogene* **38**, 1367–1380 (2019).

6. Downing, J. R. *et al.* The pediatric cancer genome project. *Nat. Genet.* **44**, 619–622 (2012).

7. Gajjar, a. *et al.* Pediatric Brain Tumors: Innovative Genomic Information Is Transforming the Diagnostic and Clinical Landscape. *J. Clin. Oncol.* (2015). doi:10.1200/JCO.2014.59.9217

8. Pajtler, K. W. *et al.* Molecular Classification of Ependymal Tumors across All CNS Compartments, Histopathological Grades, and Age Groups. *Cancer Cell* **27**, 728–43 (2015).

9. Mackay, A. *et al.* Integrated Molecular Meta-Analysis of 1,000 Pediatric High-Grade and Diffuse Intrinsic Pontine Glioma. *Cancer Cell* **32**, 520-537.e5 (2017).

10. Sharma, T. *et al.* Second-generation molecular subgrouping of medulloblastoma: an international meta-analysis of Group 3 and Group 4 subtypes. *Acta Neuropathol.* (2019). doi:10.1007/s00401-019-02020-0

11. Hovestadt, V. *et al.* Resolving medulloblastoma cellular architecture by single-cell genomics. *Nature* **572**, 74–79 (2019).

12. Zhang, L. *et al.* Single-Cell Transcriptomics in Medulloblastoma Reveals Tumor-Initiating Progenitors and Oncogenic Cascades during Tumorigenesis and Relapse. *Cancer Cell* **36**, 302-318.e7 (2019).

13. Northcott, P. A. *et al.* The whole-genome landscape of medulloblastoma subtypes. *Nature* **547**, 311–317 (2017).

14. Sturm, D. *et al.* New Brain Tumor Entities Emerge from Molecular Classification of CNS-PNETs. *Cell* **164**, 1060–1072 (2016).

15. Kopp, L. M., Gupta, P., Pelayo-Katsanis, L., Wittman, B. & Katsanis, E. Late effects in adult survivors of pediatric cancer: A guide for the primary care physician. *Am. J. Med.* **125**, 636–641 (2012).

16. David N. Louis *et al.* The 2016 World Health Organization Classification of Tumors of the Central Nervous System: a summary.

17. Stokland, T. *et al.* A multivariate analysis of factors determining tumor progression in childhood low-grade glioma: a population-based cohort study (CCLG CNS9702) Tore. **12**, 1257–1268 (2010).

18. Udaka, Y. T. & Packer, R. J. Pediatric Brain Tumors. *Neurol. Clin.* **36**, 533–556 (2018).

19. Kleinerman, R. A. Cancer risks following diagnostic and therapeutic radiation exposure in children. *Pediatr. Radiol.* **36**, 121–125 (2006).

20. Neglia, J. P. *et al.* New primary neoplasms of the central nervous system in survivors of childhood cancer: A report from the childhood cancer survivor study. *J. Natl. Cancer Inst.* **98**, 1528–1537 (2006).

21. Stålberg, K. *et al.* Prenatal X-ray exposure and childhood brain tumours: A population-based case-control study on tumour subtypes. *Br. J. Cancer* **97**, 1583–1587 (2007).

22. Khan, S. *et al.* Head injury, diagnostic X-rays, and risk of medulloblastoma and primitive neuroectodermal tumor: A children's oncology group study. *Cancer Causes Control* **21**, 1017–1023 (2010).

23. Vijapura, C. *et al.* Genetic syndromes associated with central nervous system tumors. *Radiographics* **37**, 258–280 (2017).

24. Louis, D. N. *et al.* The 2007 WHO Classification of Tumours of the Central Nervous System. *Acta Neuropathol* **114**, 97–109 (2007).

25. Desandes, E., Guissou, S., Chastagner, P. & Lacour, B. Incidence and survival of children with central nervous system primitive tumors in the French National Registry of Childhood Solid Tumors. *Neuro. Oncol.* **16**, 975–983 (2014).

26. Kool, M. *et al.* Integrated genomics

identifies five medulloblastoma subtypes with distinct genetic profiles, pathway signatures and clinicopathological features. *PLoS One* **3**, (2008).

27. Cho, Y. J. *et al.* Integrative genomic analysis of medulloblastoma identifies a molecular subgroup that drives poor clinical outcome. *J. Clin. Oncol.* **29**, 1424–1430 (2011).

28. Northcott, P. a. *et al.* Medulloblastoma comprises four distinct molecular variants. *J. Clin. Oncol.* **29**, 1408–1414 (2011).

29. Northcott, P. a. *et al.* Subgroup-specific structural variation across 1,000 medulloblastoma genomes. *Nature* **488**, 49–56 (2012).

30. Cavalli, F. M. G. *et al.* Intertumoral Heterogeneity within Medulloblastoma Subgroups. *Cancer Cell* **31**, 737-754.e6 (2017).

31. Gröbner, S. N. *et al.* The landscape of genomic alterations across childhood cancers. *Nature* **555**, 321–327 (2018).

32. Archer, T. C. *et al.* Proteomics, Post-translational Modifications, and Integrative Analyses Reveal Molecular Heterogeneity within Medulloblastoma Subgroups. *Cancer Cell* **34**, 396-410.e8 (2018).

33. Forget, A. *et al.* Aberrant ERBB4-SRC Signaling as a Hallmark of Group 4 Medulloblastoma Revealed by Integrative Phosphoproteomic Profiling. *Cancer Cell* **34**, 379-395.e7 (2018).

34. Rivero-Hinojosa, S. *et al.* Proteomic analysis of Medulloblastoma reveals functional biology with translational potential. *Acta Neuropathol. Commun.* **6**, 48 (2018).

35. Zomerman, W. W. *et al.* Identification of Two Protein-Signaling States Delineating Transcriptionally Heterogeneous Human Medulloblastoma. *Cell Rep.* **22**, 3206–3216 (2018).

36. Schwalbe, E. C. *et al.* Novel molecular subgroups for clinical classification and outcome prediction in childhood medulloblastoma: a cohort study. *Lancet Oncol.* **18**, 958–971 (2017).

37. Morrissy, A. S. *et al.* Spatial heterogeneity in medulloblastoma. *Nat. Genet.* **49**, 780–788 (2017).

38. Yeom, K. W. *et al.* MRI Surrogates for Molecular Subgroups of Medulloblastoma. *Am. J. Neuroradiol.* **35**, 1263 (2014).

39. Kool, M. *et al.* Genome sequencing of SHH medulloblastoma predicts genotype-related response to smoothened inhibition. *Cancer Cell* **25**, 393–405 (2014).

40. Northcott, P. A. *et al.* Pediatric and adult sonic hedgehog medulloblastomas are clinically and molecularly distinct. 231–240 (2011). doi:10.1007/s00401-011-0846-7

41. Rausch, T. *et al.* Genome Sequencing of Pediatric Medulloblastoma Links Catastrophic DNA Rearrangements with TP53 Mutations. **148**, 59–71 (2013).

42. Wefers, A. K. *et al.* Subgroup-specific localization of human medulloblastoma based on pre-operative MRI. *Acta Neuropathol.* **127**, 931–933 (2014).

43. Northcott, P. a *et al.* Medulloblastomics: the end of the beginning. *Nat. Rev. Cancer* **12**, 818–34 (2012).

44. Kool, M. *et al.* Genome Sequencing of SHH Medulloblastoma Predicts Genotype-Related Response to Smoothened Inhibition. *Cancer Cell* **25**, 393–405 (2014).

45. Kool, M. *et al.* Molecular subgroups of medulloblastoma: an international meta-analysis of transcriptome, genetic aberrations, and clinical data of WNT, SHH, Group 3, and Group 4 medulloblastomas. *Acta Neuropathol.* **123**, 473–84 (2012).

46. Taylor, M. D. *et al.* Molecular subgroups of medulloblastoma: The current consensus. *Acta Neuropathol.* **123**, 465–472 (2012).

47. Gibson, P. *et al.* Subtypes of medulloblastoma have distinct developmental origins. *Nature* **468**, 1095–1099 (2011).

48. Azzarelli, R., Simons, B. D. & Philpott, A. The developmental origin of brain tumours: a cellular and molecular framework. *Development* **145**, dev162693 (2018).

49. Yang, Z. J. *et al.* Medulloblastoma Can Be Initiated by Deletion of Patched in Lineage-Restricted Progenitors or Stem Cells. *Cancer Cell* (2008). doi:10.1016/j.ccr.2008.07.003

50. Oliver, T. G. *et al.* Loss of patched and disruption of granule cell development in a pre-neoplastic stage of medulloblastoma. *Development* **132**, 2425–39 (2005).

51. Jessa, S. *et al.* Stalled developmental programs at the root of pediatric brain tumors. *Nat. Genet.* **51**, 1702–1713 (2019).

52. Carter, R. A. *et al.* A Single-Cell Transcriptional Atlas of the Developing Murine Cerebellum. *Curr. Biol.* **28**, 2910-2920.e2 (2018).

53. Machold, R. & Fishell, G. Math1 is expressed in temporally discrete pools of cerebellar rhombic-lip neural progenitors. *Neuron* **48**, 17–24 (2005).

54. Leto, K. *et al.* Consensus Paper: Cerebellar Development. *Cerebellum* **15**, 789–828 (2016).

55. Wang, V. Y., Rose, M. F. & Zoghbi, H. Y. Math1 expression redefines the rhombic lip derivatives and reveals novel lineages within the brainstem and cerebellum. *Neuron* **48**, 31–43 (2005).

56. Lewis, P. M., Gritli-Linde, A., Smeyne, R., Kottmann, A. & McMahon, A. P. Sonic hedgehog signaling is required for expansion of granule neuron precursors and patterning of the mouse cerebellum. *Dev. Biol.* **270**, 393–410 (2004).

57. Dahmane, N. & Ruiz i Altaba, A. Sonic hedgehog regulates the growth and patterning of the cerebellum. *Development* **126**, 3089–100 (1999).

58. Wallace, V. A. Purkinje-cell-derived Sonic hedgehog regulates granule neuron precursor cell proliferation in the developing mouse cerebellum. *Curr. Biol.* **9**, 445–448 (1999).

59. Wechsler-Reya, R. J. & Scott, M. P. Control of neuronal precursor proliferation in the cerebellum by Sonic Hedgehog. *Neuron* **22**, 103–14 (1999).

60. Haldipur, P. *et al.* Expression of Sonic Hedgehog During Cell Proliferation in the Human Cerebellum. *Stem Cells Dev.* **21**, 1059–1068 (2012).

61. Martinez, S., Andreu, A., Mecklenburg, N. & Echevarria, D. Cellular and molecular basis of cerebellar development. *Front. Neuroanat.* **7**, 18 (2013).

62. Collins, A. T., Berry, P. A., Hyde, C., Stower, M. J. & Maitland, N. J. Prospective identification of tumorigenic prostate cancer stem cells. *Cancer Res.* **65**, 10946–10951 (2005).

63. Singh SK(1), Hawkins C, Clarke ID, Squire JA, Bayani J, Hide T, H. R. & Cusimano MD, D. P. Identification of human brain tumour initiating cells. Nature 18;432(7015):396-401

64. Ricci-Vitiani, L. *et al.* Identification and expansion of human colon-cancer-initiating cells. doi:10.1038/nature05384

65. Al-Hajj, M., Wicha, M. S., Benito-Hernandez, A., Morrison, S. J. & Clarke, M. F. Prospective identification of tumorigenic breast cancer cells. *Proc. Natl. Acad. Sci. U. S. A.* **100**, 3983–3988 (2003).

66. Singh, S. K. *et al.* Identification of a cancer stem cell in human brain tumors. *Cancer Res.* **63**, 5821–5828 (2003).

67. Vescovi, A. L., Galli, R. & Reynolds, B. A. Brain tumour stem cells. *Nat. Rev. Cancer* **6**, 425–436 (2006).

68. Galli, R. *et al.* Erratum: Isolation and characterization of tumorigenic, stem-like neural precursors from human glioblastoma (Cancer Research (October 2004) 64 (7011-7021). *Cancer Res.* **64**, 8130 (2004).

69. Sturm, D. *et al.* Hotspot mutations in H3F3A and IDH1 define distinct epigenetic and biological subgroups of glioblastoma. *Cancer Cell* **22**, 425–37 (2012).

70. Korshunov, A. *et al.* Integrated analysis of pediatric glioblastoma reveals a subset of biologically favorable tumors with associated molecular prognostic markers. *Acta Neuropathol.* **129**, 669–678 (2015).

71. Schwartzentruber, J. *et al.* Driver mutations in histone H3.3 and chromatin remodelling genes in paediatric glioblastoma. *Nature* **482**, 226–231 (2012).

72. Wu, G. *et al.* Somatic histone H3 alterations in pediatric diffuse intrinsic pontine gliomas and non-brainstem glioblastomas. *Nat. Genet.* **44**, 251–253 (2012).

73. Fontebasso, A. M. *et al.* Recurrent somatic mutations in ACVR1 in pediatric midline high-grade astrocytoma. *Nat. Genet.* **46**, 462–466 (2014).

74. Castel, D. *et al.* Histone H3F3A and HIST1H3B K27M mutations define two subgroups of diffuse intrinsic pontine gliomas with different prognosis and phenotypes. *Acta Neuropathol.* **130**, 815–827 (2015).

75. Pollack, I. F., Agnihotri, S. & Broniscer, A. Childhood brain tumors: Current management, biological insights, and future directions. *J. Neurosurg. Pediatr.* **23**, 261–273 (2019).

76. Nacev, B. A. *et al.* The expanding landscape of 'oncohistone' mutations in human cancers. *Nature* **567**, 473–478 (2019).

77. Pollack, I. F. *et al.* IDH1 mutations are common in malignant gliomas arising in adolescents: A report from the Children's Oncology Group. *Child's Nerv. Syst.* **27**, 87–94 (2011).

78. Miyata, S. *et al.* Comprehensive Metabolomic Analysis of IDH1 R132H

Clinical Glioma Samples Reveals Suppression of β-oxidation Due to Carnitine Deficiency. *Sci. Rep.* **9**, 1–11 (2019).

79. M. Gagné, L., Boulay, K., Topisirovic, I., Huot, M. É. & Mallette, F. A. Oncogenic Activities of IDH1/2 Mutations: From Epigenetics to Cellular Signaling. *Trends Cell Biol.* **27**, 738–752 (2017).

80. Mistry, M. *et al.* BRAF mutation and CDKN2A deletion define a clinically distinct subgroup of childhood secondary high-grade glioma. *J. Clin. Oncol.* **33**, 1015–1022 (2015).

81. Buczkowicz, P. *et al.* Genomic analysis of diffuse intrinsic pontine gliomas identifies three molecular subgroups and recurrent activating ACVR1 mutations. *Nat. Genet.* **46**, 451–456 (2014).

82. Korshunov, A. *et al.* H3-/IDH-wild type pediatric glioblastoma is comprised of molecularly and prognostically distinct subtypes with associated oncogenic drivers. *Acta Neuropathol.* **134**, 507–516 (2017).

83. Endersby, R. *et al.* Novel Oncogenic PDGFRA Mutations in Pediatric High-Grade Gliomas. *Cancer Res.* **73**, 6219–6229 (2013).

84. Rakic, P. A small step for the cell, a giant leap for mankind: a hypothesis of neocortical expansion during evolution. *Trends Neurosci.* **18**, 383–388 (1995).

85. Murao, N., Noguchi, H. & Nakashima, K. Epigenetic regulation of neural stem cell property from embryo to adult. *Neuroepigenetics* **5**, 1–10 (2016).

86. Albert, M. & Huttner, W. B. Epigenetic and transcriptional pre-patterning-An emerging theme in cortical neurogenesis. *Front. Neurosci.* **12**, 1–9 (2018).

87. Mukhtar, T. & Taylor, V. Untangling Cortical Complexity During Development. *J. Exp. Neurosci.* **12**, (2018).

88. Koso, H. *et al.* Transposon mutagenesis identifies genes that transform neural stem cells into glioma-initiating cells. *Proc. Natl. Acad. Sci. U. S. A.* **109**, (2012).

89. Alcantara Llaguno, S. *et al.* Malignant Astrocytomas Originate from Neural Stem/Progenitor Cells in a Somatic Tumor Suppressor Mouse Model. *Cancer Cell* **15**, 45–56 (2009).

90. Liu, C. *et al.* Mosaic analysis with double markers reveals tumor cell of origin in glioma. *Cell* **146**, 209–221 (2011).

91. Sugiarto, S. *et al.* Asymmetry-defective oligodendrocyte progenitors are glioma precursors. *Cancer Cell* **20**, 328–340 (2011).

92. Manno, G. La *et al.* Molecular architecture of the developing mouse brain. *bioRxiv* 2020.07.02.184051 (2020).

93. Vasques, L. D. R., Pujiz, R. S., Strauss, B. E. & Krieger, J. E. Knockdown of E2f1 by RNA interference impairs proliferation of rat cells in vitro. *Genet. Mol. Biol.* **33**, 17–22 (2010).

94. Pathania, M. *et al.* H3.3 K27M Cooperates with Trp53 Loss and PDGFRA Gain in Mouse Embryonic Neural Progenitor Cells to Induce Invasive High-Grade Gliomas. *Cancer Cell* **32**, 684-700.e9 (2017).

95. Monje, M. *et al.* Hedgehog-responsive candidate cell of origin for diffuse intrinsic pontine glioma. *Proc. Natl. Acad. Sci.* **108**, 4453–4458 (2011).

96. Misuraca, K. L., Hu, G., Barton, K. L., Chung, A. & Becher, O. J. A Novel Mouse Model of Diffuse Intrinsic Pontine Glioma Initiated in Pax3-Expressing Cells. *Neoplasia* **18**, 60–70 (2016).

97. Jessa, S. *et al. Stalled developmental programs at the root of pediatric brain tumors*. *Nature Genetics* **51**, (2019).

98. Misuraca, K. L. *et al.* Pax3 expression enhances PDGF-B-induced brainstem gliomagenesis and characterizes a subset of brainstem glioma. *Acta Neuropathol. Commun.* **2**, 1–17 (2014).

99. Castel, D. *et al.* Transcriptomic and epigenetic profiling of 'diffuse midline gliomas, H3 K27M-mutant' discriminate two subgroups based on the type of histone H3 mutated and not supratentorial or infratentorial location. *Acta Neuropathol. Commun.* **6**, 117 (2018).

100. Lewis, P. W. *et al.* Inhibition of PRC2 activity by a gain-of-function H3 mutation found in pediatric glioblastoma. *Science (80-.).* **340**, 857–861 (2013).

101. Buschbeck, M. & Hake, S. B. Variants of core histones and their roles in cell fate decisions, development and cancer. *Nat. Rev. Mol. Cell Biol.* **18**, 299–314 (2017).

102. Maze, I., Noh, K.-M., Soshnev, A. A. & Allis, C. D. Every amino acid matters: essential contributions of histone variants to mammalian development and disease. *Nat. Rev. Genet.* **15**, 259–71 (2014).

103. Albig, W. & Doenecke, D. The human histone gene cluster at the D6S105 locus.

Hum. Genet. **101**, 284–294 (1997).

104. Albig, W., Kioschis, P., Poustka, A., Meergans, K. & Doenecke, D. Human histone gene organization: Nonregular arrangement within a large cluster. *Genomics* **40**, 314–322 (1997).

105. Roy, D. M., Walsh, L. A. & Chan, T. A. Driver mutations of cancer epigenomes. *Protein Cell* **5**, 265–296 (2014).

106. Li, G. *et al.* Altered expression of polycomb group genes in glioblastoma multiforme. *PLoS One* **8**, e80970 (2013).

107. Su, Z. & Denu, J. M. Reading the Combinatorial Histone Language. *ACS Chem. Biol.* **11**, 564–574 (2016).

108. Kallappagoudar, S., Yadav, R. K., Lowe, B. R. & Partridge, J. F. Histone H3 mutations—a special role for H3.3 in tumorigenesis? *Chromosoma* **124**, 177–189 (2015).

109. Funato, K. & Tabar, V. Histone Mutations in Cancer. *Annu. Rev. Cancer Biol.* **2**, 337–351 (2018).

110. Behjati, S. *et al.* Distinct H3F3A and H3F3B driver mutations define chondroblastoma and giant cell tumor of bone. *Nat. Genet.* **45**, 1479–1482 (2013).

111. Lim, J. *et al.* The histone variant H3.3 G34W substitution in giant cell tumor of the bone link chromatin and RNA processing. *Sci. Rep.* **7**, 1–14 (2017).

112. Lu, C. *et al.* Histone H3K36 mutations promote sarcomagenesis through altered histone methylation landscape. *Science (80-.).* **352**, 844–849 (2016).

113. Lehnertz, B. *et al.* H3K27M/I mutations promote context-dependent transformation in acute myeloid leukemia with RUNX1 alterations. *Blood* **130**, 2204–2214 (2017).

114. Gessi, M. *et al.* Evidence of H3 K27M mutations in posterior fossa ependymomas. *Acta Neuropathol.* **132**, 635–7 (2016).

115. Papillon-Cavanagh, S. *et al.* Impaired H3K36 methylation defines a subset of head and neck squamous cell carcinomas. *Nat. Genet.* **49**, (2017).

116. Edmunds, J. W., Mahadevan, L. C. & Clayton, A. L. Dynamic histone H3 methylation during gene induction: HYPB/Setd2 mediates all H3K36 trimethylation. *EMBO J.* **27**, 406–420 (2008).

117. Wagner, E. J. & Carpenter, P. B. Understanding the language of Lys36 methylation at histone H3. *Nat. Publ. Gr.* **13**, 115–126 (2012).

118. Venkatesh, S. *et al.* Set2 methylation of histone H3 lysine 36 suppresses histone exchange on transcribed genes. *Nature* **489**, 452–455 (2012).

119. Zhang, Y. *et al.* Molecular basis for the role of oncogenic histone mutations in modulating H3K36 methylation. *Sci. Rep.* **7**, 1–9 (2017).

120. Fang, J. *et al.* Cancer-driving H3G34V/R/D mutations block H3K36 methylation and H3K36me3–MutSα interaction. *Proc. Natl. Acad. Sci.* **115**, 9598–9603 (2018).

121. Mohammad, F. & Helin, K. Oncohistones: Drivers of pediatric cancers. *Genes Dev.* **31**, 2313–2324 (2017).

122. Pai, C. C. *et al.* A histone H3K36 chromatin switch coordinates DNA double-strand break repair pathway choice. *Nat. Commun.* **5**, (2014).

123. Li, F. *et al.* The histone mark H3K36me3 regulates human DNA mismatch repair through its interaction with MutSα. *Cell* **153**, 590–600 (2013).

124. Pfister, S. X. *et al.* SETD2-Dependent Histone H3K36 Trimethylation Is Required for Homologous Recombination Repair and Genome Stability. *Cell Rep.* **7**, 2006–2018 (2014).

125. Yadav, R. K. *et al.* Histone H3G34R mutation causes replication stress, homologous recombination defects and genomic instability in S. pombe. *Elife* **6**, 1–28 (2017).

126. Bender, S. *et al.* Reduced H3K27me3 and DNA Hypomethylation Are Major Drivers of Gene Expression in K27M Mutant Pediatric High-Grade Gliomas. *Cancer Cell* **24**, 660–672 (2013).

127. Venneti, S. *et al.* Evaluation of histone 3 lysine 27 trimethylation (H3K27me3) and enhancer of zest 2 (EZH2) in pediatric glial and glioneuronal tumors shows decreased H3K27me3 in H3F3A K27M mutant glioblastomas. *Brain Pathol.* **23**, 558–564 (2013).

128. Chan, K. *et al.* The histone H3 . 3K27M mutation in pediatric glioma reprograms H3K27 methylation and gene expression Email alerting service The histone H3 . 3K27M mutation in pediatric glioma reprograms H3K27 methylation and gene expression. *Genes Dev.* **27**, 985–990 (2013).

129. Funato, K., Major, T., Lewis, P. W., Allis, C. D. & Tabar, V. Use of human embryonic

stem cells to model pediatric gliomas with H3.3K27M histone mutation. *Science (80-.).* **346**, 1529–1533 (2014).

130. Mohammad, F. *et al.* EZH2 is a potential therapeutic target for H3K27M-mutant pediatric gliomas. *Nat. Publ. Gr.* **23**, (2017).

131. Campos, E. I. & Reinberg, D. New chaps in the histone chaperone arena. *Genes Dev.* **24**, 1334–1338 (2010).

132. Müller, S., Filipescu, D. & Almouzni, G. Developmental roles of histone H3 variants and their chaperones. *Funct. Nucl.* **29**, 385–419 (2016).

133. Gröbner, S. N. *et al.* The landscape of genomic alterations across childhood cancers. *Nature* **555**, 321–327 (2018).

The developing brain
&
genome instability

2

Vulnerability to aneuploidy in the developing brain: a path to cancer ?

Irena Bočkaj [1], Floris Foijer [1] & Sophia W. M. Bruggeman [1]

[1] Department of Ageing Biology/ERIBA, University Medical Center Groningen, University of Groningen, Antonius Deusinglaan 1, 9713 AV Groningen, the Netherlands

Partly published in Bockaj I. et al., Bioessay (2017)

Aneuploidy in the (developing) brain: state-of-the-field

Maintaining genome integrity is fundamental for cellular functions and adequate growth. Therefore, cells have evolved with multiple surveillance mechanisms to help protect their genetic material and make sure it is integrally passed over generations. Any defect in these mechanisms threatens genome integrity and leads to genome instability (GIN), a hallmark of cancer and ageing[1,2]. GIN can take the form of mutations and chromosomal rearrangements or "aneuploidy". Aneuploidy is the state consequential to GIN, and defines cells that gained or lost whole or parts of chromosomes and thus harbor an aneuploid karyotype[3].

Interestingly, not all tissues within an organism are equally equipped to deal with GIN. For instance, a number of studies have shown tissue specific tolerance for aneuploidy, such as the liver and the brain [4–6]. However, why these differences exist is not well-understood. Neuronal aneuploidy has been associated with neurodevelopmental and neurodegenerative disorders such as Parkinson's or Alzheimer's Disease, Schizophrenia, Mental Retardation and Autism[7–14]. Age-related degeneration of the brain has also been associated with aneuploidy[15–18]. Consequently, a wealth of studies has investigated aneuploidy in aged human or mouse brains. Although most of the studies observed a low level of aneuploidy in aged human and mouse samples[13,14,19–24], several other studies found contradicting results. Indeed, while FISH and sequencing based studies typically identify aneuploidy rates below 4%, Pack *et al.*, Iourov *et al.* and Faggiolli *et al.* all observed aneuploidy affecting 10 to 50% of brain cells[25–27]. Interestingly, a couple of these studies revealed the presence of sub-chromosomal copy number variations (CNV) within the brain, with McConnell reporting ~41% and Cai reporting ~68% of neurons containing large-scale CNVs[24,28]. For more detail, all the studies have been reviewed here[6]. Thus, while the presence of aneuploidy in the brain is now an acknowledged feature, the observed variation in its frequency is a matter of debate. Variation of aneuploidy level within these studies might be explained by the techniques used to assess karyotype compositions but also the nature of the samples subjected to the analysis[6]. This therefore raises the need for better models to study aneuploidy in the brain[6].

Interestingly, a recent study from Andriani *et al*. compared aneuploidy levels between adult and embryonic (developing) brains and observed much higher rates during development (31% of embryonic neurons to be aneuploid compared to 0.1% of adult neurons)[20] in agreement with a previous study by Rehen *et al*.[29]. Several other studies confirmed this high level of aneuploidy in the developing cortex and all along the neural axis including the cerebellum, medulla and hippocampus[19,21,25,30–36]. Moreover, *ex-vivo* observation of mitotic features in neural stem cells from the embryonic subventricular cortical zone showed the presence of mitoses with lagging chromosomes, suggesting that ongoing chromosomal instability (CIN) might be at the root of the aneuploidy observed in the developing brain[29,31].

CIN results from chromosome segregation errors during mitosis, that can be due to intrinsic defects in the mitotic process (mitotic checkpoint deficiencies, cytokinesis failures, cohesin defects, spindle defects) or result from replication stress and un/mis-repaired DNA damage until mitosis [37–41]. While CIN has been widely investigated in embryonic development, ageing and cancer[42–44], how exactly it is involved in neurodevelopment is still a matter of debate. The interesting example of primary microcephaly disorder (MCPH), a neurodevelopmental disorder associated with reduced brain size and aneuploid neurons, points towards the brain as being particularly vulnerable to mutations in centrosome and spindle checkpoint proteins, guardians of the genome during mitosis[45]. This suggests that on one side, the developing brain is vulnerable to the CIN caused by mutations in such proteins[46]. On the other side, as discussed above, some level of CIN and aneuploidy in the developing neural progenitors seems to be tolerated as aneuploid neurons can be fully functional and may be integrated into the brain circuitry[47].

These seemingly conflicting observations suggest the presence of a threshold of CIN/aneuploidy that the neural compartment can tolerate. Indeed, punctual levels of aneuploidy may be used as a physiological developmental mechanism for neuronal diversification and mosaicism[47–49], whereas constant levels of CIN/aneuploidy imposed throughout the development (*e.g.* presence of a genetic mutation) is deleterious and triggers cell death or premature differentiation of the aneuploid cells, as seen in MCPH disorders[46].

Of note, aneuploidy and CIN are features of most tumors and have been proposed as drivers of tumorigenesis[50,51]. Therefore, increased CIN affecting developing neuronal and glial cells could be a possible factor predisposing to brain tumors[52–55]. This is an intriguing observation, since it might explain why pediatric brain cancers frequently exhibit high levels of CIN and aneuploidy (see **Chapters 1, 4** and **6** of this thesis). Ultimately, this raises the hypothesis of the presence of a window of accrued vulnerability to CIN during brain development, that would facilitate oncogenic transformation. Below we discuss possible stages in the developing brain where the neural genome is at risk for instability and potential oncogenesis.

Chromosomal instability in the developing brain: paths to aneuploidy

Endogenous DNA damage in the developing brain

The neural genome is subjected to a constant threat from endogenous events that damage DNA and can cause CIN and aneuploidy[48]. These threats can result from metabolism generating oxidative damage, but also from transcription and replication that overload repair mechanisms[48,56] (Fig 1). Most of the threats to the DNA are single-strand DNA (ssDNA) breaks that result in base mutations if unrepaired. ssDNA breaks can also become double-strand DNA (dsDNA) breaks leading to larger chromosomal rearrangements and aneuploidy. Neural progenitors are particularly sensitive to DNA damage and their susceptibility vary depending on the stage of development[57].

Development of the brain involves widespread cellular proliferation, differentiation, and maturation of NSCs to generate neurons and glia. In mice, neurogenesis in the cortex initiates during embryogenesis and is finished at birth (Fig 1). Up to E11, NSCs undergo a primary burst of proliferation. As DNA replication fastens, the stress load on DNA increases, leading to replication stress. Replication stress creates a vulnerability to acquire DNA damage and a putative window for CIN and aneuploidy[48,58,59] (Fig 1). Later in embryogenesis, high transcriptional dynamism with increasing differentiation triggers important chromatin remodeling events.

Coupled to sustained replication in the progenitor populations, this might confer yet another vulnerability to CIN and aneuploidy[48,60] (Fig 1). Finally, the mature, non-cycling brain is exposed to metabolic dependent damage, called oxidative stress, as a source of DNA damage (Fig 1)[61].

Neural cells have the entire repertoire of DNA repair pathways that protect them from the different lesions to which they are subjected[37] (Fig 1). If the repair pathways are inefficient or overloaded, a high incidence of DNA damage is counteracted by apoptotic pathways that will eliminate damaged/aneuploid cells (Fig 1). Below, we will discuss the different DNA damage routes and the mechanisms that the developing brain implements to avoid detrimental CIN and aneuploidy.

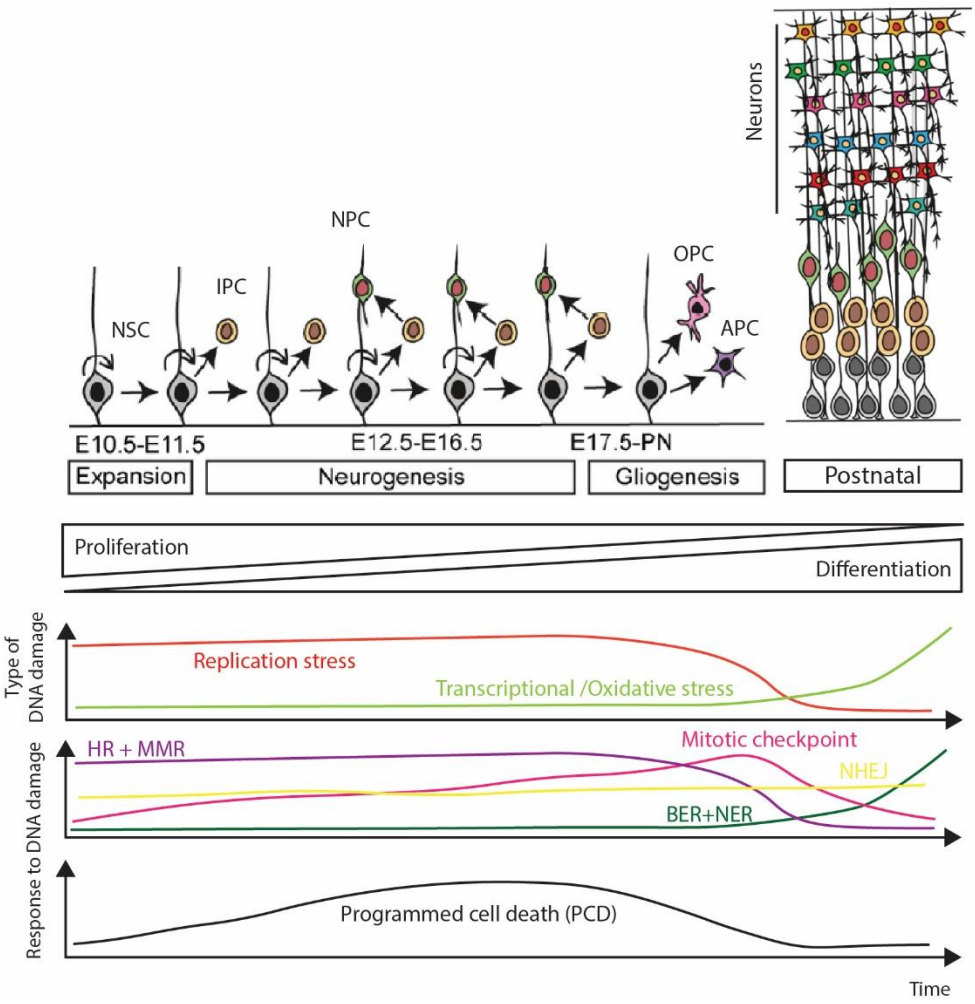

Figure 1. DNA damage and responses to DNA damage in relation to murine cortical development from early embryogenesis to postnatal development. Murine cortical development can be separated in three main phases: from E10.5 to E11.5 where the NSC pool expands to prepare for later production of neurons (neurogenesis). After neurogenesis, NSCs switch to the production of glial cells (APCs and OPCs) during a phase called gliogenesis. Postnatally, the brain cortex is composed of a basal layer of rarely dividing NSCs and neural progenitors, differentiated neurons and glial cells (not shown). During the embryonic proliferative phase, dividing neural cells accumulate replication stress-dependent DNA damage that will be repaired by DNA repair pathways including HR, NHEJ and MMR. At this stage, unrepaired DNA damage will activate an apoptotic pathway or PCD (= Programmed Cell Death). In the homeostatic differentiated brain, oxidative stress is the major source of DNA damage. Single strand breaks created by DNA adducts will be processed by Base and Nucleotide excision repair mechanisms (BER and NER); double strand breaks will be repaired by NHEJ. At this stage, PCD is not active, therefore damaged cells are not cleared out as efficiently as during development, which might predispose to neuroinflammation and neurodegeneration. E=embryonic day ; PN=postnatal ; NSC=neural stem cell ; IPC=intermediate progenitor cell ; NPC=neural progenitor cell ; OPC=oligodendrocyte progenitor cell ; APC=astrocyte progenitor cell. HR = Homologous Recombination ; NHEJ = Non-Homologous End Joining ; MMR = Mismatch Repair ; BER = Base Excision Repair ; NER = nucleotide Excision Repair. Adapted from[62].

Replicative stress

A major source of genome instability in the developing brain is replication-associated damage during the highly proliferative phase of neurogenesis[58]. Replication stress is a general term that describes all aberrant events occurring during DNA synthesis and leading to replication fork slowing or stalling[63–65]. This generates stretches of single-stranded DNA and potential collapse of the replication fork, ultimately leading to dsDNA breaks and genome instability[63,66]. RS can lead to mutations, amplifications, translocations and chromosomal rearrangements[59]. Therefore, RS has also been linked to CIN[59]. Events such as collision of the replicative machinery with pre-existing DNA adducts, with the transcriptional complex (Transcription-replication collision or TRC) or the presence of DNA:RNA hybrids (R-loops) can cause replication stress[64,67,68]. Hard to replicate DNA macro-structures (G-quadruplexes, hairpins, intramolecular triplex DNA) can also slow and stall the replicative machinery[69,70].

Interestingly, a genome-wide study of recurrent chromosomal translocations used to identify frequent dsDNA breaks in NSCs, found 27 preferred targeted genes. Induction of RS experimentally by treating NSCs with Aphidicolin enhanced the phenomenon, suggesting that RS might be a strong contributing factor to the generation of these breaks. The mechanism by which the dsDNA break occurs was imputed to transcription-replication collision (TRC)[71]. Moreover, a few of these genes were associated with neurological disorders and brain cancers, suggesting a potential role of neurodevelopmental RS in oncogenesis[71].

Furthermore, mutations in ATR – a major RS response kinase -- have been found in the microcephaly Seckel Syndrome. An *Atr Seckel* mouse model showed the ATR mutation to severely impact on neurodevelopment due to accumulation of DNA damage and cell death in neural progenitors[72,73]. Altogether, this underscores the high contribution of RS in threatening the genome during neurodevelopment and the low ability of this compartment to cope with any alteration that would damage the RS response (*e.g.* ATR mutations). This points out the special vulnerability of the developing brain to RS induced genome instability[73,74]. Altogether, any underlying mutation that would act in collaboration with RS by for instance, tolerizing the

induced GIN/CIN, might also pave the way for oncogenic transformation (see also **Chapter 6** of this thesis)[56].

Oxidative stress

While the dividing CNS is subjected to direct cell-cycle dependent DNA damage, the genome of differentiated non-cycling neural cells is not unharmed either. The more mature brain will experience another type of DNA threat, mostly linked to the generation of oxidative damage due to high metabolic activity sustaining synaptic connectivity and cognition.

Genome maintenance in mature neural tissue is different than during neurogenesis because of the absence of cell proliferation and therefore lack of RS induced DNA damage. Oxygen metabolism was shown to be a source of genomic instability in mature neurons[61]. The link between oxidative stress and DNA damage in the nervous system was shown by the direct increase of DNA breaks when elevating the levels of reactive oxygen species[75]. Because mature cells do not divide anymore, these damages do not trigger GIN or CIN. It is believed that oxidative stress is at the root of neuroinflammation, resulting in degeneration of the neurons[61,76].

Avoiding aneuploidy in the developing brain

DNA damage response

The importance of the DNA damage response in the brain is underscored by the molecular defects underlying human neurodevelopmental syndromes[77]. Most of these diseases harbor mutations in DNA repair genes, pointing out the special vulnerability of the central nervous system to this type of mutations. These pathologies are therefore indicators of the importance of specific DNA repair pathways in counteracting endogenous DNA damage and maintaining proper neurodevelopment and neuronal homeostasis. Moreover, further mechanistic insight

has been given by genetic manipulation in mouse models that demonstrated the developing nervous system to be highly sensitive to DNA repair deficiencies[78–83].

Like in all tissues, the entire set of DNA repair pathways provides neuroprotection. The time in development will dictate which DNA repair pathway will be used to most efficiently counteract the type of damage occurring at this point. Therefore, like the type of DNA damage, the maintenance factors during development and those essential in the mature – non replicating – brain are different (Fig 1).

Because RS naturally occurs during development, leading to ssDNA and dsDNA breaks, this will engage pathways that are able to repair this type of damage. DNA double strand break repair involves homologous recombination (HR) and non-homologous end joining (NHEJ)[84,85]. Mismatch repair (MMR) is also important during replication[86]. HR requires the replicated sister chromatids as a template, meaning that this pathway is not available in non-replicating or differentiated cells[48]. In non-cycling cells, the error-prone NHEJ repairs dsDNA breaks while ssDNA damage requires the nucleotide excision repair (NER) and base excision repair (BER) to remove DNA adducts created mostly by oxidative stress[87,88] (Fig 1).

Alternatively, if the DNA damage is too detrimental, neural cells can opt to undergo apoptosis or programmed cell death (PCD) (for more detail, see below). Interestingly, DNA lesions in differentiated, non-replicative cells do not activate apoptosis[89,90]. Thus, the acknowledged etiology of DNA repair enzyme mutations in neurodevelopmental diseases resulting in accumulation of DNA damage and GIN, and the fact that some of these syndromes predispose to brain cancers, brings up a role for RS and oxidative stress-dependent GIN in brain cancer initiation as well.

In fact, some somatic brain cancers, for instance H3.3 mutant gliomas, associate frequently with DNA repair proteins alterations (*e.g.* TOP3A, ATR, Chk1) and present a GIN/CIN phenotype[52] (see **Chapter 1** and **6** of this thesis). We might therefore think that the origin of these gliomas resides at a point in neurodevelopment when these DNA repair mechanisms play a particularly important role. Moreover, histone H3.3 itself has a role in DNA repair. H3.3 has been implicated

in both ss- and dsDNA break repair and H3.3 mutant cells have increased sensitivity to DNA damage[91–95]. Because H3.3 mutant glioma most likely originates from an early embryonic progenitor (see **Chapter 1** of this thesis) that would be subjected to RS induced DNA damage, it is of interest to investigate the role of H3.3 in the RS response (see **Chapter 6** of this thesis).

Mature neuronal cells need to be protected from oxidative damage by BER[61] (Fig 1). Interestingly, BER-associated neurological syndromes affect specific brain areas and the cerebellum seems particularly vulnerable given the high incidence of associated cerebellar symptoms [61]. There is evidence that the cerebellum makes greater usage of BER compared to other brain areas[96]. Oxidative damage is produced at high levels in the brain due to a high level of oxygen consumption, which rises after birth. Because cerebellar development extends postnatally (see **Chapter 1** of this thesis, Fig 3), it is subjected to yet another layer of damage (*i.e.,* oxidative) at a point where progenitor proliferation (*i.e.*, RS) is still high, altogether overloading the repair system. This might also relate to the increased incidence of cerebellar tumors that are aneuploid in older children (see **Chapter 1** of this thesis, Fig 2 and 4). These tumors might find their origin in a neonatal progenitor subjected to a high level of endogenous DNA damage and GIN.

When cells experience DNA damage, they activate DNA damage checkpoints to allow for DNA repair that mostly act during the G1, S and G2 phases of the cell cycle[97]. However, another line of defense against mis-(un)repaired DNA damage occurs during mitosis. This constitutes the final chance to avoid unscreened DNA damage to lead to GIN/CIN and aneuploidy via chromosome mis-segregations, and thereby inheritance to daughter cells.

Mitotic checkpoint

Cells have evolved several mechanisms to prevent aneuploidy and GIN caused by pre-mitotic DNA damage during M phase, such as the spindle assembly checkpoint

(SAC), or mitotic checkpoint. The SAC prevents chromosome mis-segregation in mitosis by retaining cells in metaphase until all chromosomes are properly attached to opposing spindle poles. Therefore, defects in the SAC result in flawed chromosome segregations.

The mitotic spindle is a key element in separating sister chromatids during cell division, yet it is also important for regulating the symmetry of neural stem cell divisions[98–100]. Spindle orientation is strongly linked to neurogenesis and survival, and a defective spindle can lead to aneuploidy[101,102]. Interestingly, work from Vargas-Hurtado *et al.* showed that the developing brain fluctuates its response to mitotic challenges over the course of development, with young NSCs being more vulnerable to mitotic challenges than older NSCs. This has been attributed to the spindle architecture (*i.e.,* strength), which protein-composition seem to vary over time during normal brain morphogenesis. This makes it likely that NSCs in a certain window of time (probably during early neurogenesis) exhibit greater sensitivity to any sort of mitotic challenge and therefore, if a pro-tumorigenic context is present (*e.g.* presence of a genetic alteration), would be more likely to acquire CIN and transform, ultimately promoting tumorigenesis[103,104].

While the mitotic checkpoint can prevent most mitotic abnormalities, it does not recognize merotelic attachments, in which one of the two sister chromatids is connected to both spindle poles. Such flawed attachments can lead to lagging chromosomes and aneuploid cells when unresolved. It has been proposed that a second checkpoint exists that delays chromosome decondensation and nuclear envelope reassembly (NER) when chromosomes lag behind during anaphase[105]. Interestingly, this so-called chromosome segregation checkpoint (CSC) might be relevant for histone H3.3 mutant brain cancer. Indeed, the functioning of the CSC relies on Aurora B kinase activity. However, the downstream effectors of Aurora B kinase responsible for the aneuploidy-preventive effect of the CSC have not yet been identified[106,107]. One possible target could be the serine 31 residue of Histone 3.3 ($H3.3^{S31}$)[108] (See **Appendices** for more detail about the chromosome segregation checkpoint). Given the emerging role of the histone H3.3 variant in genome maintenance, one can imagine that a mutation affecting this histone variant

might as well affect genome integrity via its putative role in the CSC. If, and how, histone H3.3 mutations disrupt genome maintenance and facilitate oncogenic transformation remains to be investigated.

Programmed cell death

During neurodevelopment and homeostasis, cells die naturally and spontaneously. This phenomenon is called programmed cell death (PCD)[109] and operates through Caspase dependent apoptotic mechanisms[89,90]. In the developing cortex, it has been suggested that a burst of cell death follows the neuron-glial switch[110] (Fig 1). Interestingly, PCD has also emerged as a quality control mechanism that clears aneuploid neurons and protects the brain against devastating consequences of developmental genomic instability[30,34,111–113]. Indeed, a correlation between rising aneuploidies and inhibited Caspase-dependent cell death pathways has been documented in the developing brain[20,34].

This highlights GIN as a physiological process by which genetic mosaicism is created for functional diversification of brain cells during brain development, as it has been shown that aneuploid neurons are fully functional and may be integrated into the brain circuitry[47]. Nonetheless, it is not a process without deleterious consequences and therefore requires fine-tuning by a clearance mechanism of cell-death to avoid the balance to be tipped towards the pathological effects of aneuploidy. Therefore, PCD might enable tolerance of mild aneuploidies, whereas extreme aneuploidies, judged detrimental, are cleared out[34]. Because some aneuploidies persist throughout development into adulthood, it remains to be determined which type of aneuploidies, and at which threshold, trigger this clearance program. One might think that any disruption in this mechanism might select for unwanted aneuploidies that could potentially be oncogenic. Therefore, it is important to better decipher the molecular triggers of the clearance mechanism in neurodevelopment.

Conclusion

While defects in cell division have been linked to microcephaly disorders[46], their relationship to tumorigenesis in the setting of pediatric brain cancers has yet to be established. In the case of microcephaly disorders, it seems that following GIN/CIN, cell death mechanisms are triggered that will clear the aneuploid progeny *en masse* and cause a hypomorphic phenotype[46,114,115]. We speculate that the tumorigenic setting is influenced by a combination of physiological events, where ***1)*** down-regulated cell death mechanisms (for instance, *TP53* loss) ; ***2)*** upregulated proliferation with the accompanying replication stress and ***3)*** an underlying driving mutation, might act in concert to promote oncogenesis. Ultimately, this would explain why the aneuploid brain phenotype is mirrored in some of the pediatric brain cancer subtypes.

REFERENCES

1. Hanahan, D. & Weinberg, R. a. Hallmarks of cancer: the next generation. *Cell* **144**, 646–74 (2011).

2. López-Otín, C., Blasco, M. A., Partridge, L., Serrano, M. & Kroemer, G. The hallmarks of aging. *Cell* **153**, 1194 (2013).

3. Orr, B., Godek, K. M. & Compton, D. Aneuploidy. *Curr. Biol.* **25**, R538–R542 (2015).

4. Duncan, A. W. *et al.* Aneuploidy as a mechanism for stress-induced liver adaptation. *J. Clin. Invest.* **122**, 3307–3315 (2012).

5. Faggioli, F., Vezzoni, P. & Montagna, C. Single-cell analysis of ploidy and centrosomes underscores the peculiarity of normal hepatocytes. *PLoS One* **6**, (2011).

6. Rosenkrantz, J. L. *et al.* Investigating somatic aneuploidy in the brain: why we need a new model. **126**, 337–350 (2018).

7. La Cognata, V., Morello, G., D'Agata, V. & Cavallaro, S. Copy number variability in Parkinson's disease: assembling the puzzle through a systems biology approach. *Human Genetics* **136**, 13–37 (2017).

8. Goate, A. *et al.* Segregation of a missense mutation in the amyloid precursor protein gene with familial Alzheimer's disease. *Nature* **349**, 704–706 (1991).

9. Shi, J. *et al.* Common variants on chromosome 6p22.1 are associated with schizophrenia. *Nature* **460**, 753–757 (2009).

10. Guffanti, G. *et al.* Increased CNV-region deletions in mild cognitive impairment (MCI) and Alzheimer's disease (AD) subjects in the ADNI sample. *Genomics* **102**, 112–22 (2013).

11. Toft, M. & Ross, O. A. Copy number variation in Parkinson's disease. *Genome Medicine* **2**, (2010).

12. Vittori, A. *et al.* Copy-number variation of the neuronal glucose transporter gene SLC2A3 and age of onset in Huntington's disease. *Hum. Mol. Genet.* **23**, 3129–37 (2014).

13. Yurov, Y. B., Vostrikov, V. M., Vorsanova, S. G., Monakhov, V. V & Iourov, I. Y. Multicolor fluorescent in situ hybridization on post-mortem brain in schizophrenia as an approach for identification of low-level chromosomal aneuploidy in neuropsychiatric diseases. *Brain Dev.* **23 Suppl 1**, S186-90 (2001).

14. Yang, Y., Geldmacher, D. S. & Herrup, K. DNA replication precedes neuronal cell death in Alzheimer's disease. *J. Neurosci.* **21**, 2661–2668 (2001).

15. Kennedy, S. R., Loeb, L. A. & Herr, A. J. Somatic mutations in aging, cancer and neurodegeneration. *Mech. Ageing Dev.* **133**, 118–126 (2012).

16. Daniel Harris, BA, Lynn McNicoll, MD, Gary Epstein-Lubow, MD, and Kali S. Thomas, P. Mechanisms and consequences of aneuploidy and chromosome instability in the aging brain. *Physiol. Behav.* **176**, 139–148 (2017).

17. Vijg, J., Dong, X., Milholland, B. & Zhang, L. Genome instability: A conserved mechanism of ageing? *Essays in Biochemistry* **61**, 305–315 (2017).

18. Zhang, L. & Vijg, J. Somatic Mutagenesis in Mammals and Its Implications for Human Disease and Aging. *Annu. Rev. Genet.* **52**, 397–419 (2018).

19. Rehen, S. K. *et al.* Constitutional aneuploidy in the normal human brain. *J. Neurosci.* **25**, 2176–2180 (2005).

20. Andriani, G. A. *et al.* Whole chromosome aneuploidy in the brain of Bub1bH/H and Ercc1-/Δ7 mice. *Hum. Mol. Genet.* **25**, 755–765 (2016).

21. Knouse, K. a., Wu, J., Whittaker, C. a. & Amon, a. Single cell sequencing reveals low levels of aneuploidy across mammalian tissues. *Proc. Natl. Acad. Sci.* **111**, 13409–13414 (2014).

22. van den Bos, H. *et al.* Single-cell whole genome sequencing reveals no evidence for common aneuploidy in normal and Alzheimer's disease neurons. *Genome Biol.* **17**, 116 (2016).

23. Cai, X. *et al.* Single-Cell, Genome-wide Sequencing Identifies Clonal Somatic Copy-Number Variation in the Human Brain. *Cell Rep.* **8**, 1280–1289 (2014).

24. McConnell, M. J. *et al.* Mosaic copy number variation in human neurons. *Science (80-.).* **342**, 632–637 (2013).

25. Faggioli, F., Wang, T., Vijg, J. & Montagna, C. Chromosome-specific accumulation of aneuploidy in the aging mouse brain. *Hum. Mol. Genet.* **21**, 5246–5253 (2012).

26. Pack, S. D. *et al.* Individual adult human neurons display aneuploidy: Detection by fluorescence in situ hybridization and single neuron PCR. *Cell Cycle* **4**, 1758–1760 (2005).

27. Iourov, I. Y., Vorsanova, S. G., Liehr, T. & Yurov, Y. B. Aneuploidy in the normal, Alzheimer's disease and ataxia-telangiectasia brain: Differential expression and pathological meaning. *Neurobiol. Dis.* **34**, 212–220 (2009).

28. Cai, X. *et al.* Report Identifies Clonal Somatic Copy-Number Variation in the Human Brain. *CELREP* **8**, 1280–1289 (2014).

29. Rehen, S. K. *et al.* Chromosomal variation in neurons of the developing and adult mammalian nervous system. *Proc. Natl. Acad. Sci. U. S. A.* **98**, 13361–13366 (2001).

30. Yurov, Y. B. *et al.* Aneuploidy and confined chromosomal mosaicism in the developing human brain. *PLoS One* **2**, 4–9 (2007).

31. Yang, A. H. *et al.* Chromosome segregation defects contribute to aneuploidy in normal neural progenitor cells. *J. Neurosci.* **23**, 10454–62 (2003).

32. Kaushal, D. *et al.* Alteration of gene expression by chromosome loss in the postnatal mouse brain. *J. Neurosci.* **23**, 5599–5606 (2003).

33. Westra, J. W. *et al.* Aneuploid mosaicism in the developing and adult cerebellar cortex. *J. Comp. Neurol.* **507**, 1944–1951 (2008).

34. Peterson, S. E. *et al.* Aneuploid cells are differentially susceptible to caspase-mediated death during embryonic cerebral cortical development. *J. Neurosci.* **32**, 16213–16222 (2012).

35. Yurov, Y. B. *et al.* The variation of aneuploidy frequency in the developing and adult human brain revealed by an interphase FISH study. *J. Histochem. Cytochem.* **53**, 385–390 (2005).

36. Yurov, Y. B., Vorsanova, S. G., Liehr, T., Kolotii, A. D. & Iourov, I. Y. X chromosome aneuploidy in the Alzheimer's disease brain. *Mol. Cytogenet.* **7**, 20 (2014).

37. Sarni, D. & Kerem, B. Oncogene-induced replication stress drives genome instability and tumorigenesis. *International Journal of Molecular Sciences* **18**, (2017).

38. Chan, K. L., Palmai-Pallag, T., Ying, S. & Hickson, I. D. Replication stress induces sister-chromatid bridging at fragile site loci in mitosis. *Nat. Cell Biol.* **11**, 753–760 (2009).

39. Giam, M. & Rancati, G. Aneuploidy and chromosomal instability in cancer: a jackpot to chaos. *Cell Div.* **10**, 3 (2015).

40. Durkin, S. G., Arlt, M. F., Howlett, N. G. & Glover, T. W. Depletion of CHK1, but not CHK2, induces chromosomal instability and breaks at common fragile sites. *Oncogene* **25**, 4381–4388 (2006).

41. Tijhuis, A. E., Johnson, S. C. & McClelland, S. E. The emerging links between chromosomal instability (CIN), metastasis, inflammation and tumour immunity. *Mol. Cytogenet.* **12**, 1–21 (2019).

42. Hassold T & Hunt P. To err (meiotically) is human: the genesis of human aneuploidy. *Nat. Rev. Genet.* **2**, 280–91 (2001).

43. Ben-David, U. & Amon, A. Context is everything: aneuploidy in cancer. *Nat. Rev. Genet.* **21**, 44–62 (2020).

44. Shahbazi, M. N. *et al.* Developmental potential of aneuploid human embryos cultured beyond implantation. *Nat. Commun.* **11**, 1–15 (2020).

45. Gilmore, E. C. & Walsh, C. A. Genetic causes of microcephaly and lessons for neuronal development. *Wiley Interdiscip. Rev. Dev. Biol.* **2**, 461–478 (2013).

46. Marthiens, V. *et al.* Centrosome amplification causes microcephaly. *Nat. Cell Biol.* **15**, 731–740 (2013).

47. Kingsbury, M. A. *et al.* Aneuploid neurons are functionally active and integrated into brain circuitry. *Proc. Natl. Acad. Sci. U. S. A.* **102**, 6143–6147 (2005).

48. Mckinnon, P. J. Maintaining genome stability in the nervous system. *Nat. Neurosci.* **16**, 1523–1529 (2013).

49. Mattson, M. P. Does DNA damage sculpt the developing brain? *Trends Neurosci.* **24**, 77 (2001).

50. Holland, A. J. & Cleveland, D. W. Boveri revisited: Chromosomal instability, aneuploidy and tumorigenesis. *Nat. Rev. Mol. Cell Biol.* **10**, 478 (2009).

51. Holland, A. J. & Cleveland, D. W. Losing balance: The origin and impact of aneuploidy in cancer. *EMBO Rep.* **13**, 501–514 (2012).

52. Mackay, A. *et al*. Integrated Molecular Meta-Analysis of 1,000 Pediatric High-Grade and Diffuse Intrinsic Pontine Glioma. *Cancer Cell* **32**, 520-537.e5 (2017).

53. Northcott, P. a. *et al.* Subgroup-specific structural variation across 1,000 medulloblastoma genomes. *Nature* **488**, 49–56 (2012).

54. Pajtler, K. W. *et al.* Molecular Classification of Ependymal Tumors across All CNS Compartments, Histopathological Grades, and Age Groups. *Cancer Cell* **27**, 728–743 (2015).

55. Gröbner, S. N. *et al.* The landscape of genomic alterations across childhood cancers. *Nature* **555**, 321–327 (2018).

56. Tubbs, A. & Nussenzweig, A. Endogenous DNA Damage as a Source of Genomic Instability in Cancer. *Cell* **168**, 644–656 (2017).

57. Orii, K. E., Lee, Y., Kondo, N. & McKinnon, P. J. Selective utilization of nonhomologous end-joining and homologous recombination DNA repair pathways during nervous system development. *Proc. Natl. Acad. Sci. U. S. A.* **103**, 10017–22 (2006).

58. Lee, Y. *et al.* Neurogenesis requires TopBP1 to prevent catastrophic replicative DNA damage in early progenitors. *Nat. Neurosci.* **15**, 819–826 (2012).

59. Burrell, R. A. *et al.* Replication stress links structural and numerical cancer chromosomal instability. *Nature* **494**, 492–496 (2013).

60. May, C., Page, S. E. E. L., Glass, C. K. & Rosenfeld, M. G. A topoisomerase IIbeta-mediated dsDNA break required for regulated transcription. 1798–1803 (2011).

61. Narciso, L. *et al.* The Response to Oxidative DNA Damage in Neurons: Mechanisms and Disease. *Neural Plast.* **2016**, (2016).

62. Mukhtar, T. & Taylor, V. Untangling Cortical Complexity During Development. *J. Exp. Neurosci.* **12**, (2018).

63. O'Driscoll, M. The pathological consequences of impaired genome integrity in humans; disorders of the DNA replication machinery. *J. Pathol.* **241**, 192–207 (2017).

64. Zeman, M. K. & Cimprich, K. A. Causes and consequences of replication stress. *Nat. Cell Biol.* **16**, 2–9 (2014).

65. Magdalou, I., Lopez, B. S., Pasero, P. & Lambert, S. A. E. The causes of replication stress and their consequences on genome stability and cell fate. *Semin. Cell Dev. Biol.* **30**, 154–164 (2014).

66. Zou, L. & Elledge, S. J. Sensing DNA damage through ATRIP recognition of RPA-ssDNA complexes. *Science (80-.).* **300**, 1542–1548 (2003).

67. Hamperl, S. & Cimprich, K. A. Conflict Resolution in the Genome: How Transcription and Replication Make It Work. *Cell* **167**, 1455–1467 (2016).

68. Gan, W. *et al.* R-loop-mediated genomic instability is caused by impairment of replication fork progression. *Genes Dev.* **25**, 2041–2056 (2011).

69. Wang, Y. *et al.* G-quadruplex DNA drives genomic instability and represents a targetable molecular abnormality in ATRX-deficient malignant glioma. *Nat. Commun.* **10**, (2019).

70. Charlier, C. F. & A P Martins, R. Protective Mechanisms Against DNA Replication Stress in the Nervous System. *Genes (Basel).* **11**, (2020).

71. Wei, P. C. *et al.* Long Neural Genes Harbor Recurrent DNA Break Clusters in Neural Stem/Progenitor Cells. *Cell* **164**, 644–655 (2016).

72. O'Driscoll, M., Ruiz-Perez, V. L., Woods, C. G., Jeggo, P. A. & Goodship, J. A. A splicing mutation affecting expression of ataxia-telangiectasia and Rad3-related protein (ATR) results in Seckel syndrome. *Nat. Genet.* **33**, 497–501 (2003).

73. Murga, M. *et al.* A mouse model of ATR-Seckel shows embryonic replicative stress and accelerated aging. *Nat. Genet.* **41**, 891–898 (2009).

74. Bellelli, R. *et al.* Polε Instability Drives Replication Stress, Abnormal Development, and Tumorigenesis. *Mol. Cell* **70**, 707-721.e7 (2018).

75. Karanjawala, Z. E., Murphy, N., Hinton, D. R., Hsieh, C. L. & Lieber, M. R. Oxygen metabolism causes chromosome breaks and is associated with the neuronal apoptosis observed in DNA double-strand break repair mutants. *Curr. Biol.* **12**, 397–402 (2002).

76. Borgesius, N. Z. *et al.* Accelerated age-related cognitive decline and neurodegeneration, caused by deficient DNA repair. *J. Neurosci.* **31**, 12543–12553 (2011).

77. McKinnon, P. J. Genome integrity and disease prevention in the nervous system. *Genes Dev.* **31**, 1180–1194 (2017).

78. Hong, S. *et al.* Defective neurogenesis and schizophrenia-like behavior in PARP-1-deficient mice. *Cell Death Dis.* **10**, (2019).

79. Onishi, K. *et al.* Genome stability by DNA

polymerase β in neural progenitors contributes to neuronal differentiation in cortical development. *J. Neurosci.* **37**, 8444–8458 (2017).

80. Buck, D. *et al.* Cernunnos, a novel nonhomologous end-joining factor, is mutated in human immunodeficiency with microcephaly. *Cell* **124**, 287–299 (2006).

81. O'Driscoll, M., Gennery, A. R., Seidel, J., Concannon, P. & Jeggo, P. A. An overview of three new disorders associated with genetic instability: LIG4 syndrome, RS-SCID and ATR-Seckel syndrome. *DNA Repair (Amst).* **3**, 1227–1235 (2004).

82. McKinnon, P. J. & Caldecott, K. W. DNA strand break repair and human genetic disease. *Annu. Rev. Genomics Hum. Genet.* **8**, 37–55 (2007).

83. McKinnon, P. J. ATM and ataxia telangiectasia. *EMBO Rep.* **5**, 772–776 (2004).

84. Jasin, M. & Rothstein, R. Repair of strand breaks by homologous recombination. *Cold Spring Harb. Perspect. Biol.* **5**, (2013).

85. Williams, G. J. *et al.* Structural insights into NHEJ: Building up an integrated picture of the dynamic DSB repair super complex, one component and interaction at a time. *DNA Repair (Amst).* **17**, 110–120 (2014).

86. Kunkel, T. A. & Erie, D. A. Eukaryotic Mismatch Repair in Relation to DNA Replication. *Annu. Rev. Genet.* **49**, 291–313 (2015).

87. Goosen, N. Nucleotide Excision Repair in Eukaryotes. *Encycl. Biol. Chem. Second Ed.* 341–344 (2013). doi:10.1016/B978-0-12-378630-2.00491-6

88. Barzilai, A. The contribution of the DNA damage response to neuronal viability. *Antioxidants Redox Signal.* **9**, 211–218 (2007).

89. Nijhawan, D., Honarpour, N. & Wang, X. Apoptosis in Neural Development and Disease. *Annu. Rev. Neurosci.* **23**, 73–87 (2000).

90. Yoshida, H. *et al.* Apaf1 is required for mitochondrial pathways of apoptosis and brain development. *Cell* **94**, 739–50 (1998).

91. Frey, A., Listovsky, T., Guilbaud, G., Sarkies, P. & Sale, J. E. Histone H3.3 is required to maintain replication fork progression after UV damage. *Curr. Biol.* **24**, 2195–2201 (2014).

92. Ray-Gallet, D. *et al.* Dynamics of Histone H3 Deposition In Vivo Reveal a Nucleosome Gap-Filling Mechanism for H3.3 to Maintain Chromatin Integrity. *Mol. Cell* **44**, 928–941 (2011).

93. Adam, S. *et al.* Real-Time Tracking of Parental Histones Reveals Their Contribution to Chromatin Integrity Following DNA Damage. *Mol. Cell* **64**, 65–78 (2016).

94. Adam, S., Polo, S. E. & Almouzni, G. XTranscription recovery after DNA damage requires chromatin priming by the H3.3 histone chaperone HIRA. *Cell* **155**, 94 (2013).

95. Luijsterburg, M. S. *et al.* PARP1 Links CHD2-Mediated Chromatin Expansion and H3.3 Deposition to DNA Repair by Non-homologous End-Joining. *Mol. Cell* **61**, 547–562 (2016).

96. Imam, S. Z., Karahalil, B., Hogue, B. A., Souza-Pinto, N. C. & Bohr, V. A. Mitochondrial and nuclear DNA-repair capacity of various brain regions in mouse is altered in an age-dependent manner. *Neurobiol. Aging* **27**, 1129–1136 (2006).

97. de Gooijer, M. C. *et al.* The G2 checkpoint—a node-based molecular switch. *FEBS Open Bio* **7**, (2017).

98. Huttner, W. B. & Kosodo, Y. Symmetric versus asymmetric cell division during neurogenesis in the developing vertebrate central nervous system. *Curr. Opin. Cell Biol.* **17**, 648–657 (2005).

99. Peyre, E. & Morin, X. An oblique view on the role of spindle orientation in vertebrate neurogenesis. *Dev. Growth Differ.* **54**, 287–305 (2012).

100. Shitamukai, A. & Matsuzaki, F. Control of asymmetric cell division of mammalian neural progenitors. *Dev. Growth Differ.* **54**, 277–286 (2012).

101. Pilaz, L.-J. *et al.* Prolonged Mitosis of Neural Progenitors Alters Cell Fate in the Developing Brain. *Neuron* **89**, 83–99 (2016).

102. Compton, D. A. Mechanism of Aneuploidy. **23**, 109–113 (2012).

103. Vargas-Hurtado, D. *et al.* Differences in Mitotic Spindle Architecture in Mammalian Neural Stem Cells Influence Mitotic Accuracy during Brain Development. *Curr. Biol.* 1–13 (2019). doi:10.1016/j.cub.2019.07.061

104. Williams, S. E. *et al.* Aspm sustains postnatal cerebellar neurogenesis and medulloblastoma growth in mice. *Development* **142**, 3921–3932 (2015).

105. Maiato, H., Afonso, O. & Matos, I. A chromosome separation checkpoint: A midzone Aurora B gradient mediates a chromosome separation checkpoint that regulates the anaphase-telophase transition. *BioEssays* **37**, 257–266 (2015).

106. Afonso, O. *et al.* Feedback control of chromosome separation by a midzone Aurora B gradient. *Science* **332**, 332–6 (2014).

107. Karg, T., Warecki, B. & Sullivan, W. Aurora B-mediated localized delays in nuclear envelope formation facilitate inclusion of late-segregating chromosome fragments. *Mol. Biol. Cell* **26**, 2227–41 (2015).

108. Li, M., Dong, Q. & Zhu, B. Aurora Kinase B Phosphorylates Histone H3.3 at Serine 31 during Mitosis in Mammalian Cells. *J. Mol. Biol.* 2–5 (2017). doi:10.1016/j.jmb.2017.01.016

109. Yamaguchi, Y. & Miura, M. Programmed Cell Death in Neurodevelopment. *Dev. Cell* **32**, 478–490 (2015).

110. Takahashi, T., Goto, T., Miyama, S., Nowakowski, R. S. & Caviness, V. S. Sequence of neuron origin and neocortical laminar fate: Relation to cell cycle of origin in the developing murine cerebral wall. *J. Neurosci.* **19**, 10357–10371 (1999).

111. Rohrback, S., Siddoway, B., Liu, C. S. & Chun, J. Genomic mosaicism in the developing and adult brain. *Dev. Neurobiol.* **78**, 1026–1048 (2018).

112. Iourov, I. Y., Vorsanova, S. G., Yurov, Y. B. & Kutsev, S. I. Ontogenetic and pathogenetic views on somatic chromosomal mosaicism. *Genes (Basel).* **10**, (2019).

113. Bushman, D. M. & Chun, J. The genomically mosaic brain: Aneuploidy and more in neural diversity and disease. *Semin. Cell Dev. Biol.* **24**, 357–369 (2013).

114. Gao, Y. *et al.* A critical role for DNA end-joining proteins in both lymphogenesis and neurogenesis. *Cell* **95**, 891–902 (1998).

115. Frank, K. M. *et al.* DNA ligase IV deficiency in mice leads to defective neurogenesis and embryonic lethality via the p53 pathway. *Mol. Cell* **5**, 993–1002 (2000).

Pediatric medulloblastoma
&
cell-of-origin

3

The developmental stage of the medulloblastoma cell-of-origin is maintained in cancer and restricts Hedgehog pathway usage and drug sensitivity

Marlinde J. Smit [1], Inna Armandari [1,5], Irena Bočkaj [1,5], Tosca E.I. Martini [1,5], Walderik W. Zomerman [1,5], Zillah Siragna [1], Tiny G.J. Meeuwsen [1], Frank J.G. Scherpen [1], Mirthe H. Schoots [2], Martha Ritsema [3], Wilfred F.A. den Dunnen [2], Eelco W. Hoving [4], Judith T.M.L. Paridaen [3], Gerald de Haan [3], Victor Guryev [3], and Sophia W.M. Bruggeman [1 *]

[1] Departments of Pediatric Oncology and Hematology/Pediatrics, UMCG, the Netherlands
[2] Pathology and Medical Biology, UMCG, the Netherlands
[3] European Research Institute for the Biology of Ageing/ERIBA, UMCG, the Netherlands
[4] Princess Máxima Center for Pediatric Oncology, Utrecht, The Netherlands
[5] Equal contribution
*Corresponding author and lead contact

ABSTRACT

Sonic Hedgehog (SHH) medulloblastoma originates from the cerebellar granule neuron progenitor (CGNP) population that depends on Hedgehog signaling for its expansion. While SHH tumors are characterized by an overall deregulation of this pathway, they also exhibit aberrations that are specific for patient age. To investigate if the developmental stage of the tumor cell-of-origin can account for these age-specific lesions, we compared transcriptomes from developing mouse CGNPs and observed highly dynamic gene expression changes as function of age. Cross-species comparison with a cohort of SHH medulloblastoma showed partial maintenance of these patterns in the different medulloblastoma patient-age groups. In particular, we found low primary cilia expression in early CGNPs and infant medulloblastoma, which coincided with insensitivity to Smoothened manipulation. Together, these findings can explain the absence of *SMOOTHENED* mutations in infant patients and suggest that drugs targeting the SHH pathway downstream of *SMOOTHENED* will be most appropriate for infant patients.

INTRODUCTION

Medulloblastoma is a malignant tumor of the cerebellum that frequently affects children. It consists of four main transcriptional subgroups that can be further subdivided upon additional molecular profiling [1–3]. The Sonic Hedgehog (SHH) subgroup of medulloblastoma, which accounts for thirty percent of all medulloblastoma cases, is believed to originate from the cerebellar granule neuron progenitor (CGNP) population that critically depends on Sonic Hedgehog pathway signaling for its perinatal expansion [4–9]. Sonic Hedgehog is a secreted morphogen that controls development and patterning in many organs including the central nervous system [10,11]. The pathway becomes active when SHH binds to its receptor PATCHED (PTCH1), which relieves inhibition of SMOOTHENED (SMO) and induces MYCN [10–13]. Activated SMO inhibits tumor suppressor protein SUFU and stimulates processing of the GLI factors into transcriptional activators. In the absence of the SHH morphogen, transcription of SHH target genes is actively

repressed by SUFU mediated formation of GLI repressors or direct transcriptional repression [14–16].

SHH medulloblastoma is characterized by an overall deregulation of SHH signaling that is often accompanied by mutually exclusive mutations in SHH pathway components, underlining the importance of this pathway in driving tumorigenesis [1,17]. Interestingly, there is also patient age-related heterogeneity within this subgroup, suggesting that developmental factors affect tumor biology [2,3,17–21]. For instance, infant and adult medulloblastoma display distinct gene expression patterns, as well as differences in copy number alterations, mutations, and tumor localization. Strikingly, mutations in SHH pathway genes are also correlated with patient age [17]. Whereas *PTCH1* mutations occur across all age groups, *SUFU* mutations are almost exclusively found in infant patients; *GLI2*, *NMYC* and *TP53* mutations in older children; and *SMO* mutations in adults.

These latter findings raise the question why the pathway is differentially perturbed depending on patient age, as these mutations would presumably have identical outcomes, *i.e.,* enhanced activation of SHH target genes. One explanation could be that the tumor cells-of-origin undergo changes in sensitivity to, or usage of, the Sonic Hedgehog signaling pathway during development, which would promote age-specific oncogenic lesions in the pathway. Assuming that tumors diagnosed during early life have their origins in earlier stages of neural development than tumors from older patients, we can speculate that some of the age-specific characteristics of their unique cells-of-origin are preserved, or even exploited, during oncogenesis. The presumed cell-of-origin for SHH medulloblastoma is part of the CGNP lineage, which is indeed a highly dynamic cell population that spans over three weeks of mouse and two years of human development [22]. Yet the precise moment of transformation is unknown [4,9,23–30]. In mice, future CGNPs become specified in the upper rhombic lip (uRL) structure of the hindbrain around embryonic day E13.5, from where they migrate across the surface of the cerebellar primordium [23–26]. Here, they form a secondary germinal zone termed external granular layer (EGL), with a peak in proliferation occurring around birth that is driven by Purkinje neuron secreted SHH. Once they reach maturity, terminally differentiating granule neurons cease

proliferation and migrate inwards until they reach their final destination in the internal granular layer (IGL) of the cerebellum [7–9,25,27]. Besides the longer gestational period, the development of human CGNPs generally resembles that of the mouse [28].

To study the potential impact of CGNP developmental age on medulloblastomagenesis, we have taken advantage of a transgenic mouse model that allows the prospective isolation of the CGNP cell lineage during embryonic and early postnatal development [31,32]. As expected, we found that CGNPs exhibit dynamic changes in gene expression in time, highlighting the identity changes of the CGNP population as neural development progresses. We also confirmed that CGNPs resemble human SHH medulloblastoma and importantly, that early embryonic CGNPs co-segregate with the youngest patients, thus establishing a relationship between cell-of-origin and patient age. In particular, primary cilia expression was low across young CGNPs and patients, which was somewhat unexpected given the importance of primary cilia for SHH pathway signaling activity [33–40]. In line, early embryonic CGNPs displayed an intrinsic unresponsiveness to SHH or Smo-mediated pathway stimulation, whereas they were partially sensitive to deletion of *Sufu* that is known to have cilia-independent functions [41,42]. These observations may have clinical implications, as patients with early developmental medulloblastoma are most likely to benefit from drugs targeting the primary cilia-independent part of the SHH pathway [43].

RESULTS

Developing cerebellar granule neuron progenitors undergo dynamic changes in gene expression that are related to medulloblastoma

To address if intrinsic changes in the developing medulloblastoma cell-of-origin could contribute to the age-dependent mutations in the *SUFU*, *MYCN, GLI2* and *SMO* genes found in SHH medulloblastoma, we made use of a transgenic mouse model that allows prospective isolation of the developing CGNP cell lineage from their specification in the cerebellar primordium onwards (Figure 1A)[31]. Hereto, the

Math1-CreER^{T2} transgenic mouse strain was combined with a conditional tdTomato fluorescent reporter strain [26,44]. The Math1-CreER^{T2} transgene drives the expression of a tamoxifen inducible CreER^{T2} under the control of the 3' *Atoh1* enhancer, which is highly specific for early specified CGNPs at 13.5 days of gestation (embryonic day E13.5)[26,45]. Accordingly, we observed that treatment of pregnant females with a single dose of tamoxifen at E13.5 induced the acute and stable labeling of CGNPs with tdTomato in the offspring (Figure 1B). Fluorescent cerebella were subsequently dissected at E15.5, E17.5, P0 (day of birth), P7 (postnatal day 7), P14 and P30; and tdTomato^{+} CGNPs were purified using fluorescence activated cell sorting (FACS)(Figure 1A). From these samples, we generated transcriptomes using RNA-seq (Figure 1C-E and Table S1). Principal component analysis revealed that more than 70% of all variation between samples could be explained by developmental age, demonstrating that CGNPs undergo significant changes in gene expression as a function of time (Figure 1C).

To further explore these dynamic changes, we performed unsupervised hierarchical clustering analysis to identify genes that were differentially expressed (DE) between at least two time points (Figure 1D and Table S2). We next divided the DE genes into five major gene clusters. The yellow cluster contained genes that were most highly expressed at embryonic time points (E15.5 and E17.5, n=471 genes), the orange cluster genes that were high during embryonic and early postnatal time points (E15.5-P7, n=1541 genes), genes in the red cluster were most highly expressed at early postnatal time points (P0 and P7, n=619 genes), and light and dark blue clusters contained the genes that were induced upon granule neuron maturation (P14 and P30, n=763 and 943 genes, respectively)(Figure 1D,E).

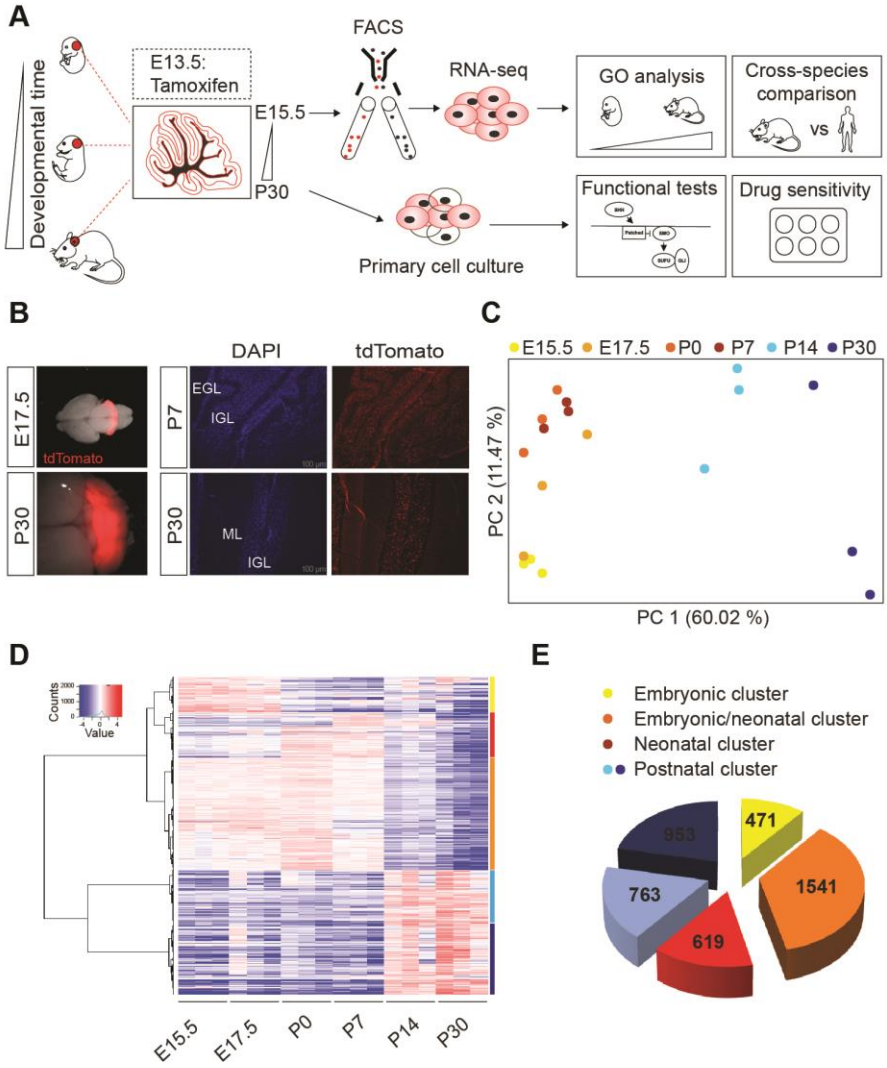

Figure 1. Developing cerebellar granule neuron progenitors (CGNPs) exhibit age-specific gene expression. (A) Schematic overview of the experimental workflow. Embryonic CGNPs are labeled with tdTomato following a single Tamoxifen pulse administered to pregnant females. Fluorescent cerebella are dissected at different time points between E15.5 and P30. tdTomato$^+$ cells are sorted by FACS for further experiments (E=embryonic day; P=postnatal day, FACS=fluorescence-activated cell sorting). **(B)** Stereoscopic (left panels) or microscopic images (middle and right panels) showing direct tdTomato fluorescence in whole mount cerebella and sagittal sections, respectively (EGL=external granular layer; IGL=internal granular layer; ML=molecular layer). **(C)** Principal component analysis of E15.5, E17.5, P0, P7, P14 and P30 CGNP transcriptomes (three biological replicates per developmental time point). (**D)** Heatmap showing differentially expressed CGNP genes as function of developmental time point (unsupervised hierarchical clustering analysis). **(E)** Pie chart showing five major clusters of differentially expressed genes. Yellow cluster (E15.5 - E17.5, n=471 genes); orange cluster (E15.5 - P7, n=1541 genes); red cluster (P0-P7, n=619 genes); light blue cluster (P14 - P30, n=763); and dark blue cluster (P14 - P30, n=943).

To identify enriched biological processes (Gene Ontology) within these gene clusters, we used the Database for Annotation, Visualization and Integrated Discovery (DAVID) and visualized the data using Cytoscape (Figures 2 and S1, and Table S3)[46]. At the early stages of CGNP development (yellow cluster), there is a strong enrichment of processes associated with early neural development such as axon and dendrite formation, axon guidance, cell migration and developmental transcription factor-driven gene expression (Figures 2 and S1). Interestingly, also genes involved in glycolysis are enriched. In comparison, processes enriched throughout embryonic and neonatal stages (orange cluster) less frequently include neurodevelopmental processes. Instead, cell proliferation and mitosis-related processes are predominant, likely reflecting the high demand for proliferation during cerebellar expansion. This surge in proliferation appears to be accompanied by DNA damage, as also processes related to DNA damage response (DDR) pathways are frequent in this cluster. The end of cerebellar proliferation is heralded by the appearance of cell cycle arrest processes, which are specific to early neonatal CGNPs (red cluster). Of note, the vast majority of orange cluster genes show the highest relative gene expression levels at P0, suggesting that CGNP proliferation peaks around birth and already declines at P7 (Figure 1D). Two orange cluster processes (GO terms: covalent chromatin modification and ATP-dependent chromatin remodeling) stand out, as genes involved in chromatin regulation like *Arid2*, are known to be mutated in medulloblastoma [47,48]. During the final stages of CGNP differentiation, different biological processes become enriched (light and dark blue clusters). They include processes that function in neuronal connectivity, such as synaptic transmission and long-term potentiation (light blue cluster). Further, processes involved in differentiation and regeneration are enriched, as well as major signal transduction routes like Bmp, TGF-beta and PI3K signaling that are also known to play a role in medulloblastoma (dark blue cluster)[20,49,50].

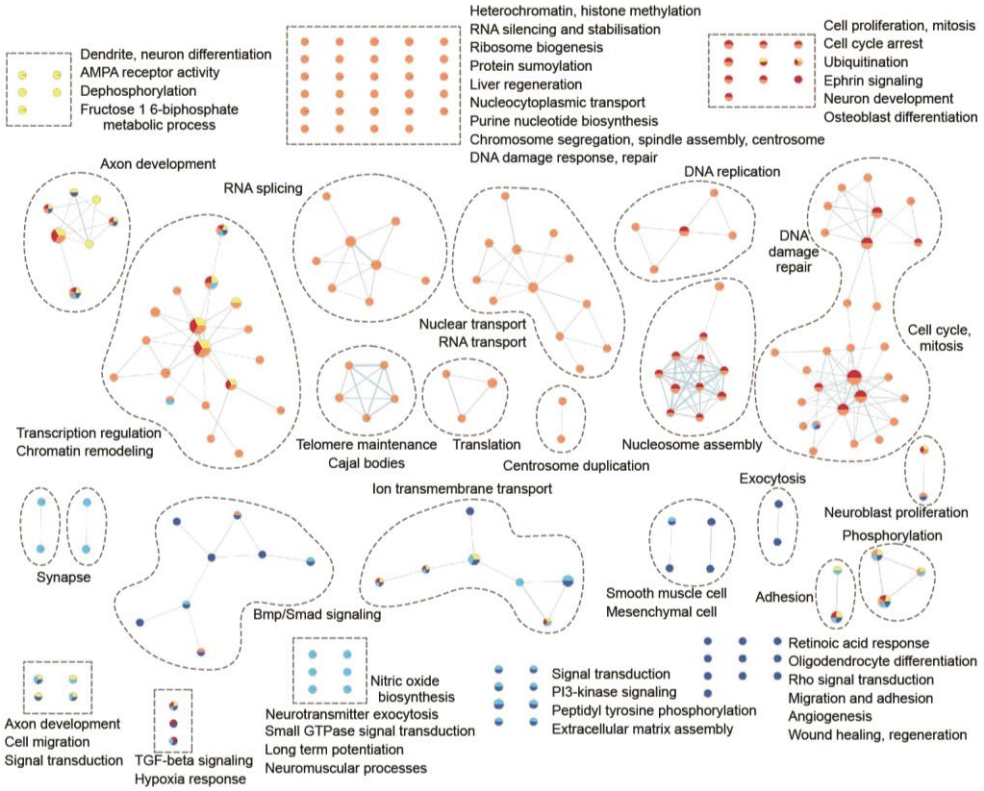

Figure 2. Specific biological processes are enriched during CGNP development.
Gene ontological analysis shows enriched biological processes in the different CGNP age-specific gene clusters. Each node represents a biological process. Related biological processes are grouped and labeled by biological theme (curved dashed lines). Individual biological processes are assembled in rectangular boxes (dashed lines). Biological processes connected by edges have genes in common. Enriched biological processes were determined with the Database of Annotation, Visualization and Integrated Discovery (DAVID), v.6.8 (Benjamini-corrected q=0.1, p=0.01) and visualized with the Enrichment Map app in Cytoscape. Yellow nodes: E15.5 - E17.5 cluster; orange nodes: E15.5 - P7 cluster; red nodes: P0 - P7 cluster; light blue nodes: P14 - P30 cluster; dark blue nodes: P14 - P30 cluster (See also Figure S1).

To further explore a potential link between CGNP gene expression and medulloblastoma, we extracted the individual gene expression profiles of n=40 genes commonly mutated in medulloblastoma and grouped them as suggested by Northcott *et al.* (Figures 3A and S2A)[3]. We found striking peaks in the expression of the genes involved in cell cycle and genome maintenance at P0, and genes involved in chromatin and transcription regulation at P7, indicating that the age of the cell-of-

origin could be related to mutations found in medulloblastoma. Interestingly, we observed the highest induction of *Tp53* expression at birth, which is most frequently mutated in children over the age of three [17].

Age-specific CGNP gene expression is preserved in human medulloblastoma

To investigate if overall CGNP gene expression is reflected in human SHH medulloblastoma, we performed a cross-species comparison between an existing cohort of human medulloblastoma and our mouse CGNP samples (Figure 3B)[17]. We reasoned that the youngest patient group (infants) is most likely to have undergone oncogenic transformation at the early stages of CGNP development. This could include CGNPs from the upper rhombic lip (E13.5 in the mouse, comparable to 8-10 weeks of human gestation) up to CGNPs from the EGL and IGL (internal granular layer) at the peak proliferation stage (mouse P0 stage, comparable to 20 weeks of human gestation up to newborn stages)[28]. The tumors from older children and adults can be derived from the entire CGNP lineage as all CGNP proliferation in humans has ceased by two years of age, yet it is likely that later diagnosed tumors will have undergone transformation at the later developmental stages. Therefore, we selected the human genes that were differentially expressed between SHH medulloblastoma patients of three age groups, *i.e.,* 0-3 years of age (infants/toddlers), 4-11 years of age (children), and 12 years and older (older children/adults). In agreement with earlier publications, we confirmed that infant and adult medulloblastoma have distinct gene expression patterns, with childhood medulloblastoma forming an intermediate group [17,18]. Interestingly, unsupervised hierarchical clustering analysis of these human genes together with their murine counterparts showed that embryonic mouse CGNPs co-cluster with the infant medulloblastomas, and older CGNPs with the tumors from older patients (Figure 3B). This demonstrates that CGNPs do resemble human medulloblastoma, and that the age of the patient is partially reflected by the age of the medulloblastoma cell-of-origin.

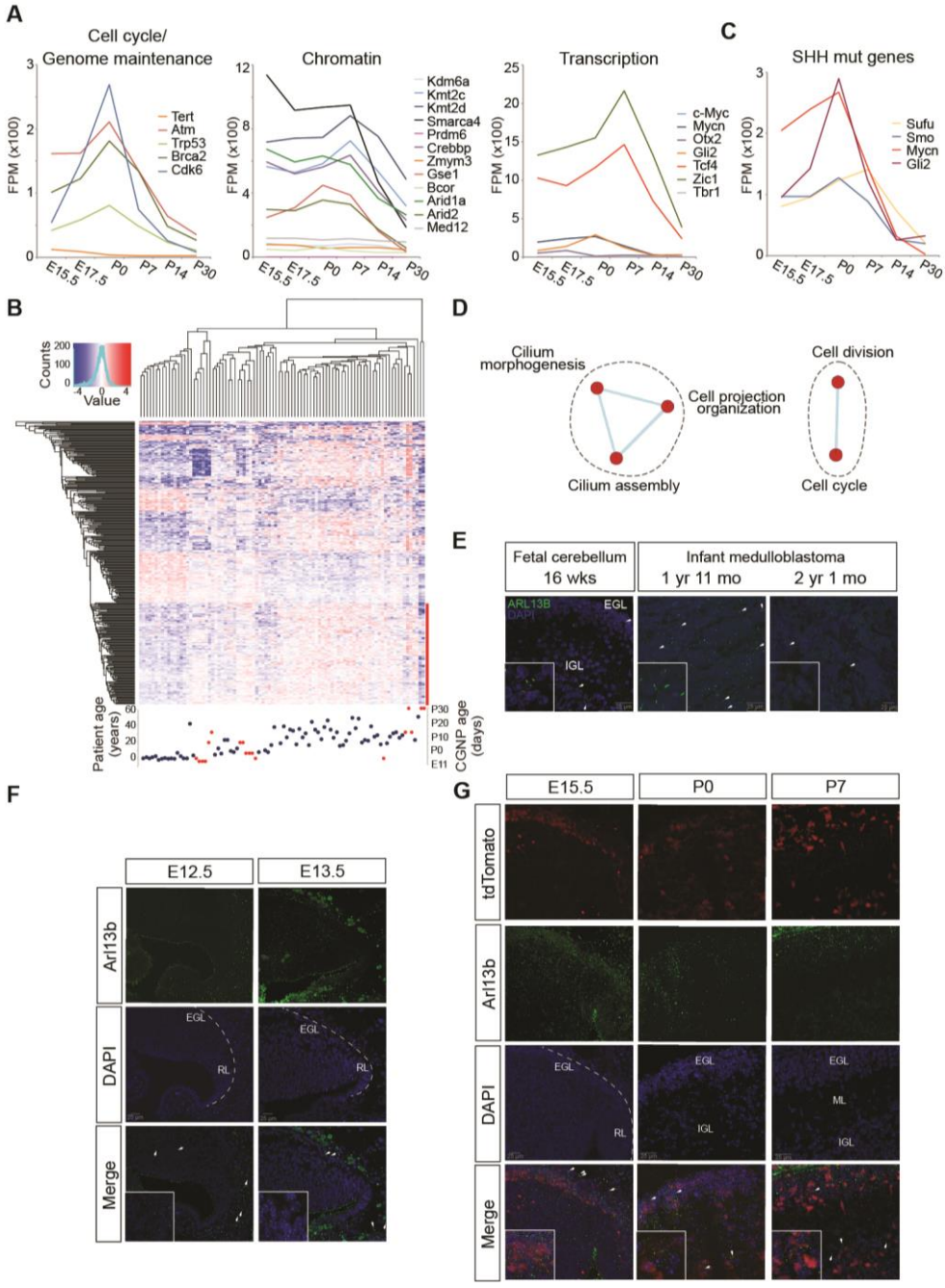

Figure 3. Cell cycle regulation and primary cilia biogenesis are age-dependent processes in CGNPs and medulloblastoma (*Legend on next page)*

Figure 3. Cell cycle regulation and primary cilia biogenesis are age-dependent processes in CGNPs and medulloblastoma (*Figure on previous page).*

(A) Gene expression profiles of CGNP genes commonly mutated in medulloblastoma, extracted from the RNA-seq data set. Curves represent the average expression level from three biological replicates (FPM=fragments per million, E=embryonic day, P=postnatal day)(See also figure S2). **(B)** Cross-species comparison. Heatmap showing unsupervised hierarchical clustering of differentially expressed human medulloblastoma genes (patient-age groups: 0-3 years, 4-11 years, 12 years and older) and CGNP orthologous genes. Blue dots represent patient samples, red dots represent CGNP samples. Lowest gene cluster indicated by red line. **(C)** Gene expression profiles of CGNP genes associated with the Sonic Hedgehog signaling pathway, extracted from the RNA-seq data set. **(D)** Enrichment map representing biological processes enriched in the lower (red) gene cluster of the cross-species comparison heatmap (B). Each node represents a biological process. Related biological processes are grouped and labeled by biological theme (curved dashed lines). Biological processes connected by edges have genes in common. Enriched biological processes were determined with the Database of Annotation, Visualization and Integrated Discovery (DAVID), v.6.8 (Benjamini-corrected q=0.1, p=0.01) and visualized with the Enrichment Map app in Cytoscape. **(E)** Confocal images showing ARL13B protein expression (primary cilia marker) in human fetal cerebellum (left panel) and infant medulloblastoma (middle and right panels). White arrows indicate primary cilia (EGL=external granular layer; IGL=internal granular layer). Scale bars indicate size. **(F)** Confocal images showing Arl13b expression in developing mouse cerebellum (E12.5 and E13.5). Dashed line outlines the cerebellar primordium. White arrows indicate primary cilia (RL=rhombic lip; E=embryonic day). **(G)** Confocal images showing Arl13b and tdTomato expression in the developing mouse cerebellum (E15.5, P0, P7). White arrows indicate primary cilia (P=postnatal day).

Cell cycle regulation and primary cilia biogenesis are age-related processes in CGNPs and medulloblastoma

Having established that developing CGNPs are suitable as model for the different medulloblastoma cells-of-origin, we mined the CGNP transcriptome data to find an explanation for the existence of age-specific Hedgehog pathway mutations. We approached this issue by hypothesizing that the mutated Hedgehog pathway genes are not equally important across the different stages of development, which could lead to a differential susceptibility to oncogenic mutation as a function of time. If true, there could be differences in peak gene expression levels for the Hedgehog pathway genes as we had observed for *Tp53*. To test this, we extracted the individual gene expression profiles of a number of genes associated with the Hedgehog signaling pathway from our CGNP transcriptome data. However, while we observed that SHH target genes like *Gli1/2*, *Ccnd1/2* and *Ptch1/2,* and to a lesser extent *Mycn*, had clear expression peaks at P0, this was not evident for either the *Sufu* or *Smo* genes that exhibit striking age-specific mutation patterns (Figures 3C and S2A). Thus, only *Gli2*

and Mycn, which are predominantly mutated in children over the age of three in conjunction with *TP53*, show age-specific gene expression [17].

We subsequently searched for alternative age-related processes that could impose differential Hedgehog pathway usage on the CGNPs, and which might explain a preferred type of mutation. Hereto, we subjected the gene clusters from the cross-species comparison to gene ontological analysis (Figure 3B,D and Table S4). We identified five biological processes that were enriched in the older CGNP/patient group. These processes were either involved in cell proliferation or in primary cilia formation (Figure 3D and Table S5). Since it is known that primary cilia are required for most of the activity of the SHH pathway, it seemed paradoxical that the youngest patients have relatively low primary cilia gene expression. We stained a panel of infant medulloblastoma for ARL13B, a marker for primary cilia [51], and confirmed that there is large variation in the number of cells expressing primary cilia between different patients, with some tumors hardly expressing any primary cilia (Figure 3E)[52,53]. Thus, low primary cilia expression can occur in infant medulloblastoma.

We next investigated primary cilia expression in normal developing CGNPs. CGNPs are specified in the upper rhombic lip from where they migrate across the cerebellar primordium to form a secondary germinal zone, the EGL. Differentiating CGNPs leave the EGL and migrate inwards to form the internal granular layer of mature granule neurons. In human second trimester fetal cerebellum, we found ciliated cells in both EGL and IGL (Figure 3E). As we had no access to first trimester embryonic human cerebellum that harbors the early specified uRL and presumptive EGL cells, we subsequently explored the developing murine cerebellum to establish primary cilia expression from the uRL stage onwards. In contrast to the general view that most cells have a primary cilium, we found that in the E12.5-E13.5 mouse cerebellum, cells in the uRL and future EGL are devoid of primary cilia whereas surrounding brain structures are heavily ciliated (Figure 3F)[39,54]. As development progresses, the number of ciliated cells in the EGL, and later also in the uRL, increases (Figure 3G). At neonatal stages, the most frequently ciliated cells are in the IGL. Presence or absence of primary cilia did not seem to correlate with cell cycle

status (Figure S2B,C). Altogether, this demonstrates that primary cilia expression is dynamic during CGNP development, and that at certain phases of medulloblastoma cell-of-origin development the primary cilium is absent.

Sufu and Smoothened expression is dynamic and partially non-overlapping during cerebellar development

Both *Smo* and *Sufu* function is essential for Hedgehog signaling in the cerebellum, with Smo acting upstream in relaying the signals from SHH morphogen-bound Ptch, and Sufu acting downstream in receiving signals from activated Smoothened to cease the inhibition of Gli [55,56]. A major difference though is their dependence on the primary cilium for pathway activation. Smo absolutely requires the primary cilia for its function whereas Sufu is known to also have cilium-independent activity [33,34,36,38,41,42,57]. If infant medulloblastoma is derived from the earliest specified CGNPs, this could explain the increased frequency of *SUFU* mutations, as these cells are mostly non-ciliated. We checked if during cerebellar development, Sufu and Smo proteins were expressed in patterns consistent with this hypothesis (Figure 4). In general, Sufu exhibited the broadest expression (Figure 4B,C). At embryonic days E13.5 and E15.5, Sufu was increasingly expressed throughout the cerebellar anlage, including in non-ciliated cells in the uRL, in the EGL, and in the future IGL. In contrast, Smo was not expressed in the uRL and appeared restricted to CGNPs just below the EGL where the future IGL would form (Figure 4A,C). These expression patterns were maintained postnatally, with Sufu being expressed in all CGNPs and Smo predominantly in the IGL. Of note, whereas Smo expression was restricted to the cytoplasm and to the primary cilium, Sufu was also expressed in the nucleus [16,58].

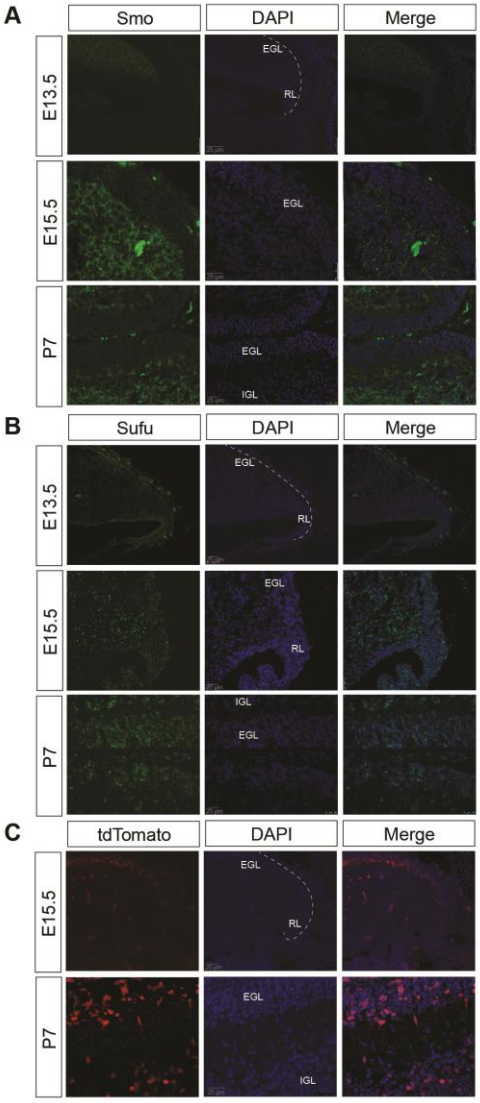

Figure 4. Differential Smoothened and Sufu expression patterns in the developing cerebellum.

Confocal images showing **(A)** Smoothened, **(B)** Sufu, and **(C)** tdTomato protein expression in the E13.5, E15.5, and P7 cerebellum. Dashed line outlines the cerebellar primordium (RL=rhombic lip; EGL=external granular layer; IGL=internal granular layer; E=embryonic day; P=postnatal day). Scale bars indicate size.

Embryonic CGNPs are insensitive to Smoothened manipulation.

We then set out to functionally test if embryonic CGNPs are differentially sensitive to SHH pathway manipulation compared to early postnatal CGNPs. Hereto, we isolated *Math1-CreER^{T2}; tdTomato* CGNPs from either E13.5, E15.5 or P7 cerebellum and cultured them for brief time periods to preserve their primary status [59–62]. In agreement with earlier publications, we observed that P7 CGNPs increase their proliferation in response to SHH treatment, as well upon overexpression of oncogenic *Smo* (SmoM2) or knockdown of *Sufu* (Figures 5A,D and S3)[7,9,55]. However, when CGNPs were derived from E15.5 cerebella, only *Sufu* knockdown cells showed a trend towards increased proliferation, whereas SHH or SmoM2 had no effect as predicted (Figure 5A,B). Surprisingly, E15.5 CGNPs in culture did initiate primary cilia expression although cilia appeared smaller than on P7 CGNPs, suggesting that other factors also contribute to resistance to SmoM2 activity (Figure 5C).

Lastly, we tested if the developmental age of the CGNP also has an effect on drug sensitivity, as this would be relevant for patient treatment. Hereto, we subjected E13.5, E15.5 and P7 CGNPs to Cyclopamine treatment. Cyclopamine is a Smo inhibitor, derivatives of which are being used in the treatment of relapsed SHH medulloblastoma [63]. Whereas proliferation of P7 CGNPs was strongly diminished by Cyclopamine treatment in agreement with earlier publications, E13.5 and E15.5 CGNPs were almost completely insensitive (Figure 5D). This shows that the age of the medulloblastoma cell-of-origin has a significant impact on drug sensitivity.

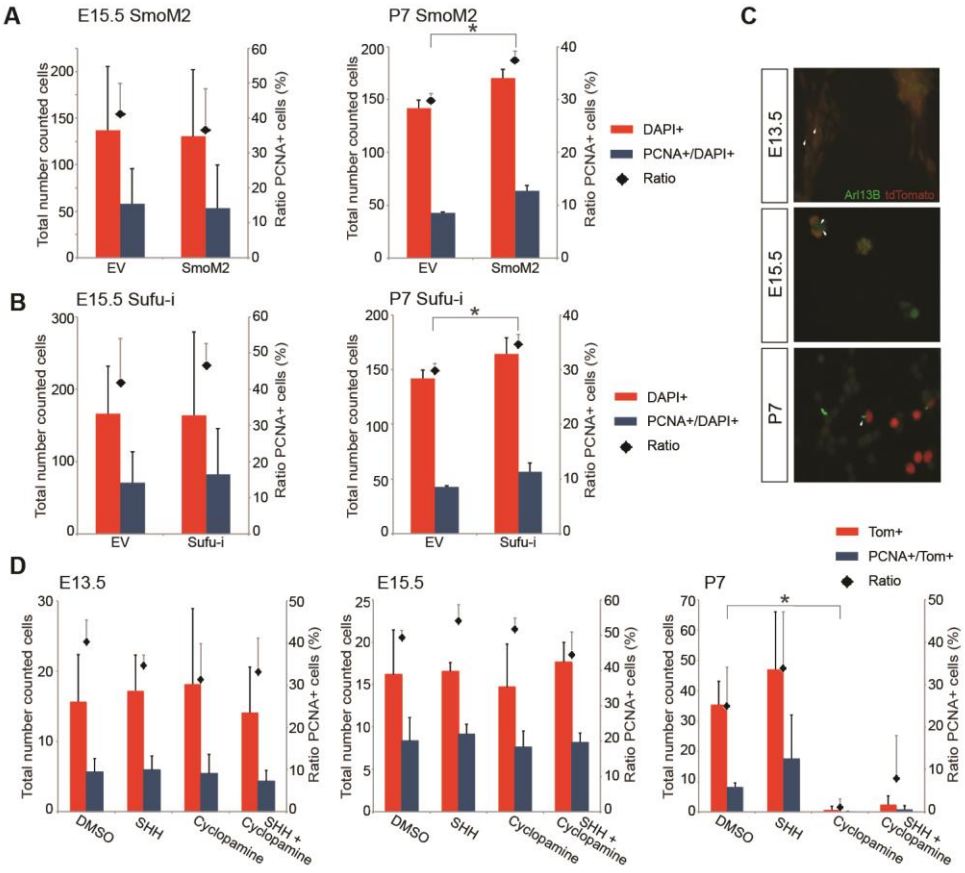

Figure 5. Embryonic CGNPs are insensitive to Smoothened manipulation.

(A) Charts showing total numbers of DAPI$^+$ (red bars) and PCNA$^+$;DAPI$^+$ (blue bars) that were counted per sample (plotted on the primary Y-axis); and the ratio of PCNA$^+$ cells (black diamonds; plotted on the secondary Y-axis) after SmoM2 or empty vector control transduction, in E15.5 (left panel) or P7 CGNP primary cultures (right panel). * = p-value < 0.05 (t-test). Results represent 2-3 independent biological replicates (mean ± SEM). **(B)** Charts showing total numbers of DAPI$^+$ (red bars) and PCNA$^+$;DAPI$^+$ (blue bars) cells that were counted per sample (plotted on the primary Y-axis); and the ratio of PCNA$^+$ cells (black diamonds; plotted on the secondary Y-axis) after Sufu shRNA knockdown or empty vector control transduction, in E15.5 (left panel) or P7 CGNP primary cultures (right panel). Results represent mean +/- SEM for two independent biological replicates. * = p-value < 0.05 (t-test). **(C)** Immunofluorescence showing Arl13b and tdTomato expression in E13.5, E15.5 and P7 primary CGNP cultures. White arrows indicate primary cilia. Scale bars indicate size. **(D)** Charts showing total numbers of tdTomato$^+$ (red bars) and PCNA$^+$;tdTomato$^+$ (blue bars) cells that were counted per sample (plotted on the primary Y-axis); and the ratio of PCNA$^+$ cells (black diamonds; plotted on the secondary Y-axis) after Mock, SHH, Cyclopamine, and SHH + Cyclopamine treatment in E13.5 (left panel), E15.5 (middle panel) or P7 CGNP primary cultures (right panel). Results represent mean +/- SEM for three independent biological replicates. * = p-value < 0.05 (t-test) (See also Figure S3).

DISCUSSION

Whereas Sonic Hedgehog medulloblastoma is generally characterized by deregulation of the Hedgehog signaling pathway, there are also features specific for patient age, suggesting that neurodevelopmental processes may underlie heterogeneity within this subgroup [3,17,18,29,64]. We set out to address if intrinsic changes between young and older cerebellar granule neuron progenitors, a cell lineage known to be highly susceptible to SHH medulloblastoma formation, can account for the age-specific characteristics of this tumor type [4,32].

The developmental age of the medulloblastoma cell-of-origin is reflected in the tumor transcriptome

Dissimilarities between SHH medulloblastomas from young and older patients have been reported for various aspects of tumor biology and include gene expression, somatic mutations, copy number alterations and tumor location [2,3,17,18,21,65,66]. Our idea that naturally occurring changes in identity of the tumor cell lineage-of-origin in time cause some of these differences, is supported by studies showing differences in tumor onset and phenotype in relation to timing of tumor induction, although the genetic lesion and heterogeneity within the population also play a role [29,65–68]. Indeed, when we compared gene expression patterns from developing CGNPs, we found enriched biological processes at specific developmental stages. Several of these processes have been linked to SHH medulloblastoma, reinforcing the CGNP as cell-of-origin. A direct connection between CGNP and patient age was evident in some but not all cases [2,3,17,18,64]. For instance, neurotransmission activity and neural development are enriched in both early embryonic CGNPs and infant medulloblastoma in line with a chronological relationship [2]. But PI3K signaling, which is also associated with infant medulloblastoma, is mostly enriched in the late postnatal CGNP samples representing maturing granule neurons [17]. Furthermore, we found processes that could play a role in tumorigenesis during a larger time period, as for example processes related to chromatin modulation are enriched in

CGNPs throughout embryonic and early postnatal stages, and likewise are linked to both infant and child/adult SHH medulloblastoma [17].

Intriguingly, there was a strong enrichment for processes related to cell cycle control and the DNA damage response throughout early CGNP development with a noticeable peak around birth. As these processes are overrepresented within the older SHH medulloblastoma subtypes, this suggests that the SHH-induced burst in CGNP proliferation, possibly coinciding with increased DNA damage due to replication stress, is a critical event during cerebellar development that brings along the risk of developing child- and adulthood medulloblastoma [2,3]. Examination of the expression levels of individual genes frequently mutated in medulloblastoma corroborated this idea, as the majority of these genes were highly expressed at birth and shortly thereafter [3]. Interestingly, genes involved in RNA metabolism, cell cycle, and genome integrity peaked just before the genes controlling chromatin and transcription, suggesting that they play consecutive roles during CGNP development. This pattern fits with an initial phase of CGNP proliferation at birth and a subsequent increase of terminal differentiation, as the onset of differentiation often requires chromatin remodeling to switch on effector genes [48,69]. The strong increase in TP53 expression at birth is particularly interesting, as it might be related to the high incidence of TP53 mutations and occurrence of chromothripsis in children [19].

Taken together, we propose that the candidate cell-of-origin for childhood and adult medulloblastoma is a SHH-stimulated proliferating CGNP that has lost control over the cell cycle and/or control over the DNA damage response, or a slightly more mature CGNP that has failed to undergo correct terminal differentiation [46]. In humans, this could include CGNPs from approximately twenty weeks gestation until the first months after birth, when Purkinje neuron-secreted SHH provides a source of mitogens [28]. The remaining question is the nature of the cell-of-origin for infant SHH medulloblastoma, which is quite distinct from the older medulloblastoma cases and therefore likely has a discrete origin. In our cross-species comparison, we found that the infant SHH medulloblastomas clustered towards the earliest embryonic CGNPs as they have certain enriched processes in common [29]. Therefore, the infant medulloblastoma cell-of-origin may either be reprogrammed towards an early

embryonic fate, or alternatively, is directly related to early CGNPs from the upper rhombic lip or the germinal zone of the cerebellar primordia, which in humans spans a time period from late first trimester through mid-second trimester [28].

Differential Hedgehog pathway regulation during cerebellar development might determine SHH medulloblastoma subtypes

While the analysis of developing CGNP transcriptomes yielded insight into the putative origin of infant and childhood/adult medulloblastoma, it did not directly elucidate why *SUFU* and *SMO* mutations are mutually exclusive in these medulloblastoma subtypes [17]. Our subsequent cross-species comparison suggested the involvement of primary cilia or associated processes. A primary cilium is a non-motile signaling organelle that protrudes from the cell membrane [70]. Whereas the function of these organelles has long been enigmatic, the discovery of the cilium being key to Hedgehog signal transduction has underlined its central role in various signaling pathways [33,40,70].

In contrast to the general belief that most cells have a primary cilium, we observed that the majority of CGNPs at the upper rhombic lip and presumptive EGL were non-ciliated [39,54]. As these are the same cells that we predict to be putative cell-of-origin for infant medulloblastoma, we wondered if this lack of primary cilia could be related to the age-specific mutations in Hedgehog components in SHH medulloblastoma. Interestingly, in contrast to *Smo, Sufu* does not absolutely depend on the primary cilium to exert its control over Hedgehog target gene expression [37,38,41,42]. Another vital difference between *Smo* and *Sufu* is their effect on Hedgehog signaling, as Smo activates, and Sufu represses target gene expression [10–13]. From this, it follows that Smo activity becomes essential when the SHH morphogen is present to activate the pathway. Sufu on the other hand may be continuously required to prevent precocious Hedgehog pathway activation, even when SHH itself is not expressed [16]. This is in line with our observations that Sufu expression precedes Smo in the early uRL and primordial EGL. Moreover, Sufu is expressed broadly throughout all CGNP layers, whereas Smo is most prominently expressed in the presumptive IGL that contains differentiating CGNPs. Therefore, we speculate

that oncogenic transformation during early development requires *SUFU* deletion to induce precocious pathway activation, but not SMO activation that in the absence of primary cilia would not have a pro-tumorigenic effect (Figure 6)[53]. This idea is supported by studies from others showing a significantly earlier role in cerebellar development for *Sufu* compared to *Smo* and *SHH* [27,55,56,71–74]. Furthermore, mutant cerebella lacking primary cilia also show relatively late developmental phenotypes, in line with primary cilia being most important during SHH-induced CGNP proliferation [57,75].

Implications for future medulloblastoma research

Only recently, it was demonstrated that the four consensus subgroups of medulloblastoma can be further sub-classified using a combination of molecular profiling techniques [2,3,17,18,76]. These studies have provided a wealth of information on the molecular genetics as well as putative regions of origin for these tumors, which are both essential pieces of information for developing appropriate preclinical models and drug testing. For instance, while several mouse models for medulloblastoma have been generated, none of them has faithfully recapitulated infant SHH medulloblastoma, suggesting that the correct cell-of-origin has not been properly targeted [77]. The importance of *bona fide* preclinical modeling is underscored by our finding that early embryonic CGNPs, which are putative cells-of-origin for infant SHH medulloblastoma, are insensitive to Smo inhibition even in the absence of *Sufu* lesions. Thus, in addition to taking into account the level at which the Hedgehog pathway is compromised when designing targeted therapy, intrinsic characteristics of the cell-of-origin preserved in the tumor should also be taken into consideration [78,79]. Especially in infants, who typically do not receive radiotherapy, the use of drugs precisely tailored to their specific medulloblastoma subtype is indispensable [80].

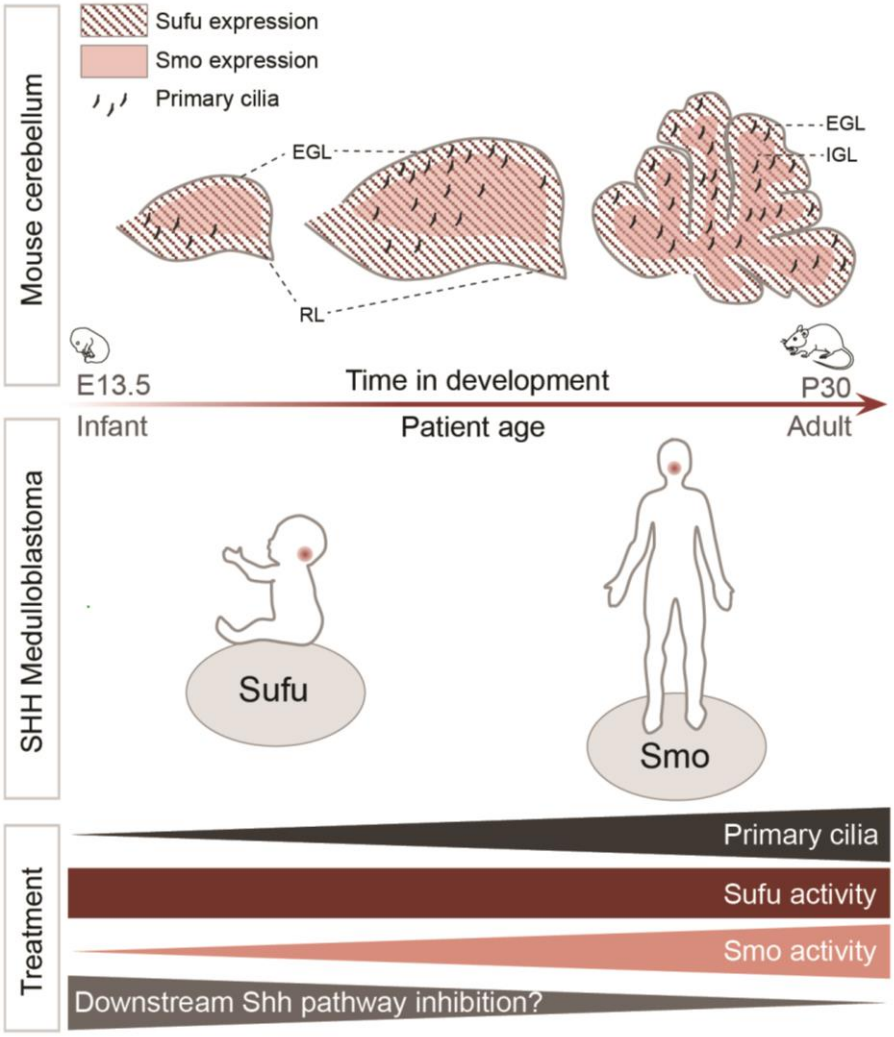

Figure 6. Model: age is a key factor in murine cerebellar development and SHH medulloblastoma etiology.

Sonic Hedgehog (SHH) medulloblastoma derives from the cerebellar granule neuron progenitor (CGNP) population. CGNPs are specified in the rhombic lip (RL) of the early embryonic cerebellum, from where they migrate across the cerebellar surface to form the external granular layer (EGL). Upon terminal differentiation, CGNPs migrate inwards to form the definitive internal granular layer (IGL). Expression of primary cilia, which are important components of upstream SHH signaling, increases as CGNP development progresses. Thus, if oncogenic transformation takes place at late stages of CGNP development, *SMO* is preferentially mutated as the primary cilia strongly enhance oncogenic SMO activity. However, if CGNP oncogenic transformation occurs at an early embryonic stage, *SUFU* is preferentially mutated, which controls downstream Sonic Hedgehog signaling independently from the primary cilium. This implies that targeted therapy for infant SHH medulloblastoma should be directed towards tumor-driving mechanisms that are not dependent on primary cilia (E=embryonic day, P=postnatal day).

AKNOWLDGEMENTS

We are grateful to Dr. Ilia Vainchtein for assistance on cerebellar granule neuron cell sorting, and Dr. Seka Lazare for assistance with RNA-seq. This work was funded by a De Cock Stichting grant to M.S.; an Indonesian Endowment Fund for Education (LPDP) grant (20151022024475) to I.A.; a Rosalind Franklin fellowship from the University of Groningen and European Union to J.P.; a Mouse Clinic for Cancer and Ageing/Large Infrastructure grant from the Netherlands Organization for Scientific Research (NWO) to G.H., a Stichting Vrienden Beatrix Kinderziekenhuis grant, a Rosalind Franklin fellowship from the University of Groningen, and a KWF Cancer Research career award (RUG 2014-6903) to S.B.

AUTHORS CONTRIBUTIONS

Conceptualization, M.S. and S.B.; methodology, M.S., J.P., V.G., and S.B.; software and formal analysis, W.Z., M.S., S.B., and V.G.; investigation, M.S., I.A., I.B., T.M., W.Z., Z.S., T.M., F.S., M.R., and S.B.; resources, M.Sc, W.D., J.P., E.H., and G.H.; data curation, V.G.; writing, M.S. and S.B.; writing-review and editing, M.S., J.P., I.B., W.Z., and S.B.; visualization, M.S., W.Z., V.G. and S.B.; supervision and project administration, S.B.; funding acquisition, M.S. and S.B.

DECLARATION OF INTEREST

The authors declare no conflicts of interest.

MATERIAL AND METHODS

Contact for reagent and resource sharing

Further information and requests for resources and reagents should be directed to and will be fulfilled by the Lead Contact, Dr. Sophia Bruggeman (s.w.m.bruggeman@umcg.nl). Materials received from third parties, as well as

constructs created by the authors, are subject to material transfer agreements. Patient material cannot be transferred due to ethical restrictions.

Experimental model and subject detail

Experimental animals and husbandry

The Math1-CreER^{T2}; tdTomato compound transgenic mouse strain was derived from the Math1CreER^{T2}, and Ai14 mouse strains (The Jackson Laboratory), and in a C57BL6/mixed background. Mice were conventionally housed, fed *ad libitum*, and routinely genotyped by PCR. Timed matings were performed overnight, with the following morning considered E0.5. Pregnancies were detected by measuring female weight gain at E13.5. A subset of pregnant females received a single dose of Tamoxifen (2 mg/100 µl peanut oil, Sigma) by oral gavaging at E13.5. Pregnant females were killed by asphyxiation (CO_2), neonatal mice until the age of P7 were killed by decapitation. Offspring from different gender were randomly assigned. All animal experiments were approved by the Institutional Animal Care and Use Committee of the University Medical Center Groningen, the Netherlands.

CGNP single cell suspension preparation

For transcriptional analyses, CGNPs were harvested from E13.5, E15.5, P0, P7, P14, and P30 tdTomato$^+$ dissected cerebella from offspring from Tamoxifen-treated females. For primary cell cultures, CGNPs were harvested from E13.5, E15.5 and P7 days old cerebella from offspring of non-treated females. Cerebellar dissection was performed using a stereomicroscope. E15-P30 Cerebella were dissociated with a Papain dissociation kit following the manufacturer's instructions (Worthington). Following papain treatment, ovomucoid was added to stop the reaction. For P14 and P30 cerebella, an additional Percoll gradient step was performed to remove myelin and debris. Cell suspensions were filtered through a 70 µm cell strainer prior to further processing.

Primary CGNP cell cultures

For embryonic CGNP cultures (E13.5 and E15.5), n=18-20 dissected cerebella were pooled. For P7 CGNP cultures, n=4-6 dissected cerebella were pooled. Single cell suspensions were obtained as described above. Cells were pelleted and resuspended in the appropriate culture media. For E13.5 and E15.5 CGNPs: BME media supplemented with 1% N2, 2% B27 (Invitrogen), and 0,1 μg/ml BMP6, BMP7 and GDF7 (Peprotech). For P7 CGNPs: DMEM-F12 media supplemented with 1% N2, 1.5% sucrose, 5 μm HEPES (Invitrogen) and 0,25 μg/ml SHH (R&D systems). Cells were filtered through a 40 μm cell strainer and counted with a Bürker-Türk counting chamber. 500.000 cells were seeded into poly-D-Lysine (100 μg/ml, Sigma) coated 12 wells plates. Two hours after plating, cells were treated with 4-Hydroxytamoxifen (1 μM, Sigma) for 36 hours.

Method details

CGNP FACS and RNA isolation for RNA-Seq

Cerebellar single cell suspensions (E15.5-P30) were subjected to fluorescence-activated cell sorting (FACS) for tdTomato$^+$ cells, using a MoFlo Astrios cell sorter (Beckman Coulter). tdTomato$^+$ cells (CGNPs) were collected in 1.5 ml tubes, centrifuged, and snap frozen. For the E15.5 and E17.5 time points, n=4-8 embryos were pooled prior to FACS; for P0-P30 time points, individual mice were sorted.

RNA was extracted using the NucleoSpin RNA XS kit (Macherey-Nagel), following the manufacturer's instructions. RNA concentration was measured with a QuBit RNA HS assay kit (Thermo Fisher) and analyzed on a bioanalyzer using the Agilent RNA 6000 Pico Kit (Agilent). 2.5-10 ng of RNA per sample was used as input for library preparation.

Library preparation and RNA-Seq

For library prepping, the Clontech SMARTer stranded total RNA-seq kit-pico was used according to the manufacturer's instructions for mammalian sample input. Three biological replicates were sequenced for each time point (Illumina HiSeq 2500). On average, 16.7 million reads (63 bp single-end) were generated for each replicate. Reads were aligned to the mouse reference genome (GRCm38 assembly, gene annotation from Ensembl release 84, http://www.ensembl.org) and quantified using STAR 2.5.3a (Dobin et al., 2013).

Lentiviral transductions

The Sufu shRNA construct was generated by cloning a Sufu-targeting 22-mer oligonucleotide into a modified pRRL-SFFV-IRES-GFP plasmid (restriction sites XhoI and EcoRI), with tNGFR replaced by GFP (kind gift from Dr. Hein schepers)(See also Table S6).

293T producer cells were transfected with prrl-SFFV-IRES-GFP, prrl-SFFV-IRES-GFP-Sufu or SmoM2 (W535L)-pcw107-V5 (Addgene) using Fugene HD transfection reagent (Promega). Embryo or P7 CGNP culture media was added to the producer cells 16 hours prior to virus harvest. CGNPs were incubated with lentiviruses for 2 hours, after which virus was gradually replaced with normal culture media to prevent cell death. Cells were fixed between 48-72 hours after transduction for further processing.

Immunofluorescence

CGNPs were fixed with 100% MeOH (for PCNA staining) or 4% formaldehyde (for Arl13b), and blocked with 0.1% triton, 1% BSA and 0.05% Tween in PBS. Primary antibodies were: Arl13b (Proteintech, 17711-1-AP, 1:400), PCNA (Abcam, ab29, 1:1000) and RFP (Rockland, 600-401-379, 1:500). Secondary antibodies were Alexa Fluor 488 (1:500) and Alexa Fluor 568 (1:500)(Invitrogen). Cells were counterstained with DAPI (Sigma).

Brains from Tamoxifen-treated Math1-CreER^{T2};tdTomato mice were dissected from the skull, fixed with 4% formaldehyde, and cryoprotected with a sucrose gradient (10%, 20 % and 30% sucrose in PBS). They were embedded into

Tissue-Tek O.C.T. compound (Sakura-FineTek) and snap frozen in liquid nitrogen. Human fetal brain and medulloblastoma tissue was obtained from the University Medical Center Groningen. Local ethics committee approval was granted for use of the patient material. Cryosections (10 µm) were generated on a Leica cryostat. Antigen retrieval was performed by boiling tissue sections in Citrate buffer (100 mM, pH 6.0), except for Arl13b and mCherry. Sections were blocked with 5% normal goat serum and 0.1% Triton (Cell Signaling) in PBS. Primary antibodies were: Arl13b (Proteintech, 17711-1-AP, 1:100), mCherry (SICGEN, AB0040-200, 1:200), PCNA (Abcam, ab29, 1:1000), RFP (Rockland, 600-401-379, 1:500), Sufu (Abcam, ab28083, 1:50), Smo (Abcam, ab38686, 1:500), Histone H3S10ph (Active Motif, 39636, 1:100). Secondary antibodies were Alexa Fluor 488 (1:500) and Alexa Fluor 568 (1:500)(Invitrogen). Slides were counterstained with DAPI (Sigma), and mounted with Vectashield (Vector Laboratories).

Microscopy

Whole mount images of fluorescent embryonic and postnatal mouse brain were made on an Olympus stereozoom SZX-16 microscope. Primary cells were imaged on an EVOS FL inverted fluorescence microscope (Life technologies). Fluorescent tissue sections were imaged on a Leica TCS SP8 confocal microscope.

Quantitative RT-PCR

RNA from E15.5 and P7 CGNPs was isolated using the RNeasy Mini Kit (Qiagen). cDNA was synthesized using random hexamer primers, dNTPs and Ribolock (Thermo Scientific). Reverse transcription was performed using Reverse Transcriptase (Thermo Scientific). Quantitative RT-PCR was performed on a BioRad CFX connect Real-time system using universal SYBR® Green supermix (BioRad). Relative gene expression is calculated using the $2^{-\Delta\Delta}$CT method. Expression levels are normalized to housekeeping gene Gapdh. For primers, see Table S6.

Quantification and statistical analysis

Quantification of proliferating cells

For quantification of PCNA or phospho-Histone H3 positive cells in primary cultures and histological sections, random microscopic images (n=8-10 per sample) were taken and blindly scored for $DAPI^+$, $tdTomato^+$, $PCNA^+$, or phospho-Histone $H3^+$ cells. Average ratios of double positive cells were determined and tested for significance ($p<0.05$) using a one-sided, paired t-test.

Hierarchical clustering analysis

For hierarchical clustering analysis, differentially expressed genes were called for all possible pairwise comparisons of developmental stages (3 replicates each) using the edgeR package. Genes were selected that significantly changed their expression (FDR<1e-5) in one or more comparisons. Log2 ratios were calculated relative to the average FPM expression of a gene. Unsupervised hierarchical clustering and heatmap plotting was performed using gplots library. The Canberra distance and Ward clustering method was used.

Cross species comparison

For comparison of gene expression profiles between mouse CGNP and human medulloblastoma patients, a published human medulloblastoma data set was downloaded from GEO (https://www.ncbi.nlm.nih.gov/geo; accession number GSE49243). Expression values were transformed into log2 fold change (compared to average expression of a gene across all patients). Unambiguous orthologs (one to one orthology) were determined using the Ensembl Biomart tool (http://www.ensembl.org/biomart). Unsupervised hierarchical clustering and heatmap plotting was done using gplots library. The Euclidean distance and Average clustering method was used.

Gene Ontology

Pathway enrichment analysis was performed by uploading lists of differentially expressed genes (gene clusters), to the Database for Annotation, Visualization and Integrated Discovery v6.8 (DAVID), and subsequent analysis for gene ontology of biological processes was performed. Lists of biological processes were imported into the Enrichmentmap app in Cytoscape v3.2.1. Biological processes were Benjamini-

corrected with a moderately permissive q value of <0.1 and a p-value of <0.01. Enrichment maps represent biological processes enriched in the gene clusters. Each node represents a biological process grouped and labeled by biological theme. Biological processes connected by edges have genes in common using a Jaccard and Overlap coefficient combined with a similarity cutoff value of 0.375.

Data and software availability

The accession number for the CGNP RNA-Seq data set is E-MTAB-7399 (https://www.ebi.ac.uk/arrayexpress/).

Key resources table

REAGENT or RESOURCE	SOURCE	IDENTIFIER
Antibodies		
Mouse monoclonal Anti-PCNA antibody [PC10]	Abcam	Cat# ab29, RRID:AB_303394
Rabbit Polyclonal Anti-RFP Antibody Pre-adsorbed	Rockland	Cat# 600-401-379, RRID:AB_2209751
Rabbit Polyclonal Anti-ARL13b Antibody	Proteintech Group	Cat# 17711-1-AP, RRID:AB_2060867
Rabbit Polyclonal Anti-Suppressor of Fused antibody	Abcam	Cat# ab28083, RRID:AB_2255467
Goat Polyclonal Anti-mCherry antibody	SICGEN	Cat# AB0040-200, RRID:AB_2333092
Mouse monoclonal anti-Histone H3S10ph antibody	Active Motif	Cat# 39636
Mouse monoclonal Smo Antibody (E-5)	Santa Cruz	Cat# sc-166685, RRID:AB_2239686

Rabbit Polyclonal Anti-Smoothened antibody	Abcam	Cat# ab38686, RRID:AB_882615
Biological Samples		
Primary human SHH medulloblastoma samples	(Kool et al., 2014)	
Human fetal cerebellum	This paper	N/A
Primary human medulloblastoma tissue	This paper	N/A
Primary mouse CGNPs	This paper	N/A
Chemicals, Peptides, and Recombinant Proteins		
Recombinant Mouse Sonic Hedgehog/SHH (C25II) N-Terminus	R&D systems	Cat#: 464-SH
InSolution™ Cyclopamine-KAAD-Calbiochem	Merck	239807; CAS 306387-90-6
4-Hydroxytamoxifen	Sigma-aldrich	Cat#: H6278
Tamoxifen	Sigma-aldrich	Cat#: T5648
Peanut oil	Sigma-aldrich	Cat#: P2144
Recombinant Human BMP-6	Peprotech	Cat# 120-06
Recombinant Human BMP-7	Peprotech	Cat# 120-03P
Recombinant Human GDF-7	Peprotech	Cat# 120-37
Critical Commercial Assays		
NucleoSpin® RNA XS	Macherey-Nagel	Cat# 740902.50
SMARTer® Stranded Total RNA-Seq Kit - Pico Input Mammalian	Clontech Laboratories	Cat# 635005
Qubit™ RNA HS Assay Kit	Invitrogen	Cat# Q32852
RNA 6000 Pico Kit	Agilent technologies	Cat# 5067-1513
Papain Dissociation System	Worthington Biochemical Corporation	Cat# LK003150

QIAquick PCR Purification Kit	Qiagen	Cat# 28104
Fugene HD Transfection Reagent	Promega	E2312
FavorPrep™ Gel/PCR Purification mini kit	FavorPrep	Cat# FAGCK001
QIAGEN Plasmid Midi Kit	Qiagen	Cat# 12145
GeneJET Plasmid miniprep kit	Thermo Scientific	K0502
Deposited Data		
RNA-seq data	This paper	
Experimental Models: Organisms/Strains		
Tg(Atoh1-cre/ESR1)14Fsh/J, Math1-CreER^{T2}	The Jackson laboratory	Stock No: 7684
B6.Cg-Gt(ROSA)26Sortm14(CAG-tdTomato)Hze/J	The Jackson laboratory	Stock No: 7914
Oligonucleotides		
Primers and oligo's, see Supplementary file.		
Recombinant DNA		
SmoM2 (W535L)-pcw107-V5		Addgene Plasmid #64628
pRRL-SFFV-IRES-GFP (modified)	Kind gift from Dr. Hein Schepers (Korthuis et al., 2015)	
Software and Algorithms		
STAR 2.5.3a	https://github.com/alexdobin/STAR	
R 3.4	https://www.r-project.org	

Ensembl Biomart	http://www.ensembl.org/biomart	
Leica Application Suite X (LasX)		https://www.leica-microsystems.com/products/microscope-software/details/product/leica-las-x-ls/
Adobe Illustrator		http://www.adobe.com/illustrator
Fiji (Image J)	(Schindelin et al., 2012)	https://fiji.sc
Database for Annotation, Visualization and Integrated Discovery (DAVID) (v6.8)	(Huang et al., 2008)	https://david.ncifcrf.gov
Cytoscape (v3.2.1)	(Shannon et al., 2003)	http://www.cytoscape.org/
Cytoscape Enrichment map (v3.0.0)	(Merico et al., 2010)	http://apps.cytoscape.org/apps/enrichmentmap
Clonemanager		http://www.scied.com/pr_cmbas.htm

References (materials and methods)

Dobin, A., Davis, C. A., Schlesinger, F., Drenkow, J., Zaleski, C., Jha, S., Batut, P., Chaisson, M. and Gingeras, T. R. (2013). STAR: Ultrafast universal RNA-seq aligner. *Bioinformatics* **29**, 15–21.

Huang, D. W., Sherman, B. T. and Lempicki, R. A. (2008). Systematic and integrative analysis of large gene lists using DAVID bioinformatics resources. *Nat. Protoc.* **4**, 44–57.

Kool, M., Jones, D. T. W., Jäger, N., Northcott, P. A., Pugh, T. J., Hovestadt, V., Piro, R. M., Esparza, L. A., Markant, S. L., Remke, M., et al. (2014). Genome sequencing of SHH medulloblastoma predicts genotype-related response to smoothened inhibition. *Cancer Cell* **25**, 393–405.

Korthuis, P. M., Berger, G., Bakker, B., Rozenveld-Geugien, M., Jaques, J., De Haan, G., Schuringa, J. J., Vellenga, E. and Schepers, H. (2015). CITED2-mediated human hematopoietic stem cell maintenance is critical for acute myeloid leukemia. *Leukemia* **29**,.

Merico, D., Isserlin, R., Stueker, O., Emili, A. and Bader, G. D. (2010). Enrichment map: A network-based method for gene-set enrichment visualization and interpretation. *PLoS One* **5**,.

Schindelin, J., Arganda-Carreras, I., Frise, E., Kaynig, V., Longair, M., Pietzsch, T., Preibisch, S., Rueden, C., Saalfeld, S., Schmid, B., et al. (2012). Fiji: An open-source platform for biological-image analysis. *Nat. Methods* **9**, 676–682.

Shannon, P., Markiel, A., Ozier, O., Baliga, N. S., Wang, J. T., Ramage, D., Amin, N., Schwikowski, B. and Ideker, T. (2003). Cytoscape: A software Environment for integrated models of biomolecular interaction networks. *Genome Res.* **13**, 2498–2504.

REFERENCES

1. Northcott, P. a *et al.* Medulloblastomics: the end of the beginning. *Nat. Rev. Cancer* **12**, 818–34 (2012).

2. Cavalli, F. M. G. *et al.* Intertumoral Heterogeneity within Medulloblastoma Subgroups. *Cancer Cell* **31**, 737-754.e6 (2017).

3. Northcott, P. A. *et al.* The whole-genome landscape of medulloblastoma subtypes. (2017). doi:10.1038/nature22973

4. Yang, Z. J. *et al.* Medulloblastoma Can Be Initiated by Deletion of Patched in Lineage-Restricted Progenitors or Stem Cells. *Cancer Cell* (2008). doi:10.1016/j.ccr.2008.07.003

5. Yokota, N. *et al.* Predominant expression of human Zic in cerebellar granule cell lineage and medulloblastoma. *Cancer Res.* **56**, 377–383 (1996).

6. Salsano, E., Pollo, B., Eoli, M., Giordana, M. T. & Finocchiaro, G. Expression of MATH1, a marker of cerebellar granule cell progenitors, identifies different medulloblastoma sub-types. *Neurosci. Lett.* **370**, 180–185 (2004).

7. Dahmane, N. & Ruiz, A. Sonic hedgehog regulates the growth and patterning of the cerebellum. *Development* **3100**, 3089–3100 (1999).

8. Wallace, V. A. Purkinje-cell-derived Sonic hedgehog regulates granule neuron precursor cell proliferation in the developing mouse cerebellum. *Curr. Biol.* **9**, 445–448 (1999).

9. Wechsler-Reya, R. J. & Scott, M. P. Control of neuronal precursor proliferation in the cerebellum by sonic hedgehog. *Neuron* **22**, 103–114 (1999).

10. Fuccillo, M., Joyner, A. L. & Fishell, G. Morphogen to mitogen: The multiple roles of hedgehog signalling in vertebrate neural development. *Nat. Rev. Neurosci.* **7**, 772–783 (2006).

11. Jiang, J. & Hui, C. Hedgehog Signaling in Development and Cancer. *Dev. Cell* **15**, 801–812 (2008).

12. Knoepfler, P. S., Cheng, P. F. & Eisenman, R. N. N-myc is essential during neurogenesis for the rapid expansion of progenitor cell populations and the inhibition of neuronal differentiation. *Genes Dev.* **16**, 2699–2712 (2002).

13. Kenney, A. M. Nmyc upregulation by sonic hedgehog signaling promotes proliferation in developing cerebellar granule neuron precursors. *Development* **130**, 15–28 (2002).

14. Monnier, V., Dussillol, F., Alves, G., Lamour-Isnard, C. & Plessis, a. Suppressor of fused links fused and Cubitus interruptus on the hedgehog signalling pathway. *Curr. Biol.* **8**, 583–586 (1998).

15. Pearse, R. V., Collier, L. S., Scott, M. P. & Tabin, C. J. Vertebrate homologs of Drosophila Suppressor of fused interact with the Gli family of transcriptional regulators. *Dev. Biol.* **212**, 323–336 (1999).

16. Cheng, S. Y. & Bishop, J. M. Suppressor of Fused represses Gli-mediated transcription by recruiting the SAP18-mSin3 corepressor complex. *Proc. Natl. Acad. Sci. U. S. A.* **99**, 5442–7 (2002).

17. Kool, M. *et al.* Genome sequencing of SHH medulloblastoma predicts genotype-related response to smoothened inhibition. *Cancer Cell* **25**, 393–405 (2014).

18. Northcott, P. A. *et al.* Pediatric and adult sonic hedgehog medulloblastomas are clinically and molecularly distinct. *Acta Neuropathol.* **122**, 231–240 (2011).

19. Rausch, T. *et al.* Genome sequencing of pediatric medulloblastoma links catastrophic DNA rearrangements with TP53 mutations. *Cell* **148**, 59–71 (2012).

20. Northcott, P. a. *et al.* Subgroup-specific structural variation across 1,000 medulloblastoma genomes. *Nature* **488**, 49–56 (2012).

21. Wefers, A. K. *et al.* Subgroup-specific localization of human medulloblastoma based on pre-operative MRI. *Acta Neuropathol.* **127**, 931–933 (2014).

22. Carter, R. A. *et al.* A Single-Cell Transcriptional Atlas of the Developing Murine Cerebellum. *Curr. Biol.* **28**, 2910-2920.e2 (2018).

23. Miale, I. L. & Sidman, R. L. An autoradiographic analysis of histogenesis in the mouse cerebellum. *Exp. Neurol.* **4**, 277–296 (1961).

24. Wang, V. Y., Rose, M. F. & Zoghbi, H. Y.

Math1 expression redefines the rhombic lip derivatives and reveals novel lineages within the brainstem and cerebellum. *Neuron* **48**, 31–43 (2005).

25. Leto, K. *et al.* Consensus Paper: Cerebellar Development. *Cerebellum* **15**, 789–828 (2016).

26. Machold, R. & Fishell, G. Math1 is expressed in temporally discrete pools of cerebellar rhombic-lip neural progenitors. *Neuron* **48**, 17–24 (2005).

27. Lewis, P. M., Gritli-Linde, A., Smeyne, R., Kottmann, A. & McMahon, A. P. Sonic hedgehog signaling is required for expansion of granule neuron precursors and patterning of the mouse cerebellum. *Dev. Biol.* **270**, 393–410 (2004).

28. Haldipur, P. *et al.* Expression of Sonic Hedgehog During Cell Proliferation in the Human Cerebellum. *Stem Cells Dev.* **21**, 1059–1068 (2012).

29. Gibson, P. *et al.* Subtypes of medulloblastoma have distinct developmental origins. *Nature* **468**, 1095–1099 (2010).

30. Schüller, U. *et al.* Acquisition of granule neuron precursor identity is a critical determinant of progenitor cell competence to form Shh-induced medulloblastoma. *Cancer Cell* **14**, 123–34 (2008).

31. Machold, R., Klein, C. & Fishell, G. Genes expressed in Atoh1 neuronal lineages arising from the r1/isthmus rhombic lip. *Gene Expr. Patterns* **11**, 349–359 (2011).

32. Hatten, M. E. & Roussel, M. F. Development and cancer of the cerebellum. *Trends in Neurosciences* **34**, 134–142 (2011).

33. Huangfu, D. *et al.* Hedgehog signalling in the mouse requires intraflagellar transport proteins. *Nature* **426**, 83–87 (2003).

34. Huangfu, D. & Anderson, K. V. Cilia and Hedgehog responsiveness in the mouse. *Proc. Natl. Acad. Sci.* **102**, 11325–11330 (2005).

35. May, S. R. *et al.* Loss of the retrograde motor for IFT disrupts localization of Smo to cilia and prevents the expression of both activator and repressor functions of Gli. *Dev. Biol.* **287**, 378–389 (2005).

36. Haycraft, C. J. *et al.* Gli2 and Gli3 Localize to Cilia and Require the Intraflagellar Transport Protein Polaris for Processing and Function. *PLoS Genet.* **1**, e53 (2005).

37. Corbit, K. C. *et al.* Vertebrate Smoothened functions at the primary cilium. *Nature* **437**, 1018–1021 (2005).

38. Rohatgi, R., Milenkovic, L. & Scott, M. P. Patched1 regulates hedgehog signaling at the primary cilium. *Science (80-.).* **317**, 372–376 (2007).

39. Bangs, F. K., Schrode, N., Hadjantonakis, A. K. & Anderson, K. V. Lineage specificity of primary cilia in the mouse embryo. *Nat. Cell Biol.* **17**, 113–122 (2015).

40. Sasai, N. & Briscoe, J. Primary cilia and graded Sonic Hedgehog signaling. *Wiley Interdiscip. Rev.* … **1**, 753–772 (2012).

41. Jia, J. *et al.* Suppressor of Fused inhibits mammalian Hedgehog signaling in the absence of cilia. *Dev. Biol.* **330**, 452–460 (2009).

42. Chen, M. H. *et al.* Cilium-independent regulation of Gli protein function by Sufu in Hedgehog signaling is evolutionarily conserved. *Genes Dev.* **23**, 1910–1928 (2009).

43. Di Magno, L., Coni, S., Di Marcotullio, L. & Canettieri, G. Digging a hole under Hedgehog: Downstream inhibition as an emerging anticancer strategy. *Biochimica et Biophysica Acta - Reviews on Cancer* **1856**, 62–72 (2015).

44. Madisen, L. *et al.* A robust and high-throughput Cre reporting and characterization system for the whole mouse brain. *Nat. Neurosci.* **13**, 133–140 (2010).

45. Feil, R., Wagner, J., Metzger, D. & Chambon, P. Regulation of Cre recombinase activity by mutated estrogen receptor ligand-binding domains. *Biochem. Biophys. Res. Commun.* **237**, 752–757 (1997).

46. Zomerman, W. W. *et al.* Identification of Two Protein-Signaling States Delineating Transcriptionally Heterogeneous Human Medulloblastoma. *Cell Rep.* **22**, 3206–3216 (2018).

47. Roussel, M. F. & Stripay, J. L. Epigenetic Drivers in Pediatric Medulloblastoma. *Cerebellum* **17**, 28–36 (2018).

48. Zhu, X. *et al.* Role of Tet1/3 Genes and Chromatin Remodeling Genes in Cerebellar Circuit Formation. *Neuron* **89**, 100–112

(2016).

49. Grimmer, M. R. & Weiss, W. A. BMPs oppose Math1 in cerebellar development and in medulloblastoma. *Genes and Development* **22**, 693–699 (2008).

50. Angley, C., Kumar, M., Dinsio, K. J., Hall, A. K. & Siegel, R. E. Signaling by Bone Morphogenetic Proteins and Smad1 Modulates the Postnatal Differentiation of Cerebellar Cells. *J. Neurosci.* **23**, 260–268 (2003).

51. Caspary, T., Larkins, C. E. & Anderson, K. V. The Graded Response to Sonic Hedgehog Depends on Cilia Architecture. *Dev. Cell* **12**, 767–778 (2007).

52. Gate, D., Danielpour, M., Bannykh, S. & Town, T. Characterization of Cancer Stem Cells and Primary Cilia in Medulloblastoma. *CNS Neurol. Disord. - Drug Targets* **14**, 600–611 (2015).

53. Han, Y. G. *et al.* Dual and opposing roles of primary cilia in medulloblastoma development. *Nat. Med.* **15**, 1062–1065 (2009).

54. Michaud, E. J. & Yoder, B. K. The primary cilium in cell signaling and cancer. *Cancer Research* **66**, 6463–6467 (2006).

55. Kim, J. J. *et al.* Suppressor of fused controls mid-hindbrain patterning and cerebellar morphogenesis via GLI3 repressor. *J. Neurosci.* **31**, 1825–36 (2011).

56. Blaess, S. Sonic hedgehog regulates Gli activator and repressor functions with spatial and temporal precision in the mid/hindbrain region. *Development* **133**, 1799–1809 (2006).

57. Spassky, N. *et al.* Primary cilia are required for cerebellar development and Shh-dependent expansion of progenitor pool. *Dev. Biol.* **317**, 246–259 (2008).

58. Kogerman, P. *et al.* Mammalian Suppressor-of-Fused modulates nuclear–cytoplasmic shuttling of GLI-1. *Nat. Cell Biol.* **1**, 312–319 (1999).

59. Hatten, M. E. Neuronal regulation of astroglial morphology and proliferation in vitro. *J. Cell Biol.* **100**, 384–396 (1985).

60. Salero, E. & Hatten, M. E. Differentiation of ES cells into cerebellar neurons. *Proc. Natl. Acad. Sci.* **104**, 2997–3002 (2007).

61. Lee, H. Y., Greene, L. a, Mason, C. a & Manzini, M. C. Isolation and culture of post-natal mouse cerebellar granule neuron progenitor cells and neurons. *J. Vis. Exp.* 20–23 (2009). doi:10.3791/990

62. Anne, S. L. *et al.* WNT3 Inhibits Cerebellar Granule Neuron Progenitor Proliferation and Medulloblastoma Formation via MAPK Activation. *PLoS One* **8**, e81769 (2013).

63. Taipale, J. *et al.* Effects of oncogenic mutations in Smoothened and Patched can be reversed by cyclopamine. *Nature* **406**, 1005–1009 (2000).

64. Kho, A. T. *et al.* Conserved mechanisms across development and tumorigenesis revealed by a mouse development perspective of human cancers. *Genes Dev.* **18**, 629–640 (2004).

65. Ohli, J., Neumann, J. E., Grammel, D. & Schüller, U. Localization of SHH medulloblastoma in mice depends on the age at its initiation. *Acta Neuropathol.* 1–3 (2015). doi:10.1007/s00401-015-1453-9

66. Tan, I.-L. *et al.* Lateral cerebellum is preferentially sensitive to high sonic hedgehog signaling and medulloblastoma formation. *Proc. Natl. Acad. Sci.* 201717815 (2018). doi:10.1073/pnas.1717815115

67. Swartling, F. J. *et al.* Distinct Neural Stem Cell Populations Give Rise to Disparate Brain Tumors in Response to N-MYC. *Cancer Cell* **21**, 601–613 (2012).

68. Dey, J. *et al.* A Distinct Smoothened Mutation Causes Severe Cerebellar Developmental Defects and Medulloblastoma in a Novel Transgenic Mouse Model. *Mol. Cell. Biol.* **32**, 4104–4115 (2012).

69. Chen, T. & Dent, S. Chromatin modifiers: regulators of cellular differentiation. *Nat. Rev. Genet.* **15**, 93–106 (2014).

70. Wheway, G., Nazlamova, L. & Hancock, J. T. Signaling through the Primary Cilium. *Front. Cell Dev. Biol.* **6**, (2018).

71. Corrales, J. D. Spatial pattern of sonic hedgehog signaling through Gli genes during cerebellum development. *Development* **131**, 5581–5590 (2004).

72. Corrales, J. D. The level of sonic hedgehog signaling regulates the complexity of cerebellar foliation. *Development* **133**, 1811–1821 (2006).

73. Varjosalo, M., Li, S. P. & Taipale, J.

Divergence of hedgehog signal transduction mechanism between Drosophila and mammals. *Dev. Cell* **10**, 177–186 (2006).

74. Svärd, J. *et al.* Genetic elimination of suppressor of fused reveals an essential repressor function in the mammalian hedgehog signaling pathway. *Dev. Cell* **10**, 187–197 (2006).

75. Chizhikov, V. V. *et al.* Cilia Proteins Control Cerebellar Morphogenesis by Promoting Expansion of the Granule Progenitor Pool. *J. Neurosci.* **27**, 9780–9789 (2007).

76. Lin, C. Y. *et al.* Active medulloblastoma enhancers reveal subgroup-specific cellular origins. *Nature* **530**, 57–62 (2016).

77. Pöschl, J. *et al.* Genomic and transcriptomic analyses match medulloblastoma mouse models to their human counterparts. *Acta Neuropathol.* **128**, 123–136 (2014).

78. Hassounah, N. B., Bunch, T. A. & McDermott, K. M. Molecular pathways: The role of primary cilia in cancer progression and therapeutics with a focus on hedgehog signaling. *Clin. Cancer Res.* **18**, 2429–2435 (2012).

79. Zhao, X. *et al.* A transposon screen identifies loss of primary cilia as a mechanism of resistance to SMO inhibitors. *Cancer Discov.* **7**, 1436–1439 (2017).

80. Sharpe, H. J. *et al.* Genomic Analysis of Smoothened Inhibitor Resistance in Basal Cell Carcinoma. *Cancer Cell* **27**, 327–341 (2015).

SUPPLEMENTAL FIGURES

Figure S1, related to Figure 2.

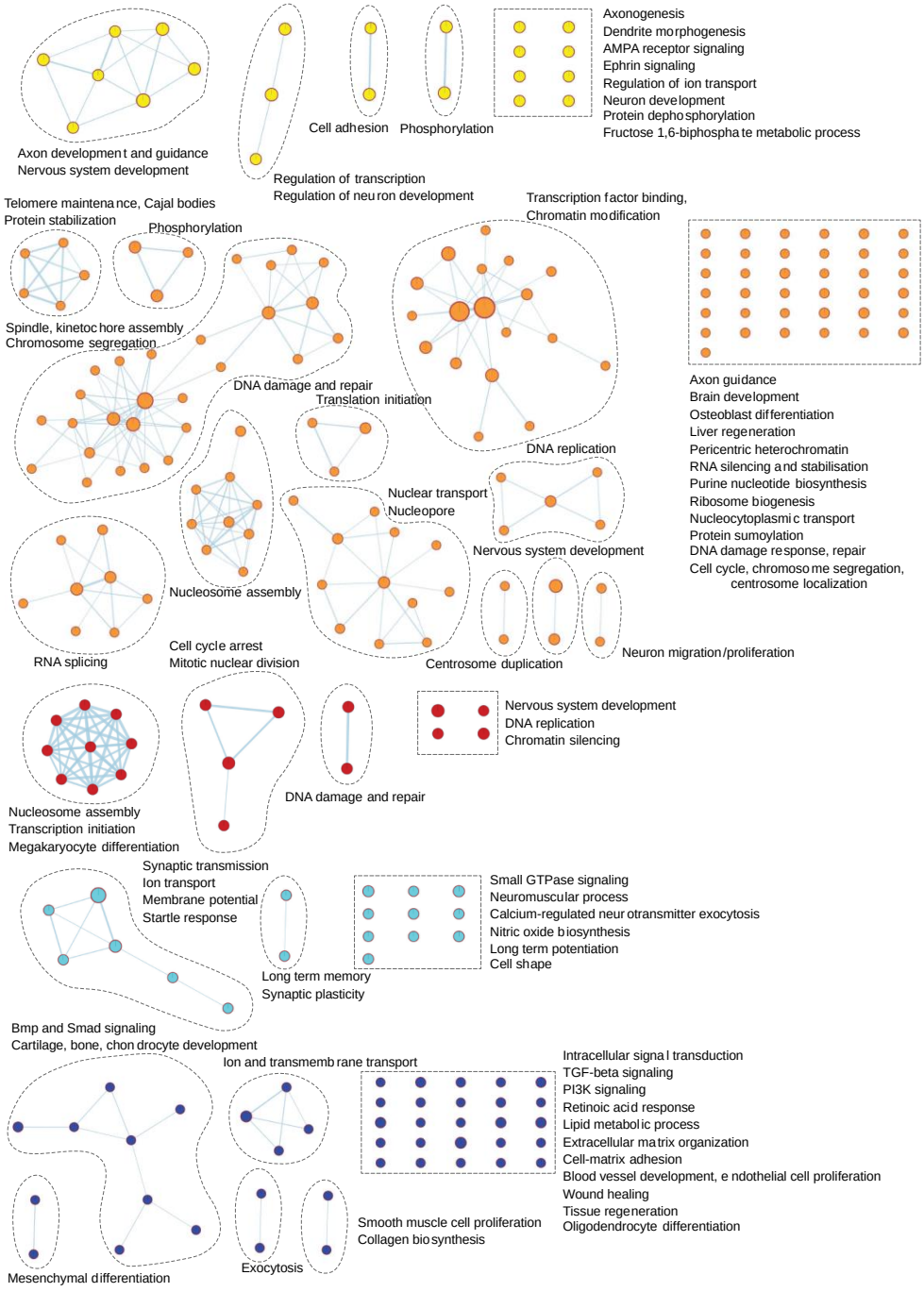

Figure S1, related to Figure 2.

Enrichment of specific biological processes during CGNP development per gene cluster.

Gene ontological analysis shows enriched biological processes per gene cluster. Each node represents a biological process. Related biological processes are grouped and labeled by biological theme (curved dashed lines). Individual biological processes are assembled in rectangular boxes (dashed lines). Biological processes connected by edges have genes in common. Enriched biological processes were determined with the Database of Annotation, Visualization and Integrated Discovery (DAVID), v.6.8 (Benjamini-corrected q = 0.1, p =0.01) and visualized with the Enrichment Map app in Cytoscape. Yellow nodes: E15.5 - E17.5 cluster; orange nodes: E15.5 - P7 clusters; red nodes: P0 - P7 cluster; light blue nodes: P14 - P30 cluster; dark blue nodes: P14 - P30 cluster.

Figure S2, related to Figure 3.

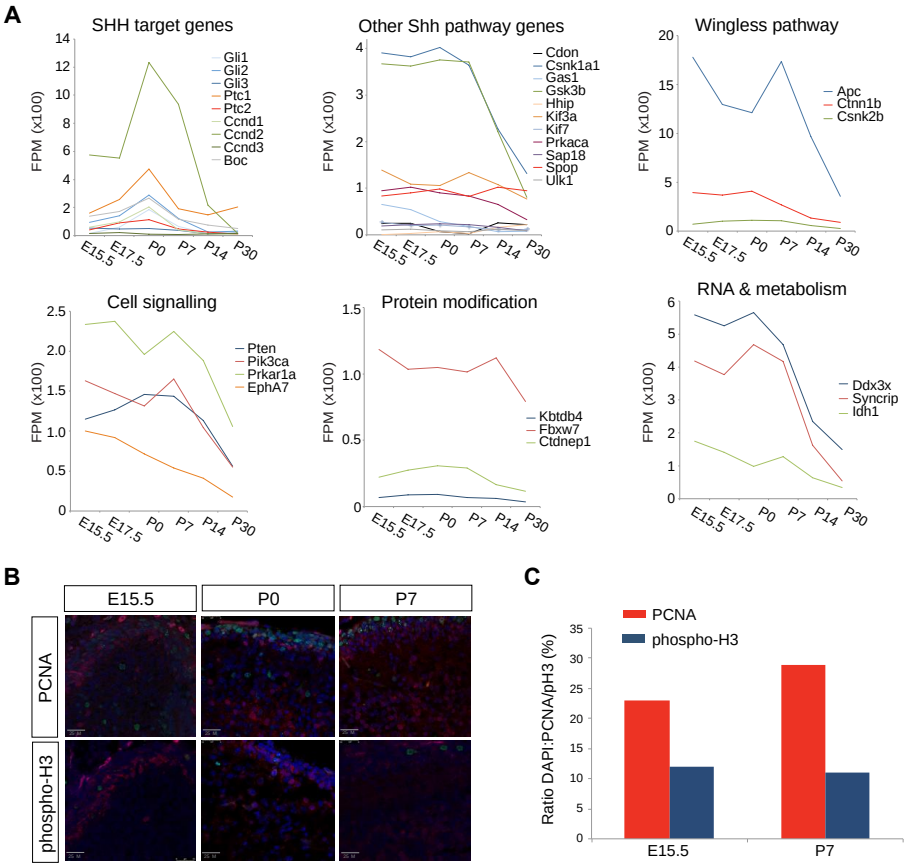

Figure S2, related to Figure 3.

Gene expression and proliferation in developing CGNPs.

(A) Gene expression profiles of CGNP genes commonly mutated in medulloblastoma extracted from the RNA-seq data set. Curves represent the average expression level from three biological replicates (FPM=fragments per million). **(B)** Confocal images showing PCNA (upper panels) and phospho-Histone H3 protein expression (lower panels) in the E15.5, P0, and P7 cerebellum. Scale bars indicate size. **(C)** Chart showing the mean ratio of $PCNA^{+}$ (red bars) or phospho-Histone $H3^{+}$ (blue bars) cells in the E15.5 and P7 cerebellum.

Figure S3, related to Figure 5.

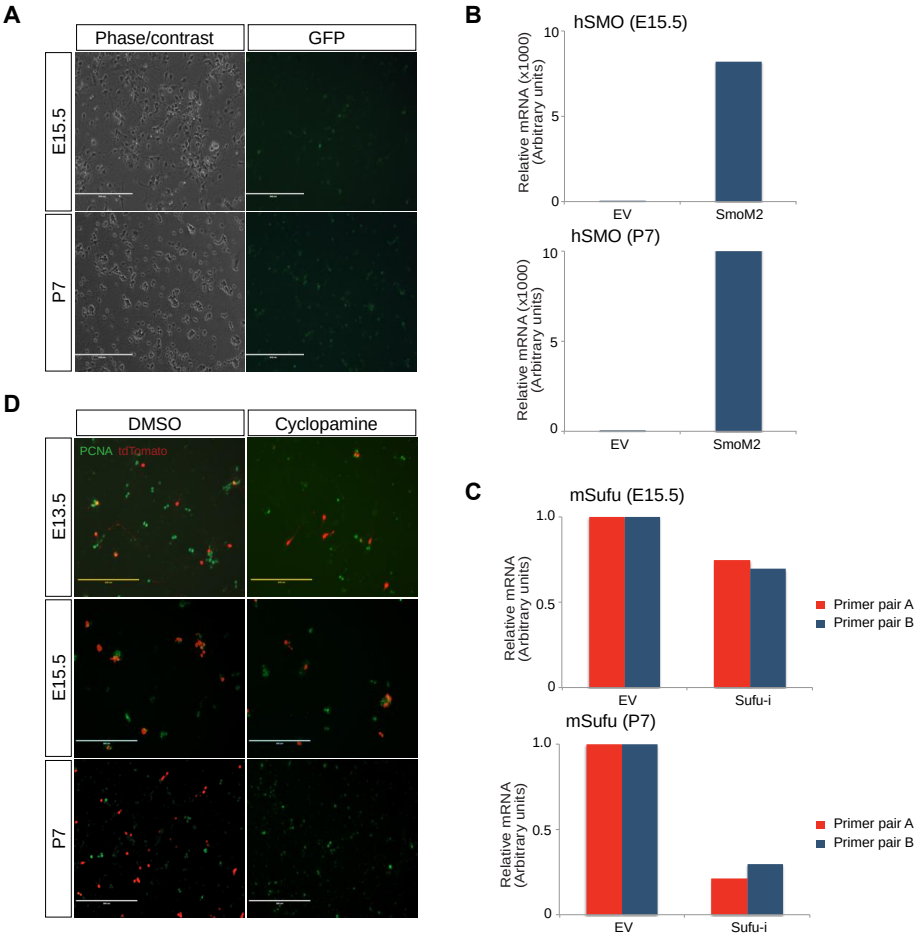

Figure S3, related to Figure 5.

Lentiviral transduction and proliferation in primary CGNP cultures.

(A) GFP fluorescence (right panels) showing representative lentiviral transduction efficiency in E15.5 and P7 CGNPs. Scale bars indicate size. **(B)** qRT-PCR showing relative mRNA expression levels in SmoM2 overexpressing versus empty vector control (EV) transduced E15.5 and P7 CGNPs. **(C)** qRT-PCR showing relative mRNA expression levels in Sufu shRNA versus empty vector control (EV) transduced E15.5 and P7 CGNPs. **(D)** Representative images of E13.5, E15.5, and P7 primary CGNP cultures immunolabeled for PCNA and tdTomato after treatment with Cyclopamine or DMSO (mock).

Table S1, related to Figure 1.

See Excel file.

Table S2, related to Figure 1.

See Excel file.

Table S3, related to Figure 2.

See Excel file.

Table S4, related to Figure 3.

See Excel file.

Table S5, related to Figure 3.

See Excel file.

Table S6, related to STAR methods and Key resource table.

Primers qRT-PCR	**Sequence**
mSufu pair A Forward	5'-TCCAGGTTACCGCTATCGTC-3'
mSufu pair A Reverse	5'-GAGATCACTCAGGCCAAAGC-3'
mSufu pair B Forward	5'-ACATCAGCTTTGGCCTGAGT-3'
mSufu pair B Reverse	5'-AAATCCACTTGGTCCGTCTG-3'
mGAPDH Forward	5'-AGGGCTCATGACCACAGTC-3'
mGAPDH Reverse	5'-GATGCAGGGATGATGTTCTG-3'
hSMO Forward	5'-TGAAGGCTGCACGAATGAGG-3'
hSMO Reverse	5'-CTTGGGGTTGTCTGTCCGAA-3'
Oligo siRNA	**Sequence**
Sufu A	5'-TTGAGTTGACGTTTCGTCTGAA-3'
Primers (cloning)	**Sequence**
miRE-XhoI Forward	5'-TGAACTCGAGAAGGTATATTGCTGTTGACAGTGAGCG-'3
miRE-EcoRI Reverse	5'-TCTCGAATTCTAGCCCCTTGAAGTCCGAGGCAGTAGGC-3'

Pediatric medulloblastoma
&
genome instability

4

A role for genomic instability in pediatric medulloblastoma: modelling medulloblastoma using CIN as a driver

Irena Bočkaj [1], Marlinde J. Smit [1,5], Inna Armandari [1,5], Bjorn Bakker [1], Tiny G.J. Meeuwsen-de Boer [2], Nancy Halsema [1], PetraL. Bakker [1], Diana C.J. Spierings [1], Eelco W. Hoving [3], Eveline S.J.M. de Bont [4], Victor Guryev [1], Floris Foijer [1] & Sophia W.M. Bruggeman [1]

[1] European Research Institute for the Biology of Ageing/ERIBA, UMCG, the Netherlands
[2] Pathology and Medical Biology, UMCG, the Netherlands
[3] Princess Máxima Center for Pediatric Oncology, Utrecht, The Netherlands
[4] Departments of Pediatric Oncology and Hematology/Pediatrics, UMCG, the Netherlands
[5] Equal contribution

ABSTRACT

Medulloblastoma is the most common pediatric brain malignancy. It comprises four molecular subgroups: SHH, WNT, Group 3 and Group 4 medulloblastoma, each thought to have a separate etiology (*e.g.* cell-of-origin) and oncogenic drivers. We and others have found that aneuploidy is a common feature of medulloblastoma that is particularly profound in a subset of SHH medulloblastoma: the SHHα subgroup. This suggests that chromosomal instability (CIN), the process leading to aneuploidy, is an important player in medulloblastoma pathophysiology.

To investigate if CIN is a driving event in medulloblastoma, we performed karyotyping of single medulloblastoma cells and demonstrated the presence of distinct tumor cell clones harboring unique copy number alterations. This indicates ongoing CIN, prompting us to set up primary medulloblastoma cell cultures to visualize mis-segregation events in real time. However, clonal heterogeneity was rapidly lost under culture conditions, forcing us to take an alternative approach to study the role of CIN in medulloblastoma. We therefore subsequently generated a cerebellar CIN mouse model that combines loss of tumor suppressor *Trp5*3 and mitotic checkpoint component *Mad2l1*. Despite loss of *Mad2l1* expression, we found no evidence for retention of aneuploid cerebellar cells, nor did we observe any developmental defects or signs of hyperplastic growth. This suggests that CIN/aneuploidy is not tolerated by the cerebellum and that CIN-driven medulloblastoma requires additional genetic lesions.

INTRODUCTION

The integrity of the genome is threatened at every cell division. Therefore, dedicated fail-safe programs have evolved that act at different phases of the cell cycle to maintain genomic integrity[1]. One of these programs, the spindle assembly checkpoint (SAC), takes place during mitosis and ensures equal chromosome segregation among two daughter cells thereby preventing mis-segregations[2]. Any impairments in this process causes chromosomal instability (CIN) resulting in aneuploidy in the daughter cells[3]. While this is mostly detrimental for normal cells, cancer cells show high rates of mis-segregation and aneuploidy[3]. In fact, seventy percent of all human cancers are aneuploid, deeming CIN a hallmark of cancer[4]. As CIN is thought to be both an initiator and facilitator of tumorigenesis, it represents an attractive therapeutic target[5].

In contrast to adult cancers, pediatric malignancies are generally devoid of chromosomal abnormalities and have a low mutational burden[6]. However, a subset of brain malignancies including medulloblastoma stand out with genomic instability rates and aneuploidy scores comparable to adult cancers[6]. Medulloblastoma is the most common pediatric brain malignancy that localizes to the posterior fossa[7,8]. It consists of four consensus molecular subgroups, each thought to have a separate etiology (*e.g*, cell of origin) and molecular driving force: Sonic-hedgehog (SHH), WNT, Group 3 and Group 4 medulloblastoma[9–11]. Aneuploidy is a common feature among all subtypes, yet particularly profound in Groups 3 and 4 and a subset of SHH medulloblastoma termed SHHα[6,10–13].

SHHα medulloblastoma has a particularly unfavorable outcome when associated with *TP53* mutations, which renders this the medulloblastoma subtype with the worst outcome[10]. Furthermore, *TP53* mutant SHH medulloblastoma associates with increased structural variant load and typical losses of 9q, 10q, and 17p[6,10,14,15]. These recurrent copy number variations suggest CIN as an important player in SHHα medulloblastoma[13].

However, the question whether there is actual ongoing CIN in medulloblastoma has not yet been addressed, nor is it known if CIN can act as a

driving event in medulloblastoma. To address this, we have performed single cell karyotype analysis on untreated human medulloblastoma samples. We found that there are multiple subclones present in the tumor that have unique copy number alterations, suggestive of ongoing CIN. Unfortunately, when we started culturing primary medulloblastoma cells with the aim of live visualizing mis-segregation events, in addition to a limited proliferative capacity we observed a rapid loss of karyotype heterogeneity in the culture. This prompted us to develop an alternative approach to address our questions: a medulloblastoma mouse model employing SAC alleviation as a tool to provoke ongoing CIN in the developing cerebellum, and possibly medulloblastoma development.

The model combines loss of tumor suppressor *Trp53*, facilitator of genomic instability[16], with loss of mitotic checkpoint component *Mad2l1*, which induces CIN[2]. These lesions are specifically targeted to the SHH medulloblastoma cell-of-origin, the cerebellar granule neuron progenitor (CGNP)[17–19]. To closely resemble the human disease, we induced loss of *Trp53* and/or *Mad2l1* in neonates using conditional alleles. We found that *Mad2l1;Trp53* deficient mice survive throughout the critical phase of cerebellar development. However, they do not exhibit cerebellar aneuploidy, developmental defects or any signs of cerebellar hyperplasia. This suggests that aneuploidy is not tolerated in the developing cerebellum and therefore by itself is not sufficient to initiate medulloblastoma. Understanding the coping mechanisms that neural progenitors use to evade aneuploidy warrants further research.

RESULTS

Single cell whole genome sequencing reveals genomic instability and intra-tumor heterogeneity in pediatric medulloblastoma

To investigate if ongoing genomic instability is a feature of pediatric medulloblastoma, a DNA single cell sequencing technology was employed (*e.g.,* shallow single cell Whole Genome Sequencing or scWGS) that allows assessing

copy number variations at the single cell level, and thereby karyotype clonality and heterogeneity within a tumor[20,21]. We first looked at the karyotypes of single cells that were isolated from four untreated medulloblastoma samples (Fig 1A). It was found that large differences existed between tumor samples, with MB-1 and MB-4 being the most heterogeneous and showing the greatest divergence from euploidy (Fig 1A-B). Sample MB-3 on the other hand was mostly euploid. Furthermore, particularly in MB-1 and MB-4, we observed coexisting clones as evidenced by single cells with varying chromosome compositions, indicating intratumor heterogeneity and ongoing chromosomal instability (Fig 1A-B).

We then wanted to study the ongoing CIN in primary human medulloblastoma cells in more detail. Hereto, we set out to generate primary cell cultures from the medulloblastoma samples, which is challenging as medulloblastoma cells are notoriously difficult to maintain under *in vitro* conditions (our own observations and M. van de Wetering, personal communication). However, we succeeded in culturing MB-1 tumor cells for several passages, and performed scWGS at passage 1 (after two weeks in culture) and passage 3 (six weeks in culture). We observed that during this relatively short period of cell culturing, there was a significant loss of karyotype diversity (Fig 1C). At the third passage, only one *in vitro* clonal population remained, causing the heterogeneity score to drop dramatically (Fig 1D). This precluded us from performing live cell imaging in human medulloblastoma cells, which is the gold standard for studying CIN phenotypes, and forced us to generate an alternative model for studying CIN in medulloblastoma.

Figure 1. Single cell whole genome sequencing reveals genomic instability and intra-tumor heterogeneity in pediatric medulloblastoma *(Figure on next page).* **(A)** scWGS data of four medulloblastoma samples. Each line represents the karyotype of a single cell (21-44 lines/sample) whereas chromosomes are depicted horizontally. The colors represent the ploidy of their corresponding region. **(B)** Heterogeneity (left) and aneuploidy scores (right) plotted for all pediatric medulloblastomas. Data was analyzed by the R-package Aneufinder. **(C)** scWGS data for in vitro cultured MB-1 as indicated. Each line represents the karyotype of a single cell (27-41 cells/sample); the colors represent the ploidy of their corresponding region. Data was analyzed by the R-package Aneufinder. **(D)** Heterogeneity and aneuploidy scored plotted for primary MB-1 sample and tissue cultured MB-1 over one passage (MB-1 p1) or over three passages (MB-1 p3).

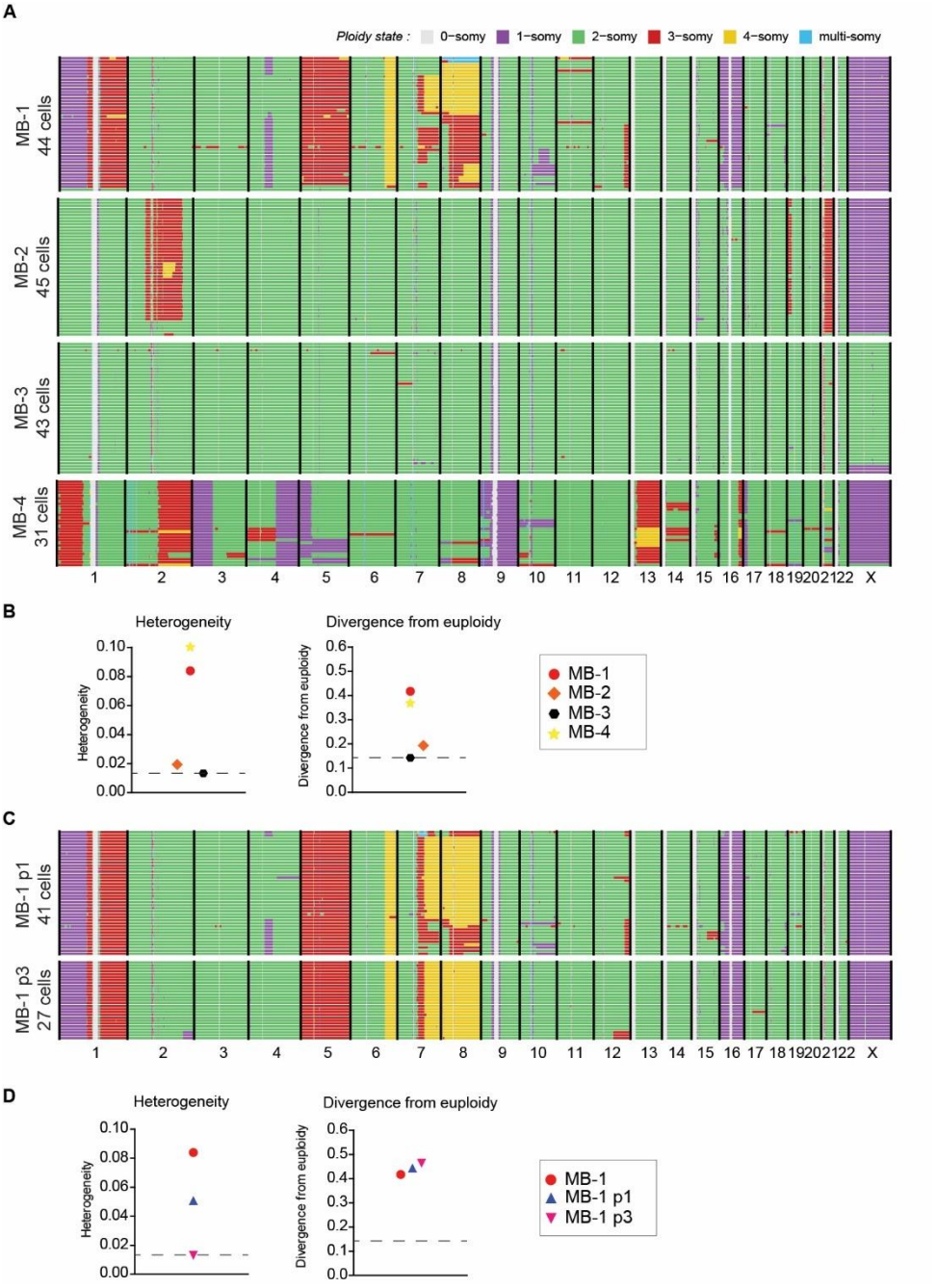

Figure 1. Single cell whole genome sequencing reveals genomic instability and intra-tumor heterogeneity in pediatric medulloblastoma *(Legend on previous page).*

Enrichment for cell cycle related processes is age-dependent in CGNPs and characterizes a subset of medulloblastoma patients.

In a previous study, we have used a transgenic mouse model to prospectively isolate the murine equivalent of the SHH medulloblastoma cell-of-origin, the cerebellar granule neuron progenitor (CGNP), at different developmental time points[22] (**Chapter 3** of this thesis). We found that CGNPs exhibited unique transcriptional profiles as a function of time, suggesting that the identity of the CGNP population shifts as cerebellar development progresses. We further confirmed that CGNPs resemble human SHH medulloblastoma in an age-dependent manner (**Chapter 3** of this thesis). This prompted us to explore the use of murine CGNPs for modelling CIN in medulloblastoma.

We first performed a cross-species comparison between dynamically expressed CGNP genes and their human medulloblastoma counterparts (extracted from a publicly available database of medulloblastoma transcriptomes) (Fig 2A)[23]. While overall, there was limited overlap, we identified a group of n=154 genes that showed co-clustering between murine CGNPs and patients: a part of the patients resembled gene expression patterns found in early CGNPs (E15.5-P7), and a part of the patients mirrored older CGNPs (P30) (Fig 2A). When focusing solely at the genes enriched in E15.5-P7 CGNPs (orange cluster, Fig 1E of Chapter 3 of this thesis), we found that n=114 genes out of the 154 genes overlapped with the orange Embryonic/Neonatal cluster (Fig 2B). GO term pathway enrichment analysis identified a “cell cycle signature” in this group of genes, since mitotic cell division, DNA repair and DNA replication related processes where highly enriched (Fig 2C and Fig S1A-B). Intriguingly, when we compared these (n=114) genes with the CIN70 signature of aneuploid cancers that has been described previously, we found substantial overlap that included spindle checkpoint gene *Mad2l1* (Fig 2D)[24]. This suggests that CIN plays a role in early CGNPs as well as in a subset of human patients, and reinforces the use of CGNPs for modelling CIN in medulloblastoma.

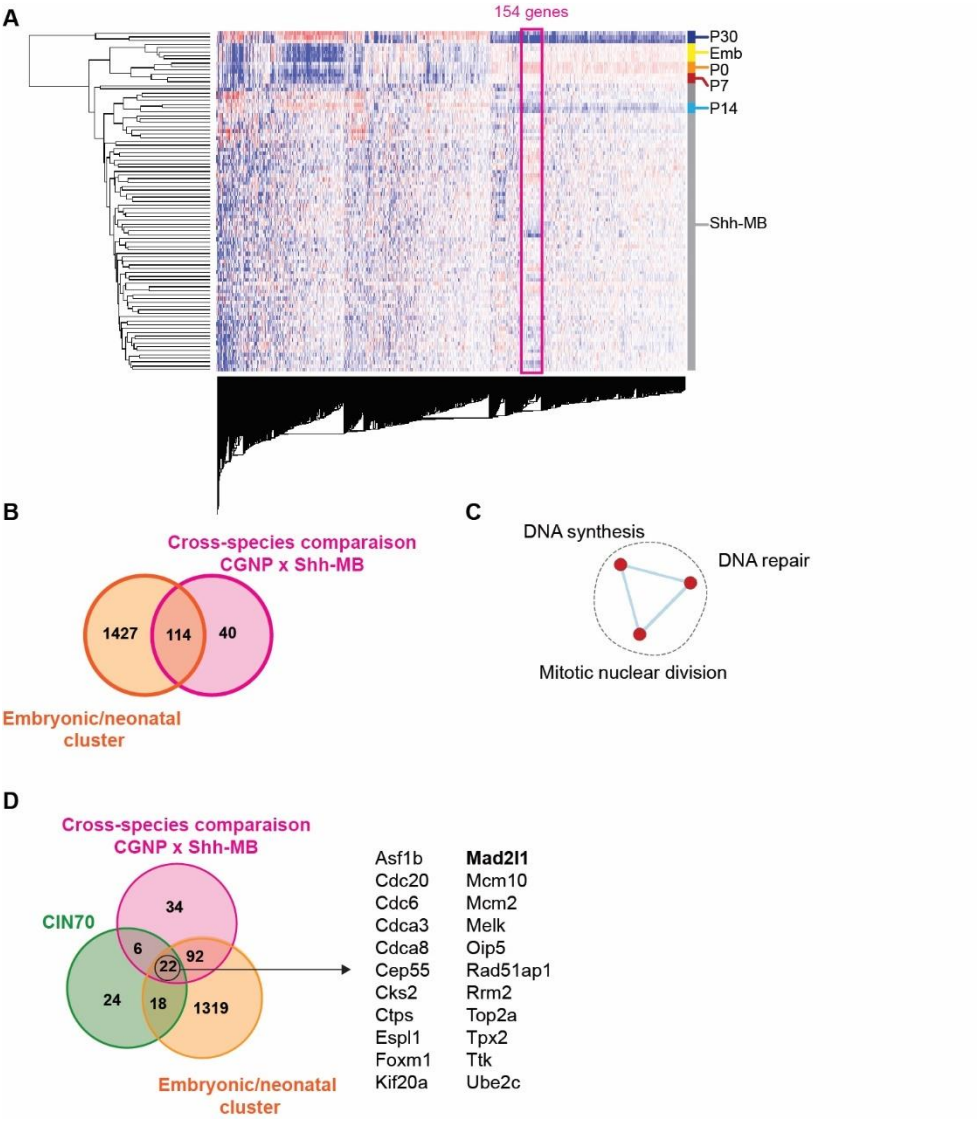

Figure 2. Enrichment for cell cycle related processes is age-dependent in CGNPs and characterizes a subset of medulloblastoma patients. (A) Reverse Frankenstein cross-species comparison heatmap showing unsupervised hierarchical clustering of human medulloblastoma genes and CGNP orthologous genes. A gene cluster (n=154) shows mixed clustering between human medulloblastomas and CGNP samples (represented by a pink rectangle). **(B)** Venn diagram representing overlapping (n=114) genes between the pink cluster from the cross-species comparison and the orange embryonic/neonatal CGNP cluster**. (C)** Enrichment map showing biological processes that predominate in the 114 common genes between the pink and orange cluster. Each node represents a biological process. **(D)** Venn diagram showing the overlap of the 114 genes and the CIN70 gene expression signature of chromosome instability (green circle) in human cancers. The 22 common genes are listed next to the Venn diagram.

Mad2l1 and Trp53 are highly expressed in neonatal CGNPs and targeted for cerebellum-specific deletion in neonatal mice.

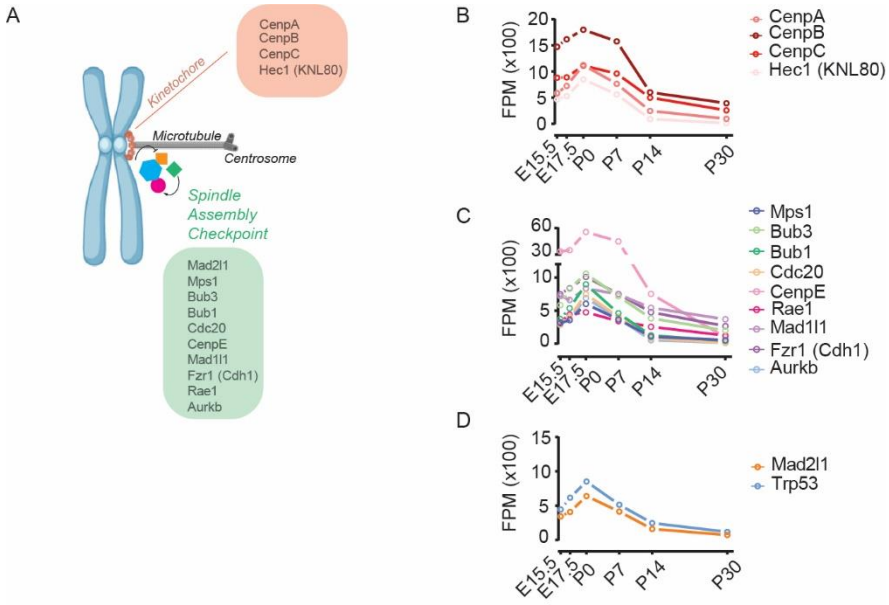

Figure 3. Age related gene expression of kinetochore and mitotic checkpoint components in the developing CGNP. (A) Illustration representing the spatial localization of kinetochore and mitotic checkpoint proteins used in mouse models for chromosomal instability. Adapted from [25] **(B-D)** Normalized gene expression in the developing CGNP for **(B)** kinetochore proteins, **(C)** spindle assembly checkpoint (SAC) proteins and **(D)** SAC protein Mad2l1 and Trp53.

To investigate the impact of CIN and aneuploidy on non-neural tissues, a number of mouse models have been established previously that rely on tissue specific deletion of mitotic checkpoint or kinetochore components (as summarized in Fig 3A and reviewed in [25]). To generate a cerebellum specific CIN/aneuploidy mouse model through CGNP targeting, we first mapped the temporal usage of checkpoint/kinetochore genes in these cells (Fig 3B-D). This revealed that expression of all checkpoint/kinetochore genes peaks around birth, consistent with the known perinatal surge in CGNP proliferation[26–28]. We therefore decided to induce chromosomal instability in CGNPs by targeting spindle checkpoint component *Mad2l1*, a strategy that has proven successful in the past[29–31]. To mitigate potential

deleterious effects on CGNP viability, we also included *Trp53* deletion in the model, a tumor suppressor gene that is frequently mutated in medulloblastoma[10]. Both *Mad2l1* and *Trp53* are highly expressed in neonatal CGNPs (Fig 3D). To obtain spatiotemporal control of *Mad2l1* and *Trp53* deletion, we combined the Math1CreER^{T2}-tdTomato transgenic mouse strain (characterized in Chapter 3 of this thesis) with the previously described *Mad2l1* and/or *Trp53* conditional knockout mouse strains[29–31] (Fig 4A-B). This yielded five experimental groups: three control groups comprising CGNP-specific single deletion of *Mad2l1* or *Trp53* (hereafter referred to as Mad2$^{-/-}$ (orange); p53$^{-/-}$ (green)), and a MathCreER^{T2}-only group (hereafter: Cre^{Negative} (white)). The two remaining groups are compound deletion mutants that are expected to exhibit mild and severe CIN, respectively (Mad2$^{+/f}$;p53$^{f/f}$ (yellow); and Mad2$^{f/f}$;p53$^{f/f}$ (blue)). Figure 4C graphically represents the anticipated cerebellar phenotypes upon treatment of new born pups (postnatal day P4).

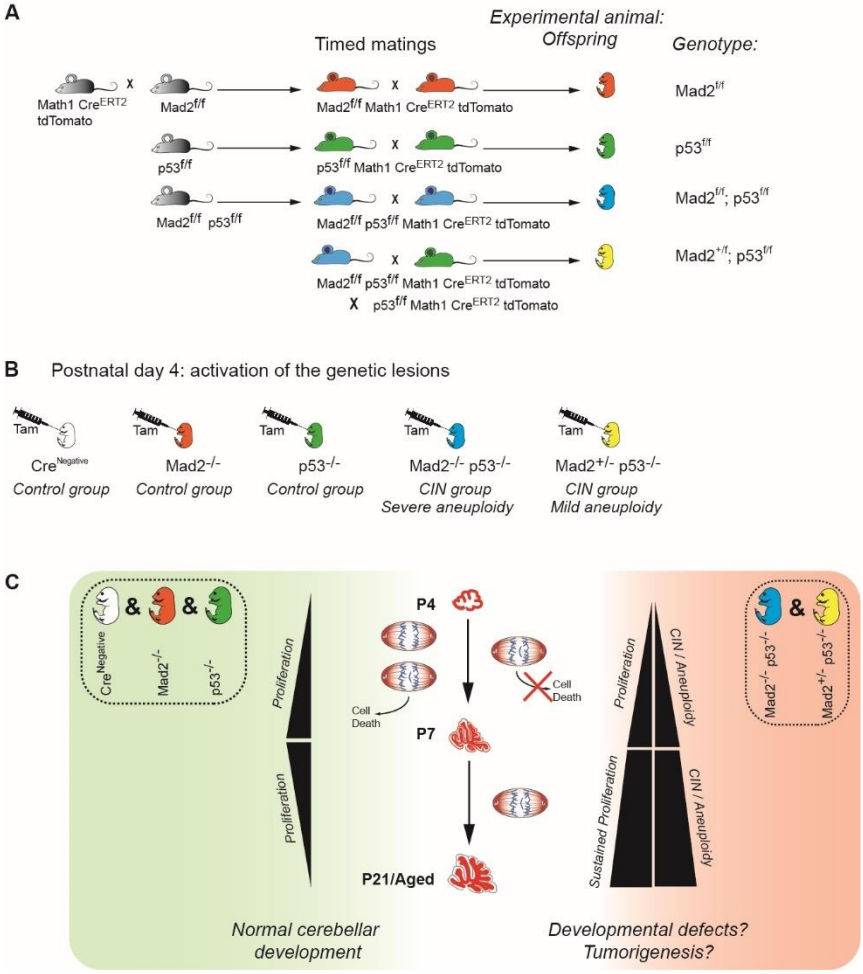

Figure 4. Establishment of a CIN driven mouse model for pediatric medulloblastoma.
(A) Generation of mouse lines**.** Schematic overview depicting the breeding scheme to obtain timely controlled activation of CIN specifically in the cerebellar compartment. Math1-Cre^{ERT2} enables tissue specific expression of the Cre-recombinase to the Math1 expressing compartment of cerebellar granule neuron progenitors (CGNP). Expression of the TdTomato cassette enables to track the switched compartment by red fluorescence. Further crossing with Mad2$^{f/f}$, p53$^{f/f}$ and Mad2$^{f/f}$; p53$^{f/f}$ lines targets allele switching to the CGNP compartment. Final timed breeding generates offspring of the desired genotypes to create the experimental groups of neonates. **(B)** Mouse groups for the study of the role of CIN in the neonatal developing cerebellum. Allele switching is performed postnatally by oral gavaging of P4 pups with tamoxifen. Five experimental groups are generated. Three groups (Cre^{Negative} , Mad2$^{f/f}$ and p53$^{f/f}$) are considered control groups, whereas Mad2$^{+/-}$; p53$^{-/-}$ and Mad2$^{-/-}$; p53$^{-/-}$ groups are considered CIN groups. **(C)** Scheme representing normal mouse postnatal cerebellar development where proliferation peaks at postnatal day 7 (Green area). In addition is depicted the expected effect of p53 deletion in the proliferative compartment of postnatal CGNPs (*Sustained proliferation*) in addition to the effect of Mad2 deletion on the maintenance of genome integrity (*Chromosomal Instability (CIN) / Aneuploidy*) (red area).

Mad2l1 but not Trp53 deletion is tolerated in the developing postnatal cerebellum.

To check whether deletion of *Mad2l1* and *Trp53* is tolerated in proliferating neonatal CGNPs, we assessed allele switching, expression levels, and karyotypic changes at different developmental time points of sorted tdTomato-positive CGNPs (Fig 5A). We observed persistent tdTomato expression in cerebellum up to at least 6 months of age, demonstrating the functionality of the Math1CreER^{T2}/tdTomato module (Fig 5B-C). This is confirmed by assessing *Mad2l1* allele switching efficiency by conventional PCR, showing comparable switching at postnatal days P7, P15, and P22 when cerebellar development is almost completed (Fig 5D). qPCR further confirmed *Mad2l1* switching in all three Mad2$^{f/f}$ groups at comparable levels (Fig 5E), which is reflected by Mad2 protein expression (Fig 5H-I). We also confirmed switching of the p53 allele at P7 (Fig 5F). Interestingly, whereas developing CGNPs seem to tolerate loss of *Mad2l1*, switching of the *Trp53* conditional allele is less efficient (Fig 5F). The same trend was observed at the mRNA level (Fig 5G).

Figure 5. Validation of the mouse model by assessment of the allele switching efficiencies *(Figure on next page)* **(A)** Schematic overview of the experimental workflow. Neonatal CGNPs are labelled with tdTomato following a single Tamoxifen pulse administered to four days old pups. Fluorescent cerebella are dissected at three key timepoints (P7, P14 and P21) (P=postnatal day). tdTomato+ cells are sorted by FACS for further experiments that include: the assessment of allele switching efficiency at DNA, RNA and protein levels; karyotyping by scGWS; characterization of consequential phenotypes by immunohistochemistry (IHC). **(B)** Stereoscopic images showing tdTomato expression in cerebellum during postnatal development. **(C)** IVIS images depicting the long-term red fluorescence in the cerebellum of aged mice (6.5 months old). **(D)** Conventional genomic PCR assessing the switching efficiency of the *Mad2l1* and *Trp53* alleles in Mad2$^{-/-}$ mice during development. **(E)** Quantitative genomic PCR assessing the switching efficiency of *Mad2l1* in Mad2$^{-/-}$, Mad2$^{+/-}$; p53$^{-/-}$, Mad2$^{-/-}$; p53$^{-/-}$ mice during development. **(F)** Conventional genomic PCR assessing the switching efficiency of the *Mad2l1* and *Trp53* alleles in Mad2$^{-/-}$; p53$^{-/-}$, Mad2$^{+/-}$; p53$^{-/-}$ and p53$^{-/-}$ mice aged P7. **(G)** Quantitative RT-PCR assessing the switching efficiency of the *Mad2l1* and *Trp53* alleles at mRNA level. One primer set was used for *Mad2l1* gene expression (left graph) and two different primer sets were used for *Trp53* gene expression (Middle and right graph). **(H) and (I)** Assessment of allele switching at the protein level by western blot. **(H)** Blots representing Mad2 protein expression in P7 CGNPs from Mad2$^{-/-}$, Mad2$^{-/-}$; p53$^{-/-}$, Mad2$^{+/-}$; p53$^{-/-}$ and p53$^{-/-}$ mice. **(I)** Graph showing the quantification results of the western blot in (H) relative to the nuclear protein histone H4 protein expression for each sample. Reference sample is P7 CGNPs from p53$^{-/-}$ mouse.

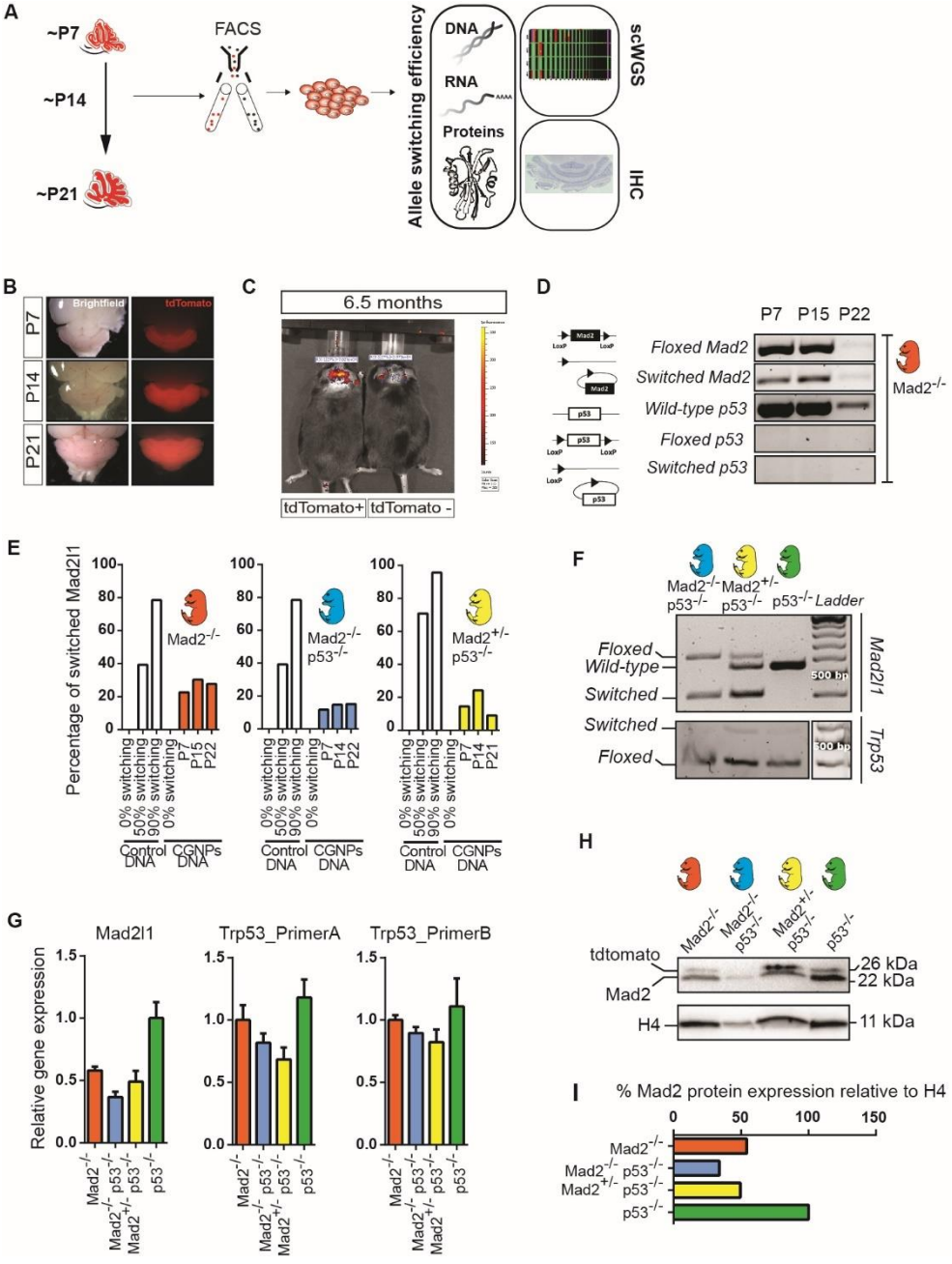

Figure 5. Validation of the mouse model by assessment of the allele switching efficiencies *(Legend on previous page)*

The *Mad2l1* null cerebellum does not show evidence of aneuploidy or medulloblastoma formation

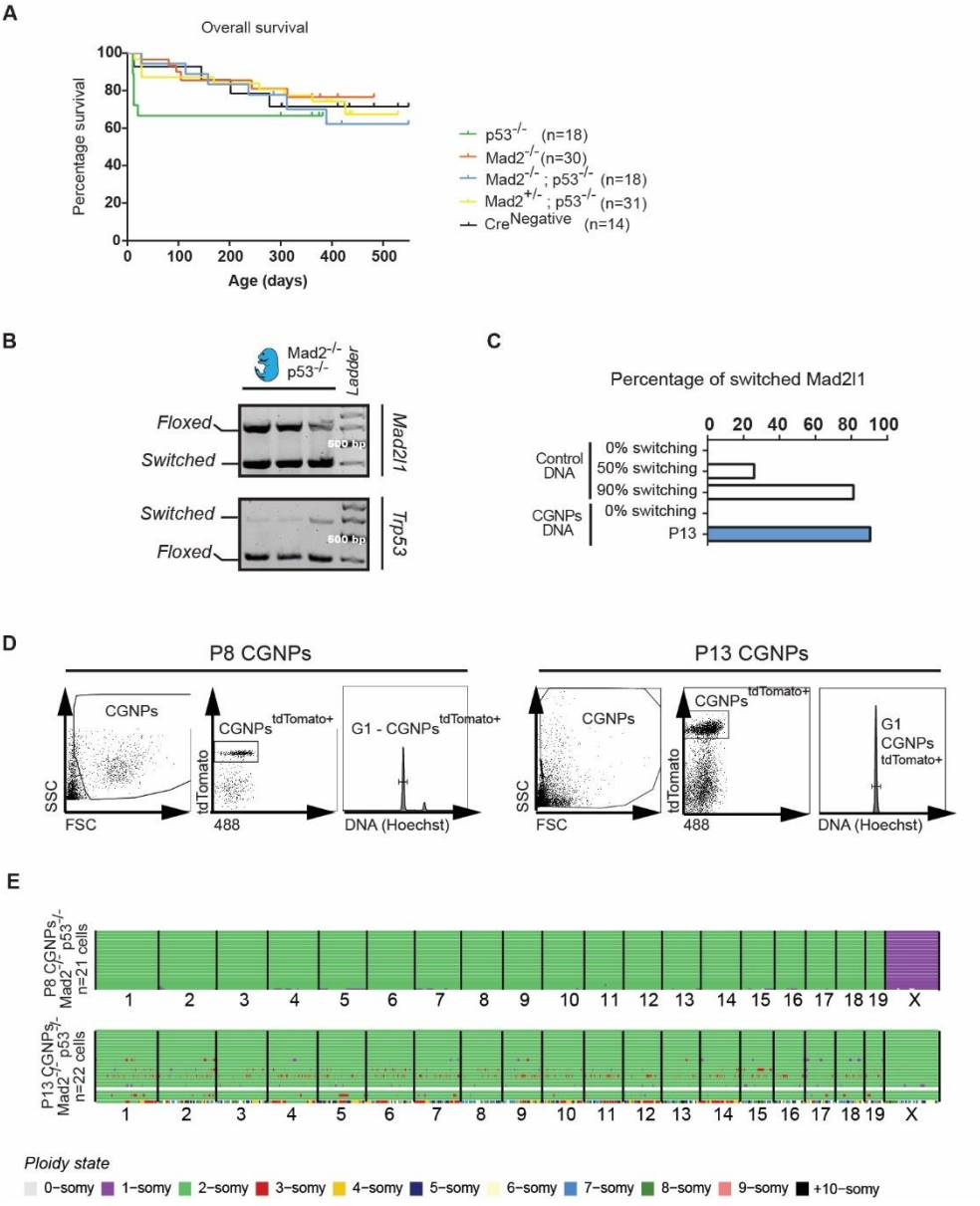

Figure 6. The Mad2l1 null cerebellum does not show evidence of aneuploidy or medulloblastoma formation *(Legend on next page)***.**

Figure 6. The Mad2l1 null cerebellum does not show evidence of aneuploidy or medulloblastoma formation *(Figure on previous page)*. **(A)** Kaplan Meier survival curve of the five experimental groups described in the graph shows overall survival. **(B)** Conventional genomic PCR assessing the switching efficiency of the *Mad2l1* and *Trp53* alleles in Mad2$^{-/-}$; p53-/- mice at postnatal day 7. **(C)** Quantitative genomic PCR assessing the switching efficiency of the *Mad2l1* alleles in Mad2$^{-/-}$; p53$^{-/-}$ mice at postnatal day 13. **(D)** Representative FACS plots depicting the sort strategy used to select for switched CGNPs (tdTomato positive) in the G1 phase of their cell-cycle. G1 CGNPs$^{tdTomato+}$ are directly sorted as single cells in 96 well plates before preparation for whole genome single cell sequencing. **(E)** Whole genome single-cell sequencing (scWGS) results for the P7 and P13 Mad2$^{-/-}$; p53$^{-/-}$ mice described above in (A) and (B). Each line represents the karyotype of a single cell (21-22 cells/sample) whereas chromosomes are depicted horizontally. The colors represent the ploidy of their corresponding region. Data was analyzed by the R-package Aneufinder.

Despite partial *Mad2l1* deletion, none of the groups developed brain tumors and they showed comparable overall survival up to 500 days of age (Fig 6A). We therefore investigated if *Mad2l1*$^{f/f}$ CGNPs exhibited evidence of CIN or aneuploidy (Fig 6B-E). We sorted tdTomato^{+} CGNPs from P8 and P13 Mad2$^{f/f}$;p53$^{f/f}$ cerebella, which showed efficient switching of the *Mad2l1* allele but not *Trp53*, as seen before (Fig 6B-D). For scWGS, the G0/G1 fraction was isolated (Fig 6D). No aneuploidies or copy number alterations (CNAs) were detected in any of the sequenced cells, suggesting that this is not tolerated in the cerebellum and explaining the absence of a tumor phenotype (Fig 6A,E). In line, we also did not observe alterations in cerebellar proliferation or development (Fig 7 and S2)[32].

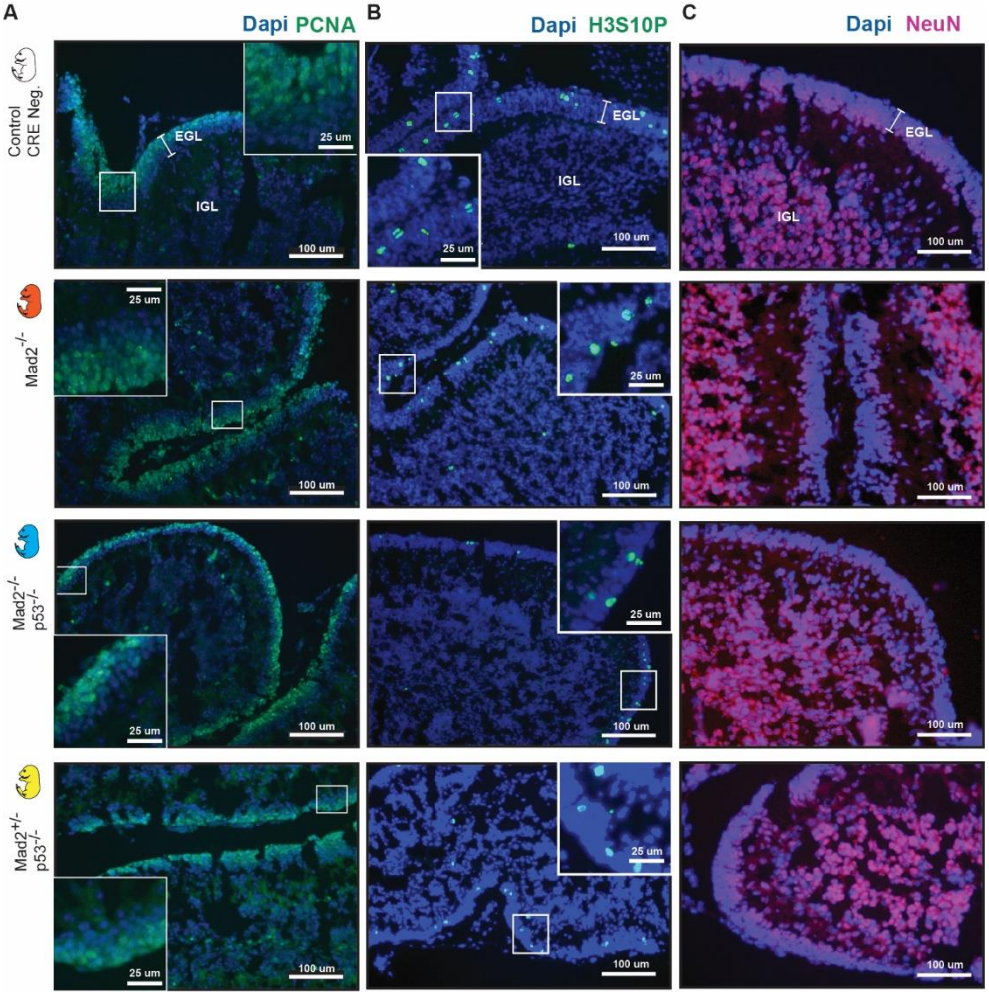

Figure 7. The Mad2l1 null cerebellum does not show alterations in cerebellar proliferation or development.
Images showing DAPI merged with **(A)** PCNA (Proliferating cell nuclear antigen**), (B)** H3S10P and **(C)** NeuN protein expression in the developing mouse cerebellum of Control (White), Mad2$^{-/-}$ (Orange), Mad2$^{-/-}$; p53$^{-/-}$ (Blue) and Mad2$^{+/-}$; p53$^{-/-}$ (Yellow) P7 pups. Scale bar is 100um unless otherwise stated.

Considering that P4 CGNPs undergo only few cell divisions before initiating terminal differentiation, we wondered if earlier *Mad2l1* deletion would be more efficient in promoting tumor formation[33]. We established a second mouse model where we induced switching *in utero* at embryonic day E13.5 (Fig 8A). At this stage, switched CGNPs complete two waves of proliferation: a first wave starting around E18.5 and a second perinatal wave[26–28], which increases the chance of acquiring chromosome mis-segregations and CNAs. However, we could not induce switching of either the *Mad2l1* or *Trp53* allele (Fig 8B), and consequently did not see reduced mRNA expression (Fig 8C). In line, we did not see any gross cerebellar abnormalities (Fig 8D-E), except for scattered apoptotic cells observed in the Purkinje and granular cell layers in both Mad2$^{f/f}$; p53$^{f/f}$ and control animals. Together, this suggests that inducing CIN in the early embryonic cerebellum is not tolerated.

Figure 8. Deletion of Mad2l1 and Trp53 at embryonic time point is not efficient *(Figure on next page)* **(A)** Schematic overview of the experimental workflow. Embryonic CGNPs are labelled with tdTomato following a single Tamoxifen pulse administered to pregnant females at E13.5. Fluorescent cerebella are dissected around birth. tdTomato+ cells are sorted by FACS for further experiments that include: the assessment of allele switching efficiency at RNA; characterization of consequential phenotypes by Immunohistochemistry (IHC). **(B)** Conventional genomic PCR assessing the switching efficiency of the *Mad2l1* and *Trp53* alleles in Mad2$^{-/-}$; p53$^{-/-}$ mice at postnatal day 1. **(C)** Quantitative RT-PCR assessing the switching efficiency of the *Mad2l1* and *Trp53* alleles at mRNA level in in Mad2$^{-/-}$; p53$^{-/-}$ (Blue) and in p53$^{-/-}$ (Green) mice. One primer set was used for *Mad2l1* gene expression (left graph) and two different primer sets were used for *Trp53* gene expression (Middle and right graph). **(D)** Transverse sections of the brains of 1-day-old mouse pups were stained with H&E for histopathologic examination (abbreviations: AB=anterobasal; AD=anterodorsal; CEN=central; CP=choroid plexus; EGL=external granular layer; INF=inferior; Mes=mesencephalon; POS=posterior). **(E)** H&E staining showing increased apoptotic features (black arrowheads) in the Purkinje and granular cell layers in both KO and WT animals.

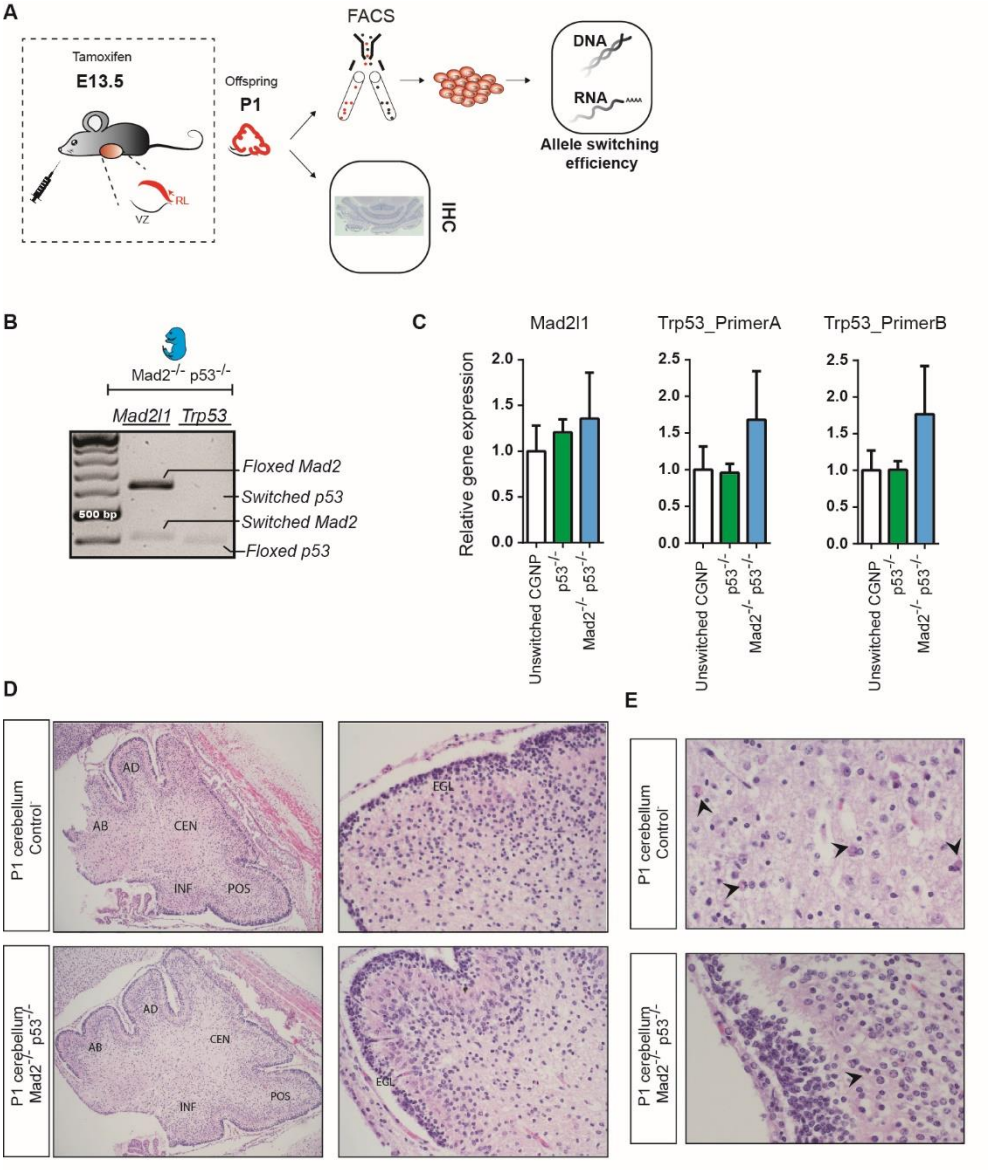

Figure 8. Deletion of Mad2l1 and Trp53 in embryonic time point is not efficient *(Legend on previous page)*

DISCUSSION

Although aneuploidy is an acknowledged feature of pediatric SHH medulloblastoma, it remains unclear if, and to what extent, chromosomal instability plays a role in driving this brain cancer. In this study, we show that aneuploid pediatric medulloblastoma are heterogenous in their karyotype composition, suggesting ongoing chromosomal rearrangements. We also show that CIN/aneuploidy is not tolerated in the murine counterpart of the medulloblastoma cell-of-origin, explaining the absence of cerebellar phenotypes and medulloblastoma development in our cerebellar CIN mouse model.

Culturing of medulloblastoma primary cells influences karyotype heterogeneity

While much effort has been made to establish patient-derived primary cultures from fresh tumor samples to replace existing, long term medulloblastoma cell lines, it remains challenging to find conditions that properly preserve tumor characteristics[34]. Our study highlights one of the caveats of *in vitro* models that has often been overlooked: the influence of culture conditions on genetic drift. As we observed a substantial divergence in karyotype heterogeneity upon prolonged culturing, it seems that there is strong selective pressure for the fittest clone *in vitro*. This problem is further underscored by the appearance of novel CNVs at later passage. Therefore, until better culture models have been developed it is recommendable to use early, non-passaged medulloblastoma cultures for (translational) research or alternatively, resume to mouse modelling as we have opted for.

Limited efficiency of allele switching in the medulloblastoma mouse model

Surprisingly, in our Math1CreER^{T2};Mad2;p53 mouse model, we found that in contrast to the *Mad2l1* allele, switching of *Trp53* was inefficient. This was unexpected since *Trp53* null (cerebellum) mouse models have been generated previously without obvious problems[35–37]. An explanation could be that timing of *Trp53* deletion is crucial. Constitutive, early *Trp53* loss may be compatible with cerebellar

development as compensatory mechanisms may take over p53 function, whereas acute loss is not tolerated at critical phases in CGNP development. Intriguingly, while we observed an overall low *Trp53* switching, efficiency increased when co-occurring with *Mad2l1* deletion suggesting some sort of genetic interaction between *Mad2l1* and *Trp53*.

In theory, even a low switching efficiency should be sufficient to initiate a hyperproliferative cluster of cells or eventually a tumor over a longer period of time. Indeed, it is enough for only one cell to be selected for and expand over time if it acquires an advantageous karyotype. However, we never observed tumor formation. It is conceivable that as such event is rare, we have to increase the numbers of mice in our cohort. Another parameter here could be the "time-window" offered to the switched, pre-malignant cells to propagate. One might think that in our first attempt of modelling CIN in medulloblastoma with neonatal deletion of *Mad2l1* and *Trp53*, there was not enough time for switched cells to establish a viable population with an advantageous karyotype, as CGNP proliferation peaks around the first week after birth and then rapidly decreases. However, a second attempt in which we induced switching at an earlier time point, leaving a longer time-window for transformation, did not show improvement in switching efficiencies. In fact, virtually no reduction in *Trp53* or *Mad2l1* expression was observed, arguing that time to transform may not be the limiting factor.

Tolerance of CIN and aneuploidy in the developing cerebellum

DNA damage induced genomic instability has previously been shown to naturally occur during neurogenesis in the cerebellum[38]. Endogenous DNA damage secondary to high replication rates or transcriptional activity creates a constant need to maintain genomic integrity and therefore adapt the DNA damage response[38]. The latter means a preference for DNA damage induced apoptosis rather than repair: emphasis is put on maintaining genome integrity over having the risk of progenitor expansion with unrepaired DNA[39]. Thus, we propose that the response to *Mad2l1* loss driven CIN triggers a similar and immediate apoptotic response. Newly born aneuploid cells might be cleared right away and will therefore be missed in our single

cell sequencing experiments. The high turnover in the progenitor population will compensate for the loss of apoptotic aneuploid cells, explaining the absence of a developmental phenotype. Together, this seems to define the cerebellar compartment as intolerant to aneuploidy.

To overcome this intolerance and allow tumor development, it is conceivable that additional genetic lesions are required. This could entail overactivation of the SHH pathway to stimulate hyperproliferation, or activation of anti-apoptotic genes. However, it is also possible that acquisition of CIN is not beneficial at medulloblastoma initiation, but rather facilitates tumor progression once sufficient genetic alterations have occurred to counteract the detrimental effects of CIN, and therefore is more important for tumor progression. Addressing these issues awaits further investigation.

MATERIALS AND METHODS

Generation and housing of Math1-CreER^{T2} Mad2l1 and Trp53 conditional knock-out mice

The Math1-CreER^{T2}; tdTomato compound transgenic mouse strain was derived from the Math1CreER^{T2}, and Ai14 mouse strains (The Jackson Laboratory), in a C57BL6/mixed background. Mad2 conditional mice were generated as described previously by introducing loxP sites flanking exons 2 and 5 of the *Mad2l1* gene [29,30,40]. Cre-dependent recombination will flox-out exons 2,3,4 and part of exon 5 creating *Mad2l1* KO alleles. Trp53 conditional mice were generated as described previously by introducing loxP sites encompassing exons 1 and 11 of the *Trp53* gene[31]. Cre-dependent recombination will flox-out exons 2-10 creating *Trp53* KO alleles. *Mad2l1$^{f/f}$* and *p53$^{f/f}$* mice were intercrossed creating compound double KOs for *Mad2l1* and *Trp53. Mad2l1$^{f/f}$*, *p53$^{f/f}$* and compound *Mad2l1$^{f/f}$* : *p53$^{f/f}$* mice were crossed to Math1-CreER^{T2}; tdTomato transgenic mice to generate cerebellar granule neuron progenitor (CGNP) specific knockouts of *Mad2l1* and/or *p53*. Mice were conventionally housed, fed ad libitum, and routinely genotyped by PCR.

Timed pregnancies and neonatal oral gavaging of tamoxifen

Timed mattings were performed overnight, with the following morning considered E0.5. Pregnancies were detected by measuring female weight gain at E13.5. Four days after birth (P4), the neonates received 0.6 mg tamoxifen in a total volume of 30 microliters dissolved in peanut oil by oral gavaging. For oral gavaging, a 24-gauge reusable gavaging needle was used, 25 mm of length; round blunted end (1.25mm diameter) (Fine Science tools, 18061-24), supplemented with a 100 ul calibrated Hamilton glass syringe. Offspring were ear-clipped when they reached the age of 7 days and genotyped. All mice were bred in the Central Animal Facility (University Medical Centre Groningen [UMCG], Groningen, The Netherlands) and were kept in conventional housing. Animal protocols were approved by the UMCG Committee on Animal Care (DEC) (DEC-16465-02-002).

Isolation and sorting of Cerebellar Granule Neuron Progenitors

CGNPs were harvested from postnatal days P7, P14-15, and P21-22 tdTomato+ cerebella from offspring Tamoxifen-treated at postnatal day P4. Samples were kept on ice throughout the isolation procedure unless otherwise stated. In short, cerebella were dissected, meninges removed and washed with cold PBS. Cerebella were dissociated into single cells with a papain dissociation kit according to the manufacturer's instructions (Worhtington). Briefly, cerebella were incubated at 37C in papain/DNAse solution, 15min for cerebella younger than 7 days and 20-30 min for 14- and 30-days old cerebella. After incubation, samples were further dissociated by trituration and filter quenched in an ovomucoid solution. Finally, samples younger than 7 days were spun down at 4C and resuspended in FACS buffer-Dapi solution. Cerebella older than 7 days old were further subjected to a percoll gradient to remove surplus of meninges, pelleted and resuspended in FACS buffer-Dapi solution. Tdtomato positive/Dapi negative cells were then sorted on a Beckman Coulter MoFlo Astrios sorter, pelleted and stored at -80C for further experiments.

CGNP RNA isolation, library preparation and RNA-Seq

For detail, see **Materials and Methods** in **Chapter 3** of this thesis.

Gene Ontology

Pathway enrichment analysis was performed by uploading lists of a gene cluster, to the Database for Annotation, Visualization and Integrated Discovery v6.8 (DAVID), and subsequent analysis for gene ontology of biological processes was performed. Lists of biological processes were imported into the Enrichment map application in Cytoscape v3.2.1. Biological processes were Benjamini corrected with a moderately permissive q value of <0.1 and a p-value of <0.01. Enrichment maps represent biological processes enriched in the gene clusters. Each node represents a biological process grouped and labeled by biological theme.

Genomic and RNA PCRs

Isolation of genomic DNA was performed with the QIAamp DNA Micro Kit (Qiagen) or AllPrep DNA/RNA/Protein Micro Kit (Qiagen) when DNA, RNA and proteins were needed from the same sample (Fig 5F-I). For conventional genomic PCR, 20 ng of gDNA was amplified using the primers described in the Table 1 below. Amplified DNA was resolved on 1.5% agarose gel and imaged on a Chemidoc Imaging System. For genomic qPCR, 50pg DNA was amplified using the primers described in the Table 1 below. Thermocycling steps were performed on a LightCycler 480 (Roche) with iTaq universal SYBR green supermix (Bio Rad). For analysis of mRNA expression, mRNA was isolated with AllPrep DNA/RNA/Protein Micro Kit (Qiagen) according to the manufactor's specifications. cDNA was synthetized from 10 ng RNA and amplified using the primers described in Table 2. Thermocycling steps were performed on a CFX96 Connect Real-Time PCR Detection System (Bio Rad) with SsoAdvanced™ universal SYBR green supermix (Bio Rad)

Table 1. Primers for genomic PCRs

Conventional genomic PCR	
Primer name	**Sequence**
Mad2 5'	AGGCTGAGCCGGGCCTTAGGAC
Mad2 3' short	CCCAGTTGAGAATGACATTTGAGAAGG
Mad2 3' end of gene	GCAGACCAAACGAACCTAAGTT
P53 delta optimized del PCR RV	AAGGCTTGGAAGGCTCTAGG
P53 optimized del PCR RV	GGAGGCAGAGACAGTTGGAG
P53 intron 2 FW corrected	GCAAACATGATACCCTTGGT
Quantitative genomic PCR	
Primer name	**Sequence**
gen 5p Qmad2 A F	TTAGGCAGGCATTGGCAGTT
gen 5p Qmad2 A R	CAGGCGTAATGAGCCCTAAG
gen del Qmad2 A F	GTGACTGGCGGTGGTTAGAT
gen del Qmad2 A R	CAGAGCATCAGAACCGTGAA

Table 2. Primers for q RTPCR

q RTPCR	
Primer name	**Sequence**
Trp53 A Fw	GTTATGTGCACGTACTCTCC
Trp53 A Rev	GTCATGTGCTGTGACTTCTTG
Trp53 B Fw	TCCGAAGACTGGATGACTG
Trp53 B Rev	AGATCGTCCATGCAGTGAG
Mad2l1 Fw	AAACTGGTGGTGGTCATCTC
Mad2l1 Rev	TTCTCTACGAACACCTTCCTC

Protein isolation and Western blot

Isolations of proteins was performed with the AllPrep DNA/RNA/Protein Micro Kit (Qiagen) according to the manufacturer's specifications. In short, at the end of the isolation procedure, total protein extracts recovered from the AllPrep protocol were precipitated in acetone at -20C overnight. The pellet was dried at room temperature for 10 min and proteins redissolved in sample buffer. Samples were boiled and loaded on Mini-PROTEAN TGX™ precast gels (Biorad). Proteins were transferred onto a PVDF membrane (Trans-Blot Turbo Transfer System, Biorad), and probed for the following antibodies: anti-Mad2l1 (Rabbit, 1/1000, Cell Signaling 4636), anti-

tdTomato (Rabbit, 1/500, Rockland 600-401-379), anti-H4 (Mouse, 1/1000, Active motif 61521). HRP labelled Goat anti-Mouse or Rabbit secondary antibodies were used to visualize protein expression using chemiluminescence substrate (SuperSignal™ West Dura Extended Duration Substrate, Thermo #34076) on a ChemiDoc imaging system (Biorad). Analysis and densitometry of the protein bands was performed with ImageLab (V5.0) software.

Immunohistochemistry

Mouse brains were kept on ice throughout the dissection procedure. In short, brains were dissected, washed in ice-cold PBS and fixed in 4% paraformaldehyde for either 1H at room temperature (cerebellar slices) or overnight at 4C (entire brains and older animals). Brains and cerebellar slices were cryoprotected with a sucrose gradient, embedded in OCT, snap-frozen on liquid nitrogen and stored at -80C. Seven µm-thick cryosections were generated on a Leica cryostat. After citrate antigen retrieval, brain sections were blocked in 5% normal goat serum and 0.1% Triton and incubated overnight at 4C with the following antibodies: anti-tdTomato (SICGEN, AB0040-200, goat 1:500), anti-PCNA (Abcam, ab29, mouse 1:1000), anti-Histone H3S10-phospho (active motif, 39636, mouse 1:1000), anti-NeuN (abcam, ab104224, mouse 1:1000). Secondary antibodies used were Alexa Fluor 488 (1:500), and Alexa Fluor 568 (1:500) (Invitrogen). Slides were counterstained with DAPI (Sigma), and mounted with Vectashield (Vector Laboratories).

Culturing of primary human medulloblastoma cells

In short, tumor material obtained from biopsy tissue was rinsed with ice cold HBSS in a 10 cm dish kept on ice. Tissue was cut into equal pieces of approximately 3 mm diameter using surgical blades. The tissue pieces were cut for single cell suspension into very small pieces and washed with ice cold HBSS. Dissociating reagent (Accutase) was added to the tissue and incubated for 15 min at 37˚C. Tubes were shaken every few minutes. After trituration, the cell suspension was washed with

basal media (DMEM-F12). One milliliter of Cambridge culture media (DMEM/F-12, glucose (1.5mg/mL), NEAA (100x stock), Antibiotic/antimycotic solution (100x), HEPES (5mM), BSA solution (120 ug/ml), 2-mercaptoethanol (0.05 mM), B27 (x50), N2 (x100)) was added to the cell suspension/pellet and cells were filtered through a 70 µm cell strainer, washed with another 0,5 – 1 ml of culture media, plated and incubated at 37C and maintained in low O_2 (2%).

Single cell Whole Genome Sequencing

The pediatric medulloblastoma samples used for scWGS were obtained following surgical resection at diagnosis. Informed consent was given and local ethics committee approval was granted for use of the patient material. On the day of surgery, a single cell suspension was freshly prepared by trituration of the tumor tissue and subsequent digestion with Accutase (Gibco). For the cultured medulloblastoma, cells where detached from the culture dish with Accutase (Gibco). The cell suspensions from fresh or cultured material were cryopreserved in 10% DMSO. For human samples that were snap-frozen on the day of surgery, single nuclei were isolated prior to the sort using a sucrose gradient ultracentrifugation as described elsewhere[41]. For single nuclei sorting, cells were resuspended in staining buffer (1M tris-HCl pH7.4, 5M NaCl, 1M CaCl2, 1M MgCl2, 7.5% BSA, 10% NP-40, ultra-pure water, 10 mg/ml Hoechst 33358, 2mg/ml propidium iodide), kept on ice in the dark for 15 min to facilitate lysis. G1 single nuclei, as assessed by PI and Hoechst staining were sorted into 96 wells plates on a MoFlo-Astrios flow cytometer (Beckman Coulter). Nuclei were lysed and DNA was barcoded, followed by automated library preparation (Agilent Bravo robot) as described previously[41]. Single cell libraries were pooled and analyzed on an Illumina Hiseq2500 sequencer. Sequencing data were analyzed with the R2-package AneuFinder as previously described[20].

For whole genome single cell sequencing of mouse samples, CGNPs were isolated as previously described. The day of single cell sort, fresh samples were resuspended in Hoechst 33342 staining buffer and G1-Phase tdTomato positive

cells were sorted as single cells in 96 wells plate (Beckman Coulter MoFlow Astrios sorter). Cells were lysed and DNA was barcode labeled followed by library preparation as described previously in an automated fashion (Agilent Bravo robot) [41]. Single cell libraries were pooled and analyzed on an Illumina Hiseq2500 sequencer. Single cell sequencing data was analyzed with the R2-package AneuFinder as previously described[20].

Histopathological analyses

Animals were euthanized and brains were harvested and rinsed in PBS. Tissues collected were fixed overnight in formalin. Fixed tissues were then stored in 70% ethanol until embedded in paraffin. Section slides were prepared and standard H&E staining were performed at The Dutch Molecular Pathology Center (Utrecht).

AUTHORS CONTRIBUTIONS

Conceptualization, I.B., F.F., and S.W.M.B.; Methodology, I.B., M.J.S., I.A., P.L.B., B.B., D.C.J.S., G.J.M.B., N.H., V.G., E.S.J.M.B., F.F., and S.W.M.B.; Software and Formal Analysis, I.B., M.J.S., V.G., B.B. ; Investigation, I.B.; Resources, I.B., M.J.S., I.A., P.L.B., E.W.H.; Data Curation, I.B., V.G., B.B.; Writing, I.B. and S.W.M.B.; Writing – Review and Editing, I.B. and S.W.M.B.; Visualization, I.B.; Supervision and Project Administration, F.F. and S.W.M.B.; Funding Acquisition, I.B., I.A., M.J.S., F.F., and S.W.M.B.

ACKNOWLEDGEMENTS

This study was supported by a De Cock-Hadders foundation grant to I.B.; a De Cock-Hadders foundation grant to M.J.S. ; an Indonesia Endowment Fund for Education (LPDP) doctoral grant (PRJ-2572/LPDP/2015) to I.A; a KWF project grant (2018-RUG-11457) to F.F; a Stichting Kinderoncologie Groningen/SKOG project grant (16-003) to S.B; a Rosalind Franklin fellowship from the University of

Groningen to S.B.; and a Dutch Cancer Society/KWF career award (RUG 2014-6903) to S.B.

CONFLICT OF INTEREST

The authors declare no conflict of interest.

REFERENCES

1. Kastan, M. B. & Bartek, J. Cell-cycle checkpoints and cancer. *Nature* **432**, 316–23 (2004).
2. Musacchio, A. & Salmon, E. D. The spindle-assembly checkpoint in space and time. *Nat. Rev. Mol. Cell Biol.* **8**, 379–93 (2007).
3. Gordon, D. J., Resio, B. & Pellman, D. Causes and consequences of aneuploidy in cancer. *Nat. Rev. Genet.* **13**, 189–203 (2012).
4. Hanahan, D. & Weinberg, R. a. Hallmarks of cancer: the next generation. *Cell* **144**, 646–74 (2011).
5. Manuscript, A. Boveri revisited: Chromosomal instability, aneuploidy and tumorigenesis. **10**, 478–487 (2011).
6. Gröbner, S. N. *et al.* The landscape of genomic alterations across childhood cancers. *Nature* **555**, 321–327 (2018).
7. Udaka, Y. T. & Packer, R. J. Pediatric Brain Tumors. *Neurol. Clin.* **36**, 533–556 (2018).
8. Desandes, E., Guissou, S., Chastagner, P. & Lacour, B. Incidence and survival of children with central nervous system primitive tumors in the French National Registry of Childhood Solid Tumors. *Neuro. Oncol.* **16**, 975–983 (2014).
9. Kool, M. *et al.* Molecular subgroups of medulloblastoma: an international meta-analysis of transcriptome, genetic aberrations, and clinical data of WNT, SHH, Group 3, and Group 4 medulloblastomas. *Acta Neuropathol.* **123**, 473–84 (2012).
10. Cavalli, F. M. G. *et al.* Intertumoral Heterogeneity within Medulloblastoma Subgroups. *Cancer Cell* **31**, 737-754.e6 (2017).
11. Northcott, P. A. *et al.* The whole-genome landscape of medulloblastoma subtypes. (2017). doi:10.1038/nature22973
12. Northcott, P. a. *et al.* Subgroup-specific structural variation across 1,000 medulloblastoma genomes. *Nature* **488**, 49–56 (2012).
13. De Smaele, E. *et al.* Chromosome 17p deletion in human medulloblastoma: A missing checkpoint in the Hedgehog pathway. *Cell Cycle* **3**, 1263–1266 (2004).
14. Menyhárt, O. & Győrffy, B. Principles of tumorigenesis and emerging molecular drivers of SHH-activated medulloblastomas. *Ann. Clin. Transl. Neurol.* **6**, 990–1005 (2019).
15. Rausch, T. *et al.* Genome Sequencing of Pediatric Medulloblastoma Links Catastrophic DNA Rearrangements with TP53 Mutations. **148**, 59–71 (2013).
16. Soto, M. *et al.* p53 Prohibits Propagation of Chromosome Segregation Errors that Produce Structural Report p53 Prohibits Propagation of Chromosome Segregation Errors that Produce Structural Aneuploidies. 2423–2431 (2017). doi:10.1016/j.celrep.2017.05.055
17. Yang, Z. J. *et al.* Medulloblastoma Can Be Initiated by Deletion of Patched in Lineage-Restricted Progenitors or Stem Cells. *Cancer Cell* (2008). doi:10.1016/j.ccr.2008.07.003
18. Oliver, T. G. *et al.* Loss of patched and disruption of granule cell development in a pre-neoplastic stage of medulloblastoma. *Development* **132**, 2425–39 (2005).
19. Hovestadt, V. *et al.* Resolving medulloblastoma cellular architecture by single-cell genomics. *Nature* **572**, 74–79

(2019).

20. Bakker, B. *et al.* Single-cell sequencing reveals karyotype heterogeneity in murine and human malignancies. *Genome Biol.* **17**, 115 (2016).

21. Bakker, B., van den Bos, H., Lansdorp, P. M. & Foijer, F. How to count chromosomes in a cell: An overview of current and novel technologies. *BioEssays* **37**, 570–577 (2015).

22. Machold, R., Klein, C. & Fishell, G. Genes expressed in Atoh1 neuronal lineages arising from the r1/isthmus rhombic lip. *Gene Expr. Patterns* **11**, 349–359 (2011).

23. Kool, M. *et al.* Genome sequencing of SHH medulloblastoma predicts genotype-related response to smoothened inhibition. *Cancer Cell* **25**, 393–405 (2014).

24. Carter, S. L., Eklund, A. C., Kohane, I. S., Harris, L. N. & Szallasi, Z. A signature of chromosomal instability inferred from gene expression profiles predicts clinical outcome in multiple human cancers. *Nat. Genet.* **38**, 1043–1048 (2006).

25. Simon, J. E., Bakker, B. & Foijer, F. CINcere Modelling: What Have Mouse Models for Chromosome Instability Taught Us? *Recent Results Cancer Res.* **200**, 39–60 (2015).

26. Leto, K. *et al.* Consensus Paper: Cerebellar Development. *Cerebellum* **15**, 789–828 (2016).

27. Lewis, P. M., Gritli-Linde, A., Smeyne, R., Kottmann, A. & McMahon, A. P. Sonic hedgehog signaling is required for expansion of granule neuron precursors and patterning of the mouse cerebellum. *Dev. Biol.* **270**, 393–410 (2004).

28. Wechsler-Reya, R. J. & Scott, M. P. Control of neuronal precursor proliferation in the cerebellum by Sonic Hedgehog. *Neuron* **22**, 103–14 (1999).

29. Foijer, F. *et al.* Spindle checkpoint deficiency is tolerated by murine epidermal cells but not hair follicle stem cells. *Proc. Natl. Acad. Sci. U. S. A.* **110**, 2928–2933 (2013).

30. Foijer, F. *et al.* Deletion of the MAD2L1 spindle assembly checkpoint gene is tolerated in mouse models of acute T-cell lymphoma and hepatocellular carcinoma. *Elife* **6**, 1–22 (2017).

31. Jonkers, J. *et al.* Synergistic tumor suppressor activity of BRCA2 and p53 in a conditional mouse model for breast cancer. *Nat. Genet.* **29**, 418–425 (2001).

32. Gogendeau, D. *et al.* Aneuploidy causes premature differentiation of neural and intestinal stem cells. *Nat. Commun.* **6**, 1–15 (2015).

33. Legue, E., Riedel, E. & Joyner, A. L. Clonal analysis reveals granule cell behaviors and compartmentalization that determine the folded morphology of the cerebellum. *Development* (2015). doi:10.1242/dev.120287

34. Ivanov, D. P., Coyle, B., Walker, D. A. & Grabowska, A. M. In vitro models of medulloblastoma: Choosing the right tool for the job. *J. Biotechnol.* **236**, 10–25 (2016).

35. Roussel, M. F. & Stripay, J. L. Modeling pediatric medulloblastoma. *Brain Pathol.* **30**, 703–712 (2020).

36. Lang, P. Y. *et al.* ATR maintains chromosomal integrity during postnatal cerebellar neurogenesis and is required for medulloblastoma formation. *Development* **143**, 4038–4052 (2016).

37. Williams, S. E. *et al.* Aspm sustains postnatal cerebellar neurogenesis and medulloblastoma growth in mice. *Development* **142**, 3921–3932 (2015).

38. Mckinnon, P. J. Maintaining genome stability in the nervous system. *Nat. Neurosci.* **16**, 1523–1529 (2013).

39. Orii, K. E., Lee, Y., Kondo, N. & McKinnon, P. J. Selective utilization of nonhomologous end-joining and homologous recombination DNA repair pathways during nervous system development. *Proc. Natl. Acad. Sci. U. S. A.* **103**, 10017–22 (2006).

40. Dobles, M., Liberal, V., Scott, M. L., Benezra, R. & Sorger, P. K. Chromosome missegregation and apoptosis in mice lacking the mitotic checkpoint protein Mad2. *Cell* **101**, 635–645 (2000).

41. van den Bos, H. *et al.* Single-cell whole genome sequencing reveals no evidence for common aneuploidy in normal and Alzheimer's disease neurons. *Genome Biol.* **17**, 116 (2016).

SUPPLEMENTARY FIGURES

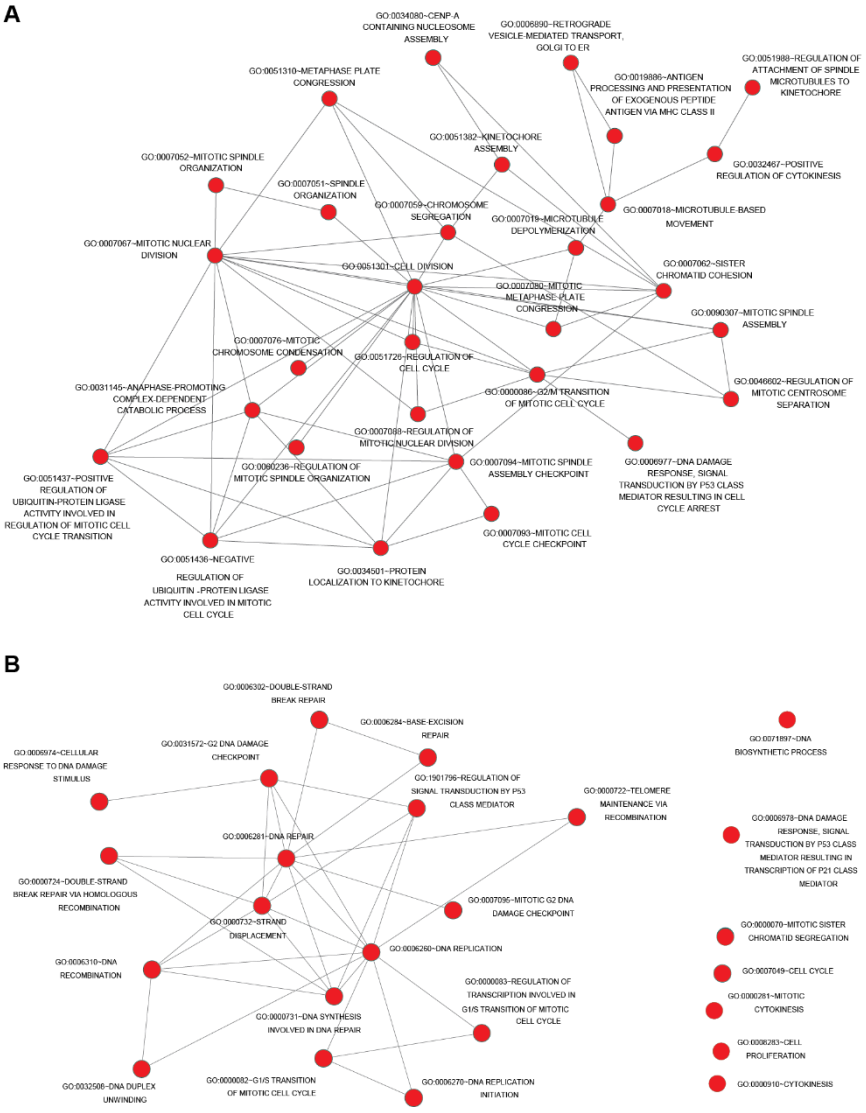

Supplemental Figure 1. Enrichment map representing biological processes that predominate in the 114 common genes between the pink cross-species cluster and the orange CGNP cluster. (A) Represents the mitotic cluster and **(B)** represents the DNA synthesis/DNA repair cluster. Each node represents a biological process. Biological processes connected by edges have proteins in common, enriched biological processes were determined with the Database of Annotation, Visualization and Integrated Discovery (DAVID), v.6.8 (Benjamini corrected q = 0,1 ; p = 0,01) and visualized with the enrichment map application in Cytoscape.

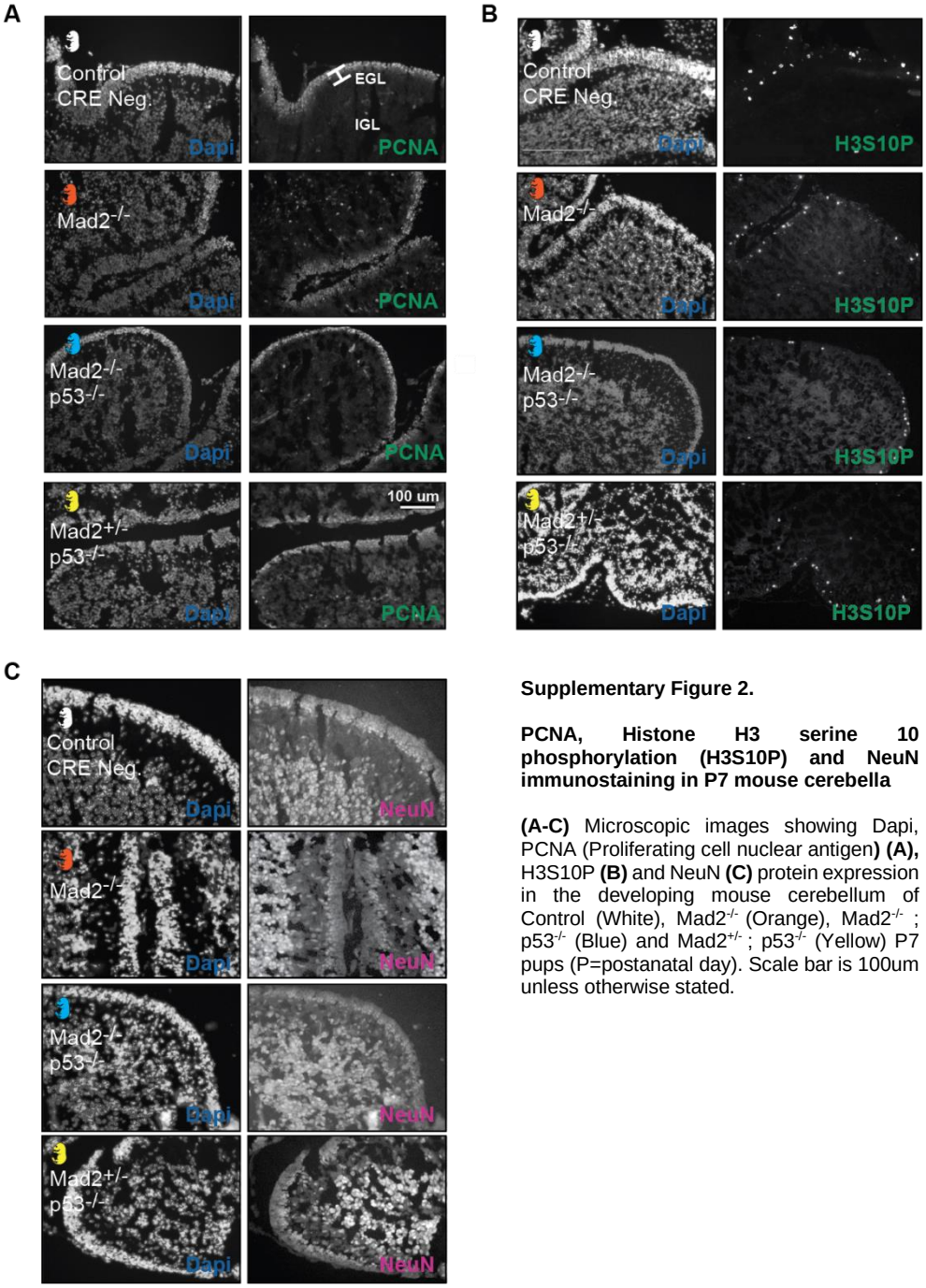

Supplementary Figure 2.

PCNA, Histone H3 serine 10 phosphorylation (H3S10P) and NeuN immunostaining in P7 mouse cerebella

(A-C) Microscopic images showing Dapi, PCNA (Proliferating cell nuclear antigen**) (A),** H3S10P **(B)** and NeuN **(C)** protein expression in the developing mouse cerebellum of Control (White), Mad2$^{-/-}$ (Orange), Mad2$^{-/-}$; p53$^{-/-}$ (Blue) and Mad2$^{+/-}$; p53$^{-/-}$ (Yellow) P7 pups (P=postanatal day). Scale bar is 100um unless otherwise stated.

Pediatric high-grade glioma
&
cell-of-origin

5

In quest of the pontine glioma cell-of-origin

Irena Bočkaj [1,2], Nynke Vellinga [1] & Sophia W. M. Bruggeman [1,2]

[1] Departments of Pediatric Oncology and Hematology/Pediatrics, UMCG, the Netherlands
[2] Department of Ageing Biology/ERIBA, UMCG, the Netherlands (present address)

ABSTRACT

Of all childhood cancers, brain tumors account for more than 20% of malignancies and remain the primary cause of death in children. The past decades have seen an improvement in the diagnosis and treatment of most childhood brain tumors; however some subtypes fail to follow this trend. Among them is pontine glioma, or DIPG, a rare type of brainstem glioma defined by its very dismal prognosis of approximately 9 months and survival rate below 1%. In 2012, the discovery of a driver mutation on histone H3 variants (H3.1/3.3-K27M mutation in DIPG) paved the way towards a better understanding of the disease. DIPG's narrow occurrence peaking between 6-9 years of age, and the prevalence of H3.3 mutations suggests a temporal window in the development of the pons where the H3.3 variant is specifically required, and therefore more prone to oncogenic events.

In this study, we aimed at identifying the developmental time point at which the putative cell-of-origin is prone to undergo such mutations. To this purpose, we first mapped the histone usage landscape across the neonatal and early postnatal mouse hindbrain. We uncovered the pons to preferentially make use of the histone variant H3.3 in early neonatal time points. Subsequent isolation and culture of the corresponding pontine neural stem cells showed maintenance of this histone usage phenotype *in vitro;* as well as retainment of pontine positional markers and SHH responsiveness described by others.

Altogether, our data demonstrate differential histone H3 variant usage in the developing hindbrain and show for the first time that mouse pontine neural stem cells can be cultured *in vitro.* Importantly, these neural stem cells retain their original core transcriptional and behavioral characteristics. This makes neonatal pontine neural stem cells a promising tool to model DIPG initiation *in vitro*.

INTRODUCTION

In the past eight years, huge efforts to unfold the genomic landscape of all childhood brain cancers revealed a far more complex collection of diseases than previously appreciated[1–4]. For instance, only within the subgroup of high-grade gliomas (HGG), six molecularly and epigenetically distinct entities have been identified[3]. Pediatric HGG are now considered a collection of different diseases rather than variations of a single type. Each subtype is defined by unique recurrent oncogenic drivers, clinical characteristics and specific neuroanatomical localizations, raising the hypothesis of a multiplicity of cells-of-origin for pediatric HGGs[3].

In 2012, the key discovery of a novel oncogenic mutation in histone genes in a striking 50% of pediatric HGG imposed a re-evaluation of disease classification with addition of the entity to the 2016 WHO classification[3,5–9]. This K27M mutation (which substitutes the lysine 27 by a methionine on the histone H3 tail) is the first reported histone mutation associated with human cancers. Since then, multiple histone (H3) mutations have been identified, all somatic, heterozygous and mutually exclusive[3,10]. The K27M substitution is the most frequent histone H3 mutation (85% of histone mutant gliomas). Albeit affecting all histone H3 variants, it is predominantly found on the histone H3.3 variant. The substitution of Glycine 34 by a Valine or Arginine (G34R/V) has only been described in histone variant H3.3 and accounts for 8% of pediatric HGG[3].

Interestingly, the different histone mutations correlate strongly with anatomical localizations of the tumors. G34 mutant gliomas are selectively hemispheric and affect older children. K27M gliomas arise mostly in the midline/brainstem region of the brain (thalamus, pons or medulla) and are found in younger patients [3]. Within the K27M subgroup, H3.1-K27M is localized only in the ventral pons, whereas H3.3-K27M mutations may be found all along the midline. Gliomas of the pons, also known as Diffuse Intrinsic Pontine Gliomas (DIPG) represent 80% of midline gliomas.

Within the DIPG subgroup, 78% will harbor a K27M histone mutation. Three out of four will affect histone variant H3.3[8,11–13]. Interestingly, the age of diagnosis

can be further split depending on the histone variant affected: H3.1-K27M is found in younger children than H3.3-K27M (mean age of 5.1 years and 7.4 years respectively), suggesting both subtypes originate from a different pontine precursor[9]. Moreover, the age and location-specific nature of DIPG indicates that the underlying pathogenesis involves dysregulated developmental processes. It is therefore clear that increasing our knowledge of the development of the pons will enlarge our understanding of this devastating disease. Thus, approaching DIPG pathobiology from the angle of neural stem cell biology might shed light on many unanswered questions. In addition, it is essential to identify the cell-of-origin for the different DIPG subtypes. Due to the scarcity of healthy human brainstem tissue available to study how DIPG initiation relates to brainstem development, cortical neuroepithelial cells have been used to model the pathways of DIPG oncogenic initiation[14,15]. However, it is now known that stem cells derived from different brain areas differ substantially at the transcriptomic level and therefore might not respond similarly to the same oncogenic drivers, thus questioning if the real DIPG cell-of-origin would respond similarly to oncohistone transformation[16,17].

Interestingly, a postnatal population of progenitor cells was found in the human and mouse pons and has been proposed as a putative cell-of-origin for DIPG[17,18]. Monje *et al*. showed that its temporal and spatial distribution correlates with DIPG incidence in childhood[19]. This finding was later confirmed in another publication[20]. Those two studies reveal a high proliferative spurt of the neural progenitor lineage which leads to an important expansion of the pontine region, peaking at postnatal day 4 (P4) in mice[20]. These studies suggest a postnatal transformation of a pontine precursor cell. However, it remains unclear why postnatal pontine progenitors would be particularly sensitive to histone mutations, and why they predominantly select for histone variant H3.3.

We propose that over the course of postnatal pontine development, histone H3.3 usage differs. Pontine progenitor cells may exhibit increased addiction to histone H3.3 variant at a certain time point of postnatal development. Therefore, this precursor lineage would exhibit greater sensitivity to H3.3 oncohistone dependent transformation. To address this, in this study we assessed histone H3 variants usage

during postnatal brainstem development in mice. We compared histone variant expression in the neonatal midbrain, medulla, pons and cerebellum. We uncovered that all brain regions do not make use of the same histone H3 variants pool over the course of postnatal development. We observed a higher usage of H3.3 variant in neonatal mouse pons compared to cerebellum, a phenotype maintained in cultured pons neural stem cells. Further, we were able to isolate the putative cell-of-origin for DIPG and show that it retained its brain patterning in an *in vitro* setting. This establishes neonatal pons neural stem cells as a promising tool to further model and therefore possibly unravel the molecular pathogenesis underlying DIPG initiation.

RESULTS

Expression of histone H3 genes in mouse postnatal brainstem and cerebellum

To unravel why a given histone H3 variant would be mutated in a specific brain area, we looked at the usage of histone H3 variants in the developing mouse brain at the transcript and protein levels. Hereto, we isolated postnatal mouse brains ranging from postnatal day 2 (P2) to adulthood, including postnatal days 7 and 14 (P7 and P14, respectively). Samples were subjected to mRNA isolation as well as histone extraction in order to draw a histone usage landscape throughout the brainstem and cerebellar postnatal development (Fig 1A). First, we sought to define histone usage at the transcript level. We performed quantitative reverse PCR of histone variant genes to assess gene expression at different postnatal time points. Non-canonical histone H3.3 is encoded by two independent genes, *H3f3a* (Chromosome 1) and *H3f3b* (Chromosome 11), whereas canonical histones H3.1 and H3.2 are each encoded by one cluster of 10 (Chromosome 13) and 3 (Chromosome 3) genes, respectively[21]. We assessed the contribution of *H3f3a* and *H3f3b* genes to H3.3 histone expression separately, whereas canonical histone H3.1 and H3.2 expressions were detected simultaneously due to primers recognizing the conserved region of the H3.1/H3.2 gene cluster[22]. We were therefore able to draw *H3f3a*, *H3f3b* and canonical histone gene expression in the postnatal brainstem and cerebellum (Fig 1B). Interestingly, we could separate the midbrain and medulla from the pons and cerebellum by postnatal histone gene expression patterns. Whereas histone gene expression did not vary over postnatal development in the midbrain and medulla, the pontine region and the cerebellum seem to be in the midst of chromatin remodeling at the nucleosomal level (Fig 1B and 1C). We could further differentiate cerebellar and pontine patterns in terms of early postnatal histone usage: at early time points, cerebellum seemed to require more of the canonical replication dependent histones H3.1 and H3.2, while the pons used the H3.3 variant in majority and steadily from P2 to P14 (Fig 1C).

Next, we sought to validate key time points in the developing cerebellum and pons at the protein level. We performed histone acid extractions on cerebellar and

pontine samples at P4, P7 and P14 (Fig 1D and 1E). Normalization of H3.3 content to histone H4 enabled to quantify H3.3 nucleosomal content over development (Fig 1E). Western blot analysis revealed a pattern of H3.3 protein usage similar to the gene expression data (Fig 1B). In the mouse pons, H3.3 nucleosomal usage was higher compared to cerebellum and peaked at P7 (Fig 1E).

Altogether, these data provide a first observation as to why histone H3.3 mutations might occur preferentially in pontine precursor cells. These data also provide us with a deeper information on a putative time point where we would be more likely to isolate the DIPG cell-of-origin in mice.

Figure 1. Histone H3 variants show age dependent and regional specific expression profiles *(Figure on next page)*

(A) Schematic overview of the experimental workflow. Mouse midbrain, pons, medulla and cerebellum were dissected at different time points between P2 and Adult. Histone proteins and RNA were isolated and processed for further experiments to determine histone variant usage during brain development. **(B)** Histone variants gene expressions as function of time. Both H3f3a (upper panel) and H3f3b (middle panel) genes encode the histone variant H3.3. One set of primers was used to assess H3.1 and H3.2 (referred to as canonical histone H3 variants) gene expression. Colors depict the various regions of the brain (Green: midbrain; Blue: pons; Pink: medulla; Orange: cerebellum). **(C)** Graph showing the histone variant gene usage as of total histone H3 pool. Data are represented per time point. **D-E** Validation of the gene expression data at the protein level. **(D)** Western blot analysis of histone extracts at three developmental time points in cerebellar and pontine regions. **(E)** Densitometry quantification from panel (D) of the protein levels of H3.3 in cerebellum and pons at P4, P7 and P14.

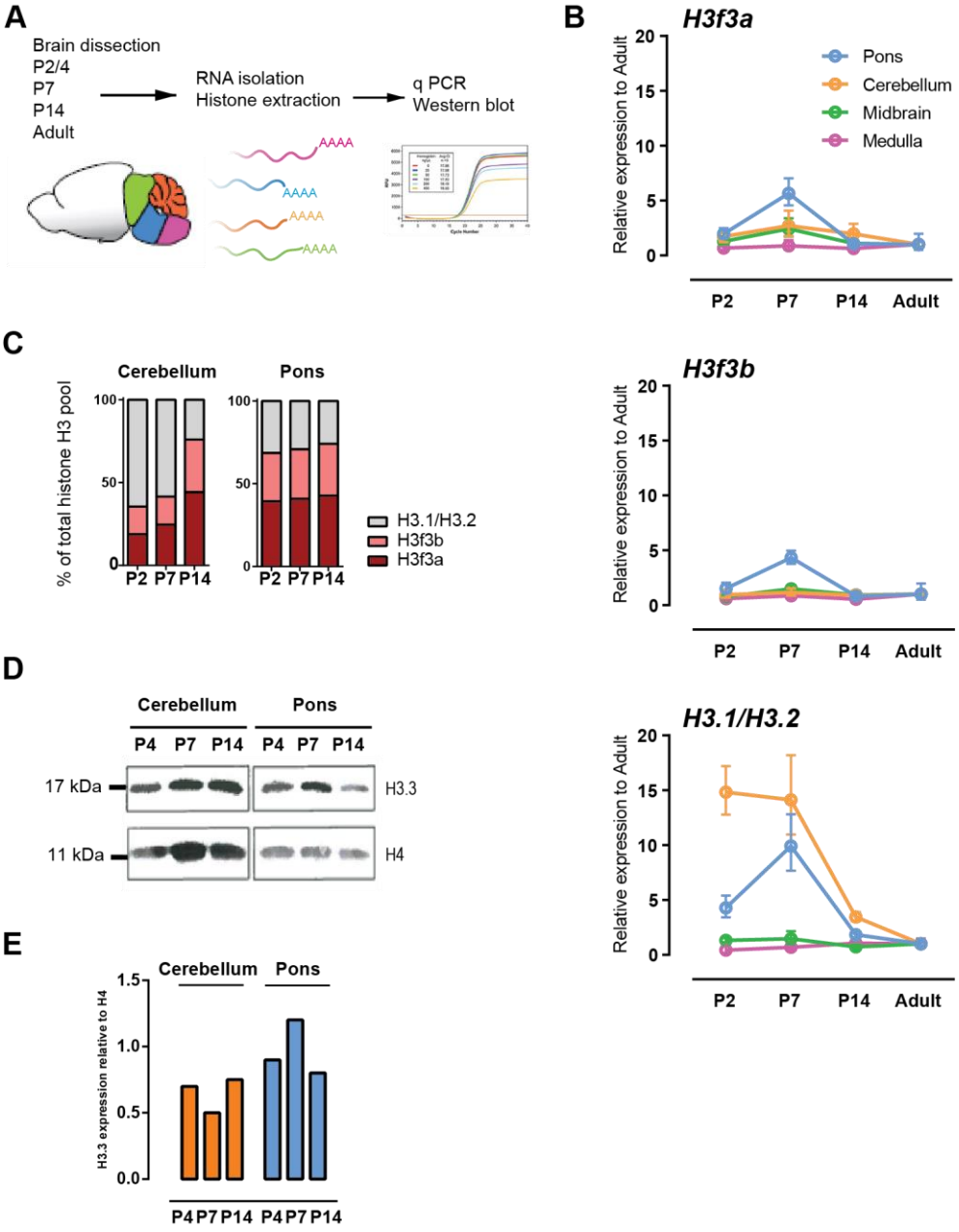

Figure 1. Histone H3 variants show age dependent and regional specific expression profiles *(Legend on previous page)*

Neonatal pons neural stem cells can be cultured in vitro, are SHH responsive and sensitive to SHH pathway inhibition.

Next, we wanted to isolate the putative DIPG cell-of-origin for further characterization. We dissected the pontine region of neonatal mice aged P2, as well as P14, to look at age-related differences in pontine neural stem cells (pNSCs) behavior (Fig 2A). Cultured DIPG tumor cells have been studied for some time, and shown to be SHH responsive and sensitive to PDGFRα signalling[19]. Therefore, we looked at SHH responsiveness in pNSCs and investigated if this response could be modulated over time. We established cultures of pNSCs with varying culture conditions including the standard growth factors (EGF and bFGF) supplemented with PDGF-AB or SHH, or both agonists together (Fig 2B). Surprisingly, while P14 pNSCs did not show neurosphere growth over time regardless of the growth factors used, neonatal NSCs clearly showed an increase in NSC expansion with the addition of SHH as assessed by the size of the neurospheres (Fig 2B, panel three). To a milder extent, addition of PDGF-AB also led to improved neurosphere growth (Fig 2B, panel two). To test the functionality of the SHH signaling pathway, we modulated the SHH response using different concentrations of the SHH ligand and looked at SHH pathway activation at the mRNA level. When secreted SHH ligand binds to its transmembrane receptor Patched-1, it alleviates its inhibition of Smoothened and activates the transcription of pro-proliferative genes such as *Mycn* and *Gli1*. This also triggers a negative feedback loop via overexpression of Patched-1[23–26]. We could observe a threshold activation from 0.75 ug SHH where *Gli1* expression started to rise. However, the threshold for *Mycn* and *Patched-1* expression required twice as much ligand as we observed an increase in expression only with 1.5 ug SHH ligand (Fig 2C). Next, we tested if SHH pathway activation could be antagonized by a selective inhibitor of the pathway, Cyclopamine-KAAD. Cyclopamine acts by inhibition of transmembrane receptor smoothened, which precludes the activation of the downstream transcription of pro-proliferative genes[27]. Treatment of neonatal pNSCs with Cyclopamine in addition of SHH for 24 hrs reduced the transcription of *Mycn*, *Gli1* and *Patched-1* (Fig 2D). Thus, we observe a cyclopamine-dependent antagonizing activity of the SHH pathway (Fig 2D). This

result validates the functionality of the SHH pathway in murine neonatal pNSCs. Subsequently, we compared pathway activation of P2 pNSCs to their older counterparts (P14) (Fig 2E). We observed a stronger response to SHH stimulation in P2 pNSCs, corroborating our first observation on neurosphere expansion in Fig 2B. Altogether, these results demonstrate an intrinsic ability to respond to SHH stimulation in early neonatal pNSCs (Fig 2D). A SHH-responsiveness that seems to be lost as these progenitors age (Fig 2B and 2E).

Figure 2. Neonatal pons neural stem cells (NSC) can be cultured *in vitro*, are SHH responsive, sensitive to SHH pathway inhibition and maintain their histone H3 usage landscape *in vitro* *(Figure on next page)*

(A) Schematic overview of the experimental workflow. Mouse pons was dissected at P2 and P14 and neural stem cells were isolated and cultured *in vitro* as neurospheres. Panel **(B)** shows pictures of cultured P2 and P14 pons NSCs in four different culture conditions (EGF=Epidermal Growth Factor; bFGF=basic Fibroblast Growth Factor; PDGF-AB=Platelet Derived Growth Factor AB; SHH=Sonic Hedgehog). **(C)** Characterization of the response levels after SHH stimulation in pons P2 NSCs by quantitative RT-PCR. **(D)** Quantification of the response to SHH pathway inhibition by Cyclopamine in neonatal pons NSC by expression of specific SHH target genes. **(E)** Characterization of the P14 pons NSCs response to SHH stimulation compared to neonatal P2 pons NSCs. **(F)** Schematic overview of the experimental workflow. Mouse neural stem cells were isolated form the pontine and subventricular regions (forebrain) and cultured *in vitro.* **(G)** Gene expression of the histone H3 variants genes was assessed in cultured pons and SVZ NSCs by quantitative RT-PCR. This graph shows the histone variant genes usage as of total histone H3 pool. Data are represented per time point.

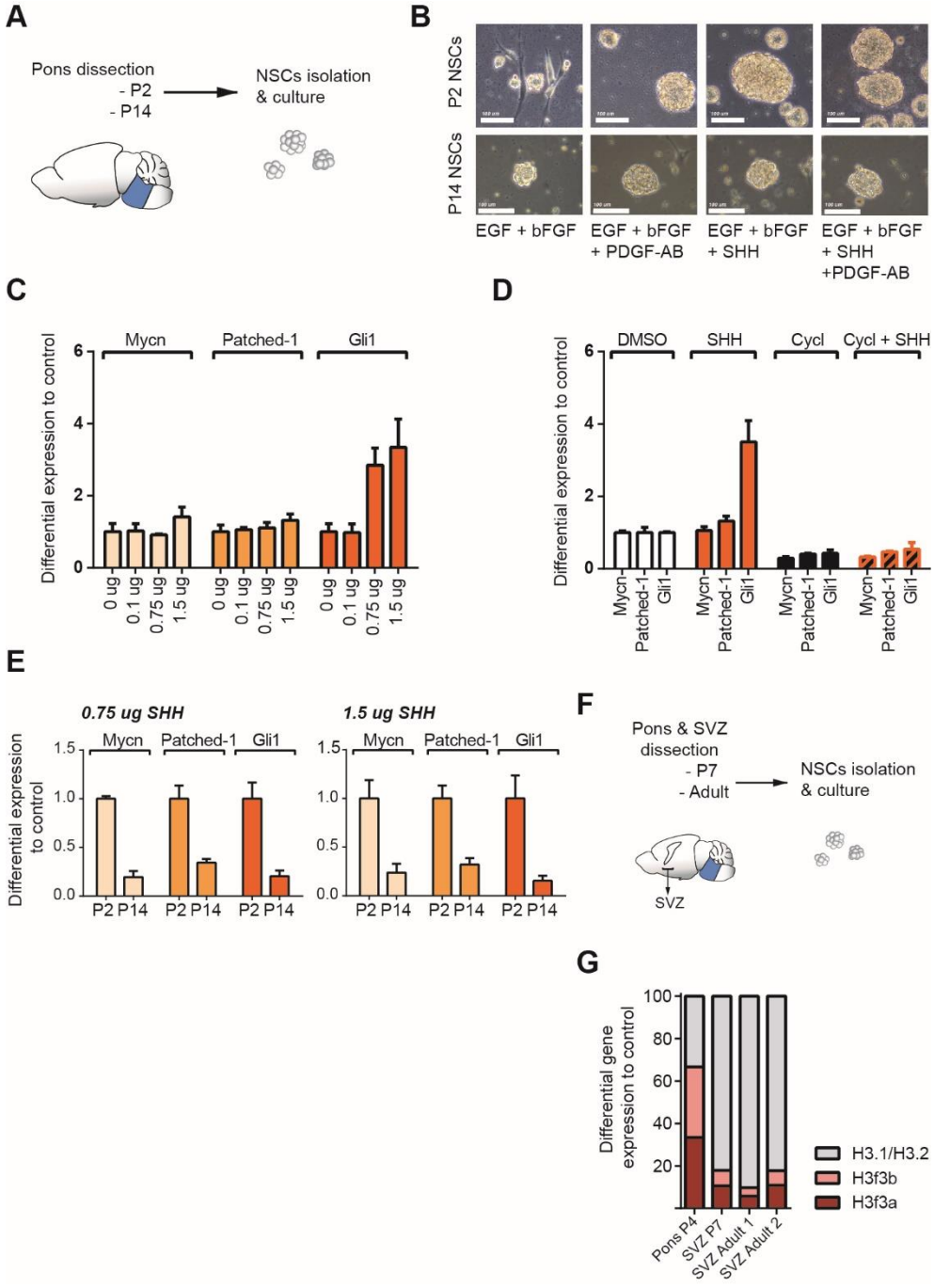

Figure 2. Neonatal pons neural stem cells (NSC) can be cultured *in vitro*, are SHH responsive, sensitive to SHH pathway inhibition and maintain their histone H3 usage landscape *in vitro* *(Legend on previous page)*

Neonatal pons neural stem cells maintain their histone H3 landscape and positional identity in culture

To further characterize pNSCs as a tool to model DIPG *in vitro*, we looked at the maintenance of their *in vivo* characteristics under cell culture conditions. To this end, we first looked at histone variant usage at the level of gene expression in comparison to subventricular zone (SVZ) NSCs, neonatal and adult (Fig 2F). Interestingly, pNSCs maintained the same ratios of histone variant usage observed in the pons tissue (Fig 2G and Fig 1C). Furthermore, neonatal and adult SVZ NSCs had similar ratios with a higher usage of canonical histones H3.1 and H3.2 (Fig 2G).

Because it is known that *in vitro* culturing of NSCs tends to induce a shift in positional identity towards a forebrain pattern, we sought to test how pNSCs behave in *in vitro* settings in terms of maintenance of positional/regional identity[28]. We again isolated subventricular and pontine NSCs from a postnatal day P4 mouse brain and cultured them under the same culture conditions including EGF and bFGF growth factors (Fig 3A). We made use of the Allen Brain Atlas repository to find regional markers for the pons and forebrain in postnatal mouse brain (Fig 3B). We identified Pax6 as a forebrain marker, Pax3 as a pre-pontine marker and Irx2 as a pontine marker (Fig 3B). To validate these candidates in our developmental time points of interest, we looked at tissue sections of postnatal P4 mouse brains (Allen Brain Atlas), which confirmed the regional specificity of Pax6 in the forebrain, Pax3 in the pre-pontine region and Irx2 in the basal pons (indicated by arrow-heads) (Fig 3C). Finally, to profile the lineage specificity of the cultured pNSCs, we performed quantitative reverse PCR for Pax6, Pax3 and Irx2 and compared their expression to SVZ NSCs. In agreement with *in situ* expression, we observed low Pax6 expression in pNSCs compared to SVZ NSCs, with increased Pax3 and strong Irx2 expression confirming the maintenance of a pontine positional identity in our candidate NSCs (Fig 3D).

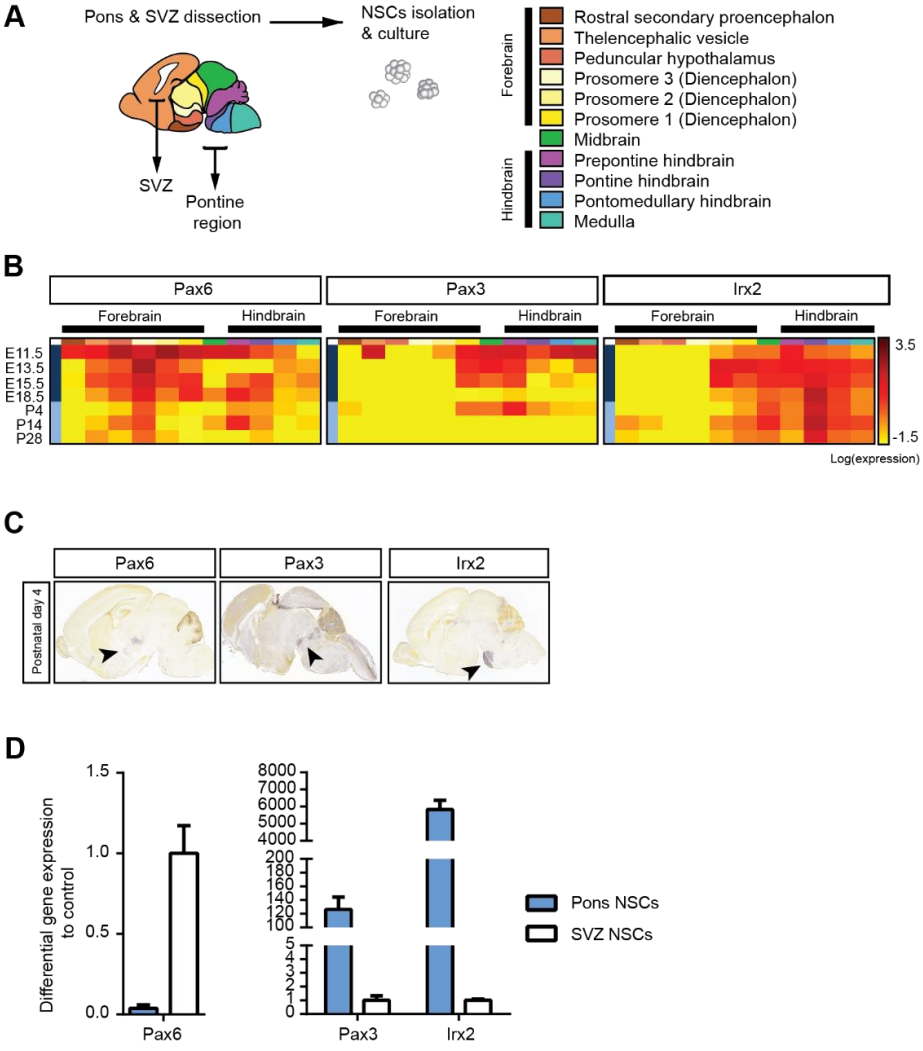

Figure 3. Pons Neural stem cells maintain their positional identity *in vitro*
(A) Schematic overview of the experimental workflow. The mouse brain image depicts the conventional regionalization scheme of a neonatal mouse brain (adapted from the Allen brain database). Every colored region is named as specified in the legend. Mouse neural stem cells were isolated form the pontine and subventricular regions (forebrain) and cultured *in vitro*. **(B)** Heatmap depicting the gene expression profiles of three regional markers: Pax6 (forebrain), Pax3 (pre-pontine region) and Irx2 (pontine region) as a function of age in mice (from embryonic day E11.5 to postnatal day P28) (yellow represents low expression and red represents high expression) (extracted and adapted from the Allen Brain Atlas). **(C)** RNA in situ hybridization images from the Allen brain atlas showing the regional specificity of the three markers Pax6, Pax3 and Irx2 in neonatal mouse brain (P4). Arrows indicate positive areas. **(D)** Gene expression of the regional markers Pax6, Pax3 and Irx2 were assessed in cultured pons and SVZ NSCs by quantitative RT-PCR.

DISCUSSION

In this study, we show that each brain region exhibits a unique histone usage landscape that varies over developmental time, which could explain the different neuroanatomical susceptibility to oncohistones. We were also able to isolate and culture a candidate cell-of-origin for DIPG, a pontine neural stem cell derived from early postnatal mouse pons. We showed that these stem/progenitor cells retain both their histone H3 variant expression pattern and their positional identity *in vitro*, suggesting that they also retain other pons-specific characteristics. Thus, these cells are a promising tool to study oncohistone driven transformation.

Pronounced postnatal growth of the pons

It is conceivable that oncogenic transformation is most likely to occur in (rapid) proliferating cells. Since proliferation takes place in waves in the developing brain and becomes increasingly rare in maturing brain, it is important to assess proliferation patterns in the developing hindbrain/midline. Therefore, a better understanding of the brain midline and pons development is crucial to unravel oncohistone driven DIPG initiation. Developmental studies in human pons samples have shown a continuous growth of the pons during childhood. As the number of proliferative cells began to decline already after birth (7 months) with only a small proliferative fraction remnant throughout childhood, the authors attributed the volumetric expansion of the ventral pons mostly to its extreme myelination process[18]. On the contrary, Monje *et al.* identified a stem population (Nestin^{+}) in the ventral pons with a characteristic bimodal proliferation pattern peaking first at birth and again at 6-8 years of age. The second proliferative wave strikingly mirrors the incidence age-peak of DIPGs[19].

Another parallel study in mice showed a peak of proliferation between P0-P4 that preceded the myelination phase, confirming the idea of Monje *et al*. that proliferating progenitors continue to divide postnatally. They also appointed the pons as the most proliferative region in the brainstem before the midbrain and medulla, however below the cerebellum[20]. This has been confirmed in human midbrain but not medullar samples[18,19]. Interestingly, the existence of a pontine progenitor

proliferating prior to myelination correlates with the histone usage data we generated in this study. The above described proliferative peak correlates with that of the histone usage in the pons[20]. Indeed, we were able to see increased histone usage at the transcriptional level in the pons compared to midbrain and medulla at neonatal stages in mice (Fig 1). Thus, it is likely that the increased histone usage is connected to the progenitor pool expansion as DNA replication and histone synthesis, displacement and exchange are associated processes[29]. Indeed, increased histone usage might be a proliferation dependent effect where the cerebellum and pons experience a major wave of growth postnatally and therefore the chromatin would shape accordingly. Thus, one would expect a preferential usage of the replicative dependent histone variants H3.1 and H3.2 over the replication independent histone variant H3.3, as seen in the developing cerebellum where when proliferation ceases (after P7), replication independent histone variant H3.3 accumulates (Fig 1C). However, despite a similar expansion course, the pons seems to use more of the H3.3 variant also during the intense replication phase (Fig 1C), which might point towards a specific role of H3.3 during proliferation in these pontine progenitors, which might be transcriptional or structural. In this regard, high proliferation in the developing brain has been linked to increased endogenous DNA damage[30,31]. In consequence, adaptive DNA damage responses have been described in the developing brain[32]. In this context, histone variants are the sites and platform for these chromatin-based processes of DNA damage repair[33]. Various roles have been attributed to the histone H3 variants, and H3.3 seems to have a preponderant function in the DNA damage response. Indeed, beyond its role in chromatin architecture and its described role in mammalian development[34,35], H3.3 is also an important player in the maintenance of genome integrity by participating in non-homologous end-joining (NHEJ), homologous recombination (HR) and UVC-DNA damage repair [22,36–40]. From our understanding, during pontine development H3.3 might be specifically required during this high neuronal proliferative spurt. This enables to maintain the genome in check and better protect and prime chromatin to respond in case of endogenous DNA damage.

Last but not least, because the lysine 27 (K27) residue on the histone N terminal tail is selectively mutated in DIPG, it remains unanswered what particular role this histone residue has in the DNA damage response and how its mutation affects these maintenance pathways. Beyond its role in regulation of gene expression, diverse lines of evidence have begun to shed light on a putative role in DNA damage repair[38,41,42]. Further deciphering these mechanisms will help understand how DIPG may form and importantly pave the way towards the identification of new actionable therapeutic targets.

Towards a more accurate identification of a DIPG cell-of-origin

Developmental studies of the pons revealed two distinct pontine regions -- the tegmentum (dorsal pons) and the basis pontis (ventral pons) -- both exhibiting different courses of expansion over time[18–20,43]. It is also believed that dorsal and ventral pons are populated by two distinct neural stem cell populations[19]. Hence, potential candidate cells-of-origin for gliomas located in the pons (DIPG), H3.1 or H3.3 mutated, include precursor cells of the ventral pons (Nestin+/Vimentin+/Olig2+) or precursor cells lining the wall of the fourth ventricle (Nestin+/ Pax3+)[19,44].

Because DIPG are often located at the ventral side of the pons, one might postulate that ventral neural stem cells would be preferentially at the root of DIPG initiation. Hence, an important caveat to our model is that we isolated the entire pontine region including a mixture of dorsal and ventral progenitors. This might hamper accurate characterization of the DIPG cell-of-origin. Indeed, single cell sequencing of human and mouse pons revealed almost two-hundred different cell types present throughout embryonic/neonatal pontine development[17]. Nonetheless, some of the data we provide correlate with previous findings: namely the SHH-responsive phenotype we observe in Figure 2 has also been described by Monje *et al.* in DIPG cancer stem cells [19]. Furthermore, previous findings in several transcriptome studies -- bulk and at the single cell level -- identified the transcription factors Pax3 and Irx2 to be overexpressed in H3.3K27M gliomas specifically, suggesting conserved transcriptional programs, which we also found enriched in our candidate cell-of-origin (Fig 3)[17,45]. Conversely, a low expression of Pax6 was

observed in H3.3K27M HGGs compared to other tumor types, and we also find this in our pNSCs[17]. Interestingly, during embryonic development Pax3 is expressed throughout the entire brainstem correlating with the localization of H3.3K27M all along the midline with a second wave of expression occurring postnatally in the pontine region only (Fig 3B)[46], making an interesting connection between Pax3+ pontine progenitor, DIPG incidence and H3.3 histone usage that warrants further investigation. Furthermore, RNA-seq data found H3.1K27M DIPGs to be enriched within the group of low-expressing Pax3 tumors, further reflecting a separate origin from the H3.3 mutated counterpart[46]. H3.1K27M DIPGs might therefore originate from the ventral pontine progenitors Nestin+/Vimentin+/Olig2+[19]. Altogether, this might suggest the embryonic Pax3+ counterpart as a more plausible candidate cell-of-origin for H3.3 mutant DIPGs. Thus, our isolated progenitors seem to share core behavioral and transcriptional programs with DIPG cells making them a promising tool to study the origins of this malignancy.

It is important to note that, even though most research on the DIPG cell-of-origin focuses on the postnatal pons, an earlier origin should be considered as well. For instance, a recent *in vivo* study from Pathania *et al.* showed that only embryonic (and not postnatal) pontine progenitors were vulnerable to oncohistone driven transformation when H3.3K27M was introduced[47]. Therefore, it remains plausible that DIPG originates from the transformation of an embryonic neural progenitor cell. Therefore, it is interesting to pursue this work on embryonic pontine progenitors, also suggested by a study by Sun *et al.* Indeed, the authors describe the isolation of hindbrain progenitor from human fetuses providing the community with a novel tool for *in vitro* modelling of DIPG[48].

Conclusion

Altogether, our study raises the need for a more thorough study of pons development. This will considerably help understand what core processes underly oncohistone-driven DIPG initiation. Developmental biologists have already suggested that a change in the nomenclature of the brainstem might be required – from an anatomical based nomenclature to a gene expression based – with the aim

of better understanding the genetic programs of this brain region and their relationship to the co-related malignancies[49].

With a deeper understanding of key developmental and tumorigenic processes, which are highly intertwined in DIPG initiation, we will be able to identify novel therapeutic targets that could help improve the current lack in specific treatments for DIPGs.

MATERIALS AND METHODS

Mice husbandry and timed pregnancies

Timed mattings were performed overnight, with the following morning considered E0.5. Pregnancies were detected by measuring female weight gain at E13.5. For the collection of postnatal time points (Four, seven or fourteen days after birth P2-4, P7, P14 or >P56), neonatal mice until the age of P7 were killed by decapitation whereas older mice were sacrificed by asphyxiation (CO2). Mice were conventionally housed and fed ad libitum. All mice were bred in the Central Animal Facility (University Medical Centre Groningen [UMCG], Groningen, The Netherlands) and were kept in conventional housing. Animal protocols were approved by the UMCG Committee on Animal Care (DEC-16465-02-002).

Isolation and culture of Pontine Neural Stem Cells (pNSCs) and Subventricular Zone Neural Stem Cells (SVZ NSCs)

Neural stem cells (NSCs) were harvested from postnatal days P2, P4, P7, P14 and adult cerebella, subventricular (SV) and pontine regions. Samples were kept on ice throughout the isolation procedure unless otherwise stated. In short, the brain regions were dissected, meninges removed and washed with cold PBS. Cerebella and pons were dissociated into single cells with a papain dissociation kit according to the manufacturer's instructions (Worhtington). Briefly, cerebella and pons were incubated at 37C in papain/DNAse solution, 15min for cerebella/pons younger than

7 days and 20-30 min for 14- and 30-days old cerebella/pons. After incubation, samples were further dissociated by trituration and filter quenched in an ovomucoid solution. Finally, samples were spun down at 4C and resuspended in neural stem-cell media containing DMEM-F12 Glutamax (Gibco), 1% N2-supplement (Thermo Fisher), 2% B27-supplement (Thermo Fisher), human-EGF (20ng/ml, PeproTech), bFGF (20ng/ml, PeproTech), human-PDGFAB (20ng/ml, PeproTech), mouse-SHH (1.5 or 1.0 ug/ml, R&D systems).

To isolate SVZ NSCs, a slice encompassing the hypothalamic region was cut sagitally in mouse forebrains to let appear the subventricular regions of the first ventricule. The SVZ were isolated with thin tweezers, dissociated into single cells by mechanical shearing with a pipette and plated in NSCs media. NSCs were grown as neurospheres, dissociated at every passage by trituration with Accutase (Gibco) to form a single cell suspension and further replated.

Quantitative RT-PCR

For analysis of mRNA expression in mouse tissue, total RNA was isolated with Trizol (Thermo Fisher). Briefly, immediately after tissue dissection, all samples were dounced in 1ml trizol on ice with a tissue grinder (pestle A followed by pestle B) until a homogenized trizol-tissue solution was obtained. Homogenized tissue in trizol was stored overnight at -80C and the isolation procedure was continued on the following day according to manufacturer's specifications. For analysis of RNA expression from cultured cells, total RNA was isolated using the RNeasy Micro Kit (Qiagen) according to the manufacturer's specifications. Either ways, At the end of the procedure, RNA was eluted in DEPC water, treated with DNAse and final RNA concentration was determined with a NanoDrop™ 1000 Spectrophotometer (Thermo Fisher). cDNA was synthetized from 1 µg RNA and amplified using the primers described in Table 1. Thermocycling steps were performed on a CFX96 Connect Real-Time PCR Detection System (Bio Rad) with SsoAdvanced™ universal SYBR green supermix (Bio Rad)

Table 1. Primers for q RTPCR

Quantitative RT PCR	
Primer name	Sequence
18s_rRNA-F1	GCTACCACATCCAAGGAAGG
18s_rRNA-R1	ATTACAGGGCCTCGAAAGAG
H3f3a-Ex1-F	CAGCGCCGCCTCTCGCTTG
H3f3a-Ex2-R	CAGTCTGCTTTGTACGAGCCATGGTA
H3f3a-Ex2-F	CTACAAAAGCCGCTCGCAAGAGT
H3f3a-Ex3-R	TTCTGATAGCGTCTGATTTCACGG
H3f3b-Ex1-F	CGATTGCGGCTCTTGTTCGAG
H3f3b-Ex2-R	TTCCCACCGGTGGACTTCCTA
H3f3b-Ex2-F	CCAAGGCGGCTCGGAAAAGC
H3f3b-Ex3-R	GGTAACGACGGATCTCTCTCAGA
H3.1/3.2-F	CGGCGCTACCAGAAGTCGACC
H3.1/3.2-R	GTCTTGAAGTCCTGCGCGATCTCG
Pax6 Fw	TGAGAAGTGTGGGAACCAGC
Pax6 Rev	AAGTCTTCTGCCTGTGAGCC
Irx2 Fw-2	TTCCCGTCCTACGTGGGCT
Irx2 Rev-2	GGTACGGGTTCTTTCGGTGT
Pax3 Fw-2	CAAACCCAAGCAGGTGACAA
Pax3 Rev-2	TTTACTCCTCAGGATGCGGC
mMycn Fwd-1	ACCTTGAGCGACTCAGATGATG
mMycn Rev-1	TCTTGGGACGCACAGTGATC
mPatch1 Fwd-1	attgcatctgttggcatcgg
mPatch1 Rev-1	agaacgggagcaaacatgtg
mGli1 Fwd-1	Acaagtgcacgtttgaaggc
mGli1 Rev-1	Tcactggcattgctaaaggc
mBactin Fwd-1	CCTCATGAAGATCCTGACTGA
mBactin Rev-1	TTTATGTCACGAACAATTTCC

Histone acid extraction

Histones form tissues were acid extracted following a protocol described previously (reef). All procedures were performed on ice, and all solutions were chilled to 4°C

prior to use unless otherwise indicated. All centrifugation steps were performed at 4°C. Briefly, dissected pons and cerebella were dounced in 1ml ice cold hypotonic lysis buffer (10mM tris-Cl pH8.0, 1mM KCl, 1.5mM MgCl2, 1mM DTT, protease inhibitors and phoSTOP cocktail) on ice with a tissue grinder (20 strokes of pestle A and pestle B) until a homogenized tissue solution was obtained. Homogenized samples were transferred to a 1.5 ml tube and the intact nuclei were pelleted by spinning in cooled centrifuge (10.000g, 10min, 4C). The nuclei pellet was resuspended in 100 µl of 0.2 M HCl and vortexed to avoid clumping. Histones were extracted for 1 hour on a rotator at 4C. Samples were centrifuged at 16,000 x g for 10 min at 4°C. The histone containing supernatant was transferred to a fresh 1.5ml tube. Histones were precipitated by adding drop by drop 30 µl of 100% trichloroacetic acid containing 4 mg/ml deoxycholic acid (deoxycholicacid was added before use). The tubes were inverted several times to mix the solutions and incubated 15-30min on ice. Histones were pelleted (16,000 x g for 30 min 4°C) and the pellet was washed with 100 µl of ice-cold acidified acetone (0.1% HCl) two times. After second wash, supernatant was carefully removed histone pellet air-dried for 20min at room temperature. The pellet was dissolved in ddH2O and stored at –80 °C.

Total protein isolation and Western blot

Total proteins were extracted from neural stem cells pellets in RIPA buffer supplemented with protease inhibitors and phoSTOP cocktail. Total protein concentration or histone concentration was determined by BCA assay (Pierce). A total of 10 ug proteins per sample or 5ug of extracted histones were boiled in sample buffer and loaded on Mini-PROTEAN TGX™ precast gels (Biorad). Proteins were transferred onto a PVDF membrane (Trans-Blot Turbo Transfer System, Biorad), and probed for the following antibodies: anti-histone H3.3 (Rabbit, 1/1000, clone RM190, RevMab Biosciences 31-1058-00), anti-H4 (Mouse, 1/1000, Active motif 61521). HRP labelled Goat anti-Mouse or Rabbit secondary antibodies were used to visualize protein expression using chemiluminescence substrate (SuperSignal™ West Dura Extended Duration Substrate, Thermo #34076) on a ChemiDoc imaging system (Biorad). Analysis and densitometry of the protein bands was performed with ImageLab (V5.0) software.

Allen Brain Atlas Immunohistochemistry and RNA-seq Databases

The Allen Brain Atlas data repository (www.allenbrainatlas.org) was used to find transcriptional specificities of mouse pontine region at neonatal time points. In short, we selected the most enriched transcription factor at the designated time point that specifically localized in the pontine region. Using the mouse development navigator, we were able to look back into the gene expression of the selected transcription factors across all brain regions and ages. The immunohistochemistry repository allowed us to visualize and corelate the protein expression of these selected markers in the neonatal mouse brain.

AUTHORS CONTRIBUTIONS

Conceptualization, I.B., and S.W.M.B.; Methodology, I.B., and N.V.; Software and Formal Analysis, I.B. and N.V. ; Investigation, I.B.; Resources, I.B. and N.V. ; Data Curation, I.B.; Writing, I.B. and S.W.M.B.; Writing – Review and Editing, I.B. and S.W.M.B.; Visualization, I.B.; Supervision and Project Administration, S.W.M.B.; Funding Acquisition, I.B. and S.W.M.B.

ACKNOWLEDGEMENTS

This study was supported by a De Cock-Hadders foundation grant to I.B.; a Stichting Kinderoncologie Groningen/SKOG project grant (16-003) to S.B; a Rosalind Franklin fellowship from the University of Groningen to S.B.; and a Dutch Cancer Society/KWF career award (RUG 2014-6903) to S.B.

CONFLICT OF INTEREST

The authors declare no conflict of interest.

REFERENCES

1. Gajjar, a. *et al.* Pediatric Brain Tumors: Innovative Genomic Information Is Transforming the Diagnostic and Clinical Landscape. *J. Clin. Oncol.* (2015). doi:10.1200/JCO.2014.59.9217

2. Pajtler, K. W. *et al.* Molecular Classification of Ependymal Tumors across All CNS Compartments, Histopathological Grades, and Age Groups. *Cancer Cell* **27**, 728–43 (2015).

3. Mackay, A. *et al.* Integrated Molecular Meta-Analysis of 1,000 Pediatric High-Grade and Diffuse Intrinsic Pontine Glioma. *Cancer Cell* **32**, 520-537.e5 (2017).

4. Sharma, T. *et al.* Second-generation molecular subgrouping of medulloblastoma: an international meta-analysis of Group 3 and Group 4 subtypes. *Acta Neuropathol.* (2019). doi:10.1007/s00401-019-02020-0

5. David N. Louis *et al.* The 2016 World Health Organization Classification of Tumors of the Central Nervous System: a summary.

6. Schwartzentruber, J. *et al.* Driver mutations in histone H3.3 and chromatin remodelling genes in paediatric glioblastoma. *Nature* **482**, 226–231 (2012).

7. Wu, G. *et al.* Somatic histone H3 alterations in pediatric diffuse intrinsic pontine gliomas and non-brainstem glioblastomas. *Nat. Genet.* **44**, 251–253 (2012).

8. Fontebasso, A. M. *et al.* Recurrent somatic mutations in ACVR1 in pediatric midline high-grade astrocytoma. *Nat. Genet.* **46**, 462–466 (2014).

9. Castel, D. *et al.* Histone H3F3A and HIST1H3B K27M mutations define two subgroups of diffuse intrinsic pontine gliomas with different prognosis and phenotypes. *Acta Neuropathol.* **130**, 815–827 (2015).

10. Nacev, B. A. *et al.* The expanding landscape of 'oncohistone' mutations in human cancers. *Nature* **567**, 473–478 (2019).

11. Skene, P. J. & Henikoff, S. Histone variants in pluripotency and disease. *Development* **140**, 2513–2524 (2013).

12. Elsaesser, S. J., Goldberg, A. D. & Allis, C. D. New functions for an old variant: no substitute for histone H3.3. *Curr. Opin. Genet. Dev.* **20**, 110–117 (2010).

13. Buczkowicz, P. *et al.* Genomic analysis of diffuse intrinsic pontine gliomas identifies three molecular subgroups and recurrent activating ACVR1 mutations. *Nat. Genet.* **46**, 451–456 (2014).

14. Lewis, P. W. *et al*. Inhibition of PRC2 activity by a gain-of-function H3 mutation found in pediatric glioblastoma. *Science (80-.).* **340**, 857–861 (2013).

15. K., F., T., M., P.W., L., C.D., A. & V., T. Use of human embryonic stem cells to model pediatric gliomas with H3.3K27M histone mutation. *Science (80-.).* **346**, 1529–1533 (2014).

16. Kang, H. J. *et al.* Spatio-temporal transcriptome of the human brain. *Nature* **478**, 483–9 (2011).

17. Jessa, S. *et al.* Stalled developmental programs at the root of pediatric brain tumors. *Nat. Genet.* **51**, 1702–1713 (2019).

18. Tate, M. C. *et al.* Postnatal growth of the human pons: A morphometric and immunohistochemical analysis. *J. Comp. Neurol.* **523**, 449–462 (2015).

19. Monje, M. *et al.* Hedgehog-responsive candidate cell of origin for diffuse intrinsic pontine glioma. *Proc. Natl. Acad. Sci.* **108**, 4453–4458 (2011).

20. Lindquist, R. A. *et al.* Identification of proliferative progenitors associated with prominent postnatal growth of the pons. *Nat. Commun.* **7**, 1–16 (2016).

21. Biterge, B. & Schneider, R. Histone variants: Key players of chromatin. *Cell Tissue Res.* **356**, 457–466 (2014).

22. Jang, C. W., Shibata, Y., Starmer, J., Yee, D. & Magnuson, T. Histone H3.3 maintains genome integrity during mammalian development. *Genes Dev.* **29**, 1377–1393 (2015).

23. Jiang, J. & Hui, C. chung. Hedgehog Signaling in Development and Cancer. *Dev. Cell* **15**, 801–812 (2008).

24. Fuccillo, M., Joyner, A. L. & Fishell, G. Morphogen to mitogen: The multiple roles of hedgehog signalling in vertebrate neural development. *Nat. Rev. Neurosci.* **7**, 772–783 (2006).

25. Ruiz i Altaba, A., Palma, V. & Dahmane, N. Hedgehog-Gli signalling and the growth of the brain. *Nat. Rev. Neurosci.* **3**, 24–33 (2002).

26. Kenney, A. M., Cole, M. D. & Rowitch, D. H. Nmyc upregulation by sonic hedgehog signaling promotes proliferation in developing cerebellar granule neuron

precursors. *Development* **130**, 15–28 (2003).

27. Heretsch, P., Tzagkaroulaki, L. & Giannis, A. Cyclopamine and hedgehog signaling: Chemistry, biology, medical perspectives. *Angew. Chemie - Int. Ed.* **49**, 3418–3427 (2010).

28. Pollard, S. M., Conti, L., Sun, Y., Goffredo, D. & Smith, A. Adherent neural stem (NS) cells from fetal and adult forebrain. *Cereb. Cortex* **16**, (2006).

29. Zhao, J. Coordination of DNA synthesis and histone gene expression during normal cell cycle progression and after DNA damage. *Cell Cycle* **3**, 693–695 (2004).

30. Mckinnon, P. J. Maintaining genome stability in the nervous system. *Nat. Neurosci.* **16**, 1523–1529 (2013).

31. Wei, P. C. *et al.* Long Neural Genes Harbor Recurrent DNA Break Clusters in Neural Stem/Progenitor Cells. *Cell* **164**, 644–655 (2016).

32. O'Driscoll, M. & Jeggo, P. A. The role of the DNA damage response pathways in brain development and microcephaly: Insight from human disorders. *DNA Repair (Amst).* **7**, 1039–1050 (2008).

33. Dien et al., 2013. Overview for the Histone Codes for DNA Repair. *Bone* **23**, 1–7 (2008).

34. Bush, K. M. *et al.* Endogenous mammalian histone H3.3 exhibits chromatin-related functions during development. *Epigenetics and Chromatin* **6**, 1–16 (2013).

35. Yadav, T., Quivy, J.-P. & Almouzni, G. Chromatin plasticity: A versatile landscape that underlies cell fate and identity. *Science (80-.).* **361**, 1332–1336 (2018).

36. Adam, S., Polo, S. E. & Almouzni, G. XTranscription recovery after DNA damage requires chromatin priming by the H3.3 histone chaperone HIRA. *Cell* **155**, 94 (2013).

37. Yang, X. *et al.* Histone acetyltransferase 1 promotes homologous recombination in DNA repair by facilitating histone turnover. *J. Biol. Chem.* **288**, 18271–18282 (2013).

38. Frey, A., Listovsky, T., Guilbaud, G., Sarkies, P. & Sale, J. E. Histone H3.3 is required to maintain replication fork progression after UV damage. *Curr. Biol.* **24**, 2195–2201 (2014).

39. Luijsterburg, M. S. *et al.* PARP1 Links CHD2-Mediated Chromatin Expansion and H3.3 Deposition to DNA Repair by Non-homologous End-Joining. *Mol. Cell* **61**, 547–562 (2016).

40. Ray-Gallet, D. *et al.* Dynamics of Histone H3 Deposition In Vivo Reveal a Nucleosome Gap-Filling Mechanism for H3.3 to Maintain Chromatin Integrity. *Mol. Cell* **44**, 928–941 (2011).

41. Rondinelli, B. *et al.* EZH2 promotes degradation of stalled replication forks by recruiting MUS81 through histone H3 trimethylation. *Nat. Cell Biol.* **19**, 1371–1378 (2017).

42. Zhang, Y. *et al.* Histone H3K27 methylation modulates the dynamics of FANCD2 on chromatin to facilitate NHEJ and genome stability. *J. Cell Sci.* **131**, jcs215525 (2018).

43. Hatta, T. *et al.* Development of the pons in human fetuses. *Congenit. Anom. (Kyoto).* **47**, 63–67 (2007).

44. Misuraca, K. L., Hu, G., Barton, K. L., Chung, A. & Becher, O. J. A Novel Mouse Model of Diffuse Intrinsic Pontine Glioma Initiated in Pax3-Expressing Cells. *Neoplasia* **18**, 60–70 (2016).

45. Jessa, S. *et al. Stalled developmental programs at the root of pediatric brain tumors*. *Nature Genetics* **51**, (2019).

46. Misuraca, K. L. *et al.* Pax3 expression enhances PDGF-B-induced brainstem gliomagenesis and characterizes a subset of brainstem glioma. *Acta Neuropathol. Commun.* **2**, 1–17 (2014).

47. Pathania, M. *et al.* H3.3 K27M Cooperates with Trp53 Loss and PDGFRA Gain in Mouse Embryonic Neural Progenitor Cells to Induce Invasive High-Grade Gliomas. *Cancer Cell* **32**, 684-700.e9 (2017).

48. Sun, Y. *et al.* Diffuse Intrinsic Pontine Gliomas Exhibit Cell Biological and Molecular Signatures of Fetal Hindbrain-Derived Neural Progenitor Cells. *Neurosci. Bull.* **35**, 216–224 (2019).

49. Watson, C., Bartholomaeus, C. & Puelles, L. Time for radical changes in brain stem nomenclature—Applying the lessons from developmental gene patterns. *Front. Neuroanat.* **13**, 1–12 (2019).

Pediatric high-grade glioma
&
genome instability

6

The H3.3K27M oncohistone affects replication stress outcome and provokes genomic instability in pediatric glioma

Irena Bočkaj [1], Tosca E. I. Martini [1,8], Eduardo S. C. Magalhaes [1,2,8], Petra L. Bakker [1], Tiny G.J. Meeuwsen-de Boer [3], Inna Armandari [1], Colin Stok [4], Yannick P. Kok [4], Bjorn Bakker [1], Diana C. J. Spierings [1], Ulrich Schüller [5,6,7], Marcel A. T. M. van Vugt [4], Floris Foijer [1,9,10], Sophia W. M. Bruggeman [1,9,10]

[1] European Research Institute for the Biology of Ageing/ERIBA, UMCG, the Netherlands
[2] Glial Cell Biology Laboratory, Biomedical Sciences Institute, Federal University of Rio de Janeiro, Brazil
[3] Pathology and Medical Biology, UMCG, the Netherlands
[4] Department of Medical Oncology, UMCG the Netherlands
[5] Research Institute Children's Cancer Center Hamburg,, Germany
[6] Department of Pediatric Hematology and Oncology, University Medical Center Hamburg-Eppendorf, Germany
[7] Institute of Neuropathology, University Medical Center Hamburg-Eppendorf, Germany
[8,9] Equal contribution
[10] Co-corresponding authors

ABSTRACT

While comprehensive molecular profiling of histone H3.3 mutant pediatric high-grade glioma has revealed extensive dysregulation of the chromatin landscape, the exact mechanisms driving tumor formation remain poorly understood. Since H3.3 mutant gliomas also exhibit remarkably high levels of copy number alterations, we set out to address if the presence of the H3.3^{K27M} oncohistone leads to destabilization of the genome. Hereto, we established a cell culture model allowing inducible H3.3^{K27M} expression and observed an increased rate of mitotic abnormalities. We identified components related to DNA replication, most prominently MCM helicase proteins, by immunoprecipitation and mass spectrometry that specifically interact with H3.3^{K27M} during mitosis. Further functional analyses uncovered increased genomic instability upon replication stress, as represented by bulky and ultra-fine DNA bridges during mitosis. This co-occurred with suboptimal 53BP1 nuclear body formation *in vitro* and *in vivo*. Together, our data uncover a role for H3.3 in DNA replication under stress conditions that is altered by the K27M mutation, promoting genomic instability and potentially facilitating the tumorigenic process in pediatric high-grade glioma.

INTRODUCTION

Pediatric high-grade glioma (HGG) is a common childhood brain malignancy for which no adequate treatment exists [1]. The discovery of mutant histones as most frequently occurring genetic alteration in these cancers provided a novel angle for developing anti-cancer therapy, and generated broad interest into these 'oncohistones' [1–3]. So far, five different histone mutants (H3.1K27M, H3.2K27M, H3.3K27M, and H3.3G34R/V) have been identified that target either Lysine 27 or Glycine 34 on one of the three histone H3 variants. Interestingly, pediatric HGG carrying different histone mutations have a distinct age of onset and harbor different anatomical, clinical and molecular features, suggesting that each mutant has unique oncogenic characteristics [4–6]. Several functional studies have confirmed the tumor-driving capacity of the oncohistones and revealed their impact on chromatin

modifying proteins, chromatin composition and gene expression [7–14]. This is in line with the apparent selective pressure to mutate residues that either are, or flank epigenetic modification sites involved in gene regulation.

However, it remains elusive how these transcriptional changes lead to tumor formation [15]. Therefore, it is possible that (onco)histone functions unrelated to gene regulation contribute to tumorigenesis as well. In this respect, it is intriguing that pediatric HGG with mutations in the non-canonical histone H3.3 exhibit particularly high rates of genomic and chromosomal instability (GIN/CIN) [16]. This raises the question whether the H3.3K27M mutation can promote GIN/CIN, as has been suggested for H3.3G34R/V, which would contribute to intra-tumor heterogeneity and tumor aggressiveness [17–22]. Indeed, in addition to its canonical role in the packaging of chromatin and modulation of gene expression, histone H3.3 carries out functions linked to maintenance of genomic integrity. For instance, H3.3 is enriched in regions where genome stability is at risk, such as telomeres and pericentric heterochromatin. Further, its loss leads to mitotic defects in mouse embryonic stem cells, suggesting a role for H3.3 in chromosomal stability. In addition, H3.3 has been implicated in both single- and double-strand DNA break repair and H3.3 mutant cells have increased sensitivity to DNA damage [23–27], suggesting ongoing genomic instability. Intriguingly, unlike H3.1 mutant HGG, which mostly harbors mutations in developmental pathways, mutations in H3.3 mutant HGG are enriched for genes involved in DNA damage repair pathways [4,28].

Since unrepaired DNA damage ultimately leads to CIN/GIN, we hypothesized that H3.3K27M establishes a permissive background for genome instability. In the developing brain, genomic integrity is mostly at stake due to highly prevalent replication stress dependent DNA lesions [29–31]. Hence, we focused on how H3.3K27M affects the response to replication stress. We found that H3.3K27M increases sensitivity to replication stress, leading to mitotic abnormalities including DNA ultra-fine bridges. These observations could explain the ongoing genomic and chromosomal instability in pediatric high-grade glioma.

RESULTS

Histone H3.3^{K27M} mutant cells exhibit mitotic abnormalities

To explore the GIN/CIN phenotype of histone mutant pediatric glioma and quantify the extent of copy number alterations, we analyzed DNA copy number variations (CNVs) in n=745 pediatric HGG using a publicly available dataset [4]. We found that histone H3.3 mutant gliomas have a greater degree of CNVs compared to histone H3.1 mutant gliomas and H3 wild type gliomas (Fig 1A and Table S1), with H3.3G34R/V HGG being more aneuploid than H3.3K27M HGG. To demonstrate ongoing chromosomal instability in H3.3K27M HGG, we performed shallow single-cell whole genome sequencing on a H3.3K27M HGG sample and determined karyotype heterogeneity [32]. Approximately half of the cells (n=13) were euploid, most likely representing healthy cells in the tumor microenvironment (Fig. 1B). The remaining cells (n= 15), showed moderate aneuploidy and gross structural abnormalities (clonal gain of 7p and 1q, and clonal loss of 7q), as well as numerical aneuploidies (clonal loss of 13 and 14), which have been described before as recurrent lesions in pediatric HGG (Fig. 1B) [4]. We also observed a number of microdeletions (on chromosome 11, 16 and 17) previously shown to be a sign of ongoing replication stress and therefore genome instability [33]. Furthermore, we identified co-existing clones with varying chromosome compositions (Fig 1C), especially on chromosomes 1, 5, 11, 15 and 22 (Fig 1C, red arrows), *i.e.* intra-tumoral heterogeneity and evidence for ongoing genomic rearrangements and genomic instability.

Together, these findings prompted us to further investigate a role for (mutant) H3.3 in the maintenance of genomic integrity. Hereto, we generated a cell culture model system that allowed us to study genomic maintenance in a non-transformed background, and thus identify primary functions of (K27M mutant) histone H3.3 (H3.3$^{WT\ or\ K27M}$) (Fig 1D-H). We took advantage of the human cell line hTert-RPE1 (hereafter referred to as RPE1), which is widely used in chromosomal instability and aneuploidy studies due to its well-defined stable karyotype [34,35]. Three different cell lines were generated: RPE1 containing doxycycline-inducible FLAG-tagged wild-type histone H3.3 (further referred to as H3.3^{WT}) to account for phenotypes due to

mild histone overexpression [36]; RPE1 containing FLAG-tagged K27M mutant histone H3.3 to identify mutation-specific phenotypes ($H3.3^{K27M}$); and an empty vector control cell line (EV) (Fig 1D-G). Importantly, the doxycycline-inducible system allowed us to tightly control timing and levels of overexpression, which is essential since only 4 to 18% of total histone H3 is mutated in HGG, and because we wished to investigate early events following H3.3 (mutant) expression [10]. Thus, we opted for subtle over-expression of the FLAG-tagged histones for all experiments, where $H3.3^{WT}$ overexpression levels were equilibrated to $H3.3^{K27M}$ by treating $H3.3^{WT}$ with a lower doxycycline concentration (150 ng/ml versus 500ng/ml for $H3.3^{WT}$) (Fig 1D *ii*). We also performed most experiments within 2-3 days after FLAG-histone expression induction.

We validated our model by confirming that FLAG-histone expression was predominantly in the nucleus (Fig 1F), and by showing a modest reduction of the H3K27 tri-methylation ($H3K27me^3$) mark in $H3.3^{K27M}$ cells after 2 days of FLAG-histone induction, as has been reported previously [10,37] (Fig 1D *i* and E). We then asked if there is a relationship between $H3.3^{K27M}$ expression and chromosomal instability. First, we verified that $H3.3^{WT}$ and $H3.3^{K27M}$ were similarly distributed on condensed chromatin during all stages of mitosis (Fig 1G). To visualize real-time chromosome behavior during mitosis, we performed time lapse imaging and quantified mitotic timing and abnormalities (Fig 1H, and see also Fig. 3F for examples of scored mitotic abnormalities). We observed mitotic abnormalities in approximately 18 percent of mitotic $H3.3^{WT}$ cells regardless of overexpression levels, as previously described by others [36]. However, the H3.3 K27M mutation increased the rate of abnormal mitoses to 29 percent, suggesting a role for the $H3.3^{K27M}$ oncohistone in chromosomal instability (Fig 1H).

To understand the origin of the observed increase in CIN, we tested whether $H3.3^{K27M}$ oncohistone expression attenuates the spindle assembly checkpoint (SAC), a key mitotic fail-safe mechanism that ensures faithful chromosome segregation in mitosis (reviewed in [38]). Hereto, we challenged doxycycline-induced cells with nocodazole, a microtubule poison that arrests cells in mitosis when the SAC is fully functional (Fig EV1A). Flow cytometry analysis did not show a difference

in the ability of either H3.3^{WT}, H3.3^{K27M}, or EV control cells to arrest in mitosis as measured by mitotic H3S10-phosphorylation (Fig EV1B, upper panel). Other mitotic phosphorylation histone marks, such as serine 28 (H3S28P) and the H3.3 specific Serine 31 (H3.3S31P) that are in the proximity of the mutated Lysine 27, were also unchanged (Fig EV1B, middle and lower panels, respectively). Furthermore, time lapse imaging showed comparable mitotic timing in all three cell lines (Fig EV1C). Altogether, this suggests adequate mitotic progression and a functional SAC in H3.3^{K27M} cells that fail to explain the increased rate of abnormal mitoses (Fig 1H).

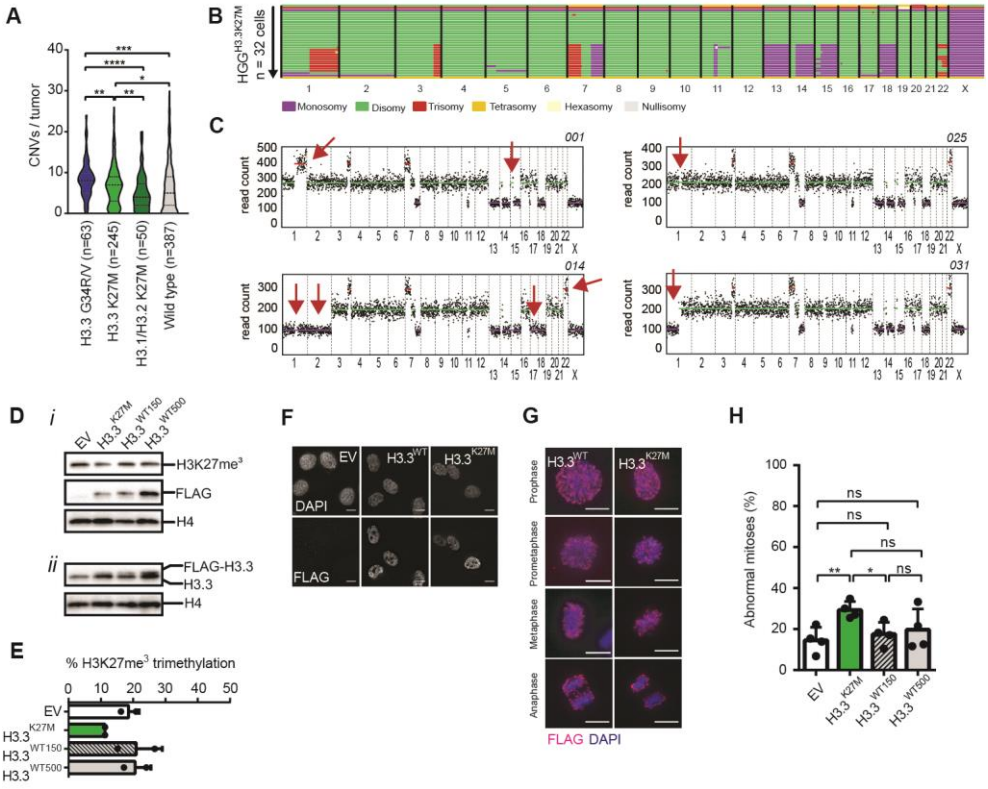

Figure 1. The H3.3^{K27M} oncohistone is associated with aneuploidy, intratumor heterogeneity, and genomic and chromosomal instability.

(A) Distribution of chromosome copy number variations (CNVs) across a set of pediatric high-grade gliomas (HGG). Data are represented as medians (**----**) and quartiles (·····) ; *P=0.0289, **P=0.0064 and p=0.0066, ***P=0.002,****P≤0.0001 (Mann Whitney non-parametric t-test). **(B)** Single-cell Whole Genome Sequencing data for n=32 cells from a human H3.3^{K27M} mutant pediatric HGG. Each line represents the karyotype of a single cell, organized by chromosome number. Colors represent ploidy. **(C)** Detailed single-cell sequencing analysis of four different HGG$^{H3.3K27M}$ cells, showing cell specific ploidy states (red arrows indicate cell-specific genomic alterations). **(D)** Western blots depicting *i)* H3K27me^3 and FLAG-H3.3 expression in H3.3^{WT}, H3.3^{K27M} and EV control cells, as quantified in **(E)** as the percentage H3K27me^3 expression compared to H4; and *ii)* showing Flag-H3.3 and endogenous H3.3 expression after 48 hrs of doxycycline treatment. H4, loading control. **(F)** Immunofluorescent images showing cellular localization of FLAG-H3.3 at interphase, and **(G)** at all stages of mitosis. Scale bars represent 10 µm. **(H)** H3.3^{K27M}, H3.3^{WT150}, H3.3^{WT500} and EV control cells were treated for 48 hrs with doxycycline and time-lapse imaged for 16 hrs. Mitotic features were scored as normal or abnormal. Data represent mean percentages of abnormal mitoses ± SD (n=4 experiments), with a minimum of 20 mitoses per condition. *P=0.016, **P=0.008 (Multiple t-tests).

The histone H3.3^{K27M} mutant has an altered protein interaction network in mitosis

In mitosis, the chromatin undergoes significant changes and histones become the substrates and scaffolds for a myriad of proteins to allow proper DNA segregation [39–41]. Therefore, we next set out to investigate the protein-histone H3.3(K27M) interactions during mitosis to further decipher the cause of the observed genomic instability. For this purpose, a FLAG-Immunoprecipitation (FLAG-IP) was performed on EV, H3.3^{WT}, and H3.3^{K27M} mitotic nuclear extracts (Fig EV2A). Flow cytometry analysis confirmed that our synchronization and shake-off protocol efficiently enriched the input fractions for mitotic H3S10P positive cells (Fig EV2A-B). Then, mass-spectrometry analysis was performed on the eluted protein fractions to identify H3.3 interactors (Fig 2, Fig EV2 and Tables S2-5). In total, around 750 proteins were identified in each cell line (Table S2). Following background subtraction and normalization, we obtained curated binding partner lists in which we identified n=199 (H3.3^{WT}) and n=102 (H3.3^{K27M}) unique interactions, and n=330 common interactions (Fig 2A). Within common interactors, n=32 (H3.3^{WT}) and n=76 (H3.3^{K27M}) interactors were enriched for either H3.3^{WT} or H3.3^{K27M}. Fig. 2B graphically represents the common (not enriched), and enriched interactors.

To identify deregulated biological processes in mitotic H3.3^{K27M} cells, we grouped interactors as either common (not enriched, n=222), or unique plus enriched (for either H3.3^{WT}, n=231; or H3.3^{K27M}, n=187), and performed GO-term analysis (STRING). As expected, common interactors showed enrichment for processes related to chromosome organization, with chaperones (*e.g.,* DAXX), histones (*e.g.,* H2A, H2B, H4) and chromatin readers and modifiers (*e.g.,* CBX3) constituting the main hits (Fig EV2C-D, Table S3). We also found enrichment for mRNA splicing via spliceosome (HNRNPR, HNRNPK, HNRNPC) and translation machinery, including ribosome components (RPL and RPS subunits) and translation initiation factors (EIF3s and EIF4s) in line with earlier findings [42] (Fig EV2C-D, Table S3).

We subsequently analyzed the H3.3^{WT} and H3.3^{K27M} unique/enriched interactions (Fig 2C-F and Tables S4-S5). Both H3.3^{K27M} (Fig 2C-D) and H3.3^{WT} (Fig 2E-F)

showed enrichment for processes related to translation, albeit through different subsets of RPS and RPL variants (Fig 2C-F and Tables S4-S5). Additionally, we observed enrichment for RNA processing in H3.3^{WT}, and mRNA splicing in H3.3^{K27M} unique/enriched interactors.

Importantly, we also identified processes that are potentially linked to the H3.3^{K27M} GIN phenotype. For instance, the H3.3^{K27M} unique/enriched interactome showed greater heterogeneity in nucleosome composition where histone H1 variants are bound equally, yet the usage of canonical histone H2A and H2B variants is different (Fig EV2E). Of note, we found an increase of macroH2A.1 (H2AY) in H3.3^{K27M}, suggesting perturbed replication in H3.3^{K27M} cells [43] (Fig EV2E). Moreover, we observed enrichment for replication-coupled histone chaperoning complexes (comprising ASF1B, NASP, FACT, RAN and Nucleophosmin (NPM)) in H3.3^{K27M} unique/enriched interactors [44–47] (Fig 2C, Table S4). Furthermore, GO-term analysis identified DNA replication, including the MCM2-7 complex, as an enriched biological process specific for H3.3^{K27M} (Fig 2C, D and G) [47,48]. The latter finding was confirmed in independent pull-down experiments, where we found increased MCM2, MCM4 and MCM7 interaction with Histone H3.3^{K27M} in mitotic cells (Fig 2H-I).

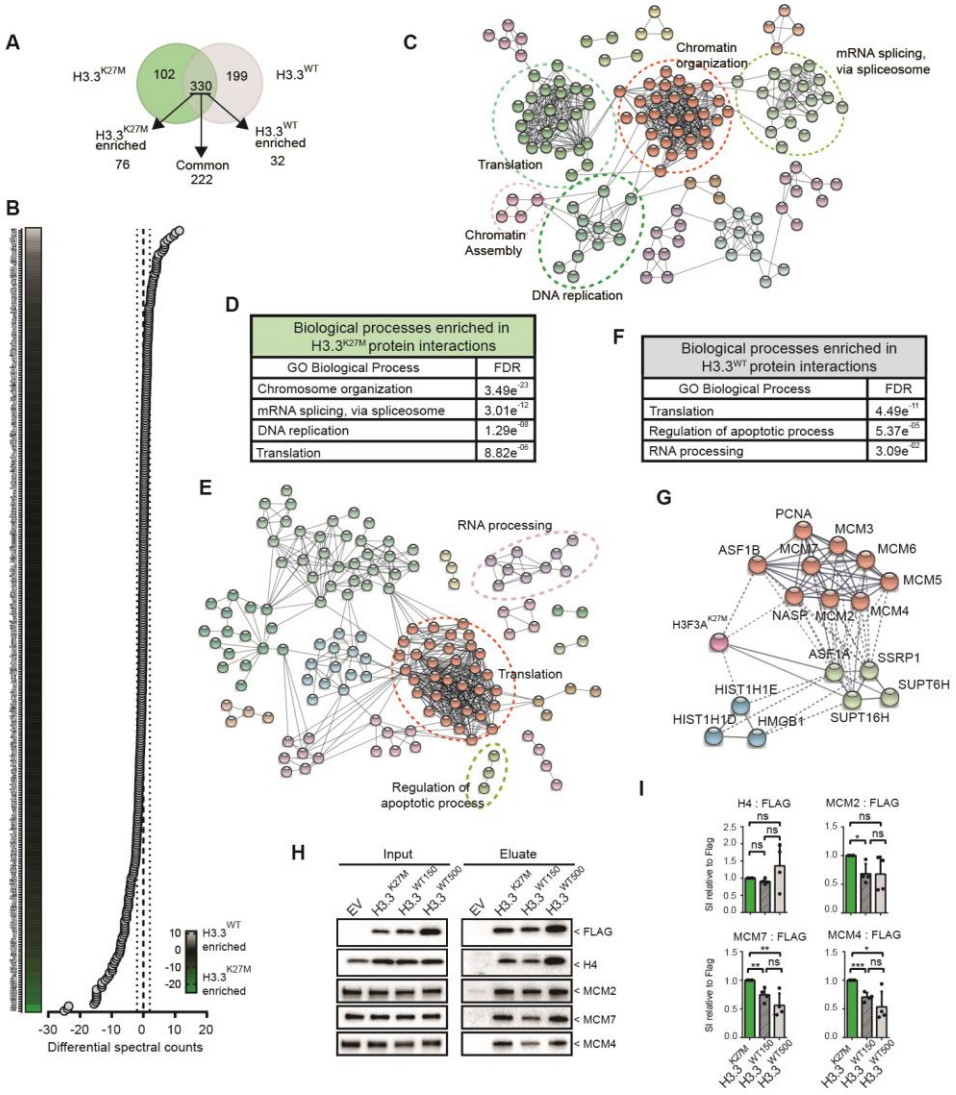

Figure 2. The Histone H3.3^{K27M} mutant has an altered mitotic protein interaction network.

(A) Venn diagram showing the distribution of FLAG-histone interacting proteins that are either specific for H3.3^{WT} (n=199) and mutant H3.3^{K27M} (n=102), or common/enriched (n=330) as identified by LC-MS/MS. **(B)** Graph depicting semi-quantitative spectral counts of H3.3^{WT} and H3.3^{K27M} common binding partners (black, n=222) (differential spectral counts between dashed lines), and enriched binding partners (green: H3.3^{K27M} - enriched, n=76 ; grey: H3.3^{WT} - enriched, n=32). **(C)** H3.3^{K27M} specific/enriched interaction network for Biological processes as analyzed using STRING. The illustrated network map was simplified for clarity by manual curation. Dashed circles represent a group of interacting proteins belonging to one biological process. **(D)** GO-term analysis (for Biological processes) of interacting proteins using STRING reveals significant enrichment for chromosome organization, mRNA splicing, DNA replication and translation in enriched H3.3^{K27M} binding partners. GO=gene ontology, FDR=false discovery rate. **(E)** H3.3^{WT} specific/enriched interaction network as analyzed using STRING. The illustrated network map was

simplified for clarity by manual curation. Dashed circles represent a group of interacting proteins belonging to one biological process. **(F)** GO-term analysis (for Biological processes) of interacting proteins using STRING reveals significant enrichments for translation, regulation of apoptotic process and RNA processing in enriched H3.3^{WT} binding partners. GO=gene ontology, FDR=false discovery rate. **(G)** DNA replication enriched network showing binding partners relation to the histone mutant H3.3^{K27M}. **(H)** Western blot validation of FLAG-immunoprecipitations in H3.3^{WT}, H3.3^{K27M} and control mitotic lysates. **(I)** Quantification of the histone-bound fraction of H4, MCM2, 7 and 4 by densitometry. Signal was normalized to FLAG, and H4 was used as positive control. Data are presented as means ±SD (n= 4 experiments). *P= 0.0138 and 0.0107; **P=0.0054 and 0.0057; ***P=0.0003 (Multiple t-tests)

H3.3^{K27M} cells are sensitive to replication stress

The enriched association of replication-specific factors with mitotic H3.3^{K27M} may appear counterintuitive at first. However, ASF1, PCNA, other components of the MCM helicase and additional replication proteins, remain associated with chromatin in mitotic cells upon replication stress [48–51]. Hence, we hypothesized that in a H3.3^{K27M} chromatin context, proceeding of the replication machinery upon encountering physical barriers is impaired. This hampers faithful completion of S-phase and eventually interferes with chromosome segregation [52]. To test this, we investigated if H3.3^{K27M} cells are sensitive to exogenous replication stress-inducing agents [25,26,53]. We first studied the UVC-induced DNA damage response that has been associated with H3.3 before [53], and observed a trend towards a greater UVC sensitivity for H3.3^{K27M} cells (22% long-term survival) compared to H3.3^{WT} (31% survival) and EV (39% survival) (Fig EV3A, left panel). In contrast, we found no differences when applying ɣ-rays (24% for H3.3^{K27M} cells, 23% for H3.3^{WT} and 39% for EV) (Fig EV3A, right panel) [54]. We then analyzed ɣ-H2AX positivity to demonstrate DNA damage in UVC-irradiated cells using flow cytometry (Fig EV3B-C). An S-phase specific ɣ-H2AX peak one hour following UVC induction was observed in all cell lines, which disappeared more rapidly in H3.3^{K27M} cells. This could mean that DNA damage is more rapidly resolved in H3.3^{K27M} cells, or alternatively, that DNA damage signaling ceases prematurely. Additionally, cell cycle analysis at 24 hrs after UVC showed a decrease in G2 arrested cells in H3.3^{K27M} (25%) compared to H3.3^{WT} (32%) and EV (36%) (Fig EV3D and EV3E), which could not be explained by a leaky G2 checkpoint (Fig EV3F-G). We therefore speculate that H3.3K27M cells experiencing UVC-induced DNA lesions take longer to complete replication.

H3.3^{K27M} mutant cells exhibit increased chromosomal instability upon replication stress.

To further determine if replication stress plays a role in the observed increase in CIN in H3.3^{K27M} cells, we studied sensitivity to the chemical compound Aphidicolin (APH), which inhibits DNA polymerases leading to replication stress [55]. We first looked at phosphorylation of RPA, an early marker for replication fork stalling [56] (Fig 3A-B). We found that upon addition of APH, RPA phosphorylation was similar in all conditions (Fig 3B). This suggests that the H3.3^{K27M} replication stress phenotype is not caused by defects in initial replication stress signaling, but rather by altered processing of stalled forks. Unresolved replication forks cause accumulation of pre-mitotic damage and subsequent mitotic defects [57]. Therefore, to determine whether replication stress can result in an abnormal mitotic progression and CIN in H3.3^{K27M} cells, we assessed mitotic abnormalities by time lapse imaging (Fig 3C). Whereas after APH treatment, an increase in abnormal mitoses was observed in all conditions, H3.3^{K27M} cells exhibited significantly more chromosome missegregation events than H3.3^{WT} or EV cells (Fig 3D). Qualitative analysis of the abnormal mitoses revealed an increase in lagging chromatin and anaphase bridges (Fig 3E-F). This is suggestive of persisting under-replicated DNA in mitosis, leading to DNA entanglements that ultimately cause segregation defects [58].

Notably, a specific class of mitotic DNA structures called Ultrafine Anaphase Bridges (UFBs) has been described to form from under-replicated DNA following replicative stress [59–61]. However, unlike bulky anaphase bridges, UFBs are histone free and cannot be visualized by common DNA binding dyes, and would thus be missed in our time lapse imaging experiments. Therefore, we again treated our cells with APH, synchronized them in mitosis with nocodazole, released them into anaphase and subsequently performed immunofluorescence for UFB marker BLM and kinetochore marker CREST (Fig 3G-I) [59,60]. This revealed a greater occurrence of BLM coated DNA fibers in H3.3^{K27M}, indicating an increase in UFBs (Fig 3I) (55%, 37%, 40%, and 37% for H3.3^{K27M}, H3.3^{WT150}, H3.3^{WT500}, and EV, respectively). Altogether, these data reveal a link between increased sensitivity to replication stress and mitotic

aberrancies that may ultimately propagate copy number alterations in an oncohistone context.

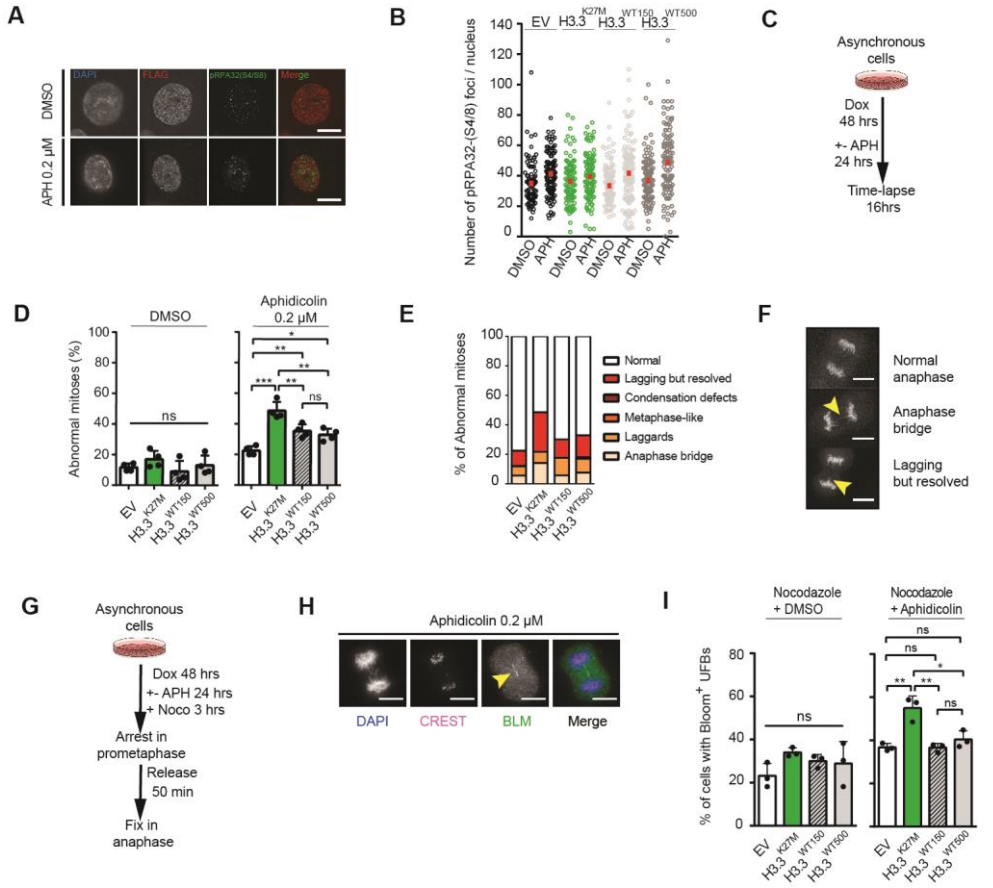

Figure 3. H3.3^{K27M} cells are sensitive to replication stress.

(A) Representative images of multiple pRPA32(S4/S8) nuclear foci in untreated and Aphidicolin (APH) treated cells. Scale bars represent 10 µm. **(B)** Quantification of the initial replication stress response by pRPA32(S4/S8) staining in DMSO or Aphidicolin (APH) treated cells. Each circle represents a single nucleus, means are represented by a red square (n=1 experiment with > 95 nuclei per condition). **(C)** Experimental outline for measuring chromosomal instability by time lapse microscopy under replication stress conditions (low dose (0.2 µM) Aphidicolin (APH) treatment for 24 hrs on 48 hrs doxycycline-treated cells). **(D)** Time lapse imaging of mitotic features following 24 hrs Aphidicolin treatment. Mitotic features were scored as normal, or abnormal. Data represent mean percentages of abnormal mitoses ± SD (n=4 experiments), with a minimum of 20 mitoses per condition), *P=0.0342, **P=0.0011, 0.0058 and 0.0070, ****P<0.0001 (two-way ANOVA, Tukey correction for multiple comparisons). **(E)** Chart representing type and distribution of mitotic abnormalities after Aphidicolin (APH) treatment. **(F)** Images showing the most common mitotic features induced by Aphidicolin treatment in H3.3^{K27M} cells. Scale bar represents 10 µm. **(G)** To determine the number of replication stress-induced DNA ultrafine bridges (UFBs), doxycycline induced asynchronized cells where treated with Aphidicolin (APH) for 24 hrs and subsequently blocked in mitosis with nocodazole to enrich for mitotic cells. After release, cells were fixed in anaphase enabling visualization of DNA UFBs coated with Bloom (BLM, immunolabeling) helicase (arrowhead) as seen in panel **(H)**. CREST immunolabeling revealing kinetochores. Scale bars represents 10 µm. **(I)** Quantification

of Bloom coated DNA UFBs upon Aphidicolin treatment. Data are represented as means ±SD (n=3 experiments with > 30 mitoses per condition), *P= 0.0161; **P=0.0025 and 0.0023, (two-way ANOVA, Tukey correction for multiple comparisons).

H3.3^{K27M} mutant cells do not induce 53BP1 nuclear bodies in response to UFBs

Unresolved UFBs tend to break during mitotic exit [62]. These breaks lead to symmetrically inherited DNA damage in daughter cells, which co-occurs with large nuclear bodies containing the p53 Binding Protein-1 (53BP1) and other proteins [63,64]. To study 53BP1 nuclear body (53BP1 NB) formation following APH treatment, we generated a new set of inducible histone cell lines co-expressing a 53BP1-EGFP fusion protein and performed time lapse imaging (Fig 4A-B). In line with the observed increase in UFBs (Fig 3I), we observed an increase in 53BP1 NBs following APH treatment in all conditions. Yet surprisingly, H3.3^{K27M} cells did not show a higher increase in 53BP1 NB formation compared to H3.3^{WT} or EV cells (Fig 4C). This either suggests that the increased replication stress is timely resolved, or alternatively, that the 53BP1 response following UFB formation is inadequate in H3.3^{K27M} cells, as we expected more 53BP1 NBs in H3.3^{K27M} cells due to the higher incidence of UFBs. To address this in an oncogenic setting, we looked at the expression of 53BP1 NBs in a panel of pediatric gliomas that were either histone wild type (WT-HGG, n=5), or H3.3 mutant (H3.3-HGG, n=6) (Fig 4D-E). We found that whereas H3.3 mutant gliomas were highly proliferative as revealed by PCNA staining (Fig 4E), they exhibited low 53BP1 nuclear body counts in comparison to histone-wild type glioma (Fig 4E). This corroborates an inadequate 53BP1 NB response in the presence of the H3.3^{K27M} oncohistone.

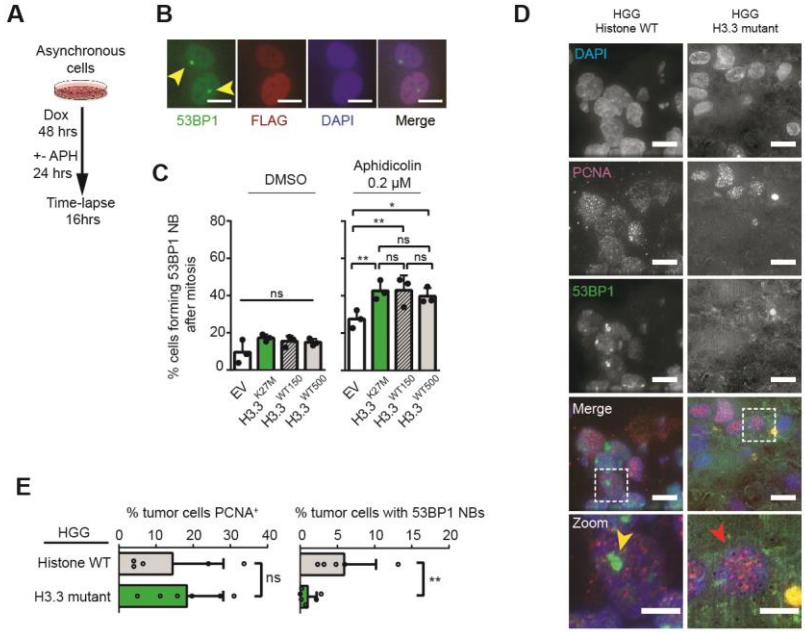

Figure 4. Altered 53BP1 response in H3.3^{K27M} cells and glioma.

(A) Experimental outline for measuring 53BP1 nuclear body formation by time lapse microscopy in replication stress conditions (Low dose Aphidicolin (0.2 uM) treatment for 24 hrs following 48 hrs of doxycycline induction). **(B)** Immunofluorescent images depicting typical mirrored 53BP1 nuclear bodies in two daughter cells commonly seen after rupture of an unresolved DNA UFB. Scale bar represents 10 µm. **(C)** Quantification of 53BP1 nuclear bodies (NB) following 24 hrs Aphidicolin treatment by time lapse microscopy. Chart representing the percentage of cells with 53BP1 nuclear body formation after mitosis. Data are represented as means ±SD (n=3 experiments with > 20 mitoses per condition), *P=0.0145, **P=0.0032, **P=0.0028 (two-way ANOVA, Tukey correction for multiple comparisons). **(D)** Representative images of two pediatric HGG samples stained for proliferation marker PCNA (red arrows) and 53BP1 (yellow arrows) to reveal the nuclear body load. Dashed squares indicate the zoomed area. Scale bar represents 10 µm (5 µm on zooms). **(E)** Quantification of the proliferation rate (*i.e.,* percentage of PCNA positive cells) and 53BP1 nuclear body (NB) load (percentage 53BP1 positive cells) per tumor. Each circle represents the number for one tumor (HGG Histone^{WT}, n=5 ; HGG Histone$^{H3.3\ Mutant}$, n=6). Data are represented as means per histone group ±SD (with > 200 cells analyzed per tumor). **P=0.0087 (Mann Whitney non-parametric t-test).

DISCUSSION

Whereas the changes in epigenetic patterning in histone mutant gliomas have been extensively investigated [1–4,6,9,65], the exact mechanisms driving oncogenesis remain elusive to date. Rather than being solely dependent on transcriptional changes, we hypothesize that pediatric high-grade glioma results from an interplay of multiple pro-tumorigenic processes that are related to the different functions of the multifaceted (onco)histone H3.3. These include H3.3 as an epigenome/transcriptome regulator, but also as important actor in different DNA damage repair mechanisms and in maintenance of genome integrity, which can explain the tendency for H3.3 mutant gliomas to be more aneuploid [4,16,24,66–68]. The latter idea was explored in this study, in which we discovered that histone mutant H3.3^{K27M} cells are more susceptible to genome instability resulting from an intrinsic sensitivity to stress during DNA replication.

While studying the mechanism underlying the strong genomic instability found in H3.3^{K27M} HGG, we made a number of observations that point at H3.3^{K27M} deregulating several, possibly distinct, processes. For instance, the more rapid resolution of the γ-H2AX signal following UVC exposure could indicate that DNA damage signaling ceases prematurely in the presence of the H3.3^{K27M} mutant histone. This could allow damaged cells to pass the G2 cell cycle checkpoint and progress into mitosis. Interestingly, in our mitotic pulldown experiments, we uncovered an enrichment for DNA replication components, comprising PCNA, Mini-Chromosome-Maintenance proteins (MCMs) and replicative histone chaperones, in H3.3^{K27M} cells. This was unexpected, as although MCM proteins have been identified as direct histone H3 interactors previously, these factors are typically unloaded prior to mitosis [47,48,69,70]. Under physiological conditions, the MCM complex assembles in G1 as a pre-replisome complex on DNA in a process called origin licensing [71]. In late G1 and S-phase, interaction with the replicative helicase converts the structure into the replicative-complex that initiates replication, or origin firing [72]. Of note, MCM complexes are widely deposited throughout the genome, but most remain dormant and only become activated during replication stress to ensure complete genome duplication [73–75]. When this process fails, PCNA and MCMs remain stably locked

with un-replicated chromatin throughout the cell cycle until the next S-phase, and this might lead to MCM binding to mitotic DNA [48,49,76,77]. Thus, the increased binding of MCM proteins to H3.3^{K27M} may result from stalled replication forks that were not resolved prior to mitosis. The reason for this remains speculative, but it is possible that replication stress-induced damage remained undetected until mitosis due to improper DNA damage signaling. An alternative explanation is that changes in the epigenetic landscape due to H3.3^{K27M} expression impair origin licensing or firing. Yet it is also possible that the Lysine 27 substitution directly interferes with MCM binding [47,48,69,70].

Further evidence for unresolved DNA replication problems in mitotic H3.3^{K27M} cells is provided by the increased numbers of UFBs. Normally, mitotic DNA synthesis (MiDAS) of under-replicated DNA provides the lattermost opportunity to complete DNA replication and therefore tackle extensive genome instability [49]. Hence, it is possible that MiDAS is also impaired in H3.3^{K27M} cells, especially since H3.3^{K27M} inhibits the EZH2 histone methyltransferase that places the H3K27me^3 mark [10,15,78,79]. H3K27me^3 is not only involved in gene repression, but also serves as docking platform for the MiDAS factor MUS81 [49,80–82]. Of note, we did not pulldown MUS81 in our immunoprecipitations, suggesting that MUS81 does not directly associate with H3.3 as proposed by others [80], or alternatively, that its association is already disrupted in mitosis.

Finally, we found that UFBs did not trigger an increased recruitment of 53BP1 nuclear bodies in H3.3^{K27M} cells, suggesting that not all UFB breaks are buffered by this salvage mechanism. This finding is in line with a study in which a lowered 53BP1 response was seen after DNA damage induction when H3K27 was hypomethylated [83]. This is further accentuated by the H3.3 mutant tumors, which exhibited relatively low numbers of 53BP1 nuclear bodies compared to histone wild type tumors. Indeed, H3.3 gliomas tend to co-mutate DNA repair enzymes that also have a role in 53BP1 nuclear body formation [4]. Disruption of such a repair mechanism might enhance genome plasticity and heterogeneity of the tumor, and ultimately help the cancer cells to thrive. Considering the additional (defective) mechanisms in which the (mutated) histone is involved, including those mentioned above, it is not difficult to

imagine that efficient targeting of pediatric high-grade glioma is highly challenging. Therefore, obtaining a full understanding of tumor biology will be instrumental in finding novel angles for therapy.

MATERIALS AND METHODS

Pediatric high-grade glioma samples and dataset

Distribution of DNA copy number alterations (CNAs) of pediatric high-grade gliomas was determined using a publicly available dataset of pediatric high-grade gliomas consisting of 4 subtypes: H3.3G34R/V mutant (n=63), H3.3K27M mutant (n=245), H3.1/H3.2K27M mutant (n=50), and H3 wild type (n=387)[4]. Autosomal copy number aberrations per tumor were summed and CNA distribution was compared between tumor subtypes (Mann Whitney).

The pediatric H3.3K27M HGG sample subjected to single-cell WGS was obtained following surgical resection at diagnosis at the University Medical Center Groningen, the Netherlands. Histone wild type and mutant HGG samples subjected to immunostainings were used in an irreversibly anonymized manner and in concordance with local ethics regulations.

Single-cell whole genome sequencing

A single cell suspension was freshly prepared by trituration of the resected tumor tissue and subsequent digestion with Accutase (Gibco A1110501). The cell suspension was cryopreserved in 10% DMSO. For single nuclei sorting, cells were resuspended in staining buffer (1M tris-HCl pH7.4, 5M NaCl, 1M $CaCl_2$, 1M $MgCl_2$, 7.5% BSA, 10% NP-40, ultra-pure water, 10 mg/ml Hoechst 33358, 2 mg/ml propidium iodide), and kept on ice in the dark to facilitate lysis. G1 single nuclei, as assessed by PI and Hoechst staining, were sorted into 96 wells plates on a MoFlo-Astrios flow cytometer (Beckman Coulter). Nuclei were lysed and DNA was barcoded, followed by automated library preparation (Agilent Bravo robot) as described previously [84]. Single cell libraries were pooled and analyzed on an Illumina

Hiseq2500 sequencer. Sequencing data were analyzed with the R-package AneuFinder as previously described [32].

Immunofluorescence labeling of pediatric high-grade glioma samples

For immunofluorescence stainings, 2 µm serial paraffin sections were deparaffinized with xylene, rehydrated with ethanol 100%, 96% and 70% and water. Antigen retrieval was performed using citrate buffer. Sections were blocked with 5% normal goat serum and 0.1% Triton in PBS and incubated overnight with anti-53BP1 antibody (1/100, Cell Signaling 4937) and anti-PCNA antibody (1/2000, Abcam Ab29). Secondary antibodies were goat anti-mouse-568 and anti-rabbit-488 (Invitrogen). Sections were counterstained with DAPI and mounted with Vectashield (Vector laboratories). Sections were imaged on a DeltaVision Elite imaging station (Applied Precision, GE Healthcare). Images were deconvolved using SoftWork suite, and blinded and randomized for analysis with ImageJ.

Generation of pLVX-tight-puro-FLAG-H3F3A-WT and K27M mutant expression vectors

pcDNA4/TO-FLAG-H3.3 was a gift from Bing Zhu (Addgene plasmid # 47980; http://n2t.net/addgene:47980; RRID:Addgene_47980) [85]. pCDNA4/TO-FLAG-H3F3A-K27M mutant was generated using Q5® Site-Directed Mutagenesis Kit (New England Biolabs Inc.) according to the manufacturer's recommendations. Mutagenesis primers used were designed using NEBaseChanger®: Forward: GCCGCTCGCAtGAGTGCGCCC; Reverse: TTTTGTAGCCAGTTGCTTCCTGGG). Vectors were sequenced to validate the presence of the mutation *A(A>T)G (nucleotide number 296)* (CMV^{Fwd}: CGCAAATGGGCGGTAGGCGTG, BGH^{Rev}: TAGAAGGCACAGTCGAGG). Both WT and mutant cloning vectors were digested with BamH1 and EcoR1 to obtain the FLAG-H3F3A and FLAG-H3F3A-K27M containing inserts that were subsequently cloned into pLVX-Tight-puromycin (Clontech).

Cell culture conditions and lentiviral transductions

All human RPE1-hTERT immortalized cell lines (hereafter referred to as RPE1) were cultured in DMEM (Gibco) + 10% FBS (Clontech) and 1% penicillin-streptomycin (Gibco). Doxycycline inducible RPE1 cell lines were generated by retroviral transduction of pRetrox-rtTA with subsequent Geneticin selection. The pLVX-Tet-On system was used and cells were transduced with either pLVX-tight-puro (hereafter referred as empty vector/EV), pLVX-tight-puro-FLAG-H3F3A-WT ($H3.3^{WT}$) or pLVX-tight-puro-FLAG-H3F3A-K27M ($H3.3^{K27M}$) lentivirus and selected with Puromycin. For visualization of 53BP1 nuclear body formation, cell lines were transduced with pLNCX-53BP1-EGFP construct kindly provided by Dr. Marcel van Vugt. The transduced population was enriched by sorting for GFP positive cells. All cell lines were tested free of mycoplasma.

Immunoprecipitation, LC/MS-MS analysis, label-free quantification and STRING analysis.

$H3.3^{WT}$, $H3.3^{K27M}$ or EV cell lines were used for FLAG pull-down of H3.3 interacting proteins from total protein extracts of synchronized mitotic fractions. Hereto, cells were incubated with doxycycline (500 ng/ml, Sigma D9891) for 48 hrs. Subsequently, cells were treated with nocodazole (100 ng/ml, Sigma M1404, 8 hrs) after which a mitotic shake off was performed. Mitotic cells were kept at 4C unless stated otherwise. Mitotic cell pellets were carefully washed with ice-cold PBS and resuspended in immunoprecipitation buffer containing 20 mM Tris at pH7.4, 100mM NaCl, 5 mM $MgCl_2$, 0.1% Triton X-100, 10% glycerol, 1 mM DTT, Complete protease inhibitors (EDTA-free, Roche 11873580001), phosphatase inhibitors (PhosSTOP, Roche 4906845001) and given 30 strokes with a douncer (Tissue grinder set 2ml, Sigma D8938). DNA was digested with 1U/µl OmniCleave™ Endonuclease (Epicentre OC7850K) for 30 minutes. The insoluble fraction was removed by centrifugation at 15,000 rpm for 10 min. Supernatant was subjected to immunoprecipitation with α-FLAG- M2 magnetic beads (Sigma, M8823) for 2 hrs with gentle rotation. Beads were washed three times with TBS. For subsequent mass-spectrometry analysis, precipitated proteins were first eluted by two rounds of competition with 3X FLAG Peptide (50 µl, Sigma F4799). Then, beads were boiled

in loading buffer without DTT to elute remaining proteins. For Western blot, precipitated proteins were eluted in sample buffer (50 mM DTT).

Eluates were submitted to an in-gel tryptic digestion and proteins were separated by LC/MS-MS (Ultimate 3000 nanoHPLC Liquid Chromatography instrument (Dionex) coupled to an LTQ-Orbitrap XL (Thermo Fisher Scientific) mass spectrometer instrument). Four technical replicates were performed per condition. Protein identification and data processing was performed using PEAKS 8.5 open-source software. To quantify the protein interactome, a label free quantification method using the spectral counts of each identified interactor was performed. Nucleosomal content and pull-down efficiency was assessed based on histone H4 spectral counts ($H4^{spec/c}$) and technical replicates with $H4^{spec/c}$ above background (e.g. average EV [$H4^{spec/c}$]) were kept for further analysis. Spectral counts in the EV cell line were considered as background and therefore subtracted from the spectral counts in $H3.3^{WT}$ and $H3.3^{K27M}$ samples. Output data was corrected for nucleosomal content by normalization to the $H4^{spec/c}$ of the $H3.3^{WT}$ sample.

Average spectral counts per precipitated protein were compared between $H3.3^{WT}$ and $H3.3^{K27M}$ samples. Precipitated proteins were classified either as *unique binding partners*, *common/not enriched binding partners* (when the difference between $H3.3^{WT}$-[$Partner^{spec/c}$] and $H3.3^{K27M}$-[$Partner^{spec/c}$] was ≤2 spectral counts), or *common/enriched binding partners* (when the difference between $H3.3^{WT}$-[$Partner^{spec/c}$] and $H3.3^{K27M}$-[$Partner^{spec/c}$] was >2 spectral counts). For identification of enriched networks, protein lists were submitted to STRING database (www.string.org). Pathway and reactome analysis were performed with the highest degree of confidence (strength of data support = 0.9) and disconnected nodes were hidden. For clustering, Markov Clustering (MCL) method was used with an inflation degree of 1.5. The illustrated network maps were simplified by manual curation for clarity.

Time lapse imaging

$H3.3^{WT}$, $H3.3^{K27M}$ or EV cells were seeded onto Lab-Tek II chambered coverglass (Thermo Fisher 155409). Expression of FLAG-$H3.3^{WT}$ was induced with 150 and 500

ng/ml doxycycline or with 500 ng/ml doxycycline for FLAG-H3.3^{K27M} for 24-48 hrs. Two hours prior to imaging, cells were refreshed with media containing 150 or 500 ng/ml doxycycline and 20 nM fluorescent DNA binding dye (SirDNA, Spirochrome TebuBio) [86]. Cells were imaged for 16 hrs on a DeltaVision Elite imaging station (Applied Precision, GE Healthcare). Movies were deconvolved using SoftWork suite and analyzed with ImageJ.

Cell culture treatments and immunofluorescence labeling

For immunofluorescence experiments on RPE1 cells, cells were treated with doxycycline for 48 hours and subsequently seeded onto 13 mm glass coverslips. They were fixed with 4% paraformaldehyde/PBS, permeabilized with 0.25% Triton X-100 and blocked with 5% BSA, 0.05% Tween20 (Sigma) in PBS. Cells were subsequently incubated overnight at 4°C (unless stated otherwise) using the following primary antibodies diluted in 1% BSA 0.05% Tween-20 in PBS: Mouse anti-FLAG (2 hours, room temperature, 1/1000, Sigma F1804), Rabbit anti-Bloom (1/200, Abcam Ab2179), Human anti-CREST (Fitzgerald, 90C-CS1058), Rabbit anti-53BP1 (1/200, Cell Signaling 4937), Rabbit anti-phosphoRPA32(S4/S8) (1/500, Bethyl A300-245A). Secondary antibodies were goat anti-rabbit Alexa-488, goat anti-mouse Alexa 568 and goat anti-human Alexa-633 (1/500, Invitrogen). Counterstaining was performed with DAPI. All coverslips were mounted using Vectashield (Vector laboratories).

Replication stress was visualized and quantified by staining for phosphorylated RPA32(S4/S8) positive nuclear foci. Cells were treated with doxycycline for 48 hrs before addition of aphidicolin or DMSO (0.4 µM). After 24 hours Aphidicolin (or DMSO) treatment, cells were fixed and stained as described above. pRPA foci were visualized on a DeltaVision Elite imaging station (Applied Precision, GE Healthcare). Cells were identified by DAPI and FLAG staining. Pictures were deconvolved using SoftWork suite and analyzed with ImageJ. pRPA foci were counted in an automated fashion using CellProfiler software (v3.1.9). For visualization of DNA ultrafine bridges coated with Bloom helicase protein, EV, H3.3^{K27M} were first treated with 500 ng/ml doxycycline and H3.3^{WT} with 150ng/ml and 500 ng/ml doxycycline for 48 hours, then

Aphidicolin (0.2 µM, Sigma)) or DMSO was added for 24 hrs. Treated cells were synchronized in prometaphase with nocodazole for 3 hrs and subsequently released and fixed after 50 min as described above. Bloom positive ultra-fine bridges were visualized on a Leica SP8X DLS confocal microscope and analyzed with ImageJ.

Western Blot

Total protein extracts and pulled-down samples were boiled in sample buffer and loaded onto Mini-PROTEAN TGX™ precast gels (Biorad). Proteins were transferred to a PVDF membrane (Trans-Blot Turbo Transfer System, Biorad), and probed for the following antibodies: Mouse anti-FLAG (1/1000, Sigma F1804), Mouse anti-total H3 (1/1000, Cell Signaling 3638), Rabbit anti-Histone H3.3 (1/1000, Clone RM190 Rev mab biosciences 31-1058-00), Rabbit anti-H3K27me^3 (1/1000, Cell signaling 9733), Mouse anti-H4 (1/1000, Active motif 61521), Goat anti-MCM2 (1/1000, Bethyl A300-122A-T), Rabbit anti-MCM7 (1/1000, Bethyl A302-584A-T), and Rabbit anti-MCM4 (1/1000, Bethyl A300-193A-T). HRP labelled Goat anti-Mouse or Rabbit, or Donkey anti-Goat secondary antibodies were used to visualize protein expression using chemiluminescence substrate (SuperSignal™ West Dura Extended Duration Substrate, Thermo 34076) on a ChemiDoc system (Biorad).

Flow cytometry

For flow cytometry analysis, cells were induced with doxycycline (500 ng/ml) for 48 hrs, and subsequently treated with Nocodazole or DNA damage inducing agents to test the integrity of the mitotic and G2 checkpoints, respectively, or to test the DNA damage response. At indicated time points, cells were resuspended dropwise in ice-cold 80% ethanol and stored at -20°C until further analysis. All primary stainings were performed overnight at 4°C. Cells were subsequently incubated with FITC-conjugated secondary antibodies (1/50, DAKO) and counterstained with Propidium Iodide (PI) (5 µg/ml) and RNAseA (10 µg/ml) solution to assess DNA content. Data were acquired by flow cytometry on a FACSCalibur station (Becton Dickinson) and analyzed with FlowJo software (v10.0.7.2, FlowJo, LLC).

Nocodazole challenge

To test the integrity of the mitotic checkpoint, doxycycline-induced cells were treated with nocodazole (12 hrs, 100 ng/ml) to challenge the spindle assembly checkpoint (SAC). Cells were fixed as described above, and the mitotic fraction was assessed by staining for the mitotic histone phosphorylation marks Mouse anti-H3S10P (1/200, Active motif 39636), Rabbit anti-H3S28P (1/200, Abcam ab32388) and Rabbit anti-H3.3S31P (1/250, Abcam ab92628).

Analysis of G2 checkpoint integrity with nocodazole block

To determine the integrity of the G2 checkpoint, asynchronized doxycycline-induced cells were treated with UVC (10 J/m^2, UVC500 Crosslinker, Amersham Biosciences Corp.), a 1 hr pulse of Cisplatin (5 µM, Accord), or γ-rays (2 Gy, IBL 637 Cesium-137γ-ray machine) to induce DNA damage. Subsequently, progression through mitosis was blocked by nocodazole treatment (100 ng/ml). Cells were fixed 24 hrs after the induction of DNA damage as described above, and mitotic content was quantified with Mouse anti-H3S10P staining (1/200, Active motif 39636)

γH2AX phosphorylation time curve and cell cycle analysis

48 hrs doxycycline treated cells were UVC irradiated (15J/m^2, UVC500 Crosslinker, Amersham Biosciences Corp.) and fixed at 1 and 6 hrs after irradiation in 1% paraformaldehyde, resuspended dropwise in ice-old 80% ethanol and stored at -20°C for at least 24 hrs. DNA damage response was assessed by staining for Rabbit anti-γH2AX (1/200, Cell Signaling 9718).

UVC and ɣ-ray proliferation assays

To perform ɣ-ray sensitivity assays, 48 hrs doxycycline induced cells were seeded into 96 wells plates and irradiated with ɣ-rays (0, 0.5 and 2 Gy, IBL 637 Cesium-137γ-ray machine) the following day. Cells were allowed to proliferate for an additional 7 days. For UVC sensitivity assays, 48 hrs doxycycline induced cells were washed thoroughly with PBS and irradiated with UVC (0, 1 and 7 J/m^2, UVC500 Crosslinker, Amersham Biosciences Corp.). Cells were then replated into 96 wells plates and grown for 7 days. Doxycycline was refreshed every 48 hrs. At day 7, cells were fixed with 8% paraformaldehyde, washed with PBS and stained with crystal

violet. Crystal violet was dissolved in 1% SDS solution and absorbance (595nm) was measured.

Statistics

Statistical analysis was done using Graphpad Prism (version 6.0). Gaussian distribution of data was tested using the Shapiro-Wilk normality test and statistical testing performed accordingly. Significance of statistical testing was assessed by two-tailed, unpaired tests and is indicated as follows: ∗∗∗∗P < 0.0001, ∗∗∗P < 0.001, ∗∗P < 0.01, and ∗P < 0.05. ns, not significant. Error bars represent SD (Standard deviation).

AUTHORS CONTRIBUTIONS

Conceptualization, I.B. M.A.T.M.v.V., F.F., and S.W.M.B.; Methodology, I.B., T.E.I.M., E.S.C.M, I.A., P.L.B., T.G.J.M.B., B.B., D.C.J.S., M.A.T.M.v.V., F.F., and S.W.M.B.; Software and Formal Analysis, I.B., T.E.I.M., E.S.C.M.; Investigation, I.B., T.E.I.M., E.S.C.M.; Resources, I.B., T.E.I.M., E.S.C.M., C.S., Y.P.K. and U.S.; Data Curation, I.B.; Writing, I.B. and S.W.M.B.; Writing – Review and Editing, I.B., T.E.I.M., E.S.C.M., U.S., M.A.T.M.v.V., F.F., and S.W.M.B.; Visualization, I.B.; Supervision and Project Administration, F.F. and S.W.M.B.; Funding Acquisition, I.B., I.A., U.S., M.A.T.M.v.V, F.F., and S.W.M.B.

ACKNOWLEDGEMENTS

This study was supported by a De Cock-Hadders foundation grant to I.B.; the Coordenação de Aperfeiçoamento de Pessoal de Nível Superior, Brasil, CAPES, Finance Code 001 (E.S.C.M.); an Indonesia Endowment Fund for Education (LPDP) doctoral grant (PRJ-2572/LPDP/2015) to I.A; the Fördergemeinschaft Kinderkrebszentrum Hamburg (U.S.); a grant from the Netherlands Organization for Scientific Research (NWO-VIDI # 917.13334) to M.A.T.M.v.V; a grant from the European Research Council (ERC-Consolidator grant “TENSION”) to M.A.T.M.v.V;

a KWF project grant (2018-RUG-11457) to F.F; a Stichting Kinderoncologie Groningen/SKOG project grant (16-003) to S.B; a Rosalind Franklin fellowship from the University of Groningen to S.B.; and a Dutch Cancer Society/KWF career award (RUG 2014-6903) to S.B.

CONFLICT OF INTEREST

The authors declare no conflict of interest.

REFERENCES

1. Castel, D. *et al.* Histone H3F3A and HIST1H3B K27M mutations define two subgroups of diffuse intrinsic pontine gliomas with different prognosis and phenotypes. *Acta Neuropathol.* **130**, 815–827 (2015).

2. Wu, G. *et al.* Somatic histone H3 alterations in pediatric diffuse intrinsic pontine gliomas and non-brainstem glioblastomas. *Nat. Genet.* **44**, 251–253 (2012).

3. Schwartzentruber, J. *et al.* Driver mutations in histone H3.3 and chromatin remodelling genes in paediatric glioblastoma. *Nature* **482**, 226–231 (2012).

4. Mackay, A. *et al.* Integrated Molecular Meta-Analysis of 1,000 Pediatric High-Grade and Diffuse Intrinsic Pontine Glioma. *Cancer Cell* **32**, 520-537.e5 (2017).

5. Sturm, D. *et al.* Hotspot mutations in H3F3A and IDH1 define distinct epigenetic and biological subgroups of glioblastoma. *Cancer Cell* **22**, 425–37 (2012).

6. Castel, D. *et al.* Transcriptomic and epigenetic profiling of 'diffuse midline gliomas, H3 K27M-mutant' discriminate two subgroups based on the type of histone H3 mutated and not supratentorial or infratentorial location. *Acta Neuropathol. Commun.* **6**, 117 (2018).

7. Larson, J. D. *et al.* Histone H3.3 K27M Accelerates Spontaneous Brainstem Glioma and Drives Restricted Changes in Bivalent Gene Expression. *Cancer Cell* **35**, 140-155.e7 (2019).

8. Pathania, M. *et al.* H3.3 K27M Cooperates with Trp53 Loss and PDGFRA Gain in Mouse Embryonic Neural Progenitor Cells to Induce Invasive High-Grade Gliomas. *Cancer Cell* **32**, 684-700.e9 (2017).

9. Bender, S. *et al.* Reduced H3K27me3 and DNA Hypomethylation Are Major Drivers of Gene Expression in K27M Mutant Pediatric High-Grade Gliomas. *Cancer Cell* **24**, 660–672 (2013).

10. Lewis, P. W. *et al.* Inhibition of PRC2 activity by a gain-of-function H3 mutation found in pediatric glioblastoma. *Science (80-.).* **340**, 857–861 (2013).

11. Venneti, S. *et al.* Evaluation of histone 3 lysine 27 trimethylation (H3K27me3) and enhancer of zest 2 (EZH2) in pediatric glial and glioneuronal tumors shows decreased H3K27me3 in H3F3A K27M mutant glioblastomas. *Brain Pathol.* **23**, 558–564 (2013).

12. Zhang, Y. *et al.* Molecular basis for the role of oncogenic histone mutations in modulating H3K36 methylation. *Sci. Rep.* **7**, 1–9 (2017).

13. Stafford, J. M. *et al.* Multiple modes of PRC2 inhibition elicit global chromatin alterations in H3K27M pediatric glioma. *Sci. Adv.* **4**, (2018).

14. Justin, N. *et al.* Structural basis of oncogenic histone H3K27M inhibition of human polycomb repressive complex 2. *Nat. Commun.* **7**, 11316 (2016).

15. Mohammad, F. *et al.* EZH2 is a potential therapeutic target for H3K27M-mutant pediatric gliomas. *Nat. Publ. Gr.* **23**, (2017).

16. Gröbner, S. N. *et al.* The landscape of genomic alterations across childhood cancers. *Nature* **555**, 321–327 (2018).

17. Paugh, B. S. *et al.* Genome-wide analyses identify recurrent amplifications of receptor tyrosine kinases and cell-cycle regulatory genes in diffuse intrinsic pontine glioma. *J. Clin. Oncol.* **29**, 3999–4006 (2011).

18. Khuong-Quang, D. A. *et al.* K27M mutation in histone H3.3 defines clinically and biologically distinct subgroups of pediatric diffuse intrinsic pontine gliomas. *Acta Neuropathol.* **124**, 439–447 (2012).

19. Zarghooni, M. *et al.* Whole-genome profiling of pediatric diffuse intrinsic pontine gliomas highlights platelet-derived growth factor receptor α and poly (ADP-ribose) polymerase as potential therapeutic targets. *J. Clin. Oncol.* **28**, 1337–1344 (2010).

20. Nikbakht, H. *et al.* Spatial and temporal homogeneity of driver mutations in diffuse intrinsic pontine glioma. *Nat. Commun.* **7**, (2016).

21. Yadav, R. K. *et al.* Histone H3G34R mutation causes replication stress, homologous recombination defects and genomic instability in S. pombe. *Elife* **6**, 1–28 (2017).

22. Fang, J. *et al.* Cancer-driving H3G34V/R/D mutations block H3K36 methylation and H3K36me3–MutSα interaction. *Proc. Natl. Acad. Sci.* **115**, 9598–9603 (2018).

23. Frey, A., Listovsky, T., Guilbaud, G., Sarkies, P. & Sale, J. E. Histone H3.3 is required to maintain replication fork progression after UV damage. *Curr. Biol.* **24**, 2195–2201 (2014).

24. Ray-Gallet, D. *et al.* Dynamics of Histone H3 Deposition In Vivo Reveal a Nucleosome Gap-Filling Mechanism for H3.3 to Maintain Chromatin Integrity. *Mol. Cell* **44**, 928–941 (2011).

25. Adam, S. *et al.* Real-Time Tracking of Parental Histones Reveals Their Contribution to Chromatin Integrity Following DNA Damage. *Mol. Cell* **64**, 65–78 (2016).

26. Adam, S., Polo, S. E. & Almouzni, G. XTranscription recovery after DNA damage requires chromatin priming by the H3.3 histone chaperone HIRA. *Cell* **155**, 94 (2013).

27. Luijsterburg, M. S. *et al.* PARP1 Links CHD2-Mediated Chromatin Expansion and H3.3 Deposition to DNA Repair by Non-homologous End-Joining. *Mol. Cell* **61**, 547–562 (2016).

28. Hoeman, C. M. *et al.* ACVR1 R206H cooperates with H3.1K27M in promoting diffuse intrinsic pontine glioma pathogenesis. *Nat. Commun.* **10**, (2019).

29. Lee, Y. *et al.* Neurogenesis requires TopBP1 to prevent catastrophic replicative DNA damage in early progenitors. *Nat. Neurosci.* **15**, 819–826 (2012).

30. Woodworth, M. B. *et al.* Somatic mutation in single human neurons tracks developmental and transcriptional history. *Science (80-.).* **350**, 94–98 (2015).

31. Wei, P. C. *et al.* Long Neural Genes Harbor Recurrent DNA Break Clusters in Neural Stem/Progenitor Cells. *Cell* **164**, 644–655 (2016).

32. Bakker, B. *et al.* Single-cell sequencing reveals karyotype heterogeneity in murine and human malignancies. *Genome Biol.* **17**, 115 (2016).

33. Durkin, S. G. *et al.* Replication stress induces tumor-like microdeletions in FHIT/FRA3B. *Proc. Natl. Acad. Sci. U. S. A.* **105**, 246–251 (2008).

34. Worrall, J. T. *et al.* Non-random Mis-segregation of Human Chromosomes. *CellReports* **23**, 3366–3380 (2018).

35. Soto, M. *et al.* p53 Prohibits Propagation of Chromosome Segregation Errors that Produce Structural Report p53 Prohibits Propagation of Chromosome Segregation Errors that Produce Structural Aneuploidies. 2423–2431 (2017). doi:10.1016/j.celrep.2017.05.055

36. Singh, R. K. *et al.* Excess histone levels mediate cytotoxicity via multiple

mechanisms. *Cell Cycle* **9**, 4236–4244 (2010).

37. Funato, K., Major, T., Lewis, P. W., Allis, C. D. & Tabar, V. Use of human embryonic stem cells to model pediatric gliomas with H3.3K27M histone mutation. *Science (80-.).* **346**, 1529–1533 (2014).

38. Foley, E. a & Kapoor, T. M. Microtubule attachment and spindle assembly checkpoint signalling at the kinetochore. *Nat. Rev. Mol. Cell Biol.* **14**, 25–37 (2013).

39. Raynaud, C. *et al.* Chromatin meets the cell cycle. **65**, 2677–2689 (2014).

40. Ohta, S., Taniguchi, T., Sato, N., Hamada, M. & Rappsilber, J. Quantitative proteomics of the mitotic chromosome scaffold Quantitative proteomics of the mitotic chromosome scaffold. 1–56 (2018).

41. Kim, J.-E. Bookmarking by histone methylation ensures chromosomal integrity during mitosis. *Arch. Pharm. Res.* (2019). doi:10.1007/s12272-019-01156-7

42. Lim, J. *et al.* The histone variant H3.3 G34W substitution in giant cell tumor of the bone link chromatin and RNA processing. *Sci. Rep.* **7**, 1–14 (2017).

43. Kim, J. *et al.* Replication Stress Shapes a Protective Chromatin Environment across Fragile Genomic Regions. *Mol. Cell* **69**, 36-47.e7 (2018).

44. Serra-Cardona, A. & Zhang, Z. Replication-Coupled Nucleosome Assembly in the Passage of Epigenetic Information and Cell Identity. *Trends Biochem. Sci.* **43**, 136–148 (2018).

45. Yang, J. *et al.* The Histone Chaperone FACT Contributes to DNA Replication-Coupled Nucleosome Assembly. *Cell Rep.* **14**, 1128–1141 (2016).

46. Grisendi, S., Mecucci, C., Falini, B. & Pandolfi, P. P. Nucleophosmin and cancer. *Nat. Rev. Cancer* **6**, 493–505 (2006).

47. Campos, E. I. *et al.* Analysis of the Histone H3.1 Interactome: A Suitable Chaperone for the Right Event. *Mol. Cell* **60**, 697–709 (2015).

48. Kuipers, M. A. *et al.* Highly stable loading of Mcm proteins onto chromatin in living cells requires replication to unload. *J. Cell Biol.* **192**, 29–41 (2011).

49. Minocherhomji, S. *et al.* Replication stress activates DNA repair synthesis in mitosis. *Nature* **528**, 286–290 (2015).

50. Pladevall-Morera, D. *et al.* Proteomic characterization of chromosomal common fragile site (CFS)-associated proteins uncovers ATRX as a regulator of CFS stability. *Nucleic Acids Res.* **47**, 8004–8018 (2019).

51. Jasencakova, Z. *et al.* Replication Stress Interferes with Histone Recycling and Predeposition Marking of New Histones. *Mol. Cell* **37**, 736–743 (2010).

52. Burrell, R. A. *et al.* Replication stress links structural and numerical cancer chromosomal instability. *Nature* **494**, 492–496 (2013).

53. Frey, A., Listovsky, T., Guilbaud, G., Sarkies, P. & Sale, J. E. Histone H3.3 is required to maintain replication fork progression after UV damage. *Curr. Biol.* (2014). doi:10.1016/j.cub.2014.07.077

54. Kaufmann, W. K. The human intra-S checkpoint response to UVC-induced DNA damage. **31**, 751–765 (2010).

55. Glover, T. W., Berger, C., Coyle, J. & Echo, B. DNA polymerase α inhibition by aphidicolin induces gaps and breaks at common fragile sites in human chromosomes. *Hum. Genet.* **67**, 136–142 (1984).

56. Ashley A. K., Shrivastav M., N. J. DNA-PK Phosphorylation of RPA32 Ser4/Ser8 Regulates Replication Stress Checkpoint Activation, Fork Restart, Homologous Recombination and Mitotic Catastrophe. *DNA Repair* 131–139 (2015). doi:10.1016/j.dnarep.2014.04.008.DNA-PK

57. Mankouri, H. W., Huttner, D. & Hickson, I. D. How unfinished business from S-phase affects mitosis and beyond. *EMBO J.* **32**, 2661–2671 (2013).

58. Fragkos, M. & Naim, V. Rescue from replication stress during mitosis. *Cell Cycle* **16**, 613–633 (2017).

59. Chan, K. L., North, P. S. & Hickson, I. D. BLM is required for faithful chromosome segregation and its localization defines a class of ultrafine anaphase bridges. *EMBO*

J. **26**, 3397–3409 (2007).

60. Baumann, C., Körner, R., Hofmann, K. & Nigg, E. A. PICH, a Centromere-Associated SNF2 Family ATPase, Is Regulated by Plk1 and Required for the Spindle Checkpoint. *Cell* **128**, 101–114 (2007).

61. Chan, K. L., Palmai-Pallag, T., Ying, S. & Hickson, I. D. Replication stress induces sister-chromatid bridging at fragile site loci in mitosis. *Nat. Cell Biol.* **11**, 753–760 (2009).

62. Chan, Y. W., Fugger, K. & West, S. C. Unresolved recombination intermediates lead to ultra-fine anaphase bridges , chromosome breaks and aberrations. (2017).

63. Lukas, C. *et al.* 53BP1 nuclear bodies form around DNA lesions generated by mitotic transmission of chromosomes under replication stress. *Nat. Cell Biol.* **13**, 243–253 (2011).

64. Hengeveld, R. C. C. *et al.* Rif1 Is Required for Resolution of Ultrafine DNA Bridges in Anaphase to Ensure Genomic Stability. *Dev. Cell* **34**, 466–474 (2015).

65. Sturm, D. *et al.* Hotspot Mutations in H3F3A and IDH1 Define Distinct Epigenetic and Biological Subgroups of Glioblastoma. *Cancer Cell* **22**, 425–437 (2012).

66. Martire, S. *et al.* Phosphorylation of histone H3 . 3 at serine 31 promotes p300 activity and enhancer acetylation. *Nat. Genet.* **51**, (2019).

67. Xia, W. & Jiao, J. Histone variant H3.3 orchestrates neural stem cell differentiation in the developing brain. *Cell Death Differ.* **24**, 1548–1563 (2017).

68. Jang, C. W., Shibata, Y., Starmer, J., Yee, D. & Magnuson, T. Histone H3.3 maintains genome integrity during mammalian development. *Genes Dev.* **29**, 1377–1393 (2015).

69. Latreille, D., Bluy, L., Benkirane, M. & Kiernan, R. E. Identification of histone 3 variant 2 interacting factors. *Nucleic Acids Res.* **42**, 3542–3550 (2014).

70. Huang, H. *et al.* A unique binding mode enables MCM2 to chaperone histones H3-H4 at replication forks HHS Public Access Author manuscript. *Nat Struct Mol Biol* **22**, 618–626 (2015).

71. Bleichert, F. Mechanisms of replication origin licensing: a structural perspective. *Curr. Opin. Struct. Biol.* **59**, 195–204 (2019).

72. Douglas, M. E., Ali, F. A., Costa, A. & Diffley, J. F. X. The mechanism of eukaryotic CMG helicase activation. *Nature* **555**, 265–268 (2018).

73. Ibarra, A., Schwob, E. & Méndez, J. Excess MCM proteins protect human cells from replicative stress by licensing backup origins of replication. *Proc. Natl. Acad. Sci. U. S. A.* **105**, 8956–8961 (2008).

74. Das, M., Singh, S., Pradhan, S. & Narayan, G. MCM Paradox: Abundance of Eukaryotic Replicative Helicases and Genomic Integrity. *Mol. Biol. Int.* **2014**, 1–11 (2014).

75. Ge, X. Q., Jackson, D. A. & Blow, J. J. Dormant origins licensed by excess Mcm2-7 are required for human cells to survive replicative stress. *Genes Dev.* **21**, 3331–3341 (2007).

76. Blow, J. J. & Dutta, A. Preventing re-replication of chromosomal DNA. *Nat. Rev. Mol. Cell Biol.* **6**, 476–86 (2005).

77. Forsburg, S. L. Eukaryotic MCM Proteins: Beyond Replication Initiation. *Microbiol. Mol. Biol. Rev.* **68**, 109–131 (2004).

78. Tatavosian, R. *et al.* Live-cell single-molecule dynamics of PcG proteins imposed by the DIPG H3.3K27M mutation. *Nat. Commun.* **9**, 1–16 (2018).

79. Chan, K. *et al.* The histone H3 . 3K27M mutation in pediatric glioma reprograms H3K27 methylation and gene expression Email alerting service The histone H3 . 3K27M mutation in pediatric glioma reprograms H3K27 methylation and gene expression. *Genes Dev.* **27**, 985–990 (2013).

80. Rondinelli, B. *et al.* EZH2 promotes degradation of stalled replication forks by recruiting MUS81 through histone H3 trimethylation. *Nat. Cell Biol.* **19**, 1371–1378 (2017).

81. Naim, V., Wilhelm, T., Debatisse, M. & Rosselli, F. ERCC1 and MUS81-EME1 promote sister chromatid separation by processing late replication intermediates at common fragile sites during mitosis. *Nat.*

Cell Biol. **15**, 1008–1015 (2013).

82. Ying, S. *et al.* MUS81 promotes common fragile site expression. *Nat. Cell Biol.* **15**, 1001–1007 (2013).

83. Zhang, Y. *et al.* Histone H3K27 methylation is required for NHEJ and genome stability by modulating the dynamics of FANCD2 on chromatin. *J. Cell Sci.* (2018).

84. van den Bos, H. *et al. Quantification of aneuploidy in mammalian systems*. *Methods in Molecular Biology* **1896**, (2019).

85. Huang, C. *et al.* H3.3-H4 Tetramer Splitting Events Feature Cell-Type Specific Enhancers. *PLoS Genet.* **9**, (2013).

86. Lukinavičius, G. *et al.* SiR-Hoechst is a far-red DNA stain for live-cell nanoscopy. *Nat. Commun.* **6**, 1–7 (2015).

SUPPLEMENTARY FIGURES

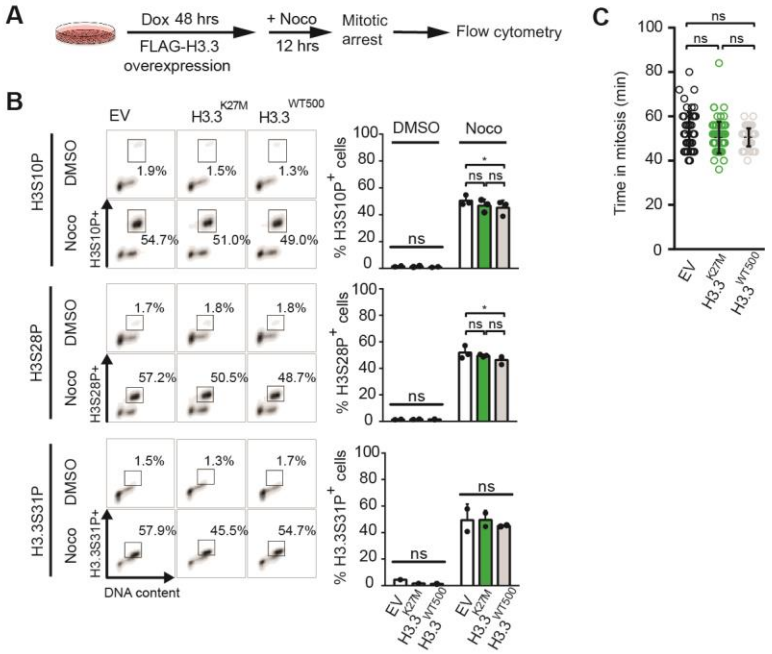

Figure EV1. H3.3^{K27M} mutant cells have an intact mitotic checkpoint.

(A) Experimental outline for testing mitotic checkpoint efficiency in H3.3^{WT}, H3.3^{K27M}, and EV cells. All three cell lines were treated with doxycycline for 48 hrs to induce FLAG-histone H3.3 overexpression (wild type or K27M mutant). Cells were subsequently treated with nocodazole for 12 hrs to induce a mitotic block in early mitosis (prometaphase). Cells were then harvested for flow cytometry analysis. **(B)** Nocodazole or DMSO treated cells were analyzed for H3S10P, H3S28P and H3.3S31P expression to determine the efficiency of histone phosphorylation in mitosis, and the proportion of cells arrested at the mitotic checkpoint using flow cytometry (left panels). Data presented as means ±SD (n=3 experiments) plotted in bar charts (right panels). *P=0.0487 and *P=0.0475 (two-way ANOVA, Tukey correction for multiple comparisons). **(C)** Time spent in mitosis was determined by time lapse imaging form nuclear envelope breakdown to end of cytokinesis. Data represent mean mitotic length ± SD (n=1 experiment), with a minimum of n=49 mitotic cells per condition (Mann Whitney non-parametric t-test).

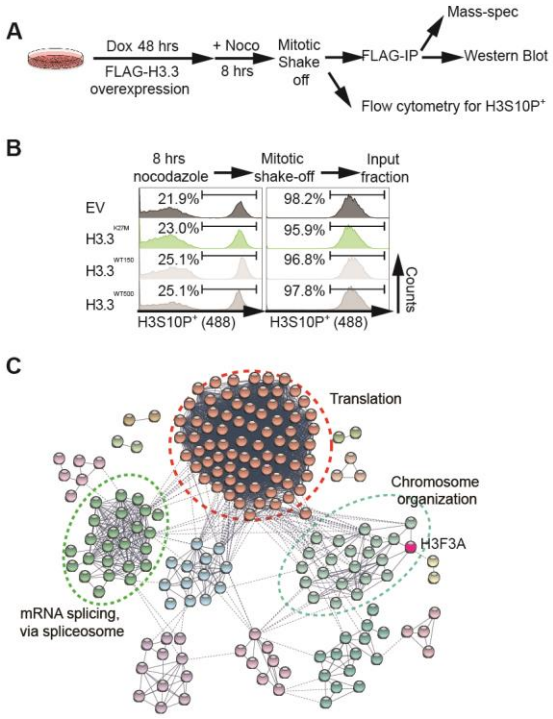

Figure EV2. FLAG-immunoprecipitation of synchronized mitotic cells identifies H3.3^{WT} and H3.3^{K27M} protein networks.

(A) Cells were treated with doxycycline for 48 hrs and synchronized in mitosis with nocodazole (8 hrs). The mitotic population was harvested by mitotic shake-off. Wild type or mutant FLAG-H3.3 were then immunoprecipitated, and the identification of their binding partners was performed by LC-MS/MS and validated by Western blotting. **(B)** A fraction of the input samples was analyzed for mitotic marker H3S10P expression to demonstrate enrichment of the mitotic population using flow cytometry. **(C)** Common histone H3.3^{WT} and H3.3^{K27M} binding partners analyzed in STRING. The illustrated network map was simplified by manual curation for clarity. Dashed circles represent a group of interacting proteins belonging to one biological process. **(D)** GO-term analysis (Biological processes) of common interacting proteins using STRING reveals significant enrichment for translation, splicing and chromatin organization. **(E)** Histone variant binding in H3.3^{WT} and H3.3^{K27M}, plotted according to differential spectral counts.

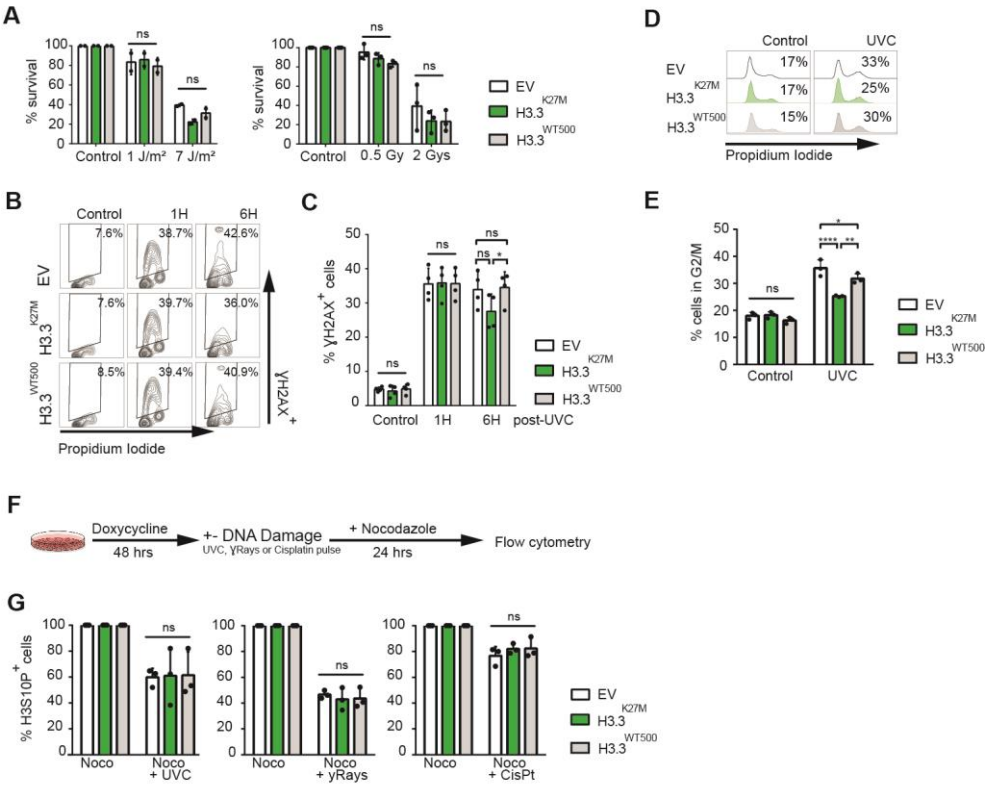

Figure EV3. H3.3^{K27M} mutant cells are more sensitive to UVC induced DNA damage.

(A) Proliferation assays show increased sensitivity of H3.3^{K27M} to UVC, but not to ɣRays at 7 days post exposure. Data are represented as means ±SD (n=2 or 3 experiments). J=joules, Gy=Grey, ns=P>0.05 (two-way ANOVA, Tukey's multiple comparisons test). **(B)** Flow cytometry analysis reveals ɣH2AX phosphorylation kinetics and dynamics at 1, and 6 hrs following 15J/m^2 UVC exposure. Cells were counterstained with Propidium Iodide. **(C)** Quantification of ɣH2AX phosphorylation by flow cytometry. Data are represented as means ±SD (n=4 experiments), *P=0.0482 (two-way ANOVA Tukey's multiple comparisons test). **(D)** Cell cycle analysis at 24 hrs following 15 J/m^2 UVC damage by flow cytometry. Representative example of normal cell cycle profiles (untreated, left panels) and UVC treated (right panels) cell cycle profiles. **(E)** Quantification of the proportion of cells in G2/M phase by flow cytometry. Data are represented as means ±SD (n=3 experiments), *P=0.0378, **P=0.0014, ****P<0.0001 (two-way ANOVA, Tukey's multiple comparisons test). **(F)** Experimental outline for quantification of G2 DNA damage checkpoint activation and efficiency. Following DNA damage (UVC, ɣRays or Cisplatin pulse), cells were blocked in mitosis with nocodazole to capture the cells that leak through the G2 block. **(G)** Flow cytometry analysis of the mitotic population using H3S10P staining and quantification. Data are represented as means ±SD (n=3 experiments), ns=P>0.05 (two-way ANOVA, Tukey's multiple comparisons test). Noco=nocodazole; CisPt=Cisplatin.

7

General discussion & conclusion

Irena Bočkaj [1] & Sophia W. M. Bruggeman [1]

[1] European Research Institute for the Biology of Ageing/ERIBA, UMCG, the Netherlands

General discussion

Pediatric brain tumors are the leading cause of cancer-related deaths in children. The high incidence of brain malignancies in children as opposed to adults is suggestive of an important role for deregulated developmental processes in driving tumorigenesis. This defines pediatric brain cancers as a disease of development. In consequence, elucidating the tumor oncogenic pathways through the lens of developmental biology might shed light on two critical questions: where do these cancers originate from, and how are they formed?

Providing answers to these questions will lead to the identification of the tumor cells-of-origin and help unravel the developmental pathways hijacked to sustain tumor growth. Ultimately, the aim is to discover novel therapeutic targets that in the future can be used to develop a precision medicine approach for these deadly diseases. The work in this thesis is directed towards these aims and focuses on the two most common pediatric brain malignancies: medulloblastoma, a neuronal tumor of the cerebellum (**Chapter 3** and **Chapter 4**) and histone mutant gliomas, a glial tumor of the brainstem (**Chapter 5** and **Chapter 6**). Below, we integrate and discuss the key findings of this thesis: Firstly, by redefining the developmental context in which medulloblastoma and high-grade glioma arise, and the key implications this offers for clinical management. Secondly, by linking medulloblastoma and high-grade glioma initiation to specific features of the developing brain - that is - its exposure to endogenous genome instability, creating a vulnerability for oncogenic transformation at multiple levels. Finally, we discuss what modelling genomic and chromosomal instability in neural stem/progenitor cells *in vitro* and *in vivo* has taught us.

Developmental origins of medulloblastoma and histone mutant gliomas

Brain malignancies are the most common solid tumors in children. In contrast to adults, where mutations observed in most tumors have an environmental etiology, a large subset of genomic alterations in pediatric brain cancers takes origin in the germline and have been related to a cancer predisposition syndrome (CPS)[1,2]. For

example, patients with Gorlin syndrome are predisposed to sonic hedgehog medulloblastoma (SHH-MB), whereas pediatric high-grade gliomas (pHGG) are commonly found in several CPS, namely Li Fraumeni syndrome (LFS), constitutional mismatch repair deficiency syndrome, and neurofibromatosis 1[2]. In total, almost 25% of pediatric HGG or SHH-MB might harbor a pathogenic germline mutation[3]. This highlights the susceptibility of neuronal tissue to genomic alterations acquired in early development. However, not all pediatric brain cancers have been linked to a CPS and their relation to brain development still remains unclear. In **Chapter 1** we review the extensive knowledge acquired on the understanding of the pathobiological mechanisms of pediatric medulloblastoma and histone mutant HGG. We highlight the age restricted anatomical distribution of these tumor types, where spatiotemporal tumor distribution strongly suggests a tight link to development. This argues towards the existence of a specific time-window in which the cancer cell-of-origin is more vulnerable to unique oncogenic hits.

In this line, **Chapter 3** aims at unravelling the temporal behavior of the SHH-MB cell-of-origin, the cerebellar granule neuron progenitor (CGNP), during cerebellar development, to identify vulnerable windows for medulloblastoma-genesis. In this study, we established the sequential transcriptional programs driving the expansion and maturation of the developing CGNP lineage. By performing a cross-species comparison between the CGNP transcriptional programs and medulloblastoma transcriptomes, we showed specific CGNP age-related gene expression programs that are mirrored in human SHH-MB, and may enable further sub-categorization into SHH-subtypes (**Chapter 1** and ref[4]). Importantly, we showed that younger CGNPs might be more affected by alterations in cell cycle regulation and genome maintenance pathways. On the contrary, older CGNPs seem to rely more on primary cilia expression, which coincides with increased sensitivity to SMO inhibition (the latter being a common strategy in treating recurrent SHH MB). This finding has an important implication for disease management, as it argues that infant and adult MB should not be treated the same way. Various clinical trials have already addressed the effects of SHH pathway inhibition with Vismodegib or Sonidegib (SMO inhibitors) in recurrent SHH-MB. Molecular analysis of the responders underscores the

importance of performing genomic characterization of the tumors to faithfully identify target populations that will benefit from SMO inhibitors, *i.e.,* SHH-MB with upstream pathway mutations, namely in PTCH1 or SMO itself[5–7]. Unfortunately, although fundamental research has enabled a significant shift in the understanding of the molecular mechanisms driving MB, a shift in clinical trial design remains to be completed, where an intelligent construction of inclusion criteria should be based on prior interrogation of molecular specificities of the patients.

Also looking beyond medulloblastoma, it seems that a "cocktail of oncogenicity" is required in the central nervous system to promote tumor initiation. This cocktail could include the intrinsic transcriptional programs of the cell-of-origin coupled to specific oncogenic triggers that would act in concert to help tumor initiation and growth. For example, similar findings have been made concerning histone mutant gliomas, where a specific oncohistone can only transform a particular glial precursor at a specific time point of its development[8]. However, unlike SHH-MB, the precise cellular origins of histone mutant gliomas are still elusive. Therefore, tracking down the cell-of-origin from the tumor's known oncogenic drivers might be a way to identify potential candidates.

Our approach to elucidate the brainstem glioma's cell-of-origin in **Chapter 5** stems from the idea that the tumor initiating environment may specifically select a H3.3 variant mutation (H3.3K27M) in the brainstem, because at the time of transformation, a particular histone variant may have a unique and indispensable role in the development of this compartment. Thus, looking at the histone variant usage over development could point towards a window of time where H3.3 is specifically required in the pons or brain midline (thalamus, medulla, spinal cord) and therefore more prone to acquire mutations. This idea echoes with findings in Xenopus development, where H3.3 seems more required at certain developmental stages, highlighting an evolutionary conserved role for H3.3 during development[9]. We and others uncovered the neonatal pontine stem cell as potential cell-of-origin candidate for DIPG due to its greater histone H3.3 usage, SHH responsiveness and preserved Pax3-dependent transcriptional programs mirrored in H3.3K27M tumors as well[10–14]. However, it remains elusive what role the histone variant H3.3 plays in

brain development pathways. Others studied the expression of H3.3 in early cortical brain development. They showed histone H3.3 to be detectable already at embryonic day 10 (E10) with a gradually increased expression until E13.5. Thereafter, the expression waned between E15.5 and birth (P0)[15]. Thus, it seems that H3.3 exerts two peaks of expression, one during embryogenesis and another perinatally (**Chapter 5**). Intriguingly, this finding of a bimodal H3.3 expression may coincide with the start of neurogenesis and gliogenesis in the CNS, processes characterized by extensive neural stem cell (NSC) proliferation and differentiation.

NSCs are cells that self-renew and differentiate into two major cell types: neurons and glial cells (astrocytes or oligodendrocytes). The shift from self-renewal to production of neurons (neurogenic switch) or glial cells (gliogenic switch) is accompanied by epigenetic and transcriptional changes[16,17]. Both neurogenic and gliogenic gene promoters undergo histone modifications, which ensure the sequential production of each cell type at appropriate stages of development. H3.3 has been shown to be deposited onto lineage-specific genes to maintain them in a poised state; a state whereby genes are silenced but ready for transcription, and thus harbor both repressive (H3K27me3) and active (H3K4me3) histone modifications[18,19]. This is thought to confer transcriptional plasticity[16,19,20]. This bivalent state has an important significance in NSCs, where the equilibrium between H3K27me3 and H3K4me3 regulates the preference for neurogenesis or gliogenesis[17]. Interestingly, Polycomb group (PcG) proteins mediate the transition from neurogenesis to gliogenesis by repressing neurogenic genes and facilitating the expression of gliogenic genes[17,21,22]. Enhancer of Zeste 2 (EZH2), one of the PcG components part of the PRC2 complex and the moiety inhibited in H3K27M gliomas, is responsible for H3K27me3 deposition[23]. At the start of the gliogenic phase, EZH2 becomes highly expressed in NSCs. Through H3K27me3 mark deposition, it prevents the expression of neuronal genes at the onset of gliogenesis[17]. This might explain why H3K27M oncohistone is prevalent in younger patients, as its functional role takes place early in gliogenesis[22,24,25]. On the other hand, the H3K36me3 modification has been shown to peak later in more committed progenitors, which correlates with the older age of H3G34R/V glioma patients[25,26]. In

this context, absence or mutations of H3.3 would exert a greater effect upon exit from stemness[18]. Interestingly, H3.3 accumulates in post-mitotic neuronal and glial chromatin with age in order to control cell type-specific gene expression programs and physiological plasticity, which underscores the importance of maintaining a H3.3 pool from neurogenic/gliogenic conversion and therafter[27].

Given the high degree of homology between H3 variants, this raises the question of the specific role of histone variant H3.3 over canonical histones during cell fate transition. H3.3 differs from canonical histone H3 by only 4–5 amino acid residues. Within the N-terminal histone tail, Serine 31 (S31) is the only residue unique to H3.3[28,29]. Importantly, a study in mouse embryonic stem cells (mESCs), and another in Xenopus, pointed out a unique role for S31. S31 phosphorylation has been shown to stimulate acetylation of H3K27 at enhancers via p300 activation, providing a chromatin state permissive to the embryonic development program, bringing a direct unique transcriptional identity to H3.3[9,30]. Cells lacking H3.3S31 exhibited reduced capacity to acetylate enhancers involved in differentiation, along with reduced ability to reprogram cell fate. Conversely, the phospho-mimetic H3.3 S31D exhibited an increase in H3.3K27ac and a loss of H3.3K27me^3 in cis[9]. Thus, the actual need for H3.3 may be linked to the capacity of its S31 residue to become phosphorylated. Moreover, the close proximity of other important histone marks might suggest a crosstalk between these marks during cell fate maintenance and conversion. Indeed, binding of an H3.3 Lysine 36 reader and elongation factor, ZMYND11, has been shown to be negatively affected by Serine 31 phosphorylation and by the H3.3 K36M and G34R/V mutations identified in human cancers[31,32]. As an alternative, the H3.3 K27M and G34R/V point mutations seen in pediatric gliomas, and H3.3 K36M in chondroblastoma, could themselves impact on H3.3 S31 modification and the residue's function(s) thereafter.

Yet it remains curious that H3.3S31 is not directly mutated in malignancies, but rather the neighboring K27, G34 and G36 residues [25,33–37]. This might be explained by the embryonic lethality that the H3.3S31 mutant would cause due to its pleiotropic roles in transcription, but also its role in maintenance of genome integrity. Indeed, knock-out of H3.3 in mESCs led to mitotic abnormalities and embryonic

lethality[38,39]. In this line, H3.3 S31 phosphorylation has been shown to coat lagging chromosomes as a radar for suppression of aneuploidy via p53 activation, and possibly be part of a chromosome separation checkpoint which role is to sense merotelic attachments otherwise unchecked by the spindle assembly checkpoint (SAC)[40,41] (see **Chapter 2** and **Appendices**).

Noteworthy, neural stem cell fate conversion dictates a switch in cell division modes from symmetric to asymmetric mode[42,43]. Asymmetric cell division allows less committed cell types to self-renew whilst producing differentiated cells of the neuronal or glial lineage[44]. This process also needs to be tightly regulated and the mitotic spindle orientation has been shown to play an important role in this[45]. The role of H3.3 in mitotic signaling is interesting, as this histone variant could in one go bridge and control two important cell-fate decision mechanisms of neurodevelopment: the transcription of cell fate determinants and the determination of cell division modes. Studies in Drosophila have shown that disruption of asymmetric cell division leads to abnormal proliferation and genomic instability[46]. Therefore, the disruption of asymmetric cell division is one possible mechanism at the root of neoplastic transformation, producing daughter cells with increased replicative potential and susceptibility to tumorigenic transformation[47,48]. It might be of interest to assess the role of H3.3(S31) in asymmetric cell division, and test if mutations in this histone variant disrupt the pathways that could also explain the genomic instability observed in these tumors (**Chapter 6** and ref[3,25]).

Altogether, more insight into the complex interplay between the H3.3S31 histone mark and other marks during reprogramming, differentiation and CNS development might shed light on why specifically H3.3 is mostly affected by point mutations in pediatric gliomas. Furthermore, deciphering the histone combinatorial code during neural development per brain area and cell-of-origin might help understand the obvious selective pressure for H3.3G34R/V oncohistone in hemispheric brain and H3.3K27M in the midline brain.

Tolerance of aneuploidy in the neural compartment: a potential route to cancer?

Aneuploidy in the brain

Not all cell types are identically sensitive to CIN nor do they tolerate aneuploidy equally[49–58]. When provoking CIN *in vivo*, tissues acquire tissue-specific copy number gains or losses, indicating tissue-specific tolerance and karyotype selection that is also mirrored in the related tumors[57,59–61]. The brain is here of particular interest as highlighted in **Chapter 2**. Studies identified over 30% of normal neurons to be aneuploid, although to date these numbers remain controversial[62]. It seems that normal brain development uses aneuploidy to shape its diversity and implement neuronal plasticity[56]. Many developmental and neuro-degenerative disorders have been linked to aneuploidy[63–66]. Moreover, brain cancers, both in adults or in children, are among the most aneuploid ones[3]. In **Chapter 1**, we asked the question as to why specific age groups of medulloblastoma and HGG are more aneuploid, whereas some subtypes are devoid of chromosome copy number alterations.

H3.3 oncohistone and genome instability

The latter is for example the case in the group of histone-mutant HGG, where gliomas harboring point mutations in the histone variant H3.3 show increased aneuploidy. In **Chapter 6**, we set out to decipher the mechanisms underlying the increased chromosomal instability observed in a H3.3 K27M overexpressing cell line. Our H3.3 K27M mass-spectrometry interactome analysis led us to investigate the response of the histone mutant cell line to replication stress, and uncovered hypersensitivity reflected by increased occurrence of DNA ultrafine bridges, a potential novel source of genome instability in H3.3 K27M tumors that deserves further investigation.

H3.3 oncohistone, replication and neurodevelopment

Our study in **Chapter 6** identified a cluster of “replicative proteins” enriched in mitotic chromatin containing the H3.3K27M mutant. Mechanistic insight into the molecular explanation for this warrants further investigation as this defective process could be exploited for treatment. Based on the current literature and on the work in this thesis,

we can already generate some fundamental hypotheses. First of all, it seems easy to conceive that any disruption of the chromatin landscape (*e.g.* histone post-translational marks) might affect separately yet simultaneously all of the phases of the cell cycle, where especially disruption of mitosis and replication would lead to GIN/CIN. Yet few studies have investigated the consequences of, for instance in our case H3K27me3 downregulation due to H3.3K27M mutant, on each phase of the cell cycle. This is where our work in **Chapter 6** appears crucial, as we unveil specific interactions of histone (mutant) H3.3 in mitosis that seems to reflect compensation from a defect in the pre-mitotic stages, presumably during replication where genomic integrity is at stake and needs to be maintained as well.

Chapter 2 highlights the role of replication stress-dependent DNA damage as a neurodevelopmental process shaping neuronal diversity at the cost of sensitizing the brain to developmental defects and degeneration[56,67–69]. Thus, the major source of genome/chromosome instability in the developing brain is attributed to replicative stress. Replicative stress describes all aberrant events occurring during DNA synthesis and leading to replication fork slowing or stalling[70–72]. Under physiological conditions, the MCM complex assembles in G1 as a pre-replisome complex on DNA in a process called origin licensing [73]. In late G1 and S-phase, interaction with the replicative helicase converts the structure into the replicative-complex that initiates replication, or origin firing [74]. The regulation of replication origin licensing counteracts replicative stress. Indeed, only a fraction of licensed origins are fired, the rest remains dormant and acts as a buffer in case of replication fork arrest[75].

From a neurodevelopmental perspective, origin licensing in the developing neural compartment is a process that needs tight regulation as any defect has been linked to neurodevelopmental disorders such as microcephaly[76]. Interestingly, the time allocated for origin licensing – during G1 phase -- in developing neural cell populations dictates their response to RS. During the expansion phase of the developing cortex, NSCs exhibit a short cell cycle while the length of the G1 phase gradually increases as these cells become more specialized[77,78]. Thus, early NSCs fire a high number of replicative origins due to this short cell cycle to enable complete DNA duplication[79]. In consequence, this restricts the number of dormant origins

available to eventually buffer replication defects. As the cell cycle length of NSCs progressively increases, more dormant origins become available and NSCs become less sensitive to replicative stress.

At the molecular level, specific chromatin states have been linked to replication origin licensing. Indeed, nucleosomes containing H3K27me3 and H3K9me3 marks have been found to bind the Origin Recognition Complex (ORC) throughout the cell cycle[80]. ORC is a member of the pre-replicative complex that licenses replication origins[81–83]. This raises the question whether a H3.3K27M chromatin would impact ORC binding and therefore replicative origin licensing, ultimately impacting the response to RS. In **Chapter 6**, together with MCMs, we also identify Nucleophosmin (NPM), which is required for the initial binding of ORC to DNA[84], however we do not identify ORC as a direct interactor with H3.3 in mitosis. It remains of interest to further investigate the relationship between H3.3-MCM, NPM and ORC as it might unveil the molecular mechanism underlying the sensitivity of H3.3K27M to replication stress by disrupted origin licensing.

H3.3 oncohistone and DNA repair

Moreover, the analysis of H3.3 K27M interactors uncovered several other differential binding partners that could be of interest for exploration. For instance, Poly (ADP-ribose) polymerase 1 (PARP1), an important actor in non-homologous-end-joining (NHEJ), homologous recombination (HR), and base/nucleotide-excision repair (BER and NER) DNA repair pathways, has been shown to loosen interaction with H3.3 K27M in our mass-spec pull-down data[85,86]. Interestingly, studies using *in vivo* conditional PARP1 deletion showed the CNS to be particularly vulnerable as PARP1 knock-out mice exhibited reduced brain weight due to defective neurogenesis[87]. In line, PARP1 was also shown to have a role in stem cell maintenance and differentiation, as loss of PARP1 pushed NSCs into differentiation and acquisition of a glial lineage[87–90]. On another line, PARP1 knock-out increases latency of TP53 knock-out tumors despite the presence of genome instability in those tumors[86,91]. It would be of interest to assess the consequence of the H3.3 K27M – PARP1 loss of interaction on PARP1 activity – residual activity or complete loss? -- and define the

consequential phenotype. Indeed, 70-100% of H3.3 mutant gliomas have alterations in the p53 pathway, thus complete inhibition of PARP1 might be a therapeutic strategy to consider[25].

In seems that a particular combination of mutations correlate with aneuploidy and plays in concert to increase genome instability in H3.3 K27M gliomas[92]. For instance, a loss-of-function mutation in Alpha-thalassemia/mental Retardation syndrome X-linked (ATRX) is an obligate partner in most H3.3 mutant gliomas[25]. Besides its H3.3-chaperoning role in deposition on pericentric and telomeric regions[93], several roles in the maintenance of genome integrity have been attributed to ATRX: a role in telomere maintenance[94], but also in replication-stress response pathways [95–99]. Indeed, ATRX was found to localize at stalled forks and on common fragile sites (CFS), the latter being late replicating regions that are first affected when RS occurs [100]. ATRX is thought to deposit H3.3 at CFS in order to regulate their stability by facilitating double strand break repair[101]. In this context, and given the results presented in **Chapter 6**, it would be of interest to draw on the existing relationship between H3.3 mutants, ATRX mutants and the replication stress response, and investigate if H3.3 and ATRX mutations display an epistatic relationship to replication stress in order to induce tumorigenesis. This cocktail of mutations might offer the possibility for a synthetic lethality approach to treat H3.3-ATRX mutant gliomas with a high proliferative index[102].

Facilitating the tolerance of aneuploidy in the brain: a central role for p53?

Inactivation of the guardian of the genome, p53, synergizes with CIN in malignant transformation and aids aneuploid cells to become cancerous[103]. p53 is activated upon DNA damage and results in G1 and G2 arrests at cellular checkpoints to enable DNA repair, or if not possible, induce apoptosis[104]. It remains intriguing that a vast majority of histone mutant aneuploid HGG co-alter p53 or other elements of the pathway, including PPM1D amplifications, which major function is to reverse the p53 response[25,105]. Moreover, the most aneuploid subtype of SHH-MB, type SHHα, is defined by *TP53* mutations as well, which suggest that in both cancer types, p53 loss facilitates tolerization of aneuploidy.

Perhaps the reason for this prevalence of *TP53* mutations in aneuploid brain cancers can be found in their neurodevelopmental origin. The developing CNS is very sensitive to p53-mediated apoptosis when DNA damage occurs[106–108]. This suggests that stringent control must prevent p53 activation when the amount of stressors is absent, or low[109,110]. It seems that the developing CNS has put on self-control mechanisms that allow high levels of proliferation during development without activating p53 responses. Thus allowing, perhaps at the expense of genome integrity, acute proliferation in the CNS. An example can be found in the developing cerebellum, where the morphogen and mitogen SHH increases MDM2-mediated degradation of p53, thus abrogating the p53-mediated cell cycle arrest and apoptosis when SHH secretion is high. This could promote tolerance of replication dependent DNA damage, aneuploidy and perhaps even neoplastic transformation[111]. Moreover, there is growing evidence that p53 may have a role in CNS development by regulating NSC self-renewal, differentiation, and cell fate determination[110,112]. It would be of interest for future studies to determine if there is a lineage and maturity-specific effect of p53 loss-of-function in the brain[47].

Modelling chromosome instability in vivo

In **Chapter 4**, we show a time point in development where neonatal CGNPs, the SHH-MB cells-of-origin, upregulate DNA repair and cell-cycle pathways at the transcriptional level, potentially to anticipate a high load of endogenous DNA damage that accompanies the surge of SHH-induced cerebellar proliferation that takes place around birth. This seems contradictory with the previous remark on SHH downregulating p53 via Mdm2[111]. It has to be noted that the above mentioned study was performed in MEFs and looked at protein levels only[111]. In our study, Mdm2 mRNA levels in CGNPs suggest stabilized levels from the start of SHH-induced proliferation (E18.5) up to P7, when proliferation ceases (data not shown), as opposed to Trp53 levels peaking at P0 and decreasing thereafter (**Chapter 4**, Fig 3). Moreover, mRNA levels of the p53 apoptotic (*i.e.*, Puma and Noxa) and cell-cycle (i.e., p21) target genes follow Trp53 levels up to E17.5, but when SHH secretion starts at E18.5, Puma, Noxa and p21 mRNA levels decrease (data not shown)[104]. This might indeed suggest a lower transcriptional p53-dependent activation of

apoptotic and cell cycle target genes despite a high proliferation when SHH pathway is active *in vivo*, which might be due to sustained p53 inhibition by Mdm2 during this period. However, this issue requires to be addressed using further functional analyses.

In **Chapter 4**, we asked a related question, namely whether this vulnerability to genomic instability during acute proliferation in the CGNP lineage could be employed for tumor initiation and growth. To test this, we modelled cerebellar CIN *in vivo* by the means of transgenic mouse models that use spindle assembly checkpoint (SAC) deficiency to trigger chromosome mis-segregations in CGNPs. The combination with *Trp53* deletion was supposed to help tolerize the acquired aneuploidy. However, to our surprise neither neonatal nor embryonic SAC and *Trp53* allele deletions led to aneuploidy. However, we noted that *Trp53* was inefficiently deleted in the developing cerebellum. The deletion was however potentiated when co-deleted with SAC component Mad2 in neonates. This finding is intriguing, as other mouse models have performed *Trp53* (co)deletion in the CGNP lineage successfully, although this was done constitutively and not using an inducible system like ours[113,114]. We also cannot rule out that the effect seen is merely technical, where for some reason the Cre recombinase is more efficient in switching out the *Mad2l1* floxed allele than *Trp53.* We would need to assess this by increasing the doses of tamoxifen and look at the *Trp53* switching landscape.

In vitro tolerance of chromosome instability in neural stem cells

Because it seems that there is a lineage-effect for the tolerance and adaptation to CIN and aneuploidy, we set out to look at how primitive, non-committed neural stem cells would respond to CIN (Fig1). To this end, we used a genetic Cre-lox system that enables induction of CIN and aneuploidy in NSCs upon 4-hydroxytamoxifen (4-OHT) induced activity of the Cre-recombinase. This leads to the genetic deletion of LoxP flanked alleles of Monopolar Spindle 1 (*Mps1*), a key element of the SAC, and/or *Trp53* (Fig 1A and B). We assessed karyotype compositions of Mps1;p53 double knock-out NSCs with metaphase spreads and showed presence of cycling aneuploid NSCs, which could be cultured, passaged and therefore maintained *in vitro* as aneuploid cells, as shown by karyotyping of these same switched cells at

later passages (Fig 1C). We ruled out that aneuploidy was due to *Trp53* loss, which is also known to induce a subtle amount of genomic instability and aneuploidy (Fig 1D)[115]. Genotyping of the NSCs to assess for allele switching over culturing-time showed an adaptation at the population level where p53 KO gave a growth advantage, however Mps1 homozygous deletion did not. Indeed, at a late passage, while Trp53 remains homozygously switched, it seems that cells heterozygously switched for Mps1 overtook the culture (Fig 1E), yet remaining aneuploid/tetraploid to some extent (Fig 1C; dark red dot plot).

This brings the idea that unlike CGNPs, NSCs can adapt to an aneuploid state. It seems that there is a threshold of SAC inhibition that NSCs can tolerate, as *in vitro*, the population selects for heterozygous loss of Mps1 thereby preserving some residual SAC activity, perhaps just enough to give rise to a tolerable amount of aneuploidy. Above this threshold, the aneuploidy induced is too high to be tolerated and triggers cell death mechanisms, such as Caspase dependent programmed cell death, previously described to be particularly active during neural development to ensure a proper balance between diversity creation and maintenance of the genome (**Chapter 2** and ref[68,116]). In future studies, it would be interesting to look at the effect of CIN and aneuploidy on the differentiation power of the NSCs and whether their specification to the different lineages is affected.

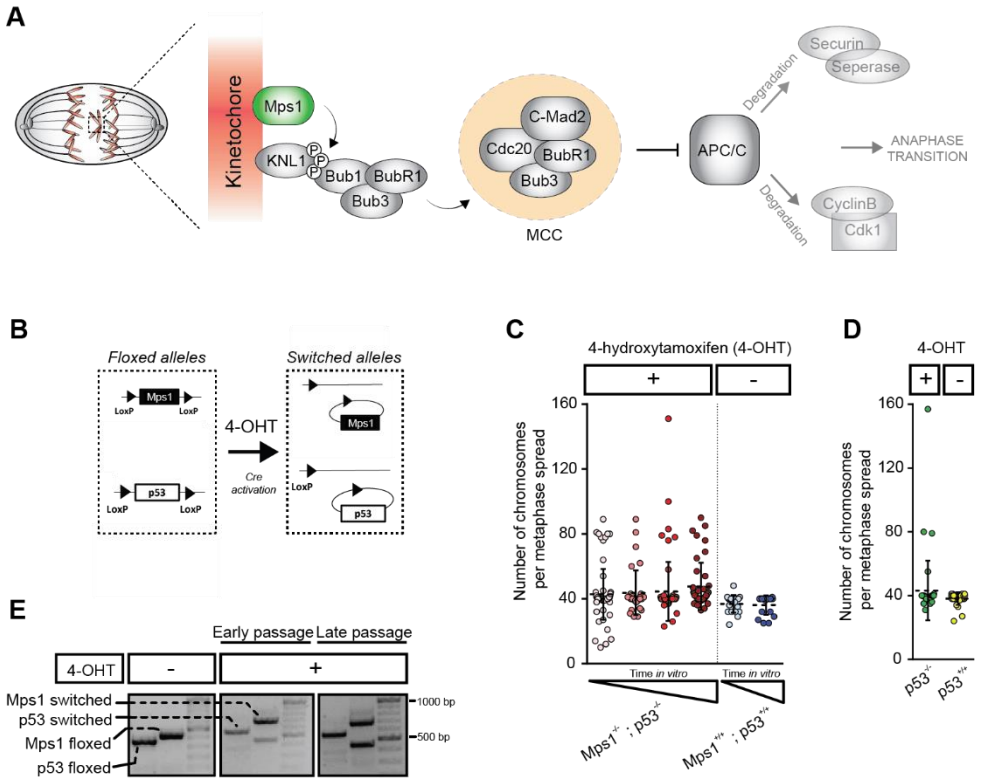

Figure 1. Inducing chromosomal instability and aneuploidy in adult murine neural stem cells

(A) Schematic overview of the role of Mps1 in the activation of the Spindle Assembly Checkpoint (SAC). The SAC is activated upon unattached kinetochores (red) to a spindle microtubule. Mps1 (green) is recruited at the kinetochore and responsible for KNL1 phosphorylation, thus promoting the recruitment of Bub3, Bub1 and BubR1. Bub1 also contributes to recruiting Cdc20. C-Mad2, together with BubR1, Bub3, and Cdc20 constitute the MCC. The MCC inhibits APC/C. In consequence, Cyclin B and Securin are not degraded and remain associated with Cdk1 and Separase, respectively, leading to mitotic arrest and delayed anaphase transition. Deletion of Mps1 alleviates SAC activation and enables anaphase transition and mitotic exit even if unattached or not properly attached kinetochores are present, leading to chromosome mis-segregations and aneuploidy (Abbreviations: Mps1 = Monopolar Spindle 1; C-Mad2 = Closed Mad2; MCC = Mitotic Checkpoint Complex; APC/C = anaphase promoting complex/cyclosome).

(B) Schematic representation of the Cre^{ERT2}-Lox system used to create Mps1 and p53 knock-out cell lines: treatment of the Cre^{ERT2}Mps1$^{f/f}$;p53$^{f/f}$ or Cre^{ERT2}p53$^{f/f}$ neural stem cells with 4-OHT *in vitro* enables Cre^{ERT2}-mediated switching of the floxed alleles. Mps1 and p53 alleles are flanked with LoxP sites that enable recognition by the Cre^{ERT2}-recombinase endonuclease and removal of the flanked DNA sequence, leading to switched alleles. Cre^{ERT}-recombinase needs 4-Hydroxytamoxifen (4-OHT) to be translocated into the nucleus and exert its nuclease activity.

(C) and (D) Karyotyping of Cre^{ERT2}Mps1$^{f/f}$;p53$^{f/f}$ or Cre^{ERT}p53$^{f/f}$ neural stem cells with and without 4-OHT at different culturing time points. (C) Cre^{ERT2}Mps1$^{f/f}$;p53$^{f/f}$ were treated with 4-OHT for 2 days and cultured for up to three weeks. Samples were taken for metaphase spreads to assess karyotype composition and aneuploidy at 6 days after initial 4-OHT treatment (light pink dot plot), at 13 days (pink dot plot), at 20 days (red dot plot) and at 27 days (dark-red dot plot). Un-treated control cells were sampled at the first (light blue dot plot) and last (dark blue dot plot) time points. **(D)** Cre^{ERT2}p53$^{f/f}$ were treated with 4-OHT for 2 days and cultured for up to two weeks. Samples were taken for metaphase spreads to assess karyotype composition and aneuploidy at 15 days after initial 4-OHT treatment (green dot plot). Un-treated control cells (yellow dot plot) were sampled at this same time point.

(E) Genotyping of Cre^{ERT2}Mps1$^{f/f}$;p53$^{f/f}$ neural stem cells with and without 4-OHT at different culturing time points. Cre^{ERT2}Mps1$^{f/f}$;p53$^{f/f}$ were treated with 4-OHT for 2 days and cultured for up to three weeks. Genomic DNA samples were taken for genotyping to assess allele switching efficiency at 6 days after initial 4-OHT treatment (early passage) and at 27 days (late passage). Un-treated control cells were sampled at the latest time point.

Concluding remarks

The work presented in this thesis addresses the contribution of genome maintenance pathways to the initiation and progression of the most common brain cancers in children, medulloblastoma and histone mutant HGG. Acquisition of genome instability during the development of these childhood brain cancers can be explained by the specific characteristics of two normal neurodevelopmental processes: firstly by the intrinsic predisposition of the highly proliferative developing CNS to endogenous DNA damage, and secondly by the evolutionary fluctuation of genome maintenance pathways in response to damage during CNS development, which allows a basal level of GIN that positively contributes to neuronal diversification and plasticity. Nonetheless, at certain time points these processes might act at the expense of genome integrity, especially when predisposing mutations co-occur (*e.g.* Histone mutations, *TP53* or *SHH* mutations). Thus, this thesis defines genome maintenance pathways as core developmental processes, which can be hijacked by the cells when becoming cancerous to accelerate the process of tumorigenesis.

Furthermore, this thesis highlights the importance of accurate models for childhood brain cancers, where the intrinsic features of the cells-of-origin need to be acknowledged. Therefore, tracking the cells-of-origin and elucidating their core behaviors regarding DNA damage control and chromosomal instability will deepen the knowledge on how they adapt to genome instability, as well as give insight in their aneuploidy-coping mechanisms that can both be employed in the related tumors. In the future, this offers new targetable opportunities to improve treatment strategies for these deadly diseases.

REFERENCES

1. Zhang, J. *et al.* Germline mutations in predisposition genes in pediatric cancer. *N. Engl. J. Med.* **373**, 2336–2346 (2015).

2. Michaeli, O. & Tabori, U. Pediatric high grade gliomas in the context of cancer predisposition syndromes. *J. Korean Neurosurg. Soc.* **61**, 319–322 (2018).

3. Gröbner, S. N. *et al.* The landscape of genomic alterations across childhood cancers. *Nature* **555**, 321–327 (2018).

4. Cavalli, F. M. G. *et al.* Intertumoral Heterogeneity within Medulloblastoma Subgroups. *Cancer Cell* **31**, 737-754.e6 (2017).

5. Robinson, G. W. *et al.* Vismodegib exerts targeted efficacy against recurrent sonic hedgehog - Subgroup medulloblastoma: Results from phase II Pediatric Brain Tumor Consortium studies PBTC-025B and PBTC-032. *J. Clin. Oncol.* **33**, 2646–2654 (2015).

6. Kieran, M. W. *et al.* Phase i study of oral sonidegib (LDE225) in pediatric brain and solid tumors and a phase II study in children and adults with relapsed medulloblastoma. *Neuro. Oncol.* **19**, 1542–1552 (2017).

7. Kool, M. *et al.* Genome Sequencing of SHH Medulloblastoma Predicts Genotype-Related Response to Smoothened Inhibition. *Cancer Cell* **25**, 393–405 (2014).

8. Pathania, M. *et al.* H3.3 K27M Cooperates with Trp53 Loss and PDGFRA Gain in Mouse Embryonic Neural Progenitor Cells to Induce Invasive High-Grade Gliomas. *Cancer Cell* **32**, 684-700.e9 (2017).

9. Sitbon, D., Boyarchuk, E. variant H. . residue S. is essential for X. gastrulation regardless of the deposition pathway, Dingli, F., Loew, D. & Almouzni, G. Histone variant H3.3 residue S31 is essential for Xenopus gastrulation regardless of the deposition pathway. *Nat. Commun.* **11**, (2020).

10. Misuraca, K. L., Hu, G., Barton, K. L., Chung, A. & Becher, O. J. A Novel Mouse Model of Diffuse Intrinsic Pontine Glioma Initiated in Pax3-Expressing Cells. *Neoplasia* **18**, 60–70 (2016).

11. Misuraca, K. L. *et al.* Pax3 expression enhances PDGF-B-induced brainstem gliomagenesis and characterizes a subset of brainstem glioma. *Acta Neuropathol. Commun.* **2**, 1–17 (2014).

12. Monje, M. *et al.* Hedgehog-responsive candidate cell of origin for diffuse intrinsic pontine glioma. *Proc. Natl. Acad. Sci.* **108**, 4453–4458 (2011).

13. Hatta, T. *et al.* Development of the pons in human fetuses. *Congenit. Anom. (Kyoto).* **47**, 63–67 (2007).

14. Tate, M. C. *et al.* Postnatal growth of the human pons: A morphometric and immunohistochemical analysis. *J. Comp. Neurol.* **523**, 449–462 (2015).

15. Xia, W. & Jiao, J. Histone variant H3.3 orchestrates neural stem cell differentiation in the developing brain. *Cell Death Differ.* **24**, 1548–1563 (2017).

16. Murao, N., Noguchi, H. & Nakashima, K. Epigenetic regulation of neural stem cell property from embryo to adult. *Neuroepigenetics* **5**, 1–10 (2016).

17. Albert, M. & Huttner, W. B. Epigenetic and transcriptional pre-patterning-An emerging theme in cortical neurogenesis. *Front. Neurosci.* **12**, 1–9 (2018).

18. Banaszynski, L. A. *et al.* Hira-dependent histone H3.3 deposition facilitates prc2 recruitment at developmental loci in ES cells. *Cell* **155**, 107–120 (2013).

19. Goldberg, A. D. *et al.* Distinct Factors Control Histone Variant H3.3 Localization at Specific Genomic Regions. *Cell* **140**, 678–691 (2010).

20. Harada, A. *et al.* Incorporation of histone H3.1 suppresses the lineage potential of skeletal muscle. *Nucleic Acids Res.* **43**, 775–786 (2015).

21. Sparmann, A. *et al.* The chromodomain helicase Chd4 is required for Polycomb-mediated inhibition of astroglial differentiation. *EMBO J.* **32**, 1598–1612 (2013).

22. Hirabayashi, Y. *et al.* Polycomb Limits the Neurogenic Competence of Neural Precursor Cells to Promote Astrogenic Fate Transition. *Neuron* **63**, 600–613 (2009).

23. Mu, W., Starmer, J., Yee, D. & Magnuson, T. EZH2 variants differentially regulate polycomb repressive complex 2 in histone methylation and cell differentiation. *Epigenetics and Chromatin* **11**, 1–14 (2018).

24. Pereira, J. D. *et al.* Ezh2, the histone methyltransferase of PRC2, regulates the balance between self-renewal and differentiation in the cerebral cortex. *Proc. Natl. Acad. Sci. U. S. A.* **107**, 15957–15962

(2010).

25. Mackay, A. *et al.* Integrated Molecular Meta-Analysis of 1,000 Pediatric High-Grade and Diffuse Intrinsic Pontine Glioma. *Cancer Cell* **32**, 520-537.e5 (2017).

26. Zhang, Z. *et al.* Histone Methylations Define Neural Stem/Progenitor Cell Subtypes in the Mouse Subventricular Zone. *Mol. Neurobiol.* **57**, 997–1008 (2020).

27. Maze, I. *et al.* Critical Role of Histone Turnover in Neuronal Transcription and Plasticity. *Neuron* **87**, 77–94 (2015).

28. Hake, S. B. *et al.* Serine 31 phosphorylation of histone variant H3.3 is specific to regions bordering centromeres in metaphase chromosomes. *Proc. Natl. Acad. Sci.* **102**, 6344–6349 (2005).

29. Chang, F. T. M. *et al.* CHK1-driven histone H3.3 serine 31 phosphorylation is important for chromatin maintenance and cell survival in human ALT cancer cells. *Nucleic Acids Res.* **43**, 2603–2614 (2015).

30. Martire, S. *et al.* Phosphorylation of histone H3 . 3 at serine 31 promotes p300 activity and enhancer acetylation. *Nat. Genet.* **51**, (2019).

31. Wen, H. *et al.* ZMYND11 links histone H3.3K36me3 to transcription elongation and tumour suppression. *Nature* **508**, 263–268 (2014).

32. Guo, R. *et al.* BS69/ZMYND11 reads and connects histone H3.3 lysine 36 trimethylation-decorated chromatin to regulated pre-mRNA processing. *Mol. Cell* **56**, 298–310 (2014).

33. Nacev, B. A. *et al.* The expanding landscape of 'oncohistone' mutations in human cancers. *Nature* **567**, 473–478 (2019).

34. Schwartzentruber, J. *et al.* Driver mutations in histone H3.3 and chromatin remodelling genes in paediatric glioblastoma. *Nature* **482**, 226–231 (2012).

35. Wu, G. *et al.* The genomic landscape of diffuse intrinsic pontine glioma and pediatric non-brainstem high-grade glioma. *Nat. Genet.* **46**, 444–450 (2014).

36. Lowe, B. R., Maxham, L. A., Hamey, J. J., Wilkins, M. R. & Partridge, J. F. Histone H3 Mutations: An Updated View of Their Role in Chromatin Deregulation and Cancer. *Cancers (Basel).* **11**, (2019).

37. Behjati, S. *et al.* Distinct H3F3A and H3F3B driver mutations define chondroblastoma and giant cell tumor of bone. *Nat. Genet.* **45**, 1479–1482 (2013).

38. Jang, C. W., Shibata, Y., Starmer, J., Yee, D. & Magnuson, T. Histone H3.3 maintains genome integrity during mammalian development. *Genes Dev.* **29**, 1377–1393 (2015).

39. Bush, K. M. *et al.* Endogenous mammalian histone H3.3 exhibits chromatin-related functions during development. *Epigenetics and Chromatin* **6**, 1–16 (2013).

40. Hinchcliffe, E. H. *et al.* Chromosome missegregation during anaphase triggers p53 cell cycle arrest through histone H3.3 Ser31 phosphorylation. *Nat. Cell Biol.* **advance on**, 668–675 (2016).

41. Bockaj, I., Bruggeman, S. W. M. & Foijer, F. Revisiting the chromosome separation checkpoint (retrospective on DOI 10.1002/bies.201400140). *BioEssays* **39**, (2017).

42. Matsuzaki, F. & Shitamukai, A. Cell division modes and cleavage planes of neural progenitors during mammalian cortical development. *Cold Spring Harb. Perspect. Biol.* **7**, (2015).

43. Fish, J. L., Dehay, C., Kennedy, H. & Huttner, W. B. Making bigger brains - The evolution of neural-progenitor-cell division. *J. Cell Sci.* **121**, 2783–2793 (2008).

44. Knoblich, J. A. Mechanisms of Asymmetric Stem Cell Division. *Cell* **132**, 583–597 (2008).

45. Vargas-Hurtado, D. *et al.* Differences in Mitotic Spindle Architecture in Mammalian Neural Stem Cells Influence Mitotic Accuracy during Brain Development. *Curr. Biol.* 1–13 (2019). doi:10.1016/j.cub.2019.07.061

46. Sean J. Morrison1 & Judith Kimble. Asymmetric and symmetric stem-cell divisions in development and cancer. *Nature* **441**, (2006).

47. Lewis, K. M. & Petritsch, C. Asymmetric cell division: Implications for glioma development and treatment. *Transl. Neurosci.* **4**, 484–503 (2013).

48. Ashkenazi, R., Gentry, S. N. & Jackson, T. L. Pathways to tumorigenesis - Modeling mutation acquisition in stem cells and their progeny. *Neoplasia* **10**, 1170–1182 (2008).

49. Cromie, G. A. & Dudley, A. M. Aneuploidy: Tolerating Tolerance. *Curr. Biol.* **25**, R771–R773 (2015).

50. Foijer, F. *et al.* Deletion of the MAD2L1 spindle assembly checkpoint gene is

tolerated in mouse models of acute T-cell lymphoma and hepatocellular carcinoma. *Elife* **6**, 1–22 (2017).

51. Simon, J. E., Bakker, B. & Foijer, F. CINcere Modelling: What Have Mouse Models for Chromosome Instability Taught Us? *Recent Results Cancer Res.* **200**, 39–60 (2015).

52. Duncan, A. W. *et al.* Aneuploidy as a mechanism for stress-induced liver adaptation. *J. Clin. Invest.* **122**, 3307–3315 (2012).

53. Faggioli, F., Vezzoni, P. & Montagna, C. Single-cell analysis of ploidy and centrosomes underscores the peculiarity of normal hepatocytes. *PLoS One* **6**, (2011).

54. Rehen, S. K. *et al.* Chromosomal variation in neurons of the developing and adult mammalian nervous system. *Proc. Natl. Acad. Sci. U. S. A.* **98**, 13361–13366 (2001).

55. Rehen, S. K. *et al.* Constitutional aneuploidy in the normal human brain. *J. Neurosci.* **25**, 2176–2180 (2005).

56. Kingsbury, M. A. *et al.* Aneuploid neurons are functionally active and integrated into brain circuitry. *Proc. Natl. Acad. Sci. U. S. A.* **102**, 6143–6147 (2005).

57. Foijer, F. *et al.* Spindle checkpoint deficiency is tolerated by murine epidermal cells but not hair follicle stem cells. *Proc. Natl. Acad. Sci. U. S. A.* **110**, 2928–2933 (2013).

58. Ben-David, U. & Amon, A. Context is everything: aneuploidy in cancer. *Nat. Rev. Genet.* **21**, 44–62 (2020).

59. Bakker, B. *et al.* Single-cell sequencing reveals karyotype heterogeneity in murine and human malignancies. *Genome Biol.* **17**, 115 (2016).

60. Worrall, J. T. *et al.* Non-random Mis-segregation of Human Chromosomes. *CellReports* **23**, 3366–3380 (2018).

61. Foijer, F. *et al.* Chromosome instability induced by Mps1 and p53 mutation generates aggressive lymphomas exhibiting aneuploidy-induced stress. *Proc. Natl. Acad. Sci. U. S. A.* **111**, 13427–13432 (2014).

62. Rohrback, S., Siddoway, B., Liu, C. S. & Chun, J. Genomic mosaicism in the developing and adult brain. *Dev. Neurobiol.* **78**, 1026–1048 (2018).

63. Polymeropoulos, M. H. *et al.* Mapping of a gene for Parkinson's disease to chromosome 4q21-q23. *Science (80-.).* **274**, 1197–1199 (1996).

64. Fischer, H. G. *et al.* Changes in neuronal DNA content variation in the human brain during aging. *Aging Cell* **11**, 628–633 (2012).

65. La Cognata, V., Morello, G., D'Agata, V. & Cavallaro, S. Copy number variability in Parkinson's disease: assembling the puzzle through a systems biology approach. *Human Genetics* **136**, 13–37 (2017).

66. Yurov, Y. B., Vorsanova, S. G., Liehr, T., Kolotii, A. D. & Iourov, I. Y. X chromosome aneuploidy in the Alzheimer's disease brain. *Mol. Cytogenet.* **7**, 20 (2014).

67. Charlier, C. F. & A P Martins, R. Protective Mechanisms Against DNA Replication Stress in the Nervous System. *Genes (Basel).* **11**, (2020).

68. Gilmore, E. C., Nowakowski, R. S., Caviness, V. S. & Herrup, K. Cell birth, cell death, cell diversity and DNA breaks: How do they all fit together? *Trends Neurosci.* **23**, 100–105 (2000).

69. Bushman, D. M. & Chun, J. The genomically mosaic brain: Aneuploidy and more in neural diversity and disease. *Semin. Cell Dev. Biol.* **24**, 357–369 (2013).

70. O'Driscoll, M. The pathological consequences of impaired genome integrity in humans; disorders of the DNA replication machinery. *J. Pathol.* **241**, 192–207 (2017).

71. Zeman, M. K. & Cimprich, K. A. Causes and consequences of replication stress. *Nat. Cell Biol.* **16**, 2–9 (2014).

72. Magdalou, I., Lopez, B. S., Pasero, P. & Lambert, S. A. E. The causes of replication stress and their consequences on genome stability and cell fate. *Semin. Cell Dev. Biol.* **30**, 154–164 (2014).

73. Bleichert, F. Mechanisms of replication origin licensing: a structural perspective. *Curr. Opin. Struct. Biol.* **59**, 195–204 (2019).

74. Douglas, M. E., Ali, F. A., Costa, A. & Diffley, J. F. X. The mechanism of eukaryotic CMG helicase activation. *Nature* **555**, 265–268 (2018).

75. Mcintosh, D. *et al.* Dormant Origins, the Licensing Checkpoint, and the Response to Replicative Stresses. 1–10 (2012).

76. De Munnik, S. A. *et al.* Meier-Gorlin syndrome Clinical genetics and genomics. *Orphanet J. Rare Dis.* **10**, 1–7 (2015).

77. Borrell, V. & Calegari, F. Mechanisms of brain evolution: Regulation of neural

progenitor cell diversity and cell cycle length. *Neurosci. Res.* **86**, 14–24 (2014).

78. Calegari, F., Haubensak, W., Haffher, C. & Huttner, W. B. Selective lengthening of the cell cycle in the neurogenic subpopulation of neural progenitor cells during mouse brain development. *J. Neurosci.* **25**, 6533–6538 (2005).

79. Ge, X. Q. *et al.* Embryonic Stem Cells License a High Level of Dormant Origins to Protect the Genome against Replication Stress. *Stem Cell Reports* **5**, 185–194 (2015).

80. Nishitani, H. Control of DNA replication licensing in a cell cycle. *Seikagaku* **80**, 661–666 (2008).

81. Vermeulen, M. *et al.* Quantitative Interaction Proteomics and Genome-wide Profiling of Epigenetic Histone Marks and Their Readers. *Cell* **142**, 967–980 (2010).

82. Worcel, A., Han, S. & Wong, M. L. Assembly of newly replicated chromatin. *Cell* **15**, 969–977 (1978).

83. Bartke, T. *et al.* Nucleosome-interacting proteins regulated by DNA and histone methylation. *Cell* **143**, 470–484 (2010).

84. Blow, J. J. & Dutta, A. Preventing re-replication of chromosomal DNA. *Nat. Rev. Mol. Cell Biol.* **6**, 476–86 (2005).

85. Luijsterburg, M. S. *et al.* PARP1 Links CHD2-Mediated Chromatin Expansion and H3.3 Deposition to DNA Repair by Non-homologous End-Joining. *Mol. Cell* **61**, 547–562 (2016).

86. De Vos, M., Schreiber, V. & Dantzer, F. The diverse roles and clinical relevance of PARPs in DNA damage repair: Current state of the art. *Biochem. Pharmacol.* **84**, 137–146 (2012).

87. Hong, S. *et al.* Defective neurogenesis and schizophrenia-like behavior in PARP-1-deficient mice. *Cell Death Dis.* **10**, (2019).

88. Ogino, H. *et al.* Loss of Parp-1 affects gene expression profile in a genome-wide manner in ES cells and liver cells. *BMC Genomics* **8**, (2007).

89. Gao, F., Kwon, S. W., Zhao, Y. & Jin, Y. PARP1 poly(ADP-ribosyl)ates Sox2 to control Sox2 protein levels and FGF4 expression during embryonic stem cell differentiation. *J. Biol. Chem.* **284**, 22263–22273 (2009).

90. Jennifer M. Plane, Steven K. Grossenbacher, and Wenbin DengJennifer M. Plane, Steven K. Grossenbacher, and W. D. PARP-1 deletion promotes subventricular zone neural stem cells toward a glial fate. *Bone* **23**, 1–7 (2008).

91. Conde, C. *et al.* Loss of poly(ADP-ribose) polymerase-1 causes increased tumour latency in p53-deficient mice. *EMBO J.* **20**, 3535–3543 (2001).

92. Auslander, N., Wolf, Y. I. & Koonin, E. V. Interplay between DNA damage repair and apoptosis shapes cancer evolution through aneuploidy and microsatellite instability. *Nat. Commun.* **11**, 1–11 (2020).

93. Lewis, P. W., Elsaesser, S. J., Noh, K.-M., Stadler, S. C. & Allis, C. D. Daxx is an H3.3-specific histone chaperone and cooperates with ATRX in replication-independent chromatin assembly at telomeres. *Proc. Natl. Acad. Sci.* **107**, 14075–14080 (2010).

94. Amorim, J. P., Santos, G., Vinagre, J. & Soares, P. The role of ATRX in the alternative lengthening of telomeres (ALT) phenotype. *Genes (Basel).* **7**, (2016).

95. Huh, M. S. *et al.* Stalled replication forks within heterochromatin require ATRX for protection. *Cell Death Dis.* **7**, e2220–e2220 (2016).

96. Raghunandan, M. *et al.* Functional crosstalk between the Fanconi anemia and ATRX/DAXX histone chaperone pathways promotes replication fork recovery. *Hum. Mol. Genet.* **1343**, 612–625 (2019).

97. Ivanochko, D., Studies, P. & Genetics, M. ATRX Protects Cells Against Replication-Induced Genomic Instability. (2016).

98. Clynes, D. *et al.* ATRX dysfunction induces replication defects in primary mouse cells. *PLoS One* **9**, (2014).

99. Leung, J. W. C. *et al.* Alpha thalassemia/mental retardation syndrome X-linked gene product ATRX is required for proper replication restart and cellular resistance to replication stress. *J. Biol. Chem.* **288**, 6342–6350 (2013).

100. Pladevall-Morera, D. *et al.* Proteomic characterization of chromosomal common fragile site (CFS)-associated proteins uncovers ATRX as a regulator of CFS stability. *Nucleic Acids Res.* **47**, 8004–8018 (2019).

101. Juhász, S., Elbakry, A., Mathes, A. & Löbrich, M. ATRX Promotes DNA Repair Synthesis and Sister Chromatid Exchange during Homologous Recombination. *Mol. Cell* **71**, 11-24.e7 (2018).

102. Haase, S. *et al.* Mutant ATRX: uncovering a new therapeutic target for glioma. *Expert*

Opin. Ther. Targets **22**, 599–613 (2018).

103. Orr, B., Godek, K. M. & Compton, D. Aneuploidy. *Curr. Biol.* **25**, R538–R542 (2015).

104. Aubrey, B. J., Kelly, G. L., Janic, A., Herold, M. J. & Strasser, A. How does p53 induce apoptosis and how does this relate to p53-mediated tumour suppression? *Cell Death Differ.* **25**, 104–113 (2018).

105. Deng, W. *et al.* The role of PPM1D in cancer and advances in studies of its inhibitors. *Biomed. Pharmacother.* **125**, 109956 (2020).

106. Gao, Y. *et al.* A critical role for DNA end-joining proteins in both lymphogenesis and neurogenesis. *Cell* **95**, 891–902 (1998).

107. Frank, K. M. *et al.* DNA ligase IV deficiency in mice leads to defective neurogenesis and embryonic lethality via the p53 pathway. *Mol. Cell* **5**, 993–1002 (2000).

108. Sugo, N. Neonatal lethality with abnormal neurogenesis in mice deficient in DNA polymerase beta. *EMBO J.* **19**, 1397–1404 (2000).

109. Komarova, E. A. *et al.* Transgenic mice with p53-responsive lacZ: p53 activity varies dramatically during normal development and determines radiation and drug sensitivity in vivo. *EMBO J.* **16**, 1391–1400 (1997).

110. Mendrysa, S. M., Ghassemifar, S. & Malek, R. P53 in the cns: Perspectives on development, stem cells, and cancer. *Genes and Cancer* **2**, 431–442 (2011).

111. Abe, Y. *et al.* Hedgehog signaling overrides p53-mediated tumor suppression by activating Mdm2. *Proc. Natl. Acad. Sci. U. S. A.* **105**, 4838–4843 (2008).

112. Barthelery, N. J. & Manfredi, J. J. Cerebellum Development and Tumorigenesis: A p53-Centric Perspective. *Trends Mol. Med.* **22**, 404–413 (2016).

113. Lang, P. Y. *et al.* ATR maintains chromosomal integrity during postnatal cerebellar neurogenesis and is required for medulloblastoma formation. *Development* **143**, 4038–4052 (2016).

114. Williams, S. E. *et al.* Aspm sustains postnatal cerebellar neurogenesis and medulloblastoma growth in mice. *Development* **142**, 3921–3932 (2015).

115. Soto, M. *et al.* p53 Prohibits Propagation of Chromosome Segregation Errors that Produce Structural Report p53 Prohibits Propagation of Chromosome Segregation Errors that Produce Structural Aneuploidies. 2423–2431 (2017). doi:10.1016/j.celrep.2017.05.055

116. Kuan, C. Y., Roth, K. A., Flavell, R. A. & Rakic, P. Mechanisms of programmed cell death in the developing brain. *Trends Neurosci.* **23**, 291–297 (2000).

Appendices

Revisiting the chromosome segregation checkpoint

Irena Bočkaj [1], Sophia Bruggeman [1] and Floris Foijer [2,*]

[1] Department of Pediatrics/Pediatric Oncology and Hematology, University of Groningen, University Medical Center Groningen, Groningen, the Netherlands

[2] European Research Institute for the Biology of Ageing, University of Groningen, University Medical Center Groningen, Groningen, the Netherlands

* Corresponding author: Floris Foijer, Email: f.foijer@umcg.nl

Adapted from Bioessays. 2017 Jul;39(7). doi: 10.1002

Errors in mitosis can lead to cells with an abnormal DNA content, a state defined as aneuploid. Cells have evolved several mechanisms to prevent aneuploidy, such as the spindle assembly checkpoint (SAC). The SAC prevents chromosome mis-segregation in mitosis by retaining cells in metaphase until all chromosomes are properly attached to opposing spindle poles. While the SAC can prevent most mitotic abnormalities, it does not recognize merotelic attachments, in which one of the two sister chromatids is connected to both spindle poles. Such flawed attachments can lead to lagging chromosomes and aneuploid cells when unresolved. Two years ago, Maiato *et al* proposed in Bioessays that in human cells a second checkpoint exists that delays chromosome decondensation and nuclear envelope reassembly (NER) when chromosomes lag behind during anaphase [1]. Since then this chromosome separation checkpoint (CSC) was also described for Drosophila, suggesting it to be conserved between species [2]. The functioning of the CSC relies on an Aurora B kinase activity gradient at the midzone and is counteracted by PP2A phosphatase activity at the poles. However, the downstream effectors of Aurora B kinase activity at the midzone responsible for the aneuploidy-preventive effect of the CSC were not identified in the first two studies [2,3]. One possible target could be the serine 31 residue of Histone 3.3 ($H3.3^{S31}$), which was recently identified as a potential Aurora B target [4]. This is particularly interesting, as this phosphorylation event has been linked to chromosome mis-segregation. While phosphorylated $H3.3^{S31}$ is normally restricted to the pericentromeric region on mitotic chromosomes, Hinchcliffe *et al*

described that phosphorylated H3.3^{S31} spreads from the pericentromeric region to the chromosome arms specifically on lagging chromosomes, thus 'labeling' the laggard [5]. This phosphorylation event results in stabilization of the tumor suppressor p53 and subsequent cell cycle arrest in the G1 phase of the cell cycle. This response was found to be independent of DNA damage and the DNA damage response, and could thus be a downstream effect of the CSC. The cell cycle arrest is a direct consequence of chromosome-wide phospho-H3.3^{S31} as micro-injection of pH3.3^{S31} antibodies can prevent the p53 accumulation. However, micro-injection of pH3.3^{S31} antibodies does not prevent nuclear envelope reassembly, indicating that other Aurora B kinase targets must be responsible for these features of the CSC. Thus, while the exact molecular mechanism of the CSC is still not fully known, together these findings suggest that the CSC might not only operate to restore lagging chromosomes as previously described by Maiato and colleagues [1], but also to prevent the propagation of aneuploid progeny of cells in which CSC-mediated repair has failed. Therefore, a better understanding of the molecular mechanism of the CSC could lead to the development of new therapeutic intervention strategies to aggravate aneuploidy to kill chromosomal instable cells in aneuploid cancer.

References

1. Maiato, H., Afonso, O. & Matos, I. A chromosome separation checkpoint: A midzone Aurora B gradient mediates a chromosome separation checkpoint that regulates the anaphase-telophase transition. *BioEssays* **37**, 257–266 (2015).
2. Karg, T., Warecki, B. & Sullivan, W. Aurora B-mediated localized delays in nuclear envelope formation facilitate inclusion of late-segregating chromosome fragments. *Mol. Biol. Cell* **26**, 2227–41 (2015).
3. Afonso, O. *et al.* Feedback control of chromosome separation by a midzone Aurora B gradient. *Science* **332**, 332–6 (2014).
4. Li, M., Dong, Q. & Zhu, B. Aurora Kinase B Phosphorylates Histone H3.3 at Serine 31 during Mitosis in Mammalian Cells. *J. Mol. Biol.* 2–5 (2017). doi:10.1016/j.jmb.2017.01.016
5. Hinchcliffe, E. H. *et al.* Chromosome missegregation during anaphase triggers p53 cell cycle arrest through histone H3.3 Ser31 phosphorylation. *Nat. Cell Biol.* **advance on**, 668–675 (2016).

LIST OF ABBREVIATIONS

APC	Astrocyte progenitor cell
BER	Base excision repair
CB	Cerebellum
CGNP	Cerebellar granule neuron progenitor
CFS	Common fragile site
CIN	Chromosomal instability
CNA	Copy number alteration
CNS	Central nervous system
CNV	Copy number variation
CSC	Cancer stem cell
CSC	Chromosome segregation checkpoint
Cycl	Cyclopamine
DDR	DNA damage response
DIPG	Diffuse Intrinsic Pontine Glioma
dsDNA	Double-strand DNA
E	Embryonic
EGL	External granule layer
EV	Empty vector
GIN	Genomic instability
GO	Gene ontology
HAT	Histone acetyl-transferase
HGG	High-grade glioma
HR	Homologous repair
IGL	Internal granule layer
IPC	Intermediate progenitor cell
LGG	Low-grade glioma
MB	Medulloblastoma
MCPH	Primary microcephaly disorder
MMR	Mismatch repair

NER	Nucleotide excision repair
NHEJ	Non-homologous end joining
NSC	Neural stem and progenitor cell
OPC	Oligodendrocyte progenitor cell
P	Postnatal
PCD	Programmed cell death
pNSC	Pons neural stem cell
PRC2	Polycomb repressive complex 2
PTCH1	Patched Homologue 1
PXA	Pleomorphic xanthoastrocytomas
RS	Replication stress
SAC	Spindle assembly checkpoint
scWGS	Single cell whole genome sequencing
SHH	Sonic Hedgehog
SMO	Smoothened Homologue
ssDNA	Single-strand DNA
SUFU	Suppressor of Fused Homologue
SVZ	Subventricular zone
TRC	Transcription-replication collision
UBC	Unipolar Brush Cells
UFB	Ultrafine DNA bridges
uRL	Upper rhombic lip
WHO	World health organization
WNT	Wingless
WT	Wild-type

Nederlandse Samenvatting (Dutch summary)

Kinderhersenkanker

Hersenkanker is de belangrijkste solide tumor bij kinderen. Jaarlijks wordt in Nederland bij meer dan 100 kinderen hersenkanker vastgesteld. Hoewel ruim 70 procent geneest, worden overlevenden op latere leeftijd geconfronteerd met verscheidene neurologische problemen, voornamelijk als gevolg van de lage specificiteit van de huidige behandelstrategie (chemotherapie, radiotherapie en / of chirurgische resectie). Deze gevolgen weerspiegelen zich tot in de volwassenheid wanneer overlevenden moeilijkheden ondervinden om aan de samenleving deel te nemen. Dit vraagt om betere strategieën om de ziekte aan te pakken, van een beter begrip van de moleculaire architectuur van de hersentumoren tot de ontwikkeling van behandelingen die specifieker gericht zijn op de tumorcel en gezond hersenweefsel onbeschadigd laten.

De term hersenkanker duidt een verscheidenheid aan verschillende tumortypen aan die afkomstig zijn van het centrale zenuwstelsel. Medulloblastoom is de meest voorkomende maligniteit van de hersenen bij kinderen en bevindt zich in het achterste gebied van de hersenen, het cerebellum. De tumoren die zich vaak in de cortex of hersenstam bevinden worden gliomen genoemd en vertegenwoordigen een andere belangrijke vorm van kinderhersenkanker. Gliomen kunnen laaggradig zijn en zijn dan meestal te genezen, maar ze kunnen ook hooggradig zijn en zijn dan zeer moeilijk te behandelen.

Hersenontwikkeling

Al vroeg in de menselijke ontwikkeling (ongeveer 3 weken na bevruchting) begint de basale hersenstructuur van de toekomstige foetus te ontwikkelen en dit duurt tot ruim 2 jaar na de geboorte. Gedurende deze lange periode delen hersencellen zich intensief om de volledige hersenstructuur te kunnen vormen, die meer dan 100 miljard cellen bevat in het volwassenen zenwustelsel. De deling van hersencellen is afhankelijk van verschillende signaleringsroutes, die de juiste deling van neurale cellen in tijd en ruimte regelen. Elke afwijking in die signaleringsroutes zal de normale ontwikkeling van de hersenen belemmeren. Heel vaak worden erfelijke

fouten in deze groeiroutes gevonden bij kinderhersenkanker. Daarom kunnen hersenkankers bij kinderen worden gedefinieerd als een ontwikkelingsziekte, waarbij de normale ontwikkeling als het ware een verkeerde wending neemt. Deze fouten zorgen ervoor dat de neurale cel zich continu kan delen, wat uiteindelijk leidt tot een tumormassa of hersenkanker.

Genoominstabiliteit

Om functioneel (hersen)weefsel op te bouwen, ondergaan cellen een vermeerderingsproces dat celdeling heet. Celdeling houdt onder meer in dat het volledige repertoire van genen (het genoom) wordt doorgegeven aan twee dochtercellen. Tijdens elke deling worden cellen geconfronteerd met bedreigingen die, als ze niet worden tegengegaan, het genoom kunnen beschadigen en tot genoominstabiliteit kunnen leiden. Genoominstabiliteit is een kenmerk van kanker, aangezien het bij meer dan 80 procent van de kankers aanwezig is in de vorm van genetische mutaties (kleine fouten in het DNA) en aneuploïdie (wanneer hele delen van chromosomen worden gewonnen of verloren gaan). Aangenomen wordt dat genoominstabiliteit aanwezig is - en beperkt blijft tot niet-pathologische niveaus - tijdens normale hersenontwikkeling als gevolg van de hoge delingssnelheid van de neurale cellen.

Doel van dit proefschrift

Het werk beschreven in dit proefschrift onderzoekt de rol van genoominstabiliteit bij het ontstaan van hersenkanker bij kinderen. Ons onderzoek maakt de weg vrij voor de ontdekking van nieuwe therapeutische doelen, die in de toekomst kunnen worden gebruikt om deze dodelijke ziekte beter te behandelen.

Samenvatting van de hoofdstukken

In het inleidende **Hoofdstuk 1** beschrijven we verstoring van genoomonderhoudspaden als een onderbelichte oncogene facilitator bij kinderhersenkanker, ondanks dat reeds bekend is dat genoominstabiliteit veelvuldig voorkomt in sommige SHH-MB (medulloblastoom) - en HGG (hooggradig glioom) -

subtypes. Daarom gaat **Hoofdstuk 2** verder in op de rol van genoominstabiliteit in de ontwikkeling van tumoren gezien door de lens van ontwikkelingsbiologie. Het beschrijft hoe wisselende afhankelijkheid van de verschillende genoomonderhoudspaden tijdens de normale ontwikkeling van het centrale zenuwstelsel, tegelijkertijd momenten van kwetsbaarheid creëert voor ontwikkelingsstoornissen en tumorvorming.

Zoekend naar de vroegste oorsprong van de hersentumoren, gaat **Hoofdstuk 3** in op de rol van dynamische genexpressie in de SHH-MB cel-van-oorsprong, de cerebellaire granule neuron progenitor (CGNP). Hier ontdekken we dat leeftijdsspecifieke genexpressie programma's van de cel-van-oorsprong worden weerspiegeld in SHH-MB, wat het mogelijk maakt om SHH-MB nauwkeuriger onder te verdelen in subtypes. Dit onderzoek heeft verder geleid tot de identificatie van een verrijking van processen die verband houden met celdeling en genoomstabiliteit in neonatale CGNPs, die we kunnen terugvinden in een specifieke groep SHH-MB patiënten. Deze bevinding suggereert dat een normale spurt in CGNP celdeling rondom de geboorte een kritieke gebeurtenis kan zijn tijdens de cerebellaire ontwikkeling, die het risico op het ontwikkelen van een medulloblastoom met zich meebrengt als gevolg van verhoogde genoominstabiliteit.

Daarom hebben we in **Hoofdstuk 4** onderzocht wat de gevolgen zijn van genoominstabiliteit tijdens cerebellaire ontwikkeling en of dit zou kunnen leiden tot het ontstaan van medulloblastomen. Door middel van een transgeen muismodel gebaseerd op *Mad2l1* en *Trp53* conditionele knock-out allelen, waren we in staat om specifiek chromosomale instabiliteit (CIN) te veroorzaken in de MB cel-van-oorsprong. We ontdekten dat het erop lijkt dat cerebellum CIN niet tolereert en alleen gezonde cellen laat overleven. We vonden dan ook geen bewijs voor het ontstaan van medulloblastomen in ons transgene muizenmodel.

In **Hoofdstuk 5** zoeken we naar de identiteit van de histon H3.3-mutante ponsglioom cel-van-oorsprong. We hebben daarvoor het gebruik van de verschillende histonvarianten tijdens de vroege postnatale ontwikkeling van de achterhersenen in kaart gebracht; en gevonden dat het pons-gebied van de achterhersenen meer H3.3

gebruikt dan andere hersendelen. Op basis van deze informatie konden we een pons neurale stamcel isoleren die tijdens het kweken het juiste gebruik van histon H3 varianten behield, evenals juiste genexpressie patronen en gevoeligheid voor signaleringsroutes. Al met al legt dit hoofdstuk de basis voor de identificatie van de mutante H3.3 ponsglioom cel-van-oorsprong, wat nieuwe mogelijkheden biedt voor het maken van betrouwbare wetenschappelijke modellen van het ponsglioom.

Om een beter begrip te krijgen van hoe het H3.3 mutante glioom ontstaat op moleculair niveau, gebruikt **Hoofdstuk 6** een celkweekmodel om de gevolgen van histon H3.3 mutaties op het behoud van genoomintegriteit te bekijken. In dit hoofdstuk ontdekken we dat in de aanwezigheid van mutant H3.3 een kwetsbaarheid voor door replicatiestress (=verhoogde/verstoorde celdeling) geïnduceerde genoominstabiliteit ontstaat. Dit hoofdstuk laat duidelijk zien dat kleine veranderingen in histonen grote pleiotrope gevolgen kunnen hebben, van verstoring van genexpressie tot schade aan het genoom.

Tenslotte geven we in **Hoofdstuk 7** duiding aan de resultaten die in dit proefschrift worden beschreven.

Acknowledgements

Naturally, I would have never been able to accomplish this research journey without the help, support and input of so many of you. These PhD years enabled me to grow not only as a scientist but also as a person -- being friends, colleagues or family, I am profoundly grateful to all of you who enriched my life over the past 6 years.

First and foremost, **Sophia**, thank you for believing in me and taking me in as one of your first PhD students. I have come to really appreciate your knowledge and all the lessons and stories you learned from your own experience and you wanted to pass on. But mostly, your way of keeping our research humane was a great motivator to me, to keep me going in this PhD. Thank you for being encouraging and finding the right words in the downs and speaking the good in the ups. The scientist and the person I have become owe you a lot. I wish you all the success in the future of the lab and your career.

I would like to thank my promoter, **Prof. Eveline de Bont** for making this PhD possible and reading & accepting this thesis.

I want to thank the members of the reading committee, **Prof. Hein te Riele**, **Prof. Marcel van Vugt** and **Prof. Bart Eggen** for taking the time to critically read my thesis.

Most importantly, I would like to thank all the patients and their parents who agreed to donate samples over the years that enabled our research, which would have been impossible without the commitment of **Prof. Eelco Hoving** and **Prof. Eveline de Bont.**

Special thanks to my Paranymphs, **Tosca** & **Harm Jan**. **Tosca,** thank you for being such a wonderful colleague and a great friend. I enjoyed so much working with you, learned a lot from your optimism and your chill-attitude. I wish you all the best for this last run, I have no doubt you will make it work. **Harm Jan**, I am grateful for so many things. For being my IT troubleshooter-rescuer 24/7, being my steady person from the beginning till the end of my Groningen years, for your support and patience, all the great talks from which I learned so much – for the music, the books, the movies, the psychology talks – all of it made my Groningen-life so much better.

Inna & **Eduardo**. **Ed**, thanks for joining the lab although only at the end, you made such a big impact on my PhD and on our research. I loved our talks in the corridor, at the coffee machine or in the bacteria lab. I wish you all the best in your future endeavours

and I cross my fingers for a successful last year of PhD. My dear **Inna**, I am very grateful we got to be colleagues and friends, you are such a wonderful person and I hope to visit you in Indonesia when the time is right again (and when you actually move there). Best of luck in the thesis writing, you will rock it!

Marlinde & **Walderik**, it was so great to share the office with you (although dusty) we always found a way to be serious and have fun at the same time. I keep so many good memories from these times. **Marlinde**, thanks for being my CDP buddy for the time being, it was great fun working with you :) I wish you the best in Utrecht. **Frank & Hassan**, thank you for being so resourceful, for the help in the lab, the support, the science and career advice. **Tiny**, thank you for being so motherly towards me (and all of us), for all the cheering up, the support (in the lab and emotional), I wish you all the best :)

I want to address a special thanks to the **Foijer lab** people. **Floris**, thank you for believing in me and giving me this postdoc opportunity in your lab. But mostly, thank you for taking up the role of mentor and for pushing me to explore what is that I really aspire to. **Sahil, Jonas, Michael**, guys, thanks for being supportive in the very last bit of my thesis writing and in the job search and mostly for putting on this bouldering group, that was so good and I hope you keep it going! **Sahil**, I am so happy to have met you, worked with you and have you as a real friend, I wish you the best of the best personally & professionally. **Christy** & **Andréa**, you girls rock it, you always impressed me and I wish you all the success, you deserve it! **Petra** thanks for being the head & heart of the lab and a great teacher! **Amanda, Catalina, Laura, Siqi, Lin, ex-foijer Klaske, Judith** & **Bjorn**, CRISPR and sequencing people **Mathilde, Jonas, Réné, Othman, Diana, Hilda, Nancy** & the **De Haan lab**, thank you for making the first floor lab such a great team to work with.

Noémie et **Alyssia**. Quelle rencontre et quel trio :) Je vous dois une de mes meilleures périodes Groningoise. Merci pour les soirées, les conversations, votre soutien inconditionnel quand les choses furent un peu plus compliquées, notre folie quand la vie était un peu plus légère – l'escalade, le boulder, le ski nautique, les bières au Koffer, les fleurs & empanadas du marché, les apérols-spritz, Sixto Rodriguez, le wadlopen, le voyage à New York, la semaine à Vienne, le week-end à Paris. Je nous manque :)

Las Chicas -- Roxana, Elena & **Bianca --** what a pleasure girls. The hang outs, the talks, the listening, the growth. I am so glad you are part of my life. Thank you for being my substitute family and cheers to so many more moments together. O mie de mulțumiri, te ador :) **& Bia**, special thanks for being the best pandemic buddy ever and an ever-growing climber. But mostly, thanks for listening and being SO supportive and patient with me.

Lucia & **Simone**. I always say that you are part of my first life in Groningen, and I am glad you are still part of it now. Thanks for being so supportive in my PhD & personal life.

Karmen i **Ana,** cure, hvala vam na pića, na razgovore i podršku oko doktorata. Sa vama sam se uvijek osječala da se mogu žaliti koliko hoću jer jednostavno znate kakva je to borba. Ogroman vam "hvala" za to! Ana, uskoro je tebe red :)

Ignasi, it was so great to have you as a friend in Gro and maybe again in Amsterdam very soon. Thanks to the **Phillips crew** for the hang outs, theclimbing & bouldering and for really making me feel part of the company ^^

Deepani & **Virginia**, PhD ladies, finally my turn :) Thank you girls for the fun we had together.

And thanks to so many others I met for a shorter or longer period: my climbing partners **Katherine** & **Takuya**, **Arthur** for Saturday coffee & stroopwaffels, hematology people **Susi**, **Kathi**, **Aida**, **Aysegul**, **Henny**, **Valerie** and so many others (please take no offense if I haven't mentioned your name!).

Faustine et **Aurélie**. Merci infiniment – je pense que des mots seuls ne suffisent pas – pour votre soutien, votre patience et votre écoute pendant ces années de doctorat, mais aussi quand j'en avais le plus besoin. Tout simplement, merci d'être toujours là.

Servane, merci d'être ma *go-to-person* quand je me trouve face au mur professionnellement. C'est incroyable à quel point tu sais toujours me redonner la gnak et la motivation !

Vincent, Chloé et **Fanny**, merci mes amis de toujours avoir pris de mes nouvelles et de vous être toujours intéressés à mon boulot et à ma recherche.

Dragi **Tata**, **Mama**, **Ivana**, **Tomo** i **Kata**. Ogromni « Hvala » na vašu ljubaznost, podržanost, predanost i što ste znali pronaći prave riječi kad bih bila pod stresom ili uznemirena, što ste podnjeli moju ponekad tešku osobnošću (već od malena!). Hvala vam što ste me izgradili dovoljno snažnom da postignem sa doktoratom. Najdraže sestre **Kata** & **Ivana** hvala vam na posjete u Amsterdamu i Groningenu, baš me usrečilo! **Tomo**, hvala na duge razgovore i za nezaboravljiv vikend u Parizu. **Carla** und **Tomi**, danke meine Lieben dass du immer ein Lächeln auf mein Gesicht ziehst. Hvala ostalim članovima obitelji, **Striku Hrvoju**, **Nadi**, **Tetki Seki**, **Viboru**, **Mirni**, **Mihi** što su uvijek pitali kako ide moj doktorat. Evo ga :). **Zrinka** draga, hvala ti što si mi uvijek bila kao sestra, i hvala ti što si me napravila ponosnom na doktoratu i na postignuću.

*I zauvijek misao na **Didu Slavku**, **Baku Veru**, **Baku Anđu** i na **Ivu**.*

A

About the Author

Irena Bočkaj was born in Mostar (Bosnia and Herzegovina, former Yugoslavia) in September 1988. At the age of three, she moved with her family to the west of France, in the city of La Roche-Sur-Yon, where she received her primary and secondary education. In 2007, she started her university education at the Faculty of Pharmaceutical Sciences, University of Nantes. Irena showed an interest for oncology and neurology early in her education when she attended her first internship in the lab of Pr. Stephane Birklé, who also later became her Pharm. D. thesis supervisor. This first research experience opened Irena's scientific career. Eager to learn more about the diseased brain functioning and modelling, Irena travelled to Australia to learn about Parkinson's disease in the lab of Pr. George Mellick. During her time at the Griffith Institute for Drug Discovery (Brisbane, Australia), the numerous research teams and topics she mingled with raised in her a deep curiosity about *cancer*, and the will to participate in research that was meaningful to her. In the next academic year, she decided to join the oncology research master at the University of Toulouse. During her research master's internship, Irena joined the neuro-oncology lab of Dr. Olaf van Tellingen at the Netherlands Cancer Institute in Amsterdam where she was able to bridge her two domains of growing expertise: brain and oncology. During this internship, she worked on a drug-screen to identify chemical compounds that were able to effectively pass through the blood-brain barrier and target the tumor brain tissue efficiently. In 2014 she successfully obtained her research Master's degree from the University of Toulouse as well as her Pharm. D. doctorate degree from the University of Nantes. Very soon after, Irena joined the lab of Dr. Sophia Bruggeman as a PhD student to study pediatric brain cancer (Department of Pediatric Oncology and Hematology at the UMCG). The work she completed during this PhD program is presented in this book. In 2019, after completing her PhD training, Irena moved to the lab of Pr. Floris Foijer where she worked for one year as a postdoctoral-fellow. Irena will continue working on neuro-related disorders as a Scientist at uniQure (Amsterdam), this time developing gene therapies.